The Pennsylvania State University

The Graduate School

Department of Electrical Engineering

SIGNAL PROCESSING SCHEMES FOR BROADBAND FSO-RF HYBRID WIRELESS COMMUNICATION SYSTEMS AND THEIR PERFORMANCE

A Thesis in

Electrical Engineering

by

Sangwoo Lee

Submitted in Partial Fulfillment
of the Requirements
for the Degree of

Doctor of Philosophy

Aug 2007

The thesis of Sangwoo Lee was reviewed and approved* by the following:

Mohsen Kavehrad
William L. Weiss Professor of Electrical Engineering
Thesis Advisor
Chair of Committee

Shizhuo Yin
Professor of Electrical Engineering

Aylin Yener
Associate Professor of Electrical Engineering

Jesse Barlow
Professor of Computer Science and Engineering

W. Kenneth Jenkins
Professor of Electrical Engineering
Head of the Department of Electrical Engineering

*Signatures are on file in the Graduate School

ABSTRACT

In semiconductors, an empirical observation known as Moore's law states that the number of transistors on an integrated circuit for minimum component cost is doubled every 24 months. In communications, faced with the recent rapid growth of internet, data services, and needs for multimedia services, there have been similar efforts to establish a similar Moore's law of bandwidth. In cable environments, modem technologies with higher bandwidth can advance rapidly, whereas in wireless environments, due to the highly regulated nature and scarcity of the RF spectrum, it can be harder to see the advent of truly wideband modem technologies in the near future.

It is well-known that through clouds or fog, free-space optical (FSO) links suffer from severe attenuation whereas RF links suffer from slight attenuation. On the other hand, in rain, FSO links undergo trivial attenuation while RF links experience high attenuation. Knowing that RF paths and FSO paths are complementary, combining the attributes of a higher data rate but bursty link (FSO) with the attributes of a lower data rate but reliable link (RF) is expected to yield attributes better than either one alone, enabling a high availability link at high data rates.

In this thesis, we propose two solutions which can aid existing wireless technologies. First, we propose FSO wireless communications as an attractive alternative to RF wireless communications. Second, as an aid to the weather-dependent FSO links, we propose multi-input-multi-output (MIMO) links with enhanced bandwidth efficiency. Whereas the traditional FSO implementations have been dependent more on truly optical devices, we focus more on FSO by digital signal processing (DSP) technologies in this

thesis. As for the MIMO RF link, we study in the context of well-known MIMO-OFDM (orthogonal frequency division multiplexing) links with coding, but we further aim at increasing the spectral efficiency by use of DSP techniques known as channel shortening equalizers. For both the FSO link and the MIMO-OFDM link, the premise in this thesis is that the use of DSP technologies is cost-effective enough to help both the RF and FSO links.

TABLE OF CONTENTS

GLOSSARY

Mathematical Notations

Notation	Description
Lower case bold	Column vector
Upper case bold	Matrix

Acronyms

Notation	Description
AoA	angle of arrival
AoD	angle of departure
AS	angle spread
ASNR	arithmetic SNR
ASP	antenna spacing
BER	bit-error rate
BPF	bandpass filter
BS	base station
BTS	basestation transceiver system
CDF	cumulative density function
CDMA	code division multiple access
CIR	channel impulse response
COTS	commercial off-the-shelf
CP	cyclic prefix
CSE	channel shortening equalizer (equalization)
CSI	channel side information
CSIT	channel side information at the transmitter
DD	direct detection
DFE	decision feedback equalization (equalizer)
DMT	discrete multitone

DoT	direction of travel
DSL	digital subscriber loop
DSP	digital signal processing
EC	Eigenvector
EDFA	erbium-doped fiber amplifier
EV	Eigenvalue
FDMA	frequency division multiple access
FEQ (FDE)	frequency domain equalizer (equalization)
FSO	free-space optical
FSOW	free-space optical wireless
GNR	gain-to-noise ratio
GSNR	geometric SNR
HPF	highpass filter
ICI	intercarrier interference
IM	intensity modulation
ISI	intersymbol interference
LC-SLM	liquid crystal spatial light modulator
LE	linear equalization (equalizer)
LED	light-emitting diode
LEO	low-earth orbit
LMDS	local multipoint distribution system
LMMSE	linear minimum mean-squared error
LMS	land mobile satellite
LMS	least-mean-square
LNA	low-noise amplifier
LOS	line-of-sight
LPF	lowpass filter
MAN	metropolitan area network

MC	multicarrier
MCM	multicarrier modulation
MIMO	multi-input-multi-output
MISO	multi-input-single-output
ML	maximum-likelihood
MLSD	maximum likelihood sequence detection
MS	mobile station
MSE	mean-square-error
NGO	non-geostationary orbit
NLE	nonlinear equalization (equalizer)
NLOS	none-line-of-sigh
OFDM	orthogonal frequency division multiplexing
OOK	on-off keying
PAS	power azimuth spectrum
PDF	probability density function
PM	phase mask
PTEQ	per-tone equalization (equalizer)
RLS	recursive-least-square
SCIR	shortened channel impulse response
SER	symbol-error rate
SFBC	space-frequency block coding
SINR	signal to interference plus noise ratio
SISO	single-input-single-output
STBC	space-time block coding
STTC	space-time trellis code
SVD	singular value decomposition
TDMA	time division multiple access
TEQ	time-domain equalization (equalizer)

TIR	target impulse response
UEC	unit-energy constraint
UTC	unit-tap constraint
WLAN	wireless local area network
WPM	wavelet packet modulation
WPT	wavelet packet tree
WSS	wide-sense stationary
ZF	zero-forcing

LIST OF FIGURES

LIST OF TABLES

ACKNOWLEDGEMENTS

I wish to express my sincere gratitude to Professor Mohsen Kavehrad, my thesis advisor. He accepted me as his student, and has been providing me not only with academic advice but also with lifetime wisdom. He gave me opportunities to work on this topic, and I could learn communications by doing research with him. I would like to also thank my other committee members, Dr. Yin, Dr. Yener, and Dr. Barlow for their time, advice and interest in my graduate researches. My special thanks go to my parents, my brother, and my sisters for all of their everlasting love, support, and understanding of me during my study in the US for the last 6 years. Finally, I'm thankful to all the members at CICTR for their friendship and advice.

Chapter 1

Introduction

In semiconductors, an empirical formula known as Moore's law predicts that the number of transistors on an integrated circuit for the minimum component cost is doubled every 24 months [**48**]. In communications, ever-increasing demand for internet, data services, and multimedia services have triggered similar research efforts to establish a similar Moore's law of bandwidth as in [**49**]. However, in communications, unlike in semiconductors which are governed mostly by enabling technologies and the market, we have one more constraint, due to the scarce availability of the RF spectrum. For example, in cable environments such as a digital subscriber loop (DSL) or in fiber optics, modem technologies with a higher bandwidth can advance rapidly. However, in wireless environments, due to the highly regulated nature of the RF spectrum, it might be harder to see the advent of truly wideband modem technologies in the near future.

In this thesis, we investigate the FSO-RF hybrid system where the complementary properties of the two systems and the channels are exploited. First, we propose an FSO wireless communication link as an attractive alternative to the RF wireless communications. Second, as an aid to the weather-dependent FSO links, we propose an RF MIMO link with enhanced efficiency. On the FSO link, whereas the traditional implementations have been dependent on truly optical devices, we focus more on DSP technologies. On the MIMO RF link, we investigate in the context of well-known MIMO-OFDM links with space-frequency coding plus time-domain equalization to

further increase the spectral efficiency. For both the FSO link and the MIMO-OFDM link, the philosophy in this thesis is that the use of DSP schemes is cost-effective enough, such that the technique can help both the RF and FSO links.

1.1 Motivation for the FSO System

FSO communication has been recently attracting considerable attention for a variety of applications [**35 - 40**]. It is well-known that FSO links suffer from severe attenuation through clouds or fog, whereas RF links suffer only slight attenuation in the same environment. On the other hand, in rain, FSO links undergo trivial attenuation whereas RF links experience high attenuation. Knowing that RF paths and FSO paths are complementary, combining the attributes of a higher data rate bursty link (FSO) with the attributes of a lower data rate reliable link (RF) is expected to yield attributes better than either alone.

FSO is a line-of-sight (LOS) technology using lasers or light emitting diodes (LED) to provide optical bandwidth connections that can transceive voice, video, and data information on invisible beams of light through the atmosphere. On the deployment side, implementations at a data rate of 2.5Gbps for link distance of up to 4km have been proven effective.

Certain characteristics of FSO make it attractive for wireless communications. First, it does not require a spectrum license. Second, its relatively narrow beamwidth enables interference-free communications between transceivers. Third, FSO's no-license availability and interference-free operation enables data transmissions at very high rates,

with the capacity limited only by enabling technologies. Fourth, its narrow beamwidth renders it relatively safe from tapping, unless the line-of-sight is physically intercepted, thus requiring no extra security measures.

By far, FSO has been considered mostly in fixed point-to-point applications to help existing networks such as metropolitan area network (MAN). It also has good potential as the last-mile connectivity providing technology to end-users. FSO technology can be used for backhauls such as local multipoint distribution system (LMDS) or cellular backhaul as well as gigabit Ethernet. FSO-based products can also be used for mobile wireless backhauls, including applications for BTS (basestation transceiver system) backhaul, WLAN (wireless local area network) hot spot connectivity, and sector re-use. Most recently, there have been ongoing research efforts to further extend the success of the ground FSO to the areas of ground-to-air links and of air-to-air links [**38 - 40**].

1.2 Motivation for the MIMO System

The interest in MIMO technology can be explained by the basic information theory. In a deterministic MIMO channel, the capacity of the channel is given by Eq. **1.1** **[32]**.

$$C = \max_{Tr(K_c)\le N} \log_2\left(\det\left[I_M + \frac{\gamma}{N}\mathbf{H}^H\mathbf{K}_c\mathbf{H}\right]\right) \text{ bits/(s Hz)},$$

γ: received SNR, $\mathbf{H}$: channel matrix, Eq. **1.1**

N: number of transmit antennas, M: number of receive antennas,

K_c covariance of the input $\mathbf{C}$

With the traditional SISO system, the only way we can improve the capacity is through higher received SNR at the receiver. In a MIMO system, the authors of [**68 - 69**] showed that the capacity grows linearly with $r = \min(N, M)$. In other words, using the singular value decomposition on (SVD) **H** as in Eq. **1.2**, it can be shown that the channel capacity with CSIT (channel side information at the transmitter) [**70**] can be expressed as a linear summation of its subchannels as in Eq. **1.3**. Therefore, in MIMO systems, we can not only increase the received SNR, but also increase the number of antennas, which will bring about linear increase in the channel capacity.

$$\mathbf{H} = \mathbf{U}\mathbf{D}\mathbf{V}^H, \quad \text{Eq. } \mathbf{1.2}$$

$\mathbf{U}$, $\mathbf{V}$: unitary matrices, $\mathbf{D}$: a diagonal matrix of singular values σ_i

$$C = \max_{\sum_{i=1}^{r}\gamma_i = \gamma} \sum_{i=1}^{r} \log_2(1 + \gamma_i \lambda_i), \quad \text{Eq. } \mathbf{1.3}$$

γ_i : transmit power distribution, $\lambda_i = \sigma_i^2$, r :rank of $\mathbf{H}$

In the past, the use of antenna arrays was highly restricted by high costs and size factors. Hence, more research efforts were made in the areas of resource reuse techniques such as time-division multiple access (TDMA), FDMA (frequency-division multiple access), and CDMA (code-division multiple access). However, with the advent of low-cost antenna arrays, the MIMO system is emerging as a promising technology for the future broadband wireless communications.

1.3 Motivation for a Hybrid System

Communications via RF signals are reliable but cannot support emerging high data rate services unless they use a large portion of the costly radio spectrum. FSO

wireless communications offer enormous data rates but operate more at the mercy of the atmospheric environment, such as scintillation and multi-scattering through fog and clouds. Since RF paths are relatively immune to these phenomena, combining the attributes of a higher data rate but bursty link (FSO) with the attributes of a lower data rate but reliable link (RF) could yield attributes better than either one alone, enabling a high availability link at high data rates. Another motivation for a hybrid is that the initial stages of FSO links such as acquisition, synchronization and light beam tracking needs assistance from the RF link.

Theoretical studies on FSO-RF hybrid links can be found in the literature. In [**11**], an RF channel model in the beyond-10GHZ spectrum was characterized in the context of weather-attenuation (by gas, fog, cloud, and rain). In addition, a cloud channel was investigated in the sense of attenuation and scattering. Based on the impulse response models for both FSO and RF links, the author further investigated the capacities of both links in various snapshots. Even though we can generate cdf (cumulative density function) or pdf (probability density function) of various signal attenuation factors and distortion factors of both FSO and RF links, we actually need a joint cdf (or pdf) of dominant factors, since it might be hard to consider all factors. Since such a joint cdf was not available, the approach adopted in [**11**] was to consider two extreme cases as bounds: the perfect dependent case and the perfect independent case. The perfect dependence assumption is that if one factor increases in its severity, all the other factors will follow the same trends. For example, it is assumed, if we have heavy rain, thick clouds will also follow. The perfect independent condition assumes that different factors are uncorrelated in their behaviors. Assuming these two ideal conditions, the joint cdf of capacity in the

air-to-ground uplink scenario was derived in [**11**]. In the case of perfect dependence, when the FSO subsystem suffers from low availability due to through-clouds scattering, the RF subsystem suffers too. But the fluctuation of the RF subsystem in the perfect dependence case was found to be small, since rain attenuation by heavy rain occurs very scarcely. Also, the outage probability was found to be worse for perfect dependence than for the perfect independent case. As a conclusion, in the case of perfect independence, or an uncorrelated case, we can expect the FSO-RF hybrid links to work like a diversity path. On the other hand, in the case of perfect dependence, or a highly correlated case, there is not much diversity gain.

One typical application of FSO-RF links is the battlefield scenario where the optical link can not only offer wideband beamwidth transmission with high security, but can also be reinforced by RF links to further improve reliability up to the military specifications. Fig. **1-1** depicts a typical battlefield scenario consisting of air-to-ground, ground-to-ground and air-to-air links between military vehicles, satellites and aerial vehicles. We can also employ RF MIMO links in this scenario.

Another scenario is non-military applications such as Fig. **1-2** where FSO can provide wide bandwidth and secure data communications between stationary fixtures such as building or base stations while RF links can provide high-mobility to the subscribers. An example of Fig. **1-2** is composed of many components. Between backbone networks, there are long-range links consisting of FSO-RF hybrid links. Received optical signals can be distributed within buildings using optical techniques, too [**52** - **55**].

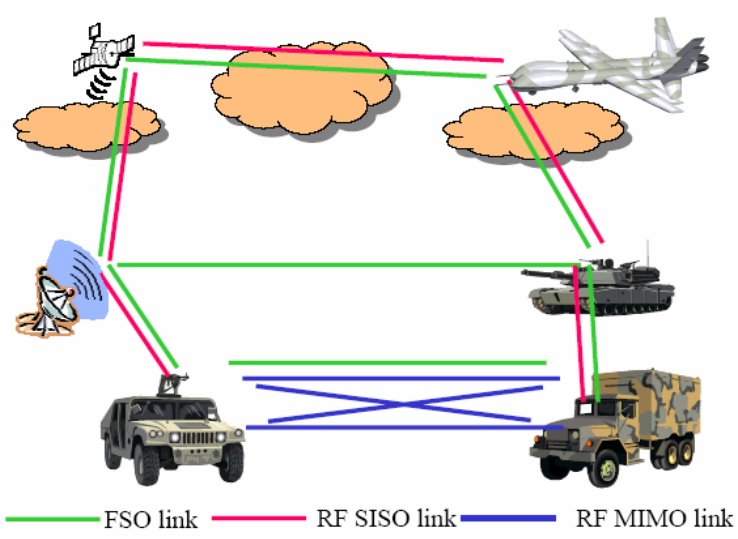

Fig. **1-1**: A military FSO-RF hybrid broadband wireless communication scenario with air-to-air, air-to-ground, ground-to-ground links

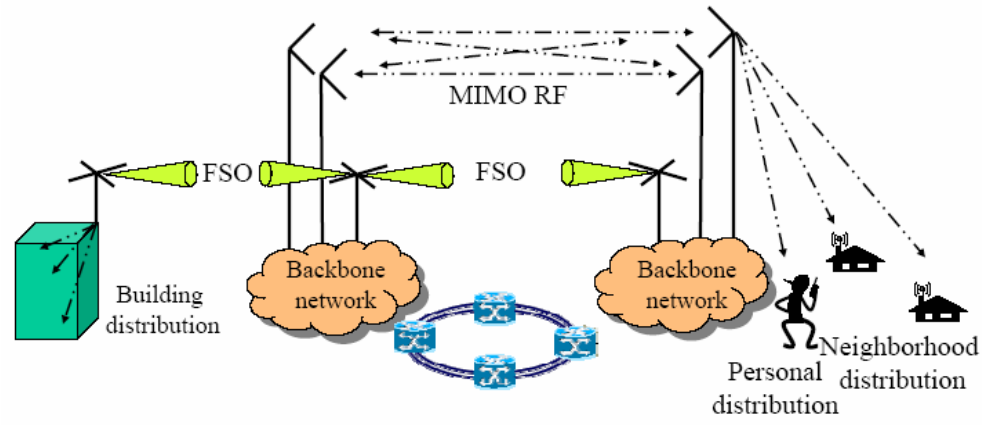

Fig. **1-2**: A typical FSO-RF hybrid broadband wireless communication scenario

1.4 Research Objective

The premise of this thesis is that the advantages of the FSO-RF hybrid systems are already well understood and that the channel models for both the RF and the FSO links are readily available. We thus focus only on appropriate signal processing schemes. In this thesis, first, on the FSO link, unlike traditional FSO systems which are heavily dependent on optical signal processing devices, we aim to devise electrical signal processing schemes for the FSO, such that reliable FSO links can be built with commercial off-the-shelf (COTS) devices and well-known algorithms. Second, on the RF link, we can incorporate schemes such as MIMO, but due to the limited availability of the RF spectrum, we aim to enhance spectral efficiency on the MIMO link. Considering the limited volume of this thesis, we chose the FSO channel for a military application in the air-to-ground through clouds sense, and a non-military channel for RF MIMO investigations. Since we needed a well-established channel model with research interest in channel equalization, we adopted the IEEE 802.20 model based on the ITU single-input-single-output channel model, and extended it to MIMO channels.

The remainder of this thesis is composed as follows. In chapter 2, an FSO channel model that we adopted in this research is presented with its various aspects, as well as a basic introduction to our FSO system design and its building blocks. In chapter 3, an RF channel model is presented with both SISO/MIMO channel characteristics considered, in addition to our RF system design. In chapter 4, we will introduce channel-shortening equalization algorithms and apply them to FSO channels, and will review their performance in various metrics. We will also evaluate its bit-error rate (BER) in

connection with the Viterbi equalizer and compare its performance with other conventional equalization schemes. Since we consider a scenario where an aerial vehicle is involved, we will consider the issues of mobility also. In chapter 5, we will further extend this TEQ (time-domain equalization) to MIMO TEQ, and see how it performs when combined with several space-frequency block code (SFBC) examples. In chapter 6, we further discuss various higher order SFBC cases combined with MIMO TEQ. In chapter 7, we will re-visit the concept of filterbank transceiver, and will introduce one example of FSO with the filterbank transceiver concept. In chapter 8, a summary and conclusions are presented, and finally, future research directions are proposed.

Chapter 2

FSO Models and Definitions

An FSO channel can be understood by the analogy with the well-understood RF channels. As has been well pointed out in [**11**], channel models for capacity evaluation or equalization consider only microscopic (or small-scale) fading factors, since we can ignore macroscopic (or large-scale) fading factors under the presence of adaptive transmit power control and slowly time-varying channel assumptions. Reference [**11**] introduced an FSO-RF hybrid channel model where the RF channel model is constructed based on an integrated set of four link attenuation models that estimates margin losses due to (1) rain, (2) fog/cloud, (3) atmospheric (water vapor and oxygen) attenuation and (4) multipath effects. Similarly, an FSO channel model considering mainly rain and fog attenuation, in addition to a small-scale fading factor such as scintillation, was introduced.

2.1 FSO Wireless Channel Model

An FSO channel is affected by various non-ideal effects [**12**]. Typically, light beam propagation through an atmospheric medium suffers from attenuation and distortion due to scattering and absorption [**11**]. However, once a proper communication window and wavelength are chosen, we can ignore absorption, and can assume that scattering is the main factor in the attenuation/distortion previously mentioned. When the atmospheric particle size is much smaller than the wavelength, the scattering behavior is

known to be Rayleigh. One example is air molecules. In this case, the scattered energy is nearly uniformly distributed in all directions. Thus, most of the scattered energy will be lost, being unable to arrive at the receiver. However, for commonly used communication windows, Rayleigh scattering is scarce because of the λ^{-4} dependence. Rather, particles comparable in size to the wavelength are the biggest challenge to FSO links, and cause Mie scattering. One example is the small water droplets in the atmosphere in the presence of haze or fog. Such scattering far exceeds the attenuation due to Rayleigh scattering and absorption. Under Mie scattering, the scattered energy's direction peaks in the forward direction, and continues to propagate. Thus, more energy can be captured at the receiver. Therefore, Mie scattering is better in the context of communications. These effects of scattering and absorption can be understood as similar to macroscopic (or large-scale) fading factors encountered in RF channels.

Another phenomenon to note in the FSO channel is turbulence, which is similar to microscopic (or small-scale) fading of RF channels. If a laser beam passes through the medium of air, even small inhomogeneities in refractive index along the propagation path distort the phase front, change beam direction (= beam wander), and cause light intensity fluctuation(= scintillation).

In [**11**], three FSO channel models were introduced, depending on the physical nature of the propagation-hampering medium: a fog-attenuated case, a cloud-attenuated-and-scattered case, and a rain-attenuated case. The main focus of this thesis is on the cloud-attenuated-and-scattered case, either air-to-ground, ground-to-air, or air-to-air. We will adopt already-published channel models to fit our research purpose, rather than suggest new channel models.

2.1.1 Physical Nature of Scattering

Scattering is basically a phenomenon of interactions between particles and a photon. For this phenomenon, we need to discuss single scattering first, and then extend it to multi-scattering. The energy loss of wave due to a single scattering incident on a particle is proportional to the extinction cross section $C_{ext}(r)$. After this energy loss, some portion of the EM (electromagnetic) wave is absorbed by the particle, whereas some other portion is scattered. This phenomenon can be described by Eq. **2.1**. In Eq. **2.1**, $C_{ext}(r)$ is given as the sum of the absorption cross section $C_{abs}(r)$ and the scatter cross section $C_{scat}(r)$. We also define the back scatter cross section $C_{back}(r)$.

$$C_{ext}(r) = C_{abs}(r) + C_{scat}(r),\ r: \text{particle radius} \qquad \text{Eq. } \mathbf{2.1}$$

Given the energy removal corresponding to $C_{ext}(r)$, we define albedo w, representing the probability of scattering, as in Eq. **2.2**. Another important definition is phase function $P(\theta)$ given in Eq. **2.3**, where $S_{11}(\theta, r)$ is a Mueller matrix element [**15**].

$$w = C_{scat}(r) / C_{ext}(r) \qquad \text{Eq. } \mathbf{2.2}$$

$$P(\theta, r) = \frac{4\pi\ S_{11}(\theta, r)}{k^2 C_{scat}(r)} \qquad \text{Eq. } \mathbf{2.3}$$

To extend this knowledge to the multi-scattering phenomenon, we need the particle size distribution $n(r)$, which defines the number of particles in a unit volume of between radius r and radius r + dr. Well-known formulas for particle size distribution follow either log-normal size distribution in the case of water clouds, or modified gamma distribution in the case of water drop size distribution. With this information, we can now

modify the previous formulas and obtain cross sections of absorption, scattering, or extinction, averaged by particle size distribution information, as in Eq. **2.4**. Furthermore, Mueller matrix elements and phase function are modified as in Eq. **2.5** and Eq. **2.6**, respectively.

$$K_i = \int_{r=0}^{\infty} C_i(r) n(r) dr \ , \ i \text{:abs, scat, or ext} \qquad \text{Eq. } \mathbf{2.4}$$

$$S_{ij}(\theta) = \int_{r=0}^{\infty} S_{ij}(\theta, r) n(r) dr \qquad \text{Eq. } \mathbf{2.5}$$

$$P(\theta) = \frac{4\pi \ S_{11}(\theta)}{k^2 k_{scat}} \qquad \text{Eq. } \mathbf{2.6}$$

Eq. **2.1** and Eq. **2.2** will be also changed to Eq. **2.7** and Eq. **2.8**.

$$K_{ext} = K_{scat} + K_{abs} \qquad \text{Eq. } \mathbf{2.7}$$

$$w = K_{scat} / K_{ext} \qquad \text{Eq. } \mathbf{2.8}$$

With this information of the multi-scattering case, we can understand a scattering phenomenon graphically by Fig. **2-1**, with the probability of absorption at each particle-wave interaction expressed by Eq. **2.9**. Angle θ between the incident photon and the scattered photon is governed by the phase function that we introduced in Eq. **2.6**. The distances between scattering events are known to follow an exponential distribution.

$$P_{absorption} = 1 - w \qquad \text{Eq. } \mathbf{2.9}$$

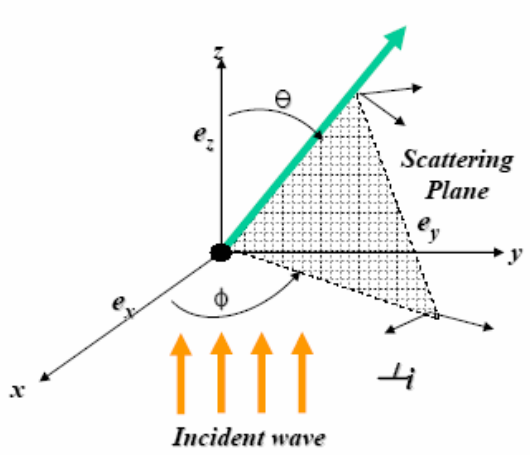

Fig. **2-1**: Light-particle interaction.

P(d): traveling distance between interactions, θ: scattering angle, Φ: scattering plane rotation, P_{scat}: probability of scattering at each interaction, P_{abs}: probability of absorption at each interaction

2.1.2 Attenuation and Scattering by Cloud

Under the effects of scattering in the through-clouds channel model, analogous to the multipath effects encountered in RF propagation scenarios, light signals coming from different paths introduce different time delays, broadening the impulse response. An analysis of this effect can be accomplished by Monte Carlo simulations [**13 - 14**].

Fig. **2-2** describes the Monte Carlo simulation scheme for light propagations with multi-scattering where θ is the polar angle between the incident ray and the scattered ray, ϕ defines the rotation angle of the scattering plane about the incident plane, d defines distances between collisions, and L defines the physical thickness of the cloud. It is assumed that a homogenous cloud lies within a cylinder. When a photon emission from a monochromatic 1550nm light source enters a cloud and collides with a particle, unless it

escapes, is absorbed or is received, it is described by aforementioned θ, ϕ and d. Respectively, the rotation angle ϕ is of uniform distribution between 0 and 2π, polar angle θ can be determined through Mie theory based on the size of the scattering particle, and distance d is of exponential distribution as in Eq. **2.10**. For light propagation, we also define a normalized distance known as optical thickness τ, defined by Eq. **2.11**, using Eq. **2.12**. For a given L, a higher d_{avg} value means a lower τ value or a less dispersive medium. Alternatively, there is a theoretical solution by Ciervo [**16**], which finds a closed-form CIR formula based on the radiation transport theory. However, this model is known to fit only optical thickness values higher than 15 [**11**].

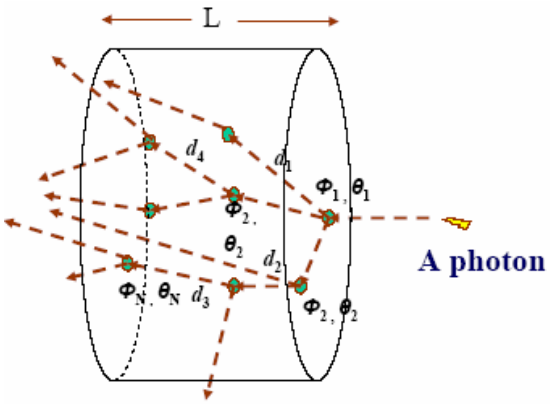

Fig. **2-2**: Light propagation with multi-scattering

$$f_D(d) = \frac{1}{d_{avg}} e^{-d/d_{avg}}, d \geq 0, d_{avg} > 0, \; d_{avg} \text{: mean free path distance} \qquad \text{Eq. } \mathbf{2.10}$$

$$\tau = L / d_{avg}, \text{ L: physical length of medium [m]} \qquad \text{Eq. } \mathbf{2.11}$$

$$d_{avg} = 1 / K_{scat}, \; d_{avg} \text{: average distance between scatterings [m]} \qquad \text{Eq. } \mathbf{2.12}$$

Overall channel modeling flow is presented in Fig. **2-3**.

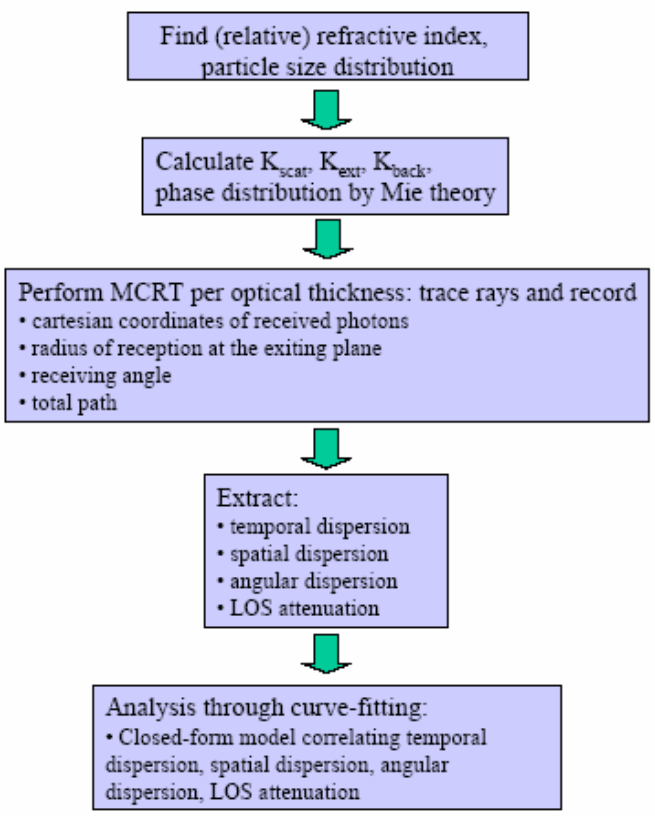

Fig. **2-3**: Overall channel modeling flow

There have been efforts to model the optical multi-scattering phenomenon by closed-form formulas as in [**22 - 25**]. Several models have been suggested in the literature as in Eq. **2.13**, Eq. **2.14** and Eq. **2.15**, all of which are defined in the optical power or intensity domain. A single gamma function of Eq. **2.13** and a double gamma function of Eq. **2.14** have been proposed so far. If the receiver aperture size is small, since only a small number of photons will reach the receiver after being scattered, we need to incorporate another path for light arriving at the receiver without being scattered, as in Eq. **2.15**. The frequency response of the optical scattering channel can be found by

Eq. **2.16**. In this thesis, we consider Eq. **2.13** introduced in [15] as one of the valid channel models.

Received optical power at the receiver can be described by Eq. **2.17** , using any of the power-domain CIRs given in Eq. **2.13**, Eq. **2.14** and Eq. **2.15**. Given the optical transmit signal $x(t)$ defined in the power domain, and the optical power channel $h(t)$, we can represent the received signal power by Eq. **2.18**.

$$h(t) = k_1 t \exp(-k_2 t),\ [m^{-2}] \qquad \text{Eq. } \mathbf{2.13}$$

$$h(t) = k_1 t \exp(-k_2 t) + k_3 t \exp(-k_4 t),\ [m^{-2}] \qquad \text{Eq. } \mathbf{2.14}$$

$$h(t) = k_1 t \exp(-k_2 t) + k_3 t \exp(-k_4 t) + k_5 \delta(t),\ [m^{-2}] \qquad \text{Eq. } \mathbf{2.15}$$

$$H(f) = \frac{k_1}{(k_2 + j2\pi f)^2} + \frac{k_3}{(k_4 + j2\pi f)^2} + k_5 \qquad \text{Eq. } \mathbf{2.16}$$

$$P_R(t, D_R, P_T) = h(t)\frac{1}{4} D_R^2 \pi P_T, \qquad \text{Eq. } \mathbf{2.17}$$

D_R : receiver aperture diameter [m], P_T : transmitter power [w]

$$y(t) = h(t) * x(t) \qquad \text{Eq. } \mathbf{2.18}$$

Fig. **2-4** shows CIRs in the power domain obtained by Eq. **2.13** for a typical cloud length of 1km and τ of 1,3,5,7. Likewise, Fig. **2-5** is for τ of 10, 20, 30, and 40. In order to see the severity of the dispersive CIR, we evaluated delay spread values in [sec] by finding the point where 99.9% of the total CIR energy can be found, and further divided it by symbol duration at a data rate of 5.333Gbps for normalization purpose. The results in Fig. **2-6** point out that for high optical thickness values, delay spread may be up to hundreds of symbols. Fig. **2-7** and Fig. **2-8** show the frequency responses of the CIRs of respective conditions.

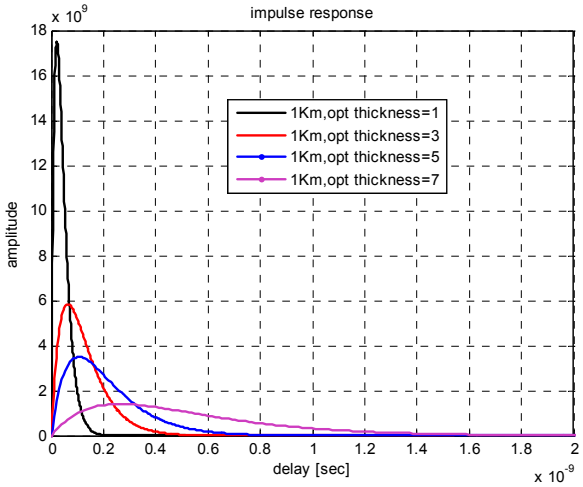

Fig. **2-4**: CIR in the power domain for a 1km-long cloud with τ = 1,3,5,7

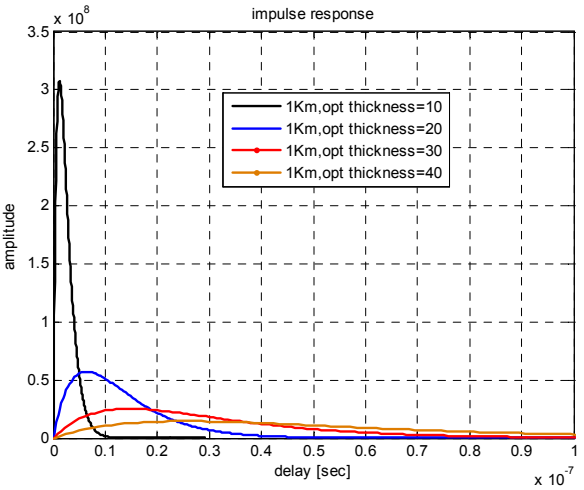

Fig. **2-5**: CIR in power domain for 1km-long cloud with τ = 10, 20, 30, 40

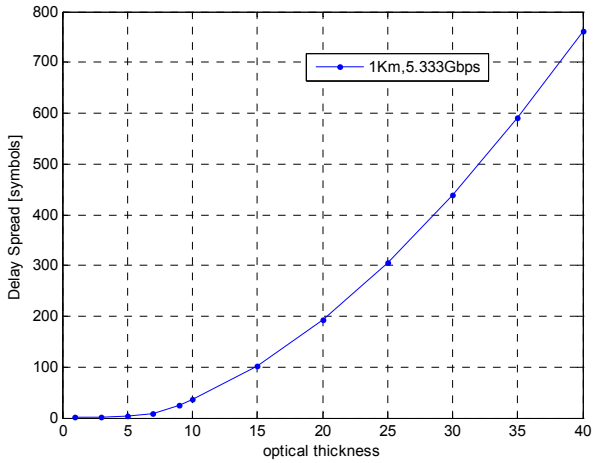

Fig. **2-6**: Channel delay spread in units of symbols for 1km-long clouds with τ values ranging from 1 through 40

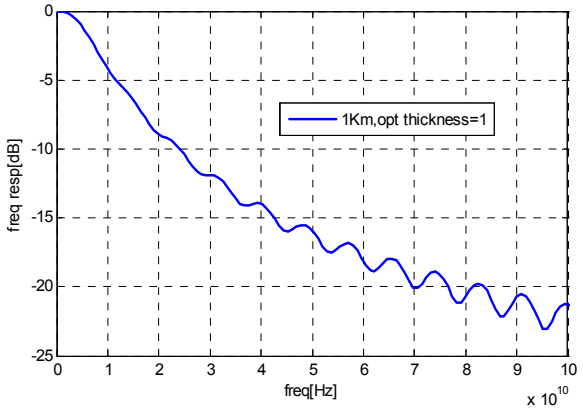

Fig. **2-7**: Frequency response of the CIR for a 1km-long cloud with $\tau = 1$

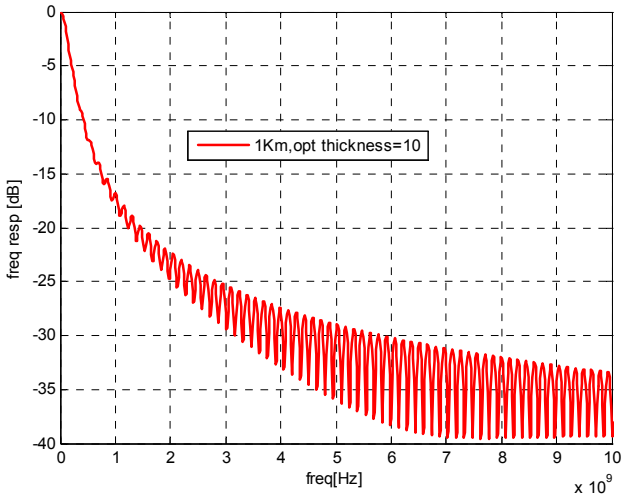

Fig. **2-8**: Frequency response of the CIR for a 1km-long cloud with $\tau = 10$

2.2 Intensity Modulated FSO System Model

Fig. **2-9** is an optical communication system model based on intensity modulation/direct detection (IM/DD). Optical intensity is defined as the optical power emitted per solid angle in units of watts per steradian. Wireless optical links transmit information by modulating the instantaneous optical intensity $I(t)$ in response to an input electrical current $x(t)$, with two constraints in non-negativity and power satisfied as in Eq. **2.19** and Eq. **2.20**.

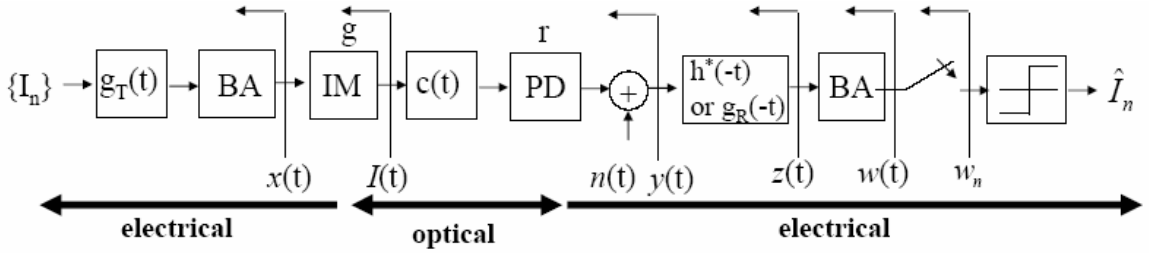

Fig. **2-9**: A system model for an optical communication system based on IM/DD.

IM: intensity modulator, c(t): channel model, n(t): electrical additive noise, BA: bias adjustment, PD: photodetector

$$I(t) \geq 0, \forall t \in R \qquad \text{Eq. } \mathbf{2.19}$$

$$\lim_{T\to\infty} \frac{1}{2T} \int_{-T}^{T} I(t)dt \leq P \text{, P: power constraint} \qquad \text{Eq. } \mathbf{2.20}$$

The binary modulated signal $x(t)$ can be expressed by Eq. **2.21**, where x_{DC} is a DC bias term added by the BA (bias adjustment) block to ensure the non-negativity constraint of Eq. **2.19**.

$$x(t) = \sum_{k} I_k g_T(t - kT_s) + x_{DC}\text{, } T_s\text{: symbol period, } I_k\text{: [0, 1]} \qquad \text{Eq. } \mathbf{2.21}$$

Denoting the optical gain of the electrical-optical conversion by g, the optical intensity modulated signal can be represented by Eq. **2.22**.

$$I(t) = g\, x(t) \qquad \text{Eq. } \mathbf{2.22}$$

Referring to the impulse response accounting for the temporal delay due to multi-scattering by $c(t)$, the received signal at the receiver front-end after photodetection can be represented by a baseband electrical model of Eq. **2.23**, where r refers to the photodetector sensitivity with unit $[A \cdot m^2 / W]$, and $n(t)$ refers to AWGN. In our following notations, we will assume $rg = 1$, for simplicity.

$$y(t) = rI(t) \otimes c(t) + n(t) = r\, g\, x(t) \otimes c(t) + n(t) \qquad \text{Eq. } \mathbf{2.23}$$

Finally, using a receive filter $g_R(t) = g_T(t)$, $y(t)$ is filtered to $z(t) = y(t) \otimes g_R(t)$. $z(t)$ can be mathematically derived in further detail as in Eq. **2.24**, using definitions of Eq. **2.25**, Eq. **2.26**, and Eq. **2.27**.

$$\begin{aligned} z(t) = y(t) \otimes g_R(t) &= \left[x(t) \otimes c(t) + n(t) \right] \otimes g_R(t) \\ &= \sum_{k} I_k f(t - kT_s) + \alpha\, x_{DC} + v(t) \end{aligned} \qquad \text{Eq. } \mathbf{2.24}$$

$$f(t) = g_T(t) \otimes c(t) \otimes g_R(t) \qquad \text{Eq. } \mathbf{2.25}$$

$$\alpha = \int \left(c(t) \otimes g_R(t) \right) dt \qquad \text{Eq. } \mathbf{2.26}$$

$$v(t) = n(t) \otimes g_R(t) \qquad \text{Eq. } \mathbf{2.27}$$

Alternatively, the equivalent discrete-time impulse response can be given by Eq. **2.28**, yielding Eq. **2.29**. The FSO system model with the discrete-time impulse response is describe in Fig. **2-10**.

$$f_k = f(t-\Delta)\big|_{t=kT_s} \quad \Delta: \text{synchronization delay} \qquad \text{Eq. } \mathbf{2.28}$$

$$z_n = \sum_k I_k f_{n-k} + \alpha x_{DC} + v_n \qquad \text{Eq. } \mathbf{2.29}$$

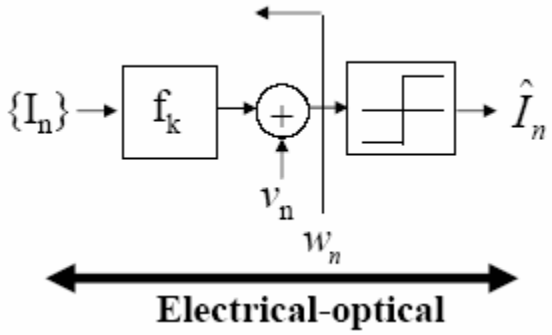

Fig. **2-10**: An equivalent discrete-time system model for an optical communication system based on IM/DD

Most of the existing DSP techniques such as equalization depend on the transmit symbol's autocorrelation property of Eq. **2.30**. In case we employ OOK (on-off keying) modulation which does not satisfy Eq. **2.30**, one good way is to adjust the DC at the receiver.

$$E(\mathrm{I_n I_m}) = \begin{Bmatrix} 0, n \neq m \\ \sigma_I^2, n = m \end{Bmatrix} \qquad \text{Eq. } \mathbf{2.30}$$

At the receiver, the BA block can first work on Eq. **2.29** to remove the DC term αx_{DC}. Furthermore, assuming a frame-by-frame transmission of frame length FR (>>L),

and the finite-length discrete-time channel $f_k, k = 0 \ldots L$, we can further adjust the DC as in Eq. **2.31**. In Eq. **2.31**, we successfully changed our transmit symbol constellation from [0, 1] to [1/2, -1/2]. However, for some portion of the received frame, $\sum_{m_1}^{m_2} f_k I_{avg}$ is time-varying. Thus, our frame structure needs a preamble longer than L+1 and a postamble longer than L. The best way to define SNR can be found after DC adjustment using Eq. **2.32**.

$$w_n = \sum_{k=m_1}^{m_2} f_k I_{n-k} - \sum_{k=m_1}^{m_2} f_k I_{avg} + v_n = \sum_{k=m_1}^{m_2} f_k (I_{n-k} - I_{avg}) + v_n = \sum_{k=m_1}^{m_2} f_k B_{n-k} + v_n$$

where B_k : [-1/2 1/2] and

1) if $0 \le n \le L$, then $m_1 = 0, m_2 = n$, and $\sum_{m_1}^{m_2} f_k I_{avg}$ is time-varying

2) if $L+1 \le n \le FR-1$, then $m_1 = 0, m_2 = L$, and $\sum_{m_1}^{m_2} f_k I_{avg}$ is constant

3) if $FR \le n \le FR+L-1$, then $m_1 = n - FR + 1, m_2 = L$, and $\sum_{m_1}^{m_2} f_k I_{avg}$ is time-varying

Eq. **2.31**

$$SNR = \frac{\sigma_B^2 \sum f_k^2}{\sigma_N^2}$$

Eq. **2.32**

In short, unlike traditional OOK-based FSO systems, the modulation scheme in this thesis needs the non-negativity constraint of Eq. **2.19** on the optical signal path and a DC bias adjustment on the electrical signal path to facilitate DSP techniques. By employing an optical path, we benefit from the non-license availability at the cost of simple OOK with cheap IM/DD implementations, while the electrical path benefits from the existing DSP signal processing techniques developed for RF signal processing, constrained only by the processing speed of the DSP given the wide optical bandwidth.

2.3 Summary and Conclusions

In this chapter, we reviewed and introduced the FSO channel model and the fundamental theories of light pulse propagation in the scattering medium. We focused mostly on multi-scattering aspects of the channel models, neglecting other aspects. One contribution of this chapter is the introduction of an optical communication system by use of electrical-optical model as in Eq. **2.21** ~ Eq. **2.32**. By this approach, we can mathematically represent an optical communication system in the same way as RF communication systems.

Chapter 3

RF Models and Definitions

In this chapter, we introduce models and definitions for the RF system. Even though we introduced an FSO channel model applicable to military avionic systems in the previous chapter, we do not want to be confined to a specific RF band suitable for military applications in this thesis. Rather, we adopted a well-established non-military band ITU SISO-based channel model for its availability of accurate model on the link level and the system level. This model is easily extendible to the MIMO channel model, or, the IEEE 802.20 channel model.

3.1 RF SISO Channel Model

A τ -based simple channel model for a SISO link is given by Eq. **3.1.** Denoting the convolution of the transmit filter and the receive filter by $p(t)$, the signal received after the receive shaping filter stage can be described by Eq. **3.2** where we assume that the complex tap gains $\alpha_l(t)$ do not change at least during a symbol period, thus further justifying replacement of $\alpha_l(t)$ by α_l. Assuming an oversampling factor of F_s at the receiver for generality, Eq. **3.2** can be further developed to Eq. **3.3**.

$$h(t) = \sum_{l=1}^{L} \alpha_l(t)\delta(t-\tau_l), \text{ where}$$

$\alpha_l(t)$: time-variant complex tap gain, assumed to be a complex Gaussian random variable with zero mean and variance σ_l^2, Eq. **3.1**

L : number of channel taps

$$r(t) = h(t) * x(t) = \left\{ \sum_{l=1}^{L} \alpha_l(t)\delta(t-\tau_l) \right\} * \sum_n I_n p(t - nT_s)$$

$$= \sum_n \sum_{l=1}^{L} I_n \int_B \alpha_l(B)\delta(B-\tau_l) p(-B+t-nT_s) dB \approx \sum_n I_n \sum_{l=1}^{L} \alpha_l(\tau_l) p(-\tau_l + t - nT_s) \quad \text{Eq. 3.2}$$

$$\approx \sum_n I_n \sum_{l=1}^{L} \alpha_l p(-\tau_l + t - nT_s)$$

I_n : transmit symbols, T_s : symbol time period

$$r(t)\big|_{t=kT_s+qT_s/F_s} \approx \sum_n I_n \sum_{l=1}^{L} \alpha_l p\left(-\tau_l + (k-n)T_s + qT_s/F_s\right) \quad \text{Eq. 3.3}$$

Letting $k - n = m$ and assuming a finite-duration discrete channel condition, Eq. **3.3** can be further developed into Eq. **3.4**. In matrix form, $h_m(q)$ can be represented by Eq. **3.5** or Eq. **3.6**.

$$r(t)\big|_{t=kT_s+qT_s/F_s} \approx \sum_{m=0}^{M} I_{k-m} \sum_{l=1}^{L} \alpha_l p\left(-\tau_l + mT_s + qT_s/F_s\right) = \sum_{m=0}^{M} I_{k-m} h_m(q) \text{ , q: 0…Q-1} \quad \text{Eq. 3.4}$$

$$\begin{bmatrix} h_0(q) \\ h_1(q) \\ \vdots \\ h_M(q) \end{bmatrix} = \begin{bmatrix} p(-\tau_1 + qT_s/F_s) & p(-\tau_2 + qT_s/F_s) & \cdots & p(-\tau_2 + qT_s/F_s) \\ p(-\tau_1 + T_s + qT_s/F_s) & p(-\tau_2 + T_s + qT_s/F_s) & \cdots & p(-\tau_2 + T_s + qT_s/F_s) \\ \vdots & \cdots & \cdots & \vdots \\ p(-\tau_1 + MT_s + qT_s/F_s) & p(-\tau_2 + MT_s + qT_s/F_s) & & p(-\tau_2 + MT_s + qT_s/F_s) \end{bmatrix} \begin{bmatrix} \alpha_1 \\ \alpha_2 \\ \vdots \\ \alpha_L \end{bmatrix} \quad \text{Eq. 3.5}$$

$$\mathbf{h}(q) = \mathbf{P}(\tau, q)\boldsymbol{\alpha} \quad \text{Eq. 3.6}$$

Table **3-1** shows ITU SISO channel model parameters for link level simulations. For coherence time, a rule of thumb of Eq. **3.7** can be used. In Fig. **3-1**, we present the power delay profiles of four different link level models.

$$T_c = \frac{1}{f_m}\sqrt{\frac{9}{16\pi}} \quad \text{Eq. 3.7}$$

Table **3-1**: ITU SISO channel model parameters applicable to IEEE 802.20 for link level simulations [27]

Models	case-I, Pedestrian-A		case-II, Vehicular-A		case-III, Pedestrian-B (Phase I)		case-IV, Vehicular-B (Phase I)	
Delay Profile	Relative power [dB]	Delay [ns]	Relative power [dB]	Delay [ns]	Relative power [dB]	Delay [ns]	Relative power [dB]	Delay [ns]
	0	0	0	0	0	0	-2.5	0
	-9.7	110	-1.0	310	-0.9	200	0	300
	-19.2	190	-9.0	710	-4.9	800	-12.8	8900
	-22.8	410	-10.0	1090	-8.0	1200	-10.0	12900
			-15.0	1730	-7.8	2300	-25.2	17100
			-20.0	2510	-23.9	3700	-16.0	20000
Average delay spread τ_m	14.428 nsec		0.25435 usec		0.40910 usec		1.4981 usec	
Coherence bandwidth B_C	69.3 MHz		3.93 MHz		2.44 MHz		0.667 MHz	
rms delay spread τ_{rms}	45.994 nsec		0.37039 usec		0.63342 usec		4.0014 usec	
Coherence time T_c	0.0609s, 0.0061s, 0.0015s		0.0061s, 0.0015, 0.0007		0.0609s		0.0061s, 0.0015s, 0.0007s	

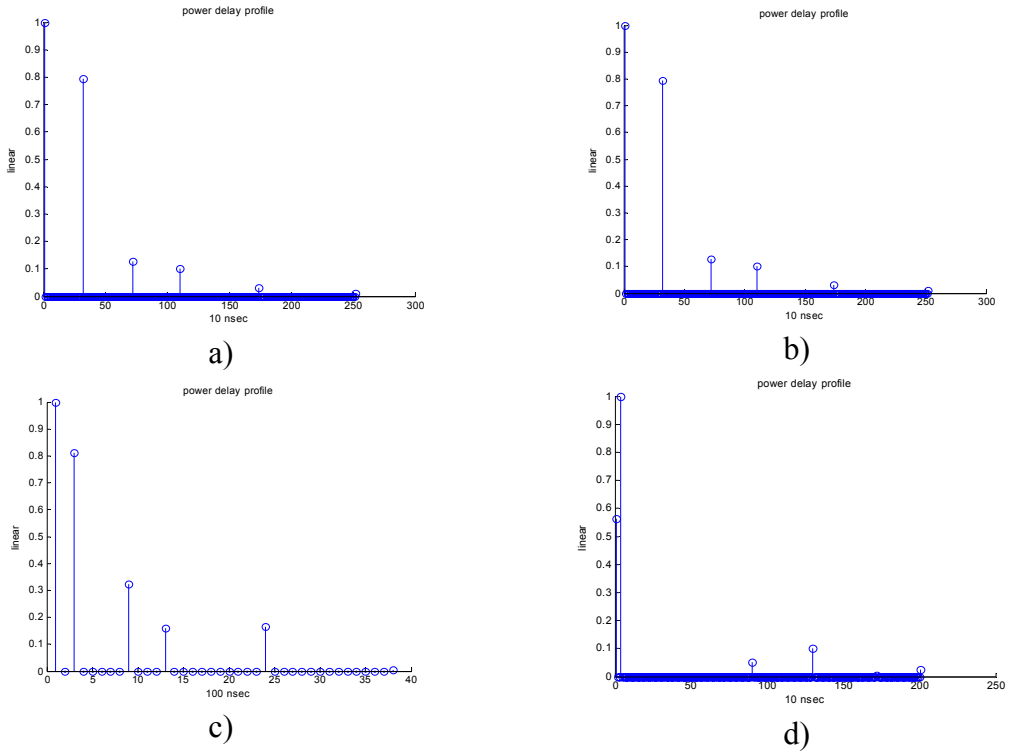

Fig. **3-1**: A τ -spaced SISO channel model, a) case-I, Pedestrian-A, b) case-II, Vehicular-A, c) case-III, Pedestrian-B (Phase I), d) case-IV, Vehicular-B

3.2 RF MIMO Channel Model

3.2.1 Extension from SISO to MIMO Channel Model

Our previous discussion of the RF SISO channel model can be further extended to an RF MIMO channel model of which an example is given in Fig. **3-2**. A MIMO channel with N transmit and M receive antennas consists of N-by-M SISO links with K multipath components. Following [28], by using the τ -spaced approach, the wideband MIMO radio channel can be expressed as $\mathbf{H}(\tau) = \sum_{l=1}^{L} \mathbf{A}_l \delta(\tau - \tau_l)$, where $\mathbf{A}_l(t) = \left\lfloor \alpha_{mn}^l \right\rfloor_{M \times N}$ is a complex

matrix describing the linear transformation between the 2 antenna arrays at delay τ_l, one at the transmitter site and the other at the receiver site. Also, n and m are indexes of transmitting antennas and receiving antennas, respectively. Assuming the same multipath structure, we can assume the same multipath delays τ_l among subchannel links, but gain taps are different across subchannel links [**46**].

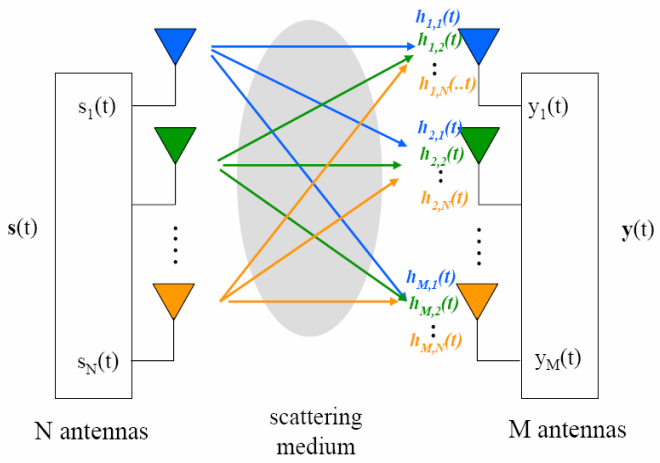

Fig. **3-2**: A MIMO channel composed of N transmit antennas and M receive antennas

Let $\boldsymbol{\alpha}_n^{(l)}(t)$ be the *l*-th column matrix of $\mathbf{A}_l(t)$, representing the *l*-th multipath component tap gains from the *n*-th transmit antenna to the M receive antennas. Likewise, let $\boldsymbol{\beta}_n^{(l)}(t)$ be the *l*-th multipath component tap gains from the N transmit antennas to the *m*-th receive antenna. Using these, we can define receive and transmit correlation matrices as given in Eq. **3.8** and Eq. **3.9**. The receive correlation matrix of Eq. **3.8** tells the correlation between M receive antennas. Likewise, the transmit correlation matrix of Eq. **3.9** tells the correlation between N transmit antennas. Of course, Eq. **3.8** and Eq. **3.9** are formulas to evaluate correlation matrices, given that we are somehow given matrices of $\boldsymbol{\alpha}_n^{(l)}(t)$ generated by some method. In practice, we generate the correlation matrix by some known approaches.

$$\mathbf{R}_r^{(l)} = E\left\{ \boldsymbol{\alpha}_n^{(l)}(t)\boldsymbol{\alpha}_n^{(l)\,H}(t)\right\},\ [M \times M] \qquad \text{Eq. } \mathbf{3.8}$$

$$\mathbf{R}_t^{(l)} = E\left\{ \boldsymbol{\beta}_n^{(l)}(t)\,\boldsymbol{\beta}_n^{(l)H}(t)\right\},\ [N \times N] \qquad \text{Eq. } \mathbf{3.9}$$

3.2.2 Link Level MIMO Channel Model

A MIMO channel with N transmit antennas and M receive antennas can be generated by $M \times N$ independent channels, aided by a transmit correlation matrix and a receive correlation matrix. First, transmission from each of the N transmit antennas to the M receive antennas can be understood by a SIMO frequency nonselective channel model in Eq. **3.10**. Second, likewise, reception by each of the M receive antennas from the N transmit antennas can be given by a MISO (multi-input-single-output) frequency nonselective channel model given in Eq. **3.11**. By combining the concepts of Eq. **3.10** and Eq. **3.11**, we can intuitively obtain a MIMO channel as in Eq. **3.12** where Eq. **3.13** is also used

$\mathbf{h}_i(t) = \sqrt{\mathbf{R}_r}\,\mathbf{g}_i(t)$,
i: transmit antenna index, i = 1…N, $\mathbf{h}_i(t)$: M-by-1,
$\mathbf{R}_r$: an M-by-M channel receive correlation matrix,
$\mathbf{g}_i(t)$: an M-by-1 independent channel vector — Eq. **3.10**

$\mathbf{h}_j(t) = \mathbf{g}_j(\tau)\sqrt{\mathbf{R}_t}$,
j: receive antenna index, j = 1…M, $\mathbf{h}_j(t)$: 1-by-N,
$\mathbf{R}_t$: an N-by-N channel transmit correlation matrix,
$\mathbf{g}_j(t)$: an 1-by-N independent channel vector — Eq. **3.11**

$\hat{\mathbf{H}}_k(t) = \sqrt{\mathbf{R}_r}\,\mathbf{H}_k(t)\sqrt{\mathbf{R}_t}$,
$\mathbf{R}_r$: M-by-M, $\mathbf{R}_t$: N-by-N, $\mathbf{H}_k(t)$: M-by-N,
k: index of discrete time instants — Eq. **3.12**

$$\mathbf{H}_k(t) = \begin{bmatrix} h_{1,1}^k(t) & \vdots & h_{1,N}^k(t) \\ \vdots & \ddots & \vdots \\ h_{M,1}^k(t) & \cdots & h_{M,N}^k(t) \end{bmatrix}, \qquad \text{Eq. } \mathbf{3.13}$$

row: Rx antenna index, column: Tx antenna index

Now, in order to generate $\mathbf{H}_k(t)$, we can resort to our previous discussion on the RF SISO channel model. The detailed generation algorithm is outlined in Table **3-2**.

Table **3-2**: Assumptions and algorithm for correlated MIMO channel generation

Assumptions
1) $N \times M$ channels are independent
2) Tap coefficients $\alpha_l(t)$ of Eq. **3.1** are independent of each other
3) A power delay profile is defined as $(\boldsymbol{\alpha}, \boldsymbol{\tau})$, $\boldsymbol{\alpha} = [\alpha_1\ \alpha_2 \cdots \alpha_L]$ and $\boldsymbol{\tau} = [\tau_1\ \tau_2 \cdots \tau_L]$

For each of the $N \times M$ independent channels,

Step 1. Generate L independent Rayleigh fading processes

Step 2. Scale the k[th] Rayleigh fading process by a factor of $\sqrt{\alpha_k / \sum_{i=1}^{L} \alpha_i}$

Step 3. Generate pulse shaping matrix $\mathbf{P}(\tau, q)$ of Eq. **3.6**. by Eq. **3.5**

Step 4. Generate Rayleigh-faded time-varying channel taps of (M+1) length, $\mathbf{h}(q) = [h_0(q)\ h_1(q) \cdots h_M(q)]^T$, by Eq. **3.6**.

Once $N \times M$ channels are found, a correlated model can be found by Eq. **3.12**

Table **3-3**: Additional MS parameters for link-level MIMO channel model simulations. ASP: antenna spacing, AoA: angle of arrival, AoD: angle of departure, AS: angle spread, PAS: power azimuth spectrum, DoT: direction of travel

	case-I, Pedestrian-A	case-II, Vehicular-A	case-III, Pedestrian-B (Phase I)	case-IV, Vehicular-B (Phase I)
ASP	0.5°			
AoA $\overline{\theta}_{AoA}$	22.5 for LOS component, 67.5 for NLOS components	67.5°	67.5°	67.5°
DoT	0°	22.5°	-22.5°	22.5°
AS σ	104° in the case of uniform PAS			
	35° in the case of Laplacian PAS			
PAS $P(\theta,\sigma,\overline{\theta}_{AoA})$	If LOS exists: Fixed AoA for LOS component + uniform PAS for NLOS components If LOS does not exist: Laplacian distribution with $\sigma = 35°$	Either Laplacian distribution with $\sigma = 35°$ or uniform PAS	Laplacian distribution with $\sigma = 35°$	Either Laplacian distribution with $\sigma = 35°$ or uniform PAS

Table **3-4**: Additional BS parameters for link-level MIMO channel model simulations

ASP	0.5 λ , 4 λ , or 10 λ
AoA $\overline{\theta}_{AoA}$	50° , if RMS AS per path is 2 ◦
	20°, if RMS AS per path is 5 ◦
AoD $\overline{\theta}_{AoD}$	Same as AoA values
AS σ	2° per path if AoD (= AoA) = 50° and if not the case of indoor pico cell
	5° per path if AoD (= AoA) = 20° and if not the case of indoor pico cell
	25° per path if AoD(= AoA) = 20° and if the case of indoor pico cell
PAS $P(\theta,\sigma,\overline{\theta}_{AoA})$	Laplacian distribution

With this knowledge, we can first expand the ITU SISO channel model already suggested in Table **3-1** and can further include MIMO spatial channel parameters on it. The MIMO spatial channel parameters have been tabulated as in Table **3-3** for MS and as in Table **3-4** for BS.

3.2.2.1 Antenna Spacing

At the BS, a linear antenna array with either 0.5λ, 4λ, or 10λ spacing is assumed. At the MS, considering the limited size of the MS, an antenna spacing of 0.5λ is assumed.

3.2.2.2 Angles

The MS' DoT is defined with regard to the broadside of the MS antenna arrays. Similarly, per path MS AoA is defined as the mean angle of an incident ray at the MS antenna array with respect to the broadside. The BS' AoD $\overline{\theta}_{AoD}$ is defined as the mean angle with which a departing ray's power is transmitted by the BS antenna array with regard to the broadside. Likewise, the BS' AoA $\overline{\theta}_{AoA}$ is defined as the mean angle with which an arriving ray's power is received at the BS array with regard to the broadside, and the value is actually the same as AoD. The BS angle spread (AS) per path σ is defined to be the RMS of angle values with which a ray's power is received or transmitted by the base station antenna array. The MS per path AS can be defined likewise.

3.2.3 System Level MIMO Channel Model

Unlike a link level MIMO channel model, a system level channel model may consist of multiple cells, multiple sectors, base stations and mobile stations. The ITU SISO channel model considers a suburban macro cell case, an urban macro cell case, and an urban micro cell case.

3.2.3.1 Antenna Pattern

$$A(\theta) = -\min\left[12\left(\frac{\theta}{\theta_{3dB}}\right)^2, A_m\right], \quad -\pi \le \theta \le \pi$$

θ: angle between the direction of interest and the broadside of the antenna array in degrees
θ_{3dB}: 3dB beamwidth in degrees
A_m: maximum attenuation

Eq. **3.14**

A sectored antenna pattern at the BS can be described by Eq. **3.14**. For a 3-sectored cells, θ_{3dB} = 70° and A_m = 20 dB are assumed. In the case of MS, an omni-directional antenna pattern is assumed, which can be described as a uniform function of θ.

3.2.3.2 Power Azimuth Spectrum

The PAS of a ray arriving at the BS antenna array shows a Laplacian distribution as presented in Eq. **3.15** where the definitions in Eq. **3.16** and Eq. **3.17** are used. PAS basically describes the average received power per path at the BS antenna array.

$$P(\theta,\sigma,\bar{\theta}_{AoA}) = N_0 \exp\left[\frac{-\sqrt{2}\left|\theta-\bar{\theta}_{AoA}\right|}{\sigma}\right] G(\theta), \theta \in [-\pi,\pi] \quad \text{Eq. } \mathbf{3.15}$$

$$G(\theta) = 10^{0.1A(\theta)},\ A(\theta)\text{: antenna pattern defined in Eq. } \mathbf{3.14} \quad \text{Eq. } \mathbf{3.16}$$

$$N_0\text{: a normalization constant such that } \int_{\theta=-\pi+\bar{\theta}}^{\theta=\pi+\bar{\theta}} P(\theta,\sigma,\bar{\theta}_{AoA})d\theta = 1 \quad \text{Eq. } \mathbf{3.17}$$

The PAS of an arriving ray at an MS antenna array can be either of uniform distribution or of Laplacian distribution, depending on cases. Even in the case of Laplacian distribution, due to the fact that we assume an omni directional antenna pattern at the MS, the expression given in Eq. **3.15** will now be modified to Eq. **3.18** such that the PAS does not depend on the function $G(\theta)$ or $A(\theta)$. N_0 can be found by Eq. **3.17**.

$$P(\theta,\sigma,\bar{\theta}_{AoA}) = N_0 \exp\left[\frac{-\sqrt{2}\left|\theta-\bar{\theta}_{AoA}\right|}{\sigma}\right], \theta \in [-\pi,\pi] \quad \text{Eq. } \mathbf{3.18}$$

3.2.3.3 Others

Other terms, definitions and parameters are organized in Table **3-5**.

Table **3-5**: Definitions for system level simulation of MIMO channel model

Definition	Description
θ_{BS}	Angle between LOS direction and the broadside direction of BS antenna array
$\delta_{n,AoD}$	AoD for the n^{th} ray (= path) with regard to the LOS direction
$\theta_{n,m,AoD}$	Absolute AoD of the m^{th} subpath of the n^{th} path (= ray) at the BS with regard to the BS broadside direction
θ_{MS}	Angle between the BS-MS LOS and MS broadside direction
$\delta_{n,AoA}$	AoA of the n^{th} ray with respect to LOS direction
$\theta_{n,m,AoA}$	Absolute AoA for the m^{th} subpath of the n^{th} path(= ray) at the MS with regard to the MS broadside direction
V	Velocity vector of the MS
θ_v	Angle of velocity vector with regard to the MS broadside direction

3.2.4 Overall Flow of MIMO Channel Coefficient Generation with Spatial Characteristics

The overall procedure of MIMO channel coefficient generation can be summarized as in Fig. **3-3**. Between a link level model and a system level model, if the system level parameters such as antenna pattern, antenna gain and power azimuth spectrum are replaced to represent a single BS/single MS/single cell/single sector case, we can obtain a link level model. Otherwise, basically the same procedure as outlined in Fig. **3-3** can be used for either system level or link level simulations. We adopted the Jake's method to obtain multiple Rayleigh fading envelopes as a part of the channel

simulator [29]. Also, we adopted quasi-static channel model assumption such that the path gains are constant over a frame of a certain length but change from frame to frame. We also assumed that when the path gains change from frame to frame, they change independently.

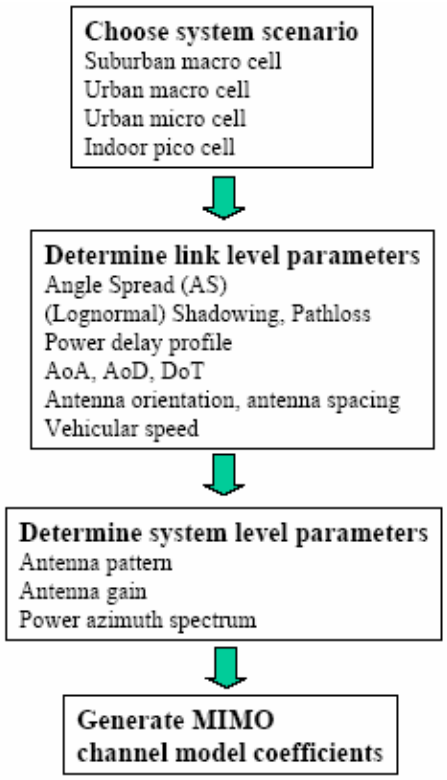

Fig. **3-3**: Overall flow of MIMO channel model coefficient generation and needed parameters

3.2.5 Generation Method of MIMO Correlation Channel Matrix

Once we obtain the parameters of Fig. **3-3**, we can proceed with the last step of the flow of Fig. **3-3**. There are several suggested methods in the literature to use the parameters thus obtained. One comprehensive formula is Eq. **3.19 [**27**]**. We can use

Eq. **3.19** repeatedly to generate $h_{u,s}^{(n)}(t)$ for each of the u, s, and n values. It is a comprehensive model incorporating both lognormal fading and time-varying Rayleigh fading.

$$h_{u,s}^{(n)}(t) = \sqrt{\frac{P_n \sigma_{SF}}{M}} \sum_{m=1}^{M} \begin{bmatrix} \sqrt{G_{BS}(\theta_{n,m,A_oD})} \exp(j[kd_s \sin(\theta_{n,m,A_oD}) + \Phi_{n,m}]) \cdot \\ \sqrt{G_{MS}(\theta_{n,m,A_oA})} \exp(jkd_u \sin(\theta_{n,m,A_oA})) \cdot \\ \exp(jk\|\mathbf{v}\|\cos(\theta_{n,m,A_oA} - \theta_v)t) \end{bmatrix}$$

P_n : power of the n[th] path of the power delay profile
σ_{SF} : lognormal shadow fading
M: number of subpaths of the n[th] path
θ_{n,m,A_oD} : AoD of the n[th] path – the m[th] subpath component
θ_{n,m,A_oA} : AoA of the n[th] path – the m[th] subpath component
$G_{BS}(\theta_{n,m,A_oD})$, $G_{MS}(\theta_{n,m,A_oA})$: antenna gain of each array element, BS or MS Eq. **3.19**
d_s : distance from the reference BS antenna element to the s[th] BS antenna element
d_u : distance from the reference MS antenna element to the u[th] MS antenna element
$\Phi_{n,m}$: phase of the n[th] path – the m[th] subpath component
$\mathbf{v}$: magnitude of MS' velocity vector
θ_v : angle of MS' velocity vector
u: index of MS antenna, u = 1…N
s: index of BS antenna, u = 1…M
n: index of power delay profile, n = 1…L

Alternatively, we can adopt a simpler method introduced in [27]. One thing to note is that unlike conditions of 3.2.5 which depends on lognormal shadowing, we actually ignore that effect, assuming that our transmitter somehow compensates for the shadowing once an exact channel estimation is made. We are interested in equalization in this thesis, thus our adoption of a channel model ignoring the macroscopic channel effects can be further justified. Recall from Eq. **3.20** that $\mathbf{H}_k(t)$ is an M-by-N channel matrix at the k[th] time instant, which is determined by the formula of a raised-cosine pulse

and time-varying faded envelope coefficient $\alpha_l(t)$. Since $\alpha_l(t)$ is a zero-mean complex Gaussian random variable, each element of $\mathbf{H}_k(t)$ is also a complex Gaussian random variable with a respective variance. Now, in order to evaluate $\mathbf{R}_r$ and $\mathbf{R}_t$, we can resort to Eq. **3.21**. where $r_{l,m}(t)$ refers to the received signal at the m^{th} receive antenna element at the l^{th} tap (= path) and time t, $g_i(t), i = 1...P$ means the P subpaths' random fading coefficients constituting the l^{th} tap, d is the physical distance between antenna elements, $D \underset{=}{\Delta} 2\pi d/\lambda$ is d normalized by wavelength, ϕ_0 is AoA (= $\overline{\theta}_{AoA}$) of the l^{th} path, and ϕ_i refers to the respective AoA of P subpaths constituting the l^{th} path.

$$r_{l,m}(t) = \sum_{i=1}^{P} g_i(t) e^{jDm\sin(\phi_0 - \phi_i)} \qquad \text{Eq. } \mathbf{3.21}$$

Assuming independence between the AoAs of different subpaths, we can derive the cross correlation between the m^{th} and the n^{th} antenna elements by Eq. **3.22**. As in the case of the MS where an omni-directional antenna is usually assumed and thus a uniform radiation pattern is assumed, Eq. **3.22** can be further simplified to Eq. **3.23**.

$$\begin{aligned} \mathbf{R}_{m,n} &= E_\phi[r_{l,m}(t) r_{l,n}^*(t)] = E_\phi\left[\left[\sum_{i=1}^{P} g_i(t) e^{jDm\sin(\phi_0-\phi_i)}\right]\left[\sum_{s=1}^{P} g_s(t) e^{jDn\sin(\phi_0-\phi_s)}\right]^*\right] \\ &= E_\phi\left[e^{jD(m-n)\sin(\phi_0-\phi)}\right] \end{aligned} \qquad \text{Eq. } \mathbf{3.22}$$

$$\mathbf{R}_{m,n} = \int_{-\pi}^{\pi} e^{jD(m-n)\sin(\phi_0-\phi)} P(\phi) d\phi \qquad \text{Eq. } \mathbf{3.23}$$

Even though we can substitute a known PAS such as a truncated Laplacian PAS into Eq. **3.23**, we will then mostly need to evaluate numerically. Instead, we use an exact expression for spatial correlation coefficients which is found as the sum of the Bessel functions of the first kind as given in Eq. **3.24**, where ϕ means subpath components'

continuous angles constituting a path arriving with (mean-sense) AoA ϕ_0 for this path, and σ_ϕ for per-path AS.

$$
\begin{aligned}
real\left([R(\phi_0,\sigma_\phi)]_{m,n}\right) &= J_0\left(D(m-n)\right) + 2\sum_{r=1}^{\infty} \frac{J_{2r}\left(D(m-n)\right)}{(\frac{\sqrt{2}}{\sigma_\phi^2})^2 + (2r)^2} \cdot \\
&\left(\cos(2r\phi_0)\right)\left\{\frac{\sqrt{2}}{\sigma_\phi^2} + \exp(-\frac{\Delta\sqrt{2}}{\sigma_\phi^2})\left[2r\sin(2r\Delta) - \frac{\sqrt{2}}{\sigma_\phi^2}\cos(2r\Delta)\right]\right\} \\
imag\left([R(\phi_0,\sigma_\phi)]_{m,n}\right) &= 2\sum_{r=1}^{\infty} \frac{J_{2r+1}\left(D(m-n)\right)}{(\frac{\sqrt{2}}{\sigma_\phi^2})^2 + (2r+1)^2}\sin\left((2r+1)\phi_0\right) \cdot \\
&\left\{\frac{\sqrt{2}}{\sigma_\phi^2} - \exp(-\frac{\Delta\sqrt{2}}{\sigma_\phi^2})\left[(2r+1)\sin((2r+1)\Delta) + \frac{\sqrt{2}}{\sigma_\phi^2}\cos((2r+1)\Delta)\right]\right\}
\end{aligned}
\qquad \text{Eq. } \mathbf{3.24}
$$

Since Eq. **3.24** is still too complicated to evaluate, we will further simplify Eq. **3.24** under the condition that Δ is very small. Under this assumption, we finally obtain Eq. **3.25**. We can use this formula for outdoor downlink MIMO channel generation.

$$
\begin{aligned}
\left[\mathbf{R}(\phi_0,\sigma_\phi)\right]_{m,n} &\approx c e^{jD(m-n)\sin(\phi_0)}\left[\mathbf{B}(\phi_0,\sigma_\phi)\right]_{m,n}, \\
\left[\mathbf{B}(\phi_0,\sigma_\phi)\right]_{m,n} &= \frac{1}{1+\frac{\sigma_\phi^2}{2}[D(m-n)\cos\phi_0]^2}
\end{aligned}
\qquad \text{Eq. } \mathbf{3.25}
$$

Table **3-6**: System level channel parameters

Channel scenario		Suburban Macro	Urban Macro		Urban Micro
Number of Paths (N)		6	6 or 11		6 or 11
Number of subpaths (M) per path		20	20		20
BS	A lognormal RV for AS	$\boldsymbol{\sigma}_{AS} = 10^{\varepsilon_{AS}\mathbf{x}+\mu_{AS}}$, $x \sim N(0,1)$			
		μ_{AS} = 0.69, ε_{AS} = 0.13	μ_{AS} = 0.810 and ε_{AS} = 0.34	μ_{AS} = 1.18 and ε_{AS} = 0.210	N/A
	Mean AS	$E[\boldsymbol{\sigma}_{AS,BS}]$ = 5°	$E[\boldsymbol{\sigma}_{AS,BS}]$ = 8°	$E[\boldsymbol{\sigma}_{AS,BS}]$ =15°	NLOS: $E[\boldsymbol{\sigma}_{AS,BS}]$ =19°
	Ratio of $\boldsymbol{\sigma}_{AoD} / \boldsymbol{\sigma}_{AS}$	1.2	1.3		N/A
	Per-path AS	2°	2°		5° (for both LOS and NLOS)
	Per-path AoD's distribution	$\sim N(\bar{\theta}_{AoD}, \boldsymbol{\sigma}^2_{AoD})$	$\sim N(\bar{\theta}_{AoD}, \boldsymbol{\sigma}^2_{AoD})$		A uniform function of U(-40°, 40°)
MS	Mean AS	$E[\boldsymbol{\sigma}_{AS,MS}]$ = 68°	$E[\boldsymbol{\sigma}_{AS,MS}]$ = 68°		$E[\boldsymbol{\sigma}_{AS,MS}]$ = 68°
	Per-path AS	35°	35°		35°

In order to numerically evaluate Eq. **3.25**, we use certain known values from [27] such that the three types of system level scenarios can be evaluated as in Table **3-6**.

3.2.6 Channel Generation Results

We generated some representative channel correlation matrices. First, Fig. **3-4** graphically explains our concepts of R_r, R_t, and the channel matrix given by Eq. **3.12** which incorporates R_r and R_t, when BS antenna spacing = 0.5λ. In Eq. **3.12**, we assumed a narrow-band channel and also assumed a stationary model for $\hat{\mathbf{H}}_k(t)$. Similarly, Fig. **3-**

5 is for the case of BS antenna spacing = 4λ, and Fig. **3-6** is for the case of BS antenna spacing = 10λ. One thing to note is that, we can compare Fig. **3-4** b), Fig. **3-5** b) and Fig. **3-6** b) to see the effects of antenna spacing on channel correlation matrices. As we have larger antenna spacing, we visibly have less cross-correlation at the base station.

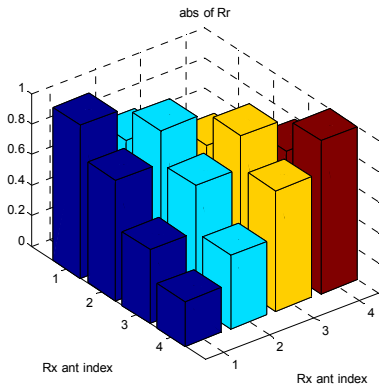

a) correlation channel matrix at the receiver (MS)

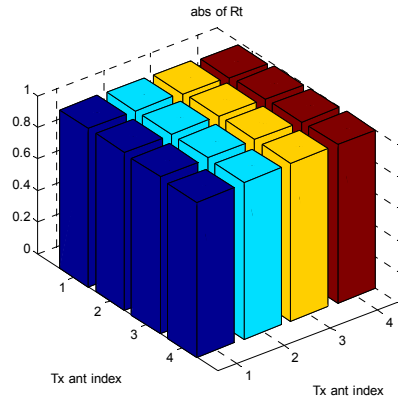

b) correlation channel matrix at the transmitter (BS)

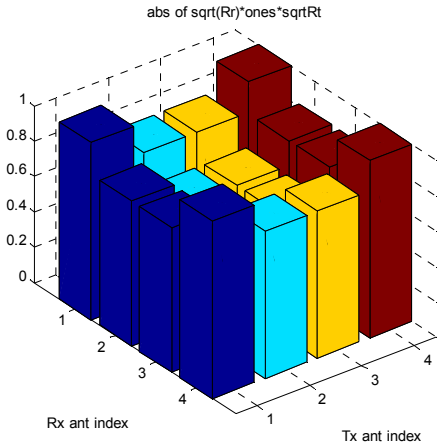

c) A Narrowband downlink channel matrix with correlation channel matrix incorporated as in Eq. **3.12**

Fig. **3-4**: Suburban macro-cell, pedestrian A case, downlink channel, BS antenna spacing = 0.5λ, a 4-by-4 MIMO link.

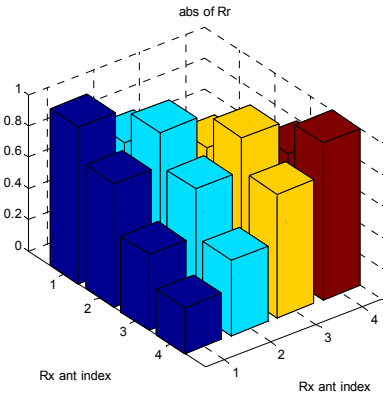

a) correlation channel matrix at the receiver (MS)

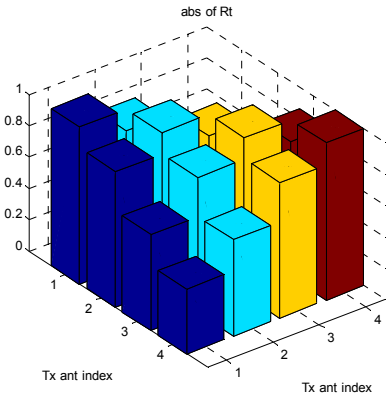

b) correlation channel matrix at the transmitter (BS)

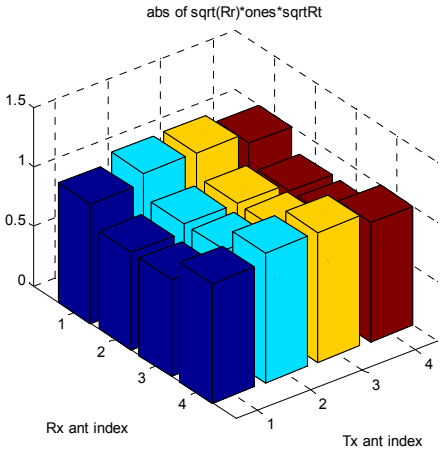

c) A Narrowband downlink channel matrix with correlation channel matrix incorporated as in Eq. **3.12**

Fig. **3-5**: Suburban macro-cell, pedestrian A case, downlink channel, BS antenna spacing $= 4\lambda$, a 4-by-4 MIMO link.

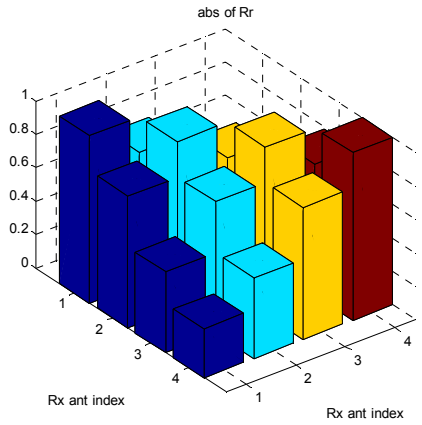

a) correlation channel matrix at the receiver (MS)

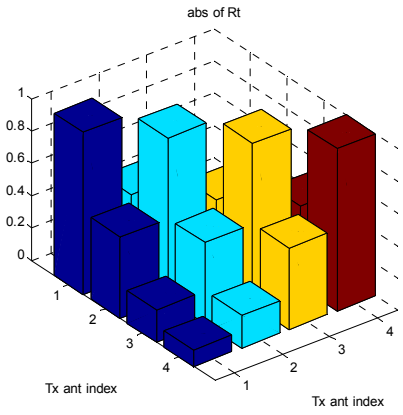

b) correlation channel matrix at the transmitter (BS)

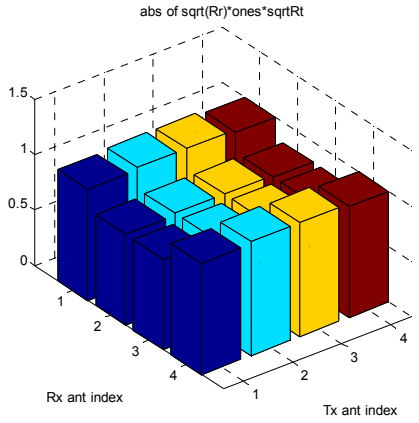

c) A Narrowband downlink channel matrix with correlation channel matrix incorporated as in Eq. **3.12**

Fig. **3-6**: Suburban macro-cell, pedestrian A case, downlink channel, BS antenna spacing = 10λ, a 4-by-4 MIMO link.

Now, with the findings in Fig. **3-4**, Fig. **3-5** and Fig. **3-6**, we further extended our investigation on MIMO channel properties to that of a time-varying frequency-selective channel and checked the 3D channel correlation matrix expressed by Eq. **3.26** for both in the time domain and in the frequency domain. Since the findings in Fig. **3-4**, Fig. **3-5** and Fig. **3-6** assumed a narrowband, time-stationary channel model, it does not give us much insight. Below, Eq. **3.26** is simply an extension from a SISO autocorrelation. Of course,

rather than finding the true MIMO correlation matrix, we will replace Eq. **3.26** by an estimate given in Eq. **3.27**.

$$\mathbf{R}_{\mathbf{HH}}(m) = E\left[\mathbf{H}(n+m)\mathbf{H}(n)^{H}\right] \qquad \text{Eq. } \mathbf{3.26}$$

$$\mathbf{R}_{\mathbf{HH}}(m) \approx \sum_{n} \mathbf{H}(n+m)\mathbf{H}(n)^{H}\ , \qquad \text{Eq. } \mathbf{3.27}$$

$\mathbf{H}(n)$: an M-by-N 2D stochastic matrix at time instant n

Since we cannot show all test cases in this limited volume of thesis, we only present Fig. **3-7**. Also, even though TEQ equalization is introduced in a later chapter, we present TEQ results here a little out of sequence, since we are interested in the channel shortening equalizer's operation on channel properties. Given an M_Rx-by-N_Tx-by-L 3D channel matrix **H** of Eq. **3.26**, at a certain delay instant m, we have an M_Rx-by-M_Rx matrix $\mathbf{R}_{\mathbf{HH}}(m)$. In $\mathbf{R}_{\mathbf{HH}}(m)$, diagonal elements at (j,j) indicate the power received at the j^{th} Rx antenna, and nondiagonal elements at (i,j) indicate the cross-correlation between two paths whose Rx index differ by |i-j|. Likewise, we can calculate the 3D correlation, but now in the frequency domain, using the channel's frequency response. We can make several observations. First, Fig. **3-7** a) shows that even though we have significant antenna spacing, there is significant cross-correlated power as we observe along index 1-2 and index 2-1. On the other hand, the time-domain correlation is low at non-zero delays, thus justifying the use of time-diversity, if possible. Second, however, if we are to employ a frequency-domain modulation such as OFDM, wavelet modulation, etc, we need to consider a correlation matrix in the frequency domain as in Fig. **3-7** b), which shows that there is significant correlation across tones and space. Third, however, Fig. **3-7** c) shows that we now have enhanced the spatial-domain correlation at the cost of a worsened time domain

correlation property. Fourth, Fig. **3-7** d) shows that, in the case of frequency domain correlation, similar to the time-domain correlation, we have here enhanced spatial-domain correlation properties. Our claim is that, through the enhancement in spatial correlation properties, channel shortening may offer additional benefits for space-time/frequency based MIMO systems.

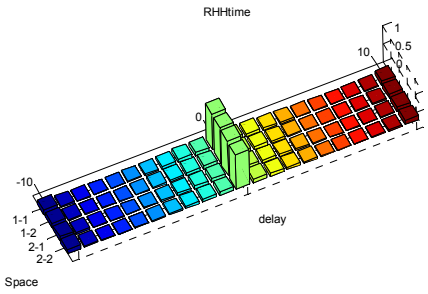

a) before TEQ,
time domain correlation

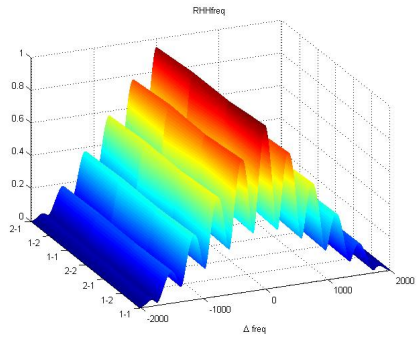

b) before TEQ,
frequency domain correlation

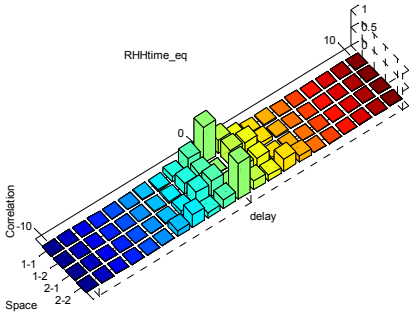

c) after TEQ,
time domain correlation

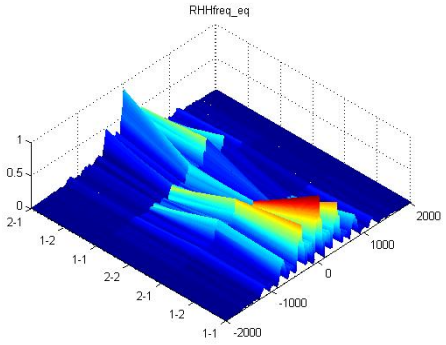

d) after TEQ,
frequency domain correlation

Fig. **3-7**: Suburban macro-cell, pedestrian A case, downlink channel, BS antenna spacing = 10λ, moving speed = 30km/h, a 2-by-2 MIMO link. 3D channel autocorrelation matrix in time/frequency before/after equalization, TEQ $N_f = 100$, $N_b = 4$

3.3 Multicarrier Modulation

Multicarrier (MC) modulation collectively refers to any systems that employ subchannel orthogonally, thus dividing the transmission bandwidth into N disjoint frequency bands. Since our FSO or RF implementations depend on MC or filterbank transceiver architecture to some extent, in this chapter we will review the basic concepts of multicarrier modulation (MCM). In MCM, we have more sophisticated control methods over each subchannel in terms of bit loading and energy loading, unlike the traditional single-carrier based systems In the MC transmission system of Fig. **3-8**, the bit stream goes through the channel encoder, the interleaver, and then the symbol mapper. The symbol mapper output is represented by Eq. **3.28**. The transmitted symbol at instant k is given by Eq. **3.29**, which is a superposition of N M-ary QAM or PSK signals.

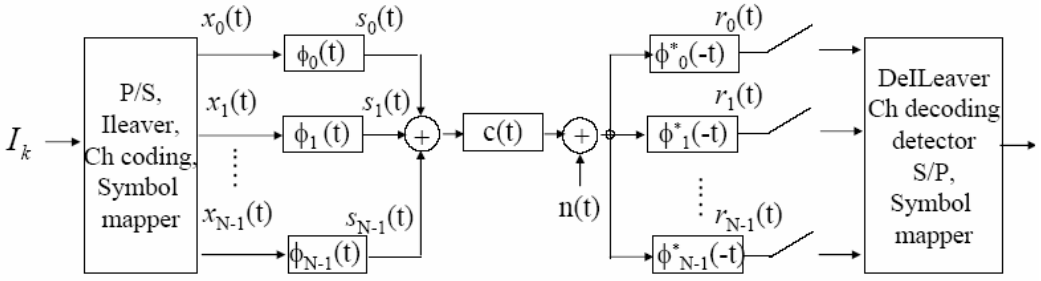

Fig. **3-8**: MC transmission system

$\widetilde{x}_{k,n}$, a complex transmit symbol, k : a MC symbol instant, n : tone index, $0 \le n \le N-1$ — Eq. **3.28**

$x(t) = \sum_{n=0}^{N-1} \widetilde{x}_{k,n} \phi_n(t - kT_s)$, where $\phi_n(t) = \phi(t) e^{j2\pi f_n t}$: bank of modulator functions — Eq. **3.29**

The presence of a receive filter bank $\phi_n(t), n = 0...N-1$ guarantees ICI (intercarrier interference)-free demodulation, but the channel delay spread can cause ISI between MC symbols. Under the assumption of $T_s >> T_m$ or a large N, we can assume a flat-channel per tone. Hence, without considering ISI or ICI, we can replace the convolution of Eq. **3.30** by a discrete-domain linear multiplication of Eq. **3.31** per tone and per symbol instant.

$$y(t) = x(t) * h(t) + n(t)\text{, h(t): channel impulse response} \qquad \text{Eq. } \mathbf{3.30}$$

$$\tilde{y}_{k,n} = \tilde{H}_n \tilde{x}_{k,n} + \tilde{n}_{k,n}\text{, } \tilde{H}_n = \tilde{H}(f)\Big|f_n\text{, k: MC symbol instant, } 0 \le n \le N-1 \qquad \text{Eq. } \mathbf{3.31}$$

In practice, we cannot employ a pulse shaping filter $\phi(t) = \text{sinc}(\pi t / T_s)$ of infinite time duration, since it is physically not realizable. Rather, we need a pulse shaping function that lasts for T_s. One way around this problem is through the use of a digital pulse shaping filter, a counterpart of an analog pulse shaping filter, combined with a guard interval. Without the presence of a guard interval, due to the delay spread of the channel with $T_m << T_s$, the first T_m sec duration of the k^{th} MC symbol would be corrupted by the last T_m portion of the $(k-1)^{th}$ MC symbol. This can be solved by introducing a guard interval of $T_g \ge T_m$ and by considering only $((k-1)T_s + T_g, kT_s)$ when demodulating the k^{th} MC symbol. Eq. **3.30** can be sampled by $f_s^{'} = 1/T_s^{'} >> 1/T_s$ to yield Eq. **3.32**.

$$y_l = \sum_{m=0}^{L} h_m x_{l-m} + n_l, y_l \underset{=}{\Delta} y(t)\Big|_{t=lT_s^{'}}, x_l \underset{=}{\Delta} x(t)\Big|_{t=lT_s^{'}}, h_l \underset{=}{\Delta} h_l(t)\Big|_{t=lT_s^{'}} \qquad \text{Eq. } \mathbf{3.32}$$

Assuming the guard interval of $v = \lfloor T_g / T_s^{'} \rfloor$ samples and $f_s^{'} = f_s(N+v)$, we need at least N received samples out of $y_{(k-1)(N+v):(k-1)(N+v)+v+N-1}$, whereas $y_{(k-1)(N+v):(k-1)(N+v)+L-1}$ needs to be ignored. Eq. **3.32**, after the guard period removal, can be alternatively expressed by Eq. **3.33**, using Eq. **3.34.**

$$\mathbf{y}_{(k-1)(N+v)+v:(k-1)(N+v)+v+N-1}^{T} = \mathbf{H}_L \mathbf{x}_{(k-1)(N+v)+v:(k-1)(N+v)+v+N-1}^{T} + \mathbf{n}_{(k-1)(N+v)+v:(k-1)(N+v)+v+N-1}^{T} \quad \text{Eq. 3.33}$$

$$\mathbf{H}_L = \begin{bmatrix} h_L & \cdots & h_0 & 0 & \cdots & 0 \\ 0 & h_L & \ddots & h_0 & \ddots & \vdots \\ \vdots & \ddots & \ddots & \ddots & \ddots & 0 \\ 0 & \cdots & 0 & h_L & & h_0 \end{bmatrix}, [N \times N] \quad \text{Eq. 3.34}$$

Since our analog transmit signal of Eq. **3.29** can be represented by Eq. **3.35** in the discrete time domain, we can represent the demodulation of the received sample vector by Eq. **3.36**. Depending on how we design the modulator matrix **G** and the demodulator matrix, we will obtain different kind of system designs.

$$x_{(k-1)(N+v):(k-1)(N+v)+v+N-1}^{T} = \sum_{n=0}^{N-1} \mathbf{g}_n \tilde{x}_{k,n} = \mathbf{G}\tilde{\mathbf{x}}_{k,N}, \quad \text{Eq. 3.35}$$

$\mathbf{g}_n$: $[(N+v)\times 1]$, discrete vector of $\phi_n(t)$, $\mathbf{G} = [\mathbf{g}_0 ... \mathbf{g}_{N-1}], [(N+v)\times v]$

$$\tilde{\mathbf{y}}_{k,N} = [\tilde{y}_{k,0:N-1}]^T = \mathbf{F}\mathbf{y}_{k,0:N-1}, \text{ F: discrete vector of } \phi_n^*(-t) \quad \text{Eq. 3.36}$$

3.3.1 OFDM Modulation and Transmitter/Receiver Structures

In OFDM [18 - 20] or DMT [17] systems, we have a cyclic prefix as a specific form of the guard interval. A cyclic prefix operation can be expressed by Eq. **3.37**. Now,

Eq. **3.33** will be changed to Eq. **3.38** using Eq. **3.39**, where $\mathbf{H}_c$ is an N-by-N circulant matrix. The presence of cyclic prefix (CP) this way renders the received vector of $\mathbf{y}_{k,0:N-1}$ in Eq. **3.38** to be the outcome of a cyclic convolution operation between $\mathbf{h}$ and $\mathbf{x}_{k,0:N-1}$. A circulant matrix can be eigenvalue-decomposed as in Eq. **3.40**.

$$\mathbf{x}_{(k-1)(N+v):(k-1)(N+v)+v+N-1} = \mathbf{P}_v \mathbf{x}_{k,0:N-1} = \left[\begin{array}{c|c} \mathbf{0}_{v\times(N-v)} & \mathbf{I}_v \\ \hline & \mathbf{I}_N \end{array}\right] \mathbf{x}_{(k-1)(N+v)+v:(k-1)(N+v)+v+N-1} \qquad \text{Eq. } \mathbf{3.37}$$

$$\begin{aligned} &\mathbf{y}_{(k-1)(N+v)+v:(k-1)(N+v)+v+N-1} \\ &= \mathbf{H}_c \mathbf{x}_{(k-1)(N+v)+v:(k-1)(N+v)+v+N-1} + \mathbf{n}_{(k-1)(N+v)+v:(k-1)(N+v)+v+N-1} \end{aligned} \qquad \text{Eq. } \mathbf{3.38}$$

$$\mathbf{H}_c \underset{=}{\Delta} \mathbf{H}_L \mathbf{P}_v \qquad \text{Eq. } \mathbf{3.39}$$

$\mathbf{H}_c = \mathcal{F}_N^H \mathbf{H}_{D,N} \mathcal{F}_N$, $\mathcal{F}_N$: a DFT (discrete Fourier transform) matrix,
$\mathbf{H}_{D,N}$: a diagonal matrix of the channel's frequency response — Eq. **3.40**

Now, if we design **G** and **F** as IDFT (inverse DFT) matrix and DFT matrix respectively, we obtain the OFDM demodulated signal as in Eq. **3.41**. That is, in so far as the OFDM system is designed with proper cyclic extension and timing, with tolerable leakage, the demodulated signal is described by Eq. **3.41** with AWGN.

$$\begin{aligned} \widetilde{\mathbf{y}}_{k,N} &= \mathbf{F}\mathbf{y}_{(k-1)(N+v)+v:(k-1)(N+v)+v+N-1} = \mathcal{F}_N \mathbf{y}_{(k-1)(N+v)+v:(k-1)(N+v)+v+N-1} \\ &= \mathcal{F}_N \left(\mathbf{H}_c \mathbf{x}_{(k-1)(N+v)+v:(k-1)(N+v)+v+N-1} + \mathbf{n}_{(k-1)(N+v)+v:(k-1)(N+v)+v+N-1})\right) \\ &= \mathcal{F}_N \left(\mathcal{F}_N^H \mathbf{H}_{D,N} \mathcal{F}_N \mathbf{x}_{(k-1)(N+v)+v:(k-1)(N+v)+v+N-1} + \mathbf{n}_{(k-1)(N+v)+v:(k-1)(N+v)+v+N-1})\right) \\ &= \mathbf{H}_{D,N} \mathcal{F}_N \mathbf{x}_{(k-1)(N+v)+v:(k-1)(N+v)+v+N-1} + \mathcal{F}_N \mathbf{n}_{(k-1)(N+v)+v:(k-1)(N+v)+v+N-1} \\ &= \mathbf{H}_{D,N} \widetilde{\mathbf{x}}_{k,N} + \widetilde{\mathbf{n}}_{k,N} \end{aligned} \qquad \text{Eq. } \mathbf{3.41}$$

Fig. **3-9** shows an overall structure of the OFDM system. In Fig. **3-9**, we incorporated a TEQ in a general approach. Also, since the OFDM modulation divided the transmission channel into a set of N parallel tones, one easy equalizer implementation is through the frequency-domain equalizer (FEQ or FDE) where each tone is scaled by the

inverse of the discrete channel frequency response $\widetilde{d}_n = \widetilde{h}_n^{-1}$. A frequency-equalization can be described by Eq. **3.42**. This implementation needs a channel estimation followed by a channel inversion.

$$\hat{\widetilde{x}}_{k,n} = \widetilde{d}_n \widetilde{y}_{k,n} = \widetilde{h}_n^{-1}(\widetilde{h}_n \widetilde{x}_{k,n} + \widetilde{n}_{k,n}) = \widetilde{x}_{k,n} + \widetilde{h}_n^{-1}\widetilde{n}_{k,n} \qquad \text{Eq. } \mathbf{3.42}$$

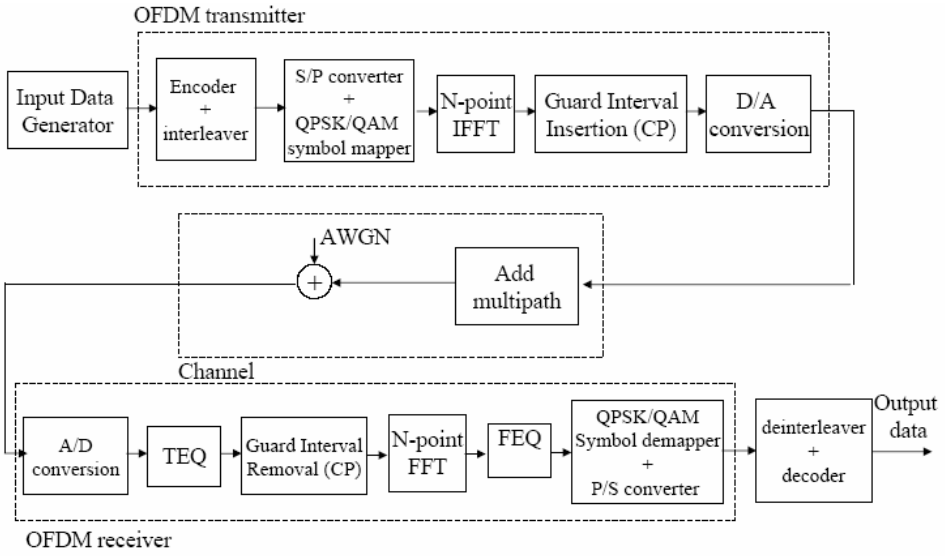

Fig. **3-9**: Overall OFDM system model and its transmitter, receiver structure

The signal bandwidth, the total transmission rate, and the bandwidth efficiency of the OFDM signal are respectively given by Eq. **3.43**, Eq. **3.44** and Eq. **3.45**. Also, the overhead in the form of a guard interval causes the bit rate or the corresponding symbol rate to be reduced by a factor of Eq. **3.46**.

$(N+1)\Delta f$, Δf : subcarrier spacing,
N: number of tones or number of subchannels — Eq. **3.43**

Total OFDM transmission rate = N/T [bits per sec],
T: an OFDM symbol's duration — Eq. **3.44**

Bandwidth efficiency $\eta = \dfrac{N/T}{(N+1)\Delta f}$, bit/sec/Hz — Eq. **3.45**

Bit rate (symbol rate) reduction ratio = $\eta = \dfrac{N}{N+v}$ — Eq. **3.46**

After OFDM demodulation by an N-point FFT (fast Fourier transform) at the receiver, from Eq. **3.42**, SNR is defined by Eq. **3.47**.

$$SNR_{symbol} = \frac{\sigma_{\tilde{x}}^2 E\left(\left|\tilde{h}_n\right|^2\right)}{\sigma_{\tilde{n}}^2} \qquad \text{Eq. } \mathbf{3.47}$$

3.3.2 Time-Domain Equalization Concepts for OFDM

So far, the time-domain equalization has been considered mostly in DSL or in landline systems, where the delay spread is severe, sometimes ranging up to hundreds of symbols' duration. In wireless OFDM, ISI is severe, but does not range up to hundreds of symbols as in DSL. Rather, the main reason that a time-domain equalization is discussed, even though it seems to contradict the original spirit of OFDM, is the lowered bandwidth efficiency as was given in Eq. **3.45** and the lowered bit rate whose reduction ratio is suggested in Eq. **3.46**. We saw not only that the length of the cyclic prefix v should be larger than the CIR (channel impulse response) length – 1 to avoid ISI, but also that a larger v will reduce the bit rate and the bandwidth efficiency. On the other hand, if we choose to increase N, this will add up to the system complexity in the context of the IFFT/FFT modulator, the coder/encoder, etc. For example, in the 4G systems where the initial conceptual studies expect giga bps range data transmission, it can be very difficult to achieve high capacity only through spectrum division. This problem caused interest in channel-shortening equalization algorithms, such that given a CIR **h** of length L+1, TEQ filter **w** with T taps, the equalized channel **c** of length L+T has most of its energy within v+1 samples. If then, with the aid of shorter guard period than the standard OFDM

designs, the ISI between OFDM symbols can be removed, and the ICI can be further removed by the ensuing FDE. In matrix form, the TEQ-equalized received signal can be represented by Eq. **3.48** using Eq. **3.49**. Of course, in case a TEQ is not used, we can replace Eq. **3.48** by Eq. **3.50**.

$$\widetilde{\mathbf{y}}_{k,N,\mathbf{w}} = F_N \mathbf{Y}_k \mathbf{w} \qquad \text{Eq. } \mathbf{3.48}$$

$$\mathbf{Y}_k = \begin{bmatrix} y_{k,0} & \cdots & y_{k,-T+1} \\ \vdots & \ddots & \vdots \\ y_{k,N-1} & \cdots & y_{k,N-T} \end{bmatrix}, \text{ an N-by-T matrix} \qquad \text{Eq. } \mathbf{3.49}$$

$$\widetilde{\mathbf{y}}_{k,N} = F_N \mathbf{Y}_k \qquad \text{Eq. } \mathbf{3.50}$$

Mathematically, following the TEQ operation, after removing the cyclic prefix, the DFT output can be understood by Eq. **3.51**, that is, the received signal at the kth tone and the nth instant is a desired signal $\widetilde{x}_{k,n}$ scaled by $\widetilde{c}_n$ and corrupted by $ISI_{k,n,\mathbf{w}}$ and $ICI_{k,n,\mathbf{w}}$. With a properly designed TEQ, we expect that the interference terms $ISI_{k,n,\mathbf{w}}$ can still be removed by cyclic prefix removal, and $ICI_{k,n,\mathbf{w}}$ can be compensated for by an FDE. $\widetilde{c}_n$, or the frequency response of our shortened channel $\mathbf{c}$, is given by Eq. **3.52**.

$$\widetilde{y}_{k,n,\mathbf{w}} = \widetilde{c}_n \widetilde{x}_{k,n} + \widetilde{n}_{k,n,\mathbf{w}} + ISI_{k,n,\mathbf{w}} + ICI_{k,n,\mathbf{w}} \qquad \text{Eq. } \mathbf{3.51}$$

$$\widetilde{c}_n = F_n[\mathbf{x}^T \mathbf{0}_{1\times(N-L-T)}] \qquad \text{Eq. } \mathbf{3.52}$$

3.4 MIMO System

A Basic narrowband MIMO system is shown in Fig. **3-2**. Given a transmit signal vector of Eq. **3.53** and a channel given by Eq. **3.54**, a received signal vector can be expressed by Eq. **3.55**.

$$\mathbf{s}(t) = [s_1(t) \cdots s_N(t)]^T \quad \text{Eq. } \mathbf{3.53}$$

$$\mathbf{H}(t) = \left[h_{m,n}\right], 1 \le m \le M \text{ : Rx antenna index, } 1 \le n \le N \text{ : Tx antenna index} \quad \text{Eq. } \mathbf{3.54}$$

$$\mathbf{y}(t) = \mathbf{H}(t)\mathbf{s}(t) + \mathbf{n}(t),\ \mathbf{y}(t)\text{: M-by-1},\ \mathbf{n}(t)\text{: M-by-1} \quad \text{Eq. } \mathbf{3.55}$$

We denote the overall power at the transmitter array by E_s. In case the transmitter does not have knowledge of the channel, then we will simply assign E_s / N to each transmitting antenna. The covariance matrices of the transmitted sequence and the received sequence can be given respectively by Eq. **3.56** and Eq. **3.57**.

$$\mathbf{R}_{ss} = \frac{E_s}{N}\mathbf{I}_{NN} \quad \text{Eq. } \mathbf{3.56}$$

$$\mathbf{R}_{yy} = E(\mathbf{y}\mathbf{y}^H) = \mathbf{H}R_{ss}\mathbf{H}^H + N_0\mathbf{I}_M \quad \text{Eq. } \mathbf{3.57}$$

A wideband model can likewise be given by Eq. **3.58** and Eq. **3.59**.

$$\mathbf{y}(t) = \sum_{k=1}^{v}\mathbf{H}(t-kT)\mathbf{s}_k + \mathbf{n}(t),\ \mathbf{y}(t)\text{: M-by-1},\ \mathbf{n}(t)\text{: M-by-1} \quad \text{Eq. } \mathbf{3.58}$$

$$\mathbf{s}_k = \mathbf{s}(t = kT) \quad \text{Eq. } \mathbf{3.59}$$

A MIMO system can be combined with OFDM and/or coding [**97** - **101**], and its transmitter/receiver structure can be described by Fig. **3-10**.

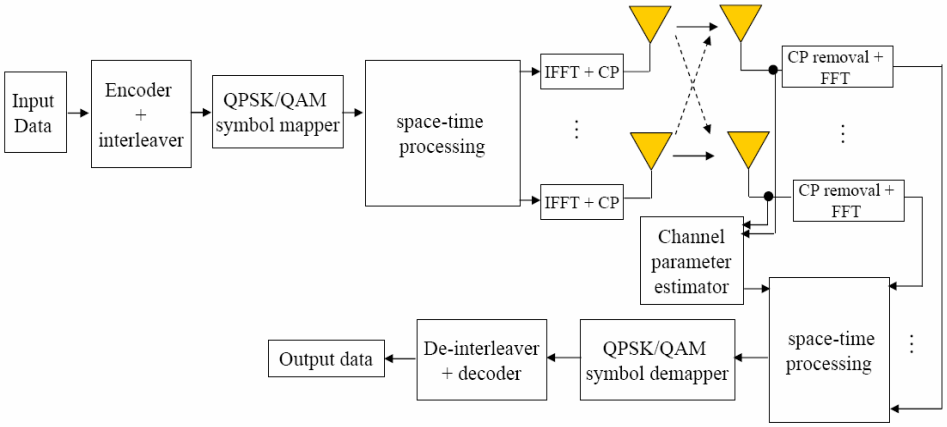

Fig. **3-10**: A MIMO-OFDM transmitter/receiver structure

MIMO systems can be implemented in many different ways to achieve either a diversity gain to combat signal fading or to obtain a capacity gain. Traditionally, there are three types of MIMO systems. The first kind seeks to improve the power efficiency by maximizing spatial diversity, and this type depends on techniques such as delay diversity, space-time block codes (STBC) [**33**][**71** - **75**], and space-time trellis codes (STTC) [**76** - **82**]. The second kind aims to increase capacity by a layered approach [**83**], and there are types such as D-BLAST and V-BLAST. The third kind uses the CSIT to decompose the channel coefficient matrix by singular value decomposition (SVD) as in Eq. **1.2**, and the SVD results are used for prefiltering and postfiltering for the purpose of achieving capacity [**84**]. Our research interest is in space-time block codes in this thesis.

To combat fading, it is common to provide different replicas of the same signal by diversity techniques. Diversity methods in many domains such as temporal diversity, frequency diversity, spatial diversity, and polarization diversity are known. Space-time codes are combinations of space diversity and temporal diversity. Among space-time codes, two well-known types are space-time block codes (STBC) and space-time trellis

codes (STTC). STBCs offer the advantage of maximum likelihood detection with linear complexity, but do not have coding gains. STTCs are combinations of modulation and trellis coding, offering both diversity and coding gain. The encoder at the transmitter of an STTC system is based on a finite state machine, and the decoder at the receiver is based on maximum likelihood sequence estimation (MLSE). One disadvantage of STTCs is that its complexity increases exponentially as a function of the diversity level and the transmission rate.

3.5 Summary and Conclusions

In this chapter, we introduced an ITU-SISO channel model, and an ITU-SISO-based MIMO channel model. With this accurate MIMO channel model that enables simulations on both link-level and system-level, we further discussed transmitter/receiver structures incorporating MIMO, OFDM, MIMO-OFDM systems as candidate transceiver structures for beyond 3G wireless communications. We briefly discussed the mathematical expressions of these transceiver technologies. Since we cannot show all the details of generated channel results, we mostly showed typical snapshots of correlation-related figures. In particular, even though it is a bit out of sequence, we showed in this chapter that the channel shortening filter TEQ has the property of changing the 3D correlation matrix of the MIMO channels.

Chapter 4

Equalization of FSO Links

In FSO communications, atmospheric turbulence can degrade the performance severely, particularly over ranges of the order of 1 km or longer. Also, multi-scattering due to aerosol particles in the atmosphere induces temporal and spatial dispersion, which at high bit rates cause intersymbol interference (ISI). Previous researches [35 - 37] assumed that in FSO operations at low altitudes, being afflicted more by atmospheric turbulence than by multi-scattering, ISI can be ignored at low data rates. On the other hand, recent researches [38 - 39] found that under the assumption of ground-to-air links through the air, the links suffer more from multi-scattering than from atmospheric scintillation, causing ISI.

In the broad area of optical communications, literature surveys show that efforts have traditionally been made more in optical signal processing techniques than in electrical signal processing techniques. In [**93**], an optical device for equalization before the photodetector stage, aided by electrical equalization formulas, was investigated to combat distortions specific in optical fiber communications. Many papers approach the optical signal processing using the Fourier domain relationship as in [**96**]. In [**94**], the authors approached the challenges of fiber optical communications by purely electrical signal processing by combining the MAP equalization with the turbo-product coding. In [**95**], investigations were made for the performance of the MLSD algorithm in fiber optical communications.

One way to enhance error performance in FSO channels with ISI is through linear minimum mean-squared error (LMMSE) equalization or through decision-feedback equalization (DFE). Another recent proposal is an FSO system for through-clouds communications consisting of a channel shortening equalizer (CSE or TEQ) followed by MLSD [40]. Since the use of TEQ at the receiver after sampler causes colored noise, we cannot use a Viterbi equalizer in the strict sense, even though this problem is bypassed in the existing literature by assuming that we still have white Gaussian noise after the TEQ. This can be solved by placing the TEQ at the transmitter. Also, in order to adopt the existing TEQ solutions to our case of TEQ-in-the-transmitter configuration, the author shows how the existing solutions' framework can be further adjusted to fit our problem. Since our FSO scenario consists of airborne links, we also dealt with the issue of channel estimation errors, their effects on BER, and considerations for a TEQ adaptation time interval. The author of this thesis claims that, to the author's best knowledge, there have not been any previous research efforts on TEQ in the optical links.

4.1 Channel Estimation

Often, equalizations assume known channel information at the receiver, but in practice, this requires channel estimation. Fig. **4-1** shows an FSO channel estimated by a training sequence to minimize MSE between the actual discrete channel $\mathbf{h}$ and the estimated discrete channel $\hat{\mathbf{h}}$. We can see that with the aid of training sequence of length 9000 at SNR 40dB, we can expect MSE of -40dB. Fig. **4-1** b) also shows that the discrete channel can be relatively well estimated by our MSE criterion.

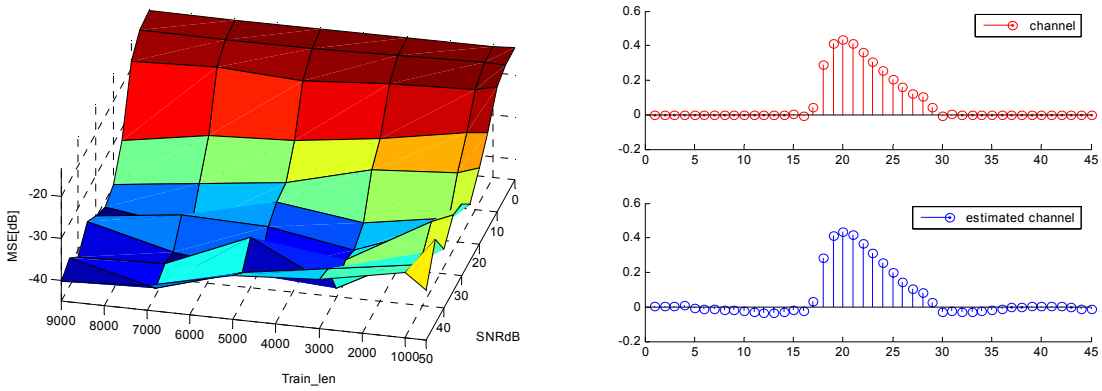

a) b)

Fig. **4-1**: τ =8, channel estimated by the MSE algorithm

4.2 Review of Conventional Equalizations

Conventionally, equalizers can be categorized into a linear equalizer (LE) such as a zero-forcing (ZF) equalizer, an MMSE equalizer, and a nonlinear equalizer (NLE) such as a decision feedback equalizer (DFE), and a maximum likelihood sequence detection (MLSD) equalizer. An equalizer not only mitigates ISI but is also accompanied by noise enhancement, since basically the idea of equalization itself involves higher gain at the frequencies of higher attenuation. Between the LE and the NLE, the NLE suffers less from noise enhancement at the cost of a heavier computational complexity. Also, the DFE, a typical NLE, suffers more in low SNR due to error propagation than the LE. The MLSD is known to be optimal, but its complexity and memory requirements grow exponentially with the length of the delay spread, and is thus prohibitively costly in channels of long delay spreads.

The philosophy of conventional linear equalization is to minimize MSE defined as $J = E[I_k - \hat{I}_k]^2$, where I_k means the sequence of the transmit symbols, $\hat{I}_k$ means the sequence of the received and equalized symbols, and $E[]^2$ means a statistical expectation operation. For ZF or MMSE equalization to yield a good error performance, it expects an equalized CIR that is close to the ideal CIR, or, a Dirac delta function $\delta(t)$, such that the Euclidian distance between the transmitted symbol and the equalized symbol is somehow minimized.

As alternatives to these conventional well-established equalizers, the equalizer of our research interest in this thesis is the channel-shortening equalizer. In the '70s, an MMSE-based filter was suggested as a way to release the computational burden of the MLSD equalization [4]. In the '90s, the MMSE channel shortening filter was applied to the time-domain equalizations of the discrete multitone (DMT) multicarrier modulation or OFDM systems [5 - 8]. Both for MLSD-based systems and for MCM-based systems, the philosophy here is not to bring back the CIR gradually close to a single tap Dirac delta function, but rather to shorten it to a few taps, when the subsequent block can handle the shortened impulse response.

4.3 Theories of Channel-Shortening Time-Domain Equalizations

So far, TEQ designs have been considered mostly in the DSL (DMT) applications, where the CIR is usually very long. The two most popular channel-shortening TEQs are the minimum mean-square-error (MMSE) TEQ and the maximum shortening-SNR (MSSNR) TEQ. TEQ is basically an optimization problem, and many researchers have

come up with different solutions, depending on how we set up and solve the optimization problems. Nevertheless, the solutions of different algorithms are more or less similar.

4.3.1 Unified Formula

Many TEQ designs problems can be expressed by a unified formula in Eq. **4.1 [**1**]**, where $\mathbf{w}$ is a $[T \times 1]$ TEQ vector, M is either equal to 1 or to the number of active tones, and A_n, B_n are $[T \times T]$ matrices specific for TEQ designs. In cases when we have M = 1, the solution is known to be the dominant eigenvector of the generalized eigenvalue problem expressed by Eq. **4.2**. Likewise, the same problem can be alternatively expressed by Eq. **4.3** , and the solution will be found by Eq. **4.4** as the generalized eigenvector corresponding to the smallest eigenvalue. In this thesis, TEQ formulas have been adopted from existing references, re-formulated if needed, and are presented in the FSO context.

$$\max_{\mathbf{w}} \prod_{n=0}^{M-1} \frac{\mathbf{w}^T \mathbf{B}_n \mathbf{w}}{\mathbf{w}^T \mathbf{A}_n \mathbf{w}} \qquad \text{Eq. } \mathbf{4.1}$$

$$\mathbf{B}\mathbf{w} = \lambda \mathbf{A}\mathbf{w} \qquad \text{Eq. } \mathbf{4.2}$$

$$\min_{\mathbf{w}} \prod_{n=0}^{M-1} \frac{\mathbf{w}^T \mathbf{A}_n \mathbf{w}}{\mathbf{w}^T \mathbf{B}_n \mathbf{w}} \qquad \text{Eq. } \mathbf{4.3}$$

$$\mathbf{A}\mathbf{w} = \lambda \mathbf{B}\mathbf{w} \qquad \text{Eq. } \mathbf{4.4}$$

4.3.2 MMSE-TEQ

Fig. **4-2** shows a discrete-time model for a communication link with an MMSE-TEQ. The philosophy here is to minimize MSE between the actual shortened signal $y_{l,\mathbf{w}}$

and a virtual signal delayed and received by a target impulse response (TIR). At a time instant l, given a $[(v+1)\times 1]$ discrete transmit sequence $\mathbf{x}_l = [x_l ... x_{l-v}]^T$, and a $[(L+1)\times 1]$ CIR $\mathbf{h}$, the received sequence after corruption by a noise sequence $\mathbf{n}_l$ is expressed by a $[T\times 1]$ vector $\mathbf{y}_l = [y_l ... y_{l-T+1}]^T$. Through equalization by a $[T\times 1]$ TEQ $\mathbf{w} = [w_0 ... w_{T-1}]^T$, $\mathbf{y}_l$ yields $y_{l,\mathbf{w}} = \mathbf{y}_l^T \mathbf{w}$. On the other hand, $\mathbf{x}_l$ is delayed by Δ and filtered by a $[(v+1)\times 1]$ TIR $\mathbf{b} = [b_0 ... b_v]^T$ to yield $d_l = \mathbf{x}_{l-\Delta}^T \mathbf{b}$. The error signal is compared and minimized in the MMSE sense by defining Eq. **4.5** first and then by Eq. **4.6.** Assuming wide-sense stationarity (WSS), Eq. **4.6** can be further developed to Eq. **4.7**, using definitions of Eq. **4.8**, Eq. **4.9**, and Eq. **4.10**.

As various research efforts in the literature point out, MMSE-TEQ is indeed a generalization from the conventional MMSE equalization, except that here we have additional freedom of TIR and delay. On the other hand, however, in so far as we are interested in channel shortening, we cannot use the conventional MMSE equalization, since it will usually return a center-tap with residual precursors and postcursors, whereas an MMSE-TEQ returns a brick-wall kind of shortened channel impulse response (SCIR) in the time domain.

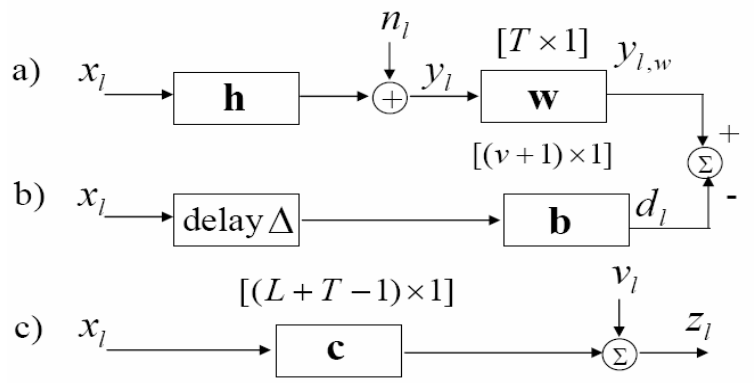

Fig. **4-2:** Block diagram for an MMSE-TEQ a) A discrete-time model with TEQ b) delay Δ and TIR $\mathbf{b}$ c) equalized and delayed channel

$$J \underset{=}{\Delta} E\left\{\left|e_l\right|^2\right\} = E\left\{\left|\mathbf{y}_l^T\mathbf{w} - \mathbf{x}_{l-\Delta}^T\mathbf{b}\right|^2\right\}$$
$$= E\left\{\mathbf{w}^T\mathbf{y}_l\mathbf{y}_l^T\mathbf{w} - 2\mathbf{b}^T\mathbf{x}_{l-\Delta}\mathbf{y}_l^T\mathbf{w} + \mathbf{b}^T\mathbf{x}_{l-\Delta}\mathbf{x}_{l-\Delta}^T\mathbf{b}\right\} \quad \text{Eq. } \mathbf{4.5}$$

$$\min_{\mathbf{b},\mathbf{w}} J = \min_{\mathbf{b},\mathbf{w}} E\left\{\left|e_l\right|^2\right\} = \min_{\mathbf{b},\mathbf{w}} E\left\{\left|\mathbf{y}_l^T\mathbf{w} - \mathbf{x}_{l-\Delta}^T\mathbf{b}\right|^2\right\}$$
$$= \min_{\mathbf{b},\mathbf{w}} E\left\{\mathbf{w}^T\mathbf{y}_l\mathbf{y}_l^T\mathbf{w} - 2\mathbf{b}^T\mathbf{x}_{l-\Delta}\mathbf{y}_l^T\mathbf{w} + \mathbf{b}^T\mathbf{x}_{l-\Delta}\mathbf{x}_{l-\Delta}^T\mathbf{b}\right\} \quad \text{Eq. } \mathbf{4.6}$$
$$= \min_{\mathbf{b},\mathbf{w}} E\left\{\mathbf{w}^T\mathbf{y}_l\mathbf{y}_l^T\mathbf{w} - 2\mathbf{b}^T\mathbf{x}_{l-\Delta}\mathbf{y}_l^T\mathbf{w} + \mathbf{b}^T\mathbf{x}_{l-\Delta}\mathbf{x}_{l-\Delta}^T\mathbf{b}\right\}$$
$$\min_{\mathbf{b},\mathbf{w}} \mathbf{w}^T\mathbf{R}_{yy}\mathbf{w} - 2\mathbf{b}^T\mathbf{R}_{xy}^{\Delta}\mathbf{w} + \mathbf{b}^T\mathbf{R}_{xx}\mathbf{b} \quad \text{Eq. } \mathbf{4.7}$$

$$\mathbf{R}_{yy} \underset{=}{\Delta} E\left\{\mathbf{y}_l\mathbf{y}_l^T\right\}, \left[\mathbf{R}_{yy}\right]_{m,n} = r_{yy}(m-n), 0 \le m,n < T \quad \text{Eq. } \mathbf{4.8}$$

$$\mathbf{R}_{xx} \underset{=}{\Delta} E\left\{\mathbf{x}_l\mathbf{x}_l^T\right\}, \left[\mathbf{R}_{xx}\right]_{m,n} = r_{xx}(m-n), 0 \le m,n < v+1 \quad \text{Eq. } \mathbf{4.9}$$

$$\mathbf{R}_{xy}^{\Delta} \underset{=}{\Delta} E\left\{\mathbf{x}_{l-\Delta}\mathbf{y}_l^T\right\}, \left[\mathbf{R}_{xy}^{\Delta}\right]_{m,n} = r_{xy}(m-n), 0 \le m < v+1,\ 0 \le n < T \quad \text{Eq. } \mathbf{4.10}$$

4.3.2.1 Solution by Unit-Energy Constraint (UEC) on the TEQ

A solution of Eq. **4.7** via a unit-energy constraint on $\mathbf{w}$,or $\mathbf{w}^T\mathbf{w} = 1$, can be found by applying a Lagrangian multiplier and by the steps of Eq. **4.11**. From the step 2 of Eq. **4.11**, by eliminating $\mathbf{b}$, we can arrive at the step 3, which is the same as a generalized

eigenvalue problem. Hence, this can be concluded as a specific solution of Eq. **4.1** and Eq. **4.2,** where Eq. **4.12,** Eq. **4.13** and Eq. **4.14** hold. Given Eq. **4.12** and Eq. **4.13**, $\mathbf{w}$ can be found as the eigenvector (EC) corresponding to the smallest eigenvalue (EV) of $\mathbf{A}$ given in Eq. **4.12**. The vector $\mathbf{w}$ found this way can be substituted into Eq. **4.6** to find MMSE values.

Alternatively, we can substitute the second condition of the step 2 of Eq. **4.11** into J of Eq. **4.11**. By this, we obtain an alternative problem setup as in Eq. **4.15**, which is equivalent to Eq. **4.16**, Eq. **4.12** and Eq. **4.13**. Once again the solution to the Rayleigh quotient can be found by the generalized eigenvalue problem.

Step 1.

$$J_{\text{cost}} = J - \lambda(\mathbf{w}^T\mathbf{w} - 1) = \mathbf{w}^T\mathbf{R}_{yy}\mathbf{w} - 2\mathbf{b}^T\mathbf{R}_{xy}^{\Delta}\mathbf{w} + \mathbf{b}^T\mathbf{R}_{xx}\mathbf{b} - \lambda(\mathbf{w}^T\mathbf{w} - 1)$$

Step 2. $\dfrac{\partial J_{\text{cost}}}{\partial \mathbf{w}} = \mathbf{R}_{yy}\mathbf{w} - \mathbf{R}_{xy}^{\Delta T}\mathbf{b} + \lambda\mathbf{w} = 0$, $\dfrac{\partial J_{\text{cost}}}{\partial \mathbf{b}} = \mathbf{R}_{xx}\mathbf{b} - \mathbf{R}_{xy}^{\Delta}\mathbf{w} = 0$ Eq. **4.11**

Step 3. $-\lambda\mathbf{w} = \left(\mathbf{R}_{yy} - \mathbf{R}_{xy}^{\Delta T}\mathbf{R}_{xx}^{-1}\mathbf{R}_{xy}^{\Delta}\right)\mathbf{w}$

$$\mathbf{A} = \mathbf{R}_{yy} - \mathbf{R}_{xy}^{\Delta T}\mathbf{R}_{xx}^{-1}\mathbf{R}_{xy}^{\Delta},\ [(T+1)\times(T+1)] \qquad \text{Eq. } \mathbf{4.12}$$

$$\mathbf{B} = \mathbf{I},\ [(T+1)\times(T+1)] \qquad \text{Eq. } \mathbf{4.13}$$

$$\text{Let } \lambda \to -1/\lambda \qquad \text{Eq. } \mathbf{4.14}$$

$$\min_{\mathbf{w}} J \text{ subj to } \mathbf{w}^T\mathbf{w} = 1,\ J = \mathbf{w}^T\left(\mathbf{R}_{yy} - \mathbf{R}_{xy}^{\Delta T}\mathbf{R}_{xx}^{-1}\mathbf{R}_{xy}^{\Delta}\right)\mathbf{w} \qquad \text{Eq. } \mathbf{4.15}$$

$$\min_{\mathbf{w}} \frac{\mathbf{w}^T\mathbf{A}\mathbf{w}}{\mathbf{w}^T\mathbf{w}} \qquad \text{Eq. } \mathbf{4.16}$$

4.3.2.2 Solution By Unit-Energy Constraint (UEC) on the TIR

In this solution, we need to solve Eq. **4.7** subject to $\mathbf{b}^T\mathbf{b} = 1$. The solution is given by Eq. **4.1** with definitions of Eq. **4.17** and Eq. **4.18**. $\mathbf{b}$ can be found as the EC

corresponding to the smallest EV of $\mathbf{A}$. Finally, from the orthogonality principle of Eq. **4.19**, $\mathbf{w}$ can be found as Eq. **4.20**. By substituting Eq. **4.20** into J of Eq. **4.5**, MMSE can be further expressed by Eq. **4.21**.

$$\mathbf{A} = \mathbf{R}_{xx} - \mathbf{R}_{xy}^{\Delta}\mathbf{R}_{yy}^{-1}\mathbf{R}_{xy}^{\Delta,T} \quad \text{Eq. 4.17}$$

$$\mathbf{B} = \mathbf{I},\ [(v+1)\times(v+1)] \quad \text{Eq. 4.18}$$

$$E[e_l y_l^*] = E[(y_{l,\mathbf{w}} - d_l)y_l^*] = 0 \quad \text{Eq. 4.19}$$

$$\mathbf{w} = \mathbf{R}_{yy}^{-1}\mathbf{R}_{xy}^{\Delta,T}\mathbf{b} \quad \text{Eq. 4.20}$$

$$\begin{aligned} J_{\min} &= E\left\{\mathbf{b}^T\mathbf{R}_{xy}^{\Delta}\mathbf{R}_{yy}^{-1,T}\mathbf{R}_{yy}\mathbf{R}_{yy}^{-1}\mathbf{R}_{xy}^{\Delta,T}\mathbf{b} - 2\mathbf{b}^T\mathbf{R}_{xy}^{\Delta}\mathbf{R}_{yy}^{-1}\mathbf{R}_{xy}^{\Delta,T}\mathbf{b} + \mathbf{b}^T\mathbf{R}_{xx}\mathbf{b}\right\} \\ &= E\left\{\mathbf{b}^T\mathbf{R}_{xy}^{\Delta}\mathbf{R}_{yy}^{-1}\mathbf{R}_{xy}^{\Delta,T}\mathbf{b} - 2\mathbf{b}^T\mathbf{R}_{xy}^{\Delta}\mathbf{R}_{yy}^{-1}\mathbf{R}_{xy}^{\Delta,T}\mathbf{b} + \mathbf{b}^T\mathbf{R}_{xx}\mathbf{b}\right\} \\ &= E\left\{-\mathbf{b}^T\mathbf{R}_{xy}^{\Delta}\mathbf{R}_{yy}^{-1}\mathbf{R}_{xy}^{\Delta,T}\mathbf{b} + \mathbf{b}^T\mathbf{R}_{xx}\mathbf{b}\right\} \end{aligned} \quad \text{Eq. 4.21}$$

4.3.2.3 Solution by Unit-Tap Constraint (UTC) on the TEQ

The UTC constraint on TEQ can be mathematically stated by Eq. **4.22** where the j[th] tap of $\mathbf{w}$ is 1. This is a specific case of Eq. **4.1** and Eq. **4.2** with definitions of Eq. **4.23** and Eq. **4.24**. $\mathbf{w}$ can be finally found by Eq. **4.25**.

$$\mathbf{e}_j^T\mathbf{w} = 1,\ 0 \le j \le T-1,\ \text{where } \mathbf{e}_j^T \underset{=}{\Delta} [0...1...0] \text{ with 1 at the j[th] position} \quad \text{Eq. 4.22}$$

$$\mathbf{A} = \mathbf{R}_{yy} - \mathbf{R}_{xy}^{\Delta,T}\mathbf{R}_{xx}^{-1}\mathbf{R}_{xy}^{\Delta} \quad \text{Eq. 4.23}$$

$$\mathbf{B} = \mathbf{e}_j\mathbf{e}_j^T \quad \text{Eq. 4.24}$$

$$\mathbf{w} = \frac{\mathbf{A}^{-1}\mathbf{e}_j}{\mathbf{e}_j^T\mathbf{A}^{-1}\mathbf{e}_j} \quad \text{Eq. 4.25}$$

4.3.2.4 Solution by Unit-Tap Constraint on the TIR

In this case, the constraint can be cast as in Eq. **4.26** where the j[th] tap of **b** is 1**.** Using definitions of Eq. **4.27** and Eq. **4.28**, **b** can be found as in Eq. **4.29** and **w** can be found by Eq. **4.30**.

$$\mathbf{e}_j\mathbf{b} = 1, \text{ where } \mathbf{e}_j^T \underline{\Delta} [0...1...0] \text{ with 1 at the j}^{\text{th}} \text{ position} \quad \text{Eq. } \mathbf{4.26}$$

$$\mathbf{A} = \mathbf{R}_{xx} - \mathbf{R}_{xy}^{\Delta}\mathbf{R}_{yy}^{-1}\mathbf{R}_{xy}^{\Delta,T} \quad \text{Eq. } \mathbf{4.27}$$

$$\mathbf{B} = \mathbf{e}_j\mathbf{e}_j^T \quad \text{Eq. } \mathbf{4.28}$$

$$\mathbf{b} = \frac{\mathbf{A}^{-1}\mathbf{e}_j}{\mathbf{e}_j^T\mathbf{A}^{-1}\mathbf{e}_j} \quad \text{Eq. } \mathbf{4.29}$$

$$\mathbf{w} = \mathbf{R}_{yy}^{-1}\mathbf{R}_{xy}^{\Delta,T}\mathbf{b} \quad \text{Eq. } \mathbf{4.30}$$

4.3.2.5 Solution by Unit-Energy Constraint (UEC) on the TEQ-Filtered Output and/or the TIR-Filtered Input

There were several algorithms proposed with constraint(s) such as UEC on TIR-filtered **x** and/or UEC on TEQ-filtered $\mathbf{y}_l$ [**67**]. The constraints can be expressed by Eq. **4.33**, using Eq. **4.31** and Eq. **4.32**. The solution is presented in Eq. **4.34** and Eq. **4.35**.

$$E\left[d_l^2\right] = E\left[\mathbf{b}^T\mathbf{x}_{l-\Delta}\mathbf{x}_{l-\Delta}^T\mathbf{b}\right] = \mathbf{b}^T\mathbf{R}_{xx}\mathbf{b} \quad \text{Eq. } \mathbf{4.31}$$

$$E\left[y_{l,\mathbf{w}}^2\right] = E\left[\mathbf{w}^T\mathbf{y}_l\mathbf{y}_l^T\mathbf{w}\right] = \mathbf{w}^T\mathbf{R}_{yy}\mathbf{w} \quad \text{Eq. } \mathbf{4.32}$$

$$\mathbf{b}^T\mathbf{R}_{xx}\mathbf{b} = 1 \text{ and/or } \mathbf{w}^T\mathbf{R}_{yy}\mathbf{w} = 1 \quad \text{Eq. } \mathbf{4.33}$$

$$\mathbf{A} = \mathbf{R}_{yy} - \mathbf{R}_{xy}^{\Delta}\mathbf{R}_{xx}^{-1}\mathbf{R}_{xy}^{\Delta} \quad \text{Eq. } \mathbf{4.34}$$

$$\mathbf{B} = \mathbf{R}_{yy} \quad \text{Eq. } \mathbf{4.35}$$

4.3.3 MSSNR-TEQ

An alternative criterion of channel shortening equalization is the maximum-shortening SNR (MSSNR) TEQ criterion. It was originally proposed by P. J. W. Melsa et. al. [5], and was later further investigated by R. Schur et. al [9] and M. Milosevic[10]. Its principle can be explained graphically by Fig. **4-3**, where $\mathbf{h}_{sh}$ is a $[(L+T)\times 1]$ SCIR, $\mathbf{h}_{sh,win}$ is a $[(v+1)\times 1]$ vector into which we want to force most of SCIR's energy, $\mathbf{h}_{sh,wall,1}$ is a $[\Delta\times 1]$ vector corresponding to the postcursor ISI, $\mathbf{h}_{sh,wall,2}$ is a $[(L+T-\Delta-v-1)\times 1]$ vector corresponding to the precursor ISI, and Δ is a delay introduced.

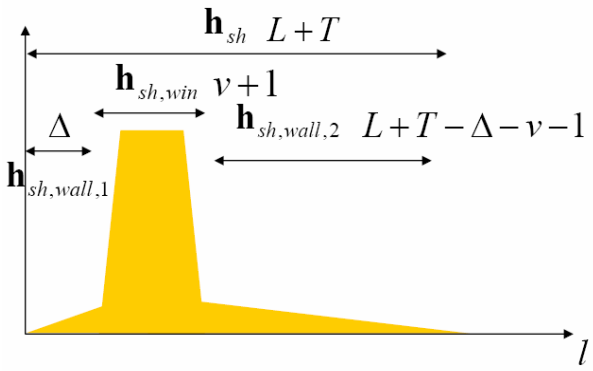

Fig. **4-3**: An example of SCIR

For mathematical derivations, we define matrices Eq. **4.36**, Eq. **4.37**, Eq. **4.38**, Eq. **4.39** and Eq. **4.40** based on the CIR $\mathbf{h}$. As implied in Fig. **4-3**, what the MSSNR TEQ does is to attempt to minimize the energy within the vector $\mathbf{h}_{sh,wall} = \left[\mathbf{h}_{sh,wall,1}^{T} \quad \mathbf{h}_{sh,wall,2}^{T}\right]^{T}$ while trying to maximize the energy contained within the vector $\mathbf{h}_{sh,win}$.

$$\mathbf{H}_{wall,1}=\begin{bmatrix} h_{\Delta-T} & \cdots & h_0 & \cdots & 0 \\ \vdots & \ddots & \vdots & \ddots & \vdots \\ h_{\Delta-1} & \cdots & h_{\Delta-T} & \cdots & h_0 \end{bmatrix},\ [T\times\Delta],\ \text{defined based on } [h_0 \ldots h_{\Delta-T}] \quad \text{Eq. 4.36}$$

$$\mathbf{H}_{wall,2}=\begin{bmatrix} h_L & \cdots & h_{\Delta+v+1} & \cdots & h_{\Delta+v-T+2} \\ \vdots & \ddots & \vdots & \ddots & \vdots \\ 0 & \cdots & h_L & \cdots & h_{\Delta+v+1} \end{bmatrix}, \quad \text{Eq. 4.37}$$

$[T\times(L-\Delta-v+T-1)]$, defined based on $[h_{\Delta+v-T+2} \ldots h_L]$

$$\mathbf{H}_{win}=\begin{bmatrix} h_{\Delta+v-T+1} & \cdots & h_{\Delta-T+1} \\ \vdots & \ddots & \vdots \\ h_{\Delta+v} & \cdots & h_{\Delta} \end{bmatrix},\ [T\times(v+1)],\ \text{defined based on } [h_{\Delta-T+1} \ldots h_{\Delta+v}] \quad \text{Eq. 4.38}$$

$$\mathbf{H}_{wall}=\begin{bmatrix}\mathbf{H}_{wall,2} & \mathbf{H}_{wall,1}\end{bmatrix},\ [T\times(L-v+T-1)] \quad \text{Eq. 4.39}$$

$$\mathbf{H}_{T}=\begin{bmatrix}\mathbf{H}_{wall,2} & \mathbf{H}_{win} & \mathbf{H}_{wall,1}\end{bmatrix},\ [T\times(L+T)] \quad \text{Eq. 4.40}$$

Vectors $\mathbf{h}_{sh,wall}$ and $\mathbf{h}_{sh,win}$ can then be further expressed using the CIR as in Eq. **4.41** and Eq. **4.42,** where $\mathbf{J}_n$ is an $[n\times n]$ exchange matrix with ones on the antidiagonal positions and zeros elsewhere. Now, energies within and outside the window can be described by Eq. **4.43** and Eq. **4.44**.

$$\mathbf{h}_{sh,wall}=\begin{bmatrix}\mathbf{h}_{sh,wall,1}^T & \mathbf{h}_{sh,wall,2}^T\end{bmatrix}^T=\overset{\Delta}{\mathbf{H}}_{wall}\,\mathbf{w}=\left(\mathbf{J}_T\mathbf{H}_{wall}\mathbf{J}_{L+T-v-1}\right)^T\mathbf{w} \quad \text{Eq. 4.41}$$

$,[1\times(L+T-v-1)]$

$$\mathbf{h}_{sh,win}=\overset{\Delta}{\mathbf{H}}_{win}\,\mathbf{w}=\left(\mathbf{J}_T\mathbf{H}_{win}\mathbf{J}_{v+1}\right)^T\mathbf{w},\ [1\times(v+1)] \quad \text{Eq. 4.42}$$

$$E_{win}=\mathbf{h}_{sh,win}^T\mathbf{h}_{sh,win}=\mathbf{w}^T\mathbf{B}\mathbf{w}=\mathbf{w}^T\,\overset{\Delta}{\mathbf{H}}{}_{win}^{T}\,\overset{\Delta}{\mathbf{H}}_{win}\,\mathbf{w},\ \text{where}\ \mathbf{B}=\overset{\Delta}{\mathbf{H}}{}_{win}^{T}\,\overset{\Delta}{\mathbf{H}}_{win} \quad \text{Eq. 4.43}$$

$$\begin{aligned} E_{wall}&=\mathbf{h}_{sh,wall}^T\mathbf{h}_{sh,wall}=\begin{bmatrix}\mathbf{h}_{sh,wall,1}^T & \mathbf{h}_{sh,wall,2}^T\end{bmatrix}\begin{bmatrix}\mathbf{h}_{sh,wall,1}^T & \mathbf{h}_{sh,wall,2}^T\end{bmatrix}^T \\ &=\mathbf{h}_{sh,wall,1}^T\mathbf{h}_{sh,wall,1}+\mathbf{h}_{sh,wall,2}^T\mathbf{h}_{sh,wall,2}=\mathbf{w}^T\mathbf{A}\mathbf{w}\ ,\ \text{where}\ \mathbf{A}=\overset{\Delta}{\mathbf{H}}{}_{wall}^{T}\,\overset{\Delta}{\mathbf{H}}_{wall} \end{aligned} \quad \text{Eq. 4.44}$$

One method of achieving the MSSNR objective is by minimizing E_{wall} while constraining E_{win} to be 1 as in Eq. **4.45** [5], or equivalently by Eq. **4.46 [**26**]**.

$$\min_{\mathbf{w}} E_{wall} \text{ subject to } E_{win} = 1 \qquad \text{Eq. } \mathbf{4.45}$$

$$\max_{\mathbf{w}} E_{win} \text{ subject to } E_{wall} = 1 \qquad \text{Eq. } \mathbf{4.46}$$

[26**]** gives the optimal solution of Eq. **4.47** and Eq. **4.50,** where definitions in Eq. **4.48** and Eq. **4.49** are used.

$$\mathbf{w}_{opt} = \left(\mathbf{L}_A^T\right)^{-1}\mathbf{u}_{\max} \qquad \text{Eq. } \mathbf{4.47}$$

$\mathbf{A} = \mathbf{L}_A\mathbf{L}_A^T$, $\mathbf{L}_A$: a lower triangular matrix Eq. **4.48**

$\mathbf{u}_{\max}$: normalized eigenvector of matrix $(\mathbf{L}_A)^{-1}\mathbf{B}(\mathbf{L}_A)^{-1}$ corresponding to the largest eigenvalue $\lambda_{\max}$ Eq. **4.49**

$$SSNR_{opt} = 10\log_{10}\left(\frac{\mathbf{w}_{opt}^T\mathbf{B}\mathbf{w}_{opt}}{\mathbf{w}_{opt}^T\mathbf{A}\mathbf{w}_{opt}}\right) = 10\log_{10}(\lambda_{\max}) \qquad \text{Eq. } \mathbf{4.50}$$

We can also extend MSSNR criterion to MSSNRn by considering additive input noise to the TEQ. In this case, SSNR's definition will be changed as the signal power of the window energy over the sum of wall energy plus noise power at the shortening equalizer output. For this calculation, definition of $\mathbf{A}$ in Eq. **4.48** needs to be modified to Eq. **4.51**. We can call this MSSNRn criterion. Otherwise, the eigen problem can be solved in the same way to derive a solution.

$\mathbf{A} = \overset{\Delta}{\mathbf{H}}_{wall}^T\overset{\Delta}{\mathbf{H}}_{wall} + \mathbf{R}_{nn}$, $\mathbf{R}_{nn}$: noise covariance matrix at shortening equalizer input Eq. **4.51**

4.3.4 Considerations of Optimality Criterion, TEQ Length and TIR Length

Even though the BER or the SER (symbol error rate) is the ultimate criterion of performance evaluation, it needs exhaustive simulations in order to design a channel

shortening filter best in the BER sense. Since we know that the error performance depends on parameters such as the number of TEQ filter taps T and the number of SCIR taps $L+T$, as a computationally practical alternative, we can devise an easy-to-calculate metric which is somehow related to parameters such as T and $L+T$. This is how we have come up with metrics such as MSE, SSNR or $SSNR_n$. Another fact to note is that, unlike the conventional equalization methods such as LMMSE or DFE whose BER performance shows only 1-dimensional dependence on the number of equalizer taps, the TEQ shows two-dimensional dependence on both T and $L+T$. Thus, apart from the TEQ formulations that we can use once we have determined the appropriate values for T and $L+T$, we need to somehow establish the appropriate values of T and $L+T$ in the beginning.

In this sense, the approach in this thesis is, from a practical engineering perspective, to find a local minimum point considering the TEQ length and the TIR length as arbitrary constraints. Thus, we will avoid a detailed discussion on finding the global minimum. We can make several points about the optimality criteria. First, looking at the formulation for MMSE, it minimizes the error between the actual path and the virtual path in the MSE sense. However, this does not always assure that the SCIR is the best for the Viterbi equalizer to work further on. Second, as for the MSSNR and the $MSSNR_n$ metrics, given a range of TEQ lengths and the TIR lengths as the constraint, there may not be a direct relationship between a boosted MSSNR (or $MSSNR_n$) and a lowered BER. For example, in so far as we can boost MSSNR (or $MSSNR_n$), the MSSNR (or $MSSNR_n$) algorithm may return an SCIR with a wider discrete-time window size as

the best. However, an SCIR with a wider window means more error propagation, so is not always translated into a lowered BER.

In order to explain the usefulness of $MSSNR_n$ in an intuitive sense, but not in the strict sense, we introduce two alternative metrics given in Eq. **4.52** and Eq. **4.53**. Eq. **4.52** is defined at the TEQ output, and here we try to minimize the loss due to the residual taps of $\mathbf{h}_{sh,wall}$. If we have an SCIR which has almost zero energy in $\mathbf{h}_{sh,wall}$, then Eq. **4.52** will degenerate to minimizing the ratio of $E_{sh} / E_{sh,win}$. Thus, Eq. **4.52** can be understood as a more general expression than the dual of SSNR.

$$\begin{aligned} SNR\_crit\_1 &= SNR_o - SSNR_n \\ &= 10\log 10\left(\frac{\mathbf{h}_{sh}^T\mathbf{h}_{sh}}{\mathbf{w}^T\mathbf{R}_{nn}\mathbf{w}}\right) - 10\log 10\left(\frac{\mathbf{h}_{sh,win}^T\mathbf{h}_{sh,win}}{\mathbf{h}_{sh,wall}^T\mathbf{h}_{sh,wall} + \mathbf{w}^T\mathbf{R}_{nn}\mathbf{w}}\right) \end{aligned} \qquad \text{Eq. } \mathbf{4.52}$$

Eq. **4.53** describes the ratio of signal power changes over noise power changes through the TEQ. However, this metric does not describe how shortened the SCIR is.

$$SNR\_crit\_2 = 10\log 10\left(\frac{S_o / S_i}{N_o / N_i}\right) = 10\log 10\left(\frac{\mathbf{h}_{sh}^T\mathbf{h}_{sh} / \mathbf{h}^T\mathbf{h}}{\mathbf{w}^T\mathbf{w}}\right) \qquad \text{Eq. } \mathbf{4.53}$$

We can finally define Eq. **4.54** using Eq. **4.52** and Eq. **4.53**, such that we aim at increasing Eq. **4.53** while decreasing Eq. **4.52**. Thus, we can at once increase the SSNR (or $SSNR_n$) and increase the ratio of signal power changes over noise power changes. After several manipulations on Eq. **4.54**, we obtain Eq. **4.55**, expressing that SNR_crit_3, which aims at increasing SNR_o / SNR_i given a TEQ while decreasing loss due to the residual ISI after shortening, turns out to be the same metric as $SSNR_n$ scaled by SNR. Thus, SNR_crit_3, at a certain SNR, will always be commensurate with $SSNR_n$.

Thus, we claim that the $MSSNR_n$ metric, at a certain SNR, will always boost the SNR changes through the TEQ, while decreasing the loss due to the residual ISI after shortening.

$$\begin{aligned} SNR\_crit\_3 &= SNR\_crit\_2 - SNR\_crit\_1 \\ &= 10\log 10\left(\frac{\mathbf{h}_{sh}^T\mathbf{h}_{sh}/\mathbf{h}^T\mathbf{h}}{\mathbf{w}^T\mathbf{w}}\right) \\ &\quad -10\log 10\left(\frac{\mathbf{h}_{sh}^T\mathbf{h}_{sh}}{\mathbf{w}^T\mathbf{R}_{nn}\mathbf{w}}\right)+10\log 10\left(\frac{\mathbf{h}_{sh,win}^T\mathbf{h}_{sh,win}}{\mathbf{h}_{sh,wall}^T\mathbf{h}_{sh,wall}+\mathbf{w}^T\mathbf{R}_{nn}\mathbf{w}}\right) \end{aligned} \quad \text{Eq. } \mathbf{4.54}$$

$$\begin{aligned} SNR\_crit\_3 &= 10\log 10\left(\frac{\mathbf{h}_{sh,win}^T\mathbf{h}_{sh,win}}{\mathbf{h}_{sh,wall}^T\mathbf{h}_{sh,wall}+\mathbf{w}^T\mathbf{R}_{nn}\mathbf{w}}\right)-10\log 10\left(\frac{\mathbf{h}^T\mathbf{h}}{\sigma_N^2}\right) \\ &= 10\log 10(SSNRn)-10\log 10(SNR) \end{aligned} \quad \text{Eq. } \mathbf{4.55}$$

4.3.5 Considerations from FSO Implementation Perspective

One problem of channel shortening is in that it causes colored noise. Originally, the MLSD algorithm was proposed under the assumption that we have a white Gaussian noise sequence. If we have a colored noise sequence, then depending on the correlation in the time domain, we can still use the Viterbi equalizer, but then the BER is no longer optimal. In our case of FSO, the lengths of the discrete channels, depending on the data rate, will sometimes require TEQs of lengths around 100 taps, rendering the performance of the Viterbi equalizer under the presence of colored noise bad. If we place a whitening filter at the receiver, it would nullify what the TEQ had done.

One way around this dilemma is to place the TEQ at the transmitter, while keeping the Viterbi equalizer at the receiver. For this configuration to work, we can benefit from a separate link, or an RF link, which provides channel side information

(CSI) from the receiver to the transmitter. Also, the formulations have to be re-considered overall. In the case of the MMSE-TEQ at the transmitter, we used the equations Eq. **4.17** ~ Eq. **4.21**, but let the noise power to be zero, similar to how an LMMSE equalizer behaves similar to a ZF equalizer, and then switched the locations of the TEQ and the channel $\mathbf{h}$. Similar to the reason we can satisfactorily use a ZF equalizer in channels without nulls rather than an LMMSE equalizer, we can use this algorithm without significant noise enhancement. In the case of the $MSSNR_n$ algorithm, we used Eq. **4.36** ~ Eq. **4.50**, but between $\mathbf{h}$ and the TEQ, we assume that the virtual noise power enters the TEQ such that we can re-use the existing solutions, and after obtaining the TEQ, we switched $\mathbf{h}$ and the TEQ.

4.4 Results of TEQ Equalizations of FSO Links

4.4.1 Discrete Channel Models

In this research, assuming that the channel model presented in [15] is valid, we present some snapshots of the discrete channel model based on the single-gamma function. Since our interest is in application of shortening equalizers for low-to-mid optical thickness values, we consider τ values of 5, 7, 8, 9, 10, 11, 12, 13, 14 and 15, and present some snapshots as in Fig. **4-4**. These chosen τ values do not always exist in the real world, however, since as [15] shows, each of the realistic cloud types has a different average τ value and a typical coefficient value for k_{scat}. Nevertheless, since we are interested more in DSP techniques' capability and their feasibility in FSO, we need the

channel model somehow to gradually change. The author also mentions that our discrete channel snapshots consist of 5, 8, 16, 24, 34, 44, 55, 67, 81 and 95 taps for the aforementioned τ values, when 99.9% of the total channel energy is counted. We also mention that, since we approach FSO in the equalization context, we adopted a channel model without considering attenuation, assuming that attenuation has somehow been compensated for by power control.

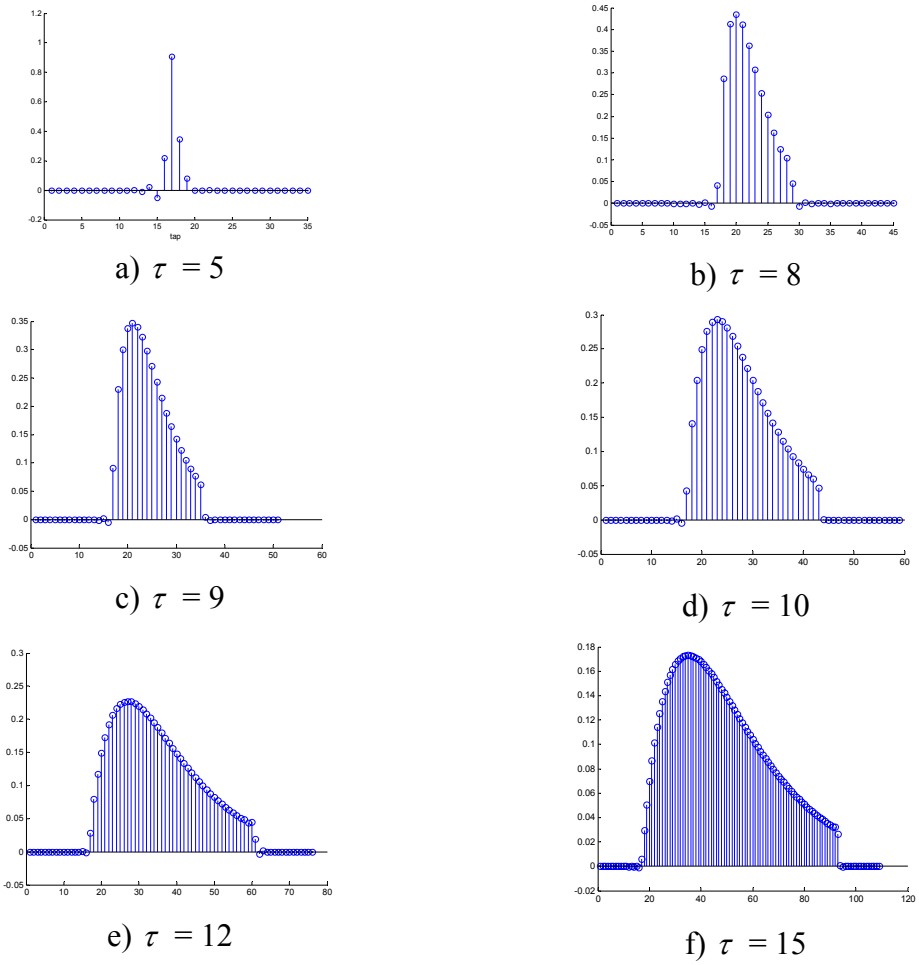

a) $\tau = 5$ b) $\tau = 8$ c) $\tau = 9$ d) $\tau = 10$ e) $\tau = 12$ f) $\tau = 15$

Fig. **4-4**: Discrete FSO channels based on [15] for a 1000m cloud with various optical thickness values. $R_b = 5.333$Gbps.

Assumed that different snapshots represent different kind of clouds with different K_{scat}, while keeping same L.

4.4.2 BER Results of Conventional Equalizations

In this section, we first present an overview of the performance of conventional equalizations, both LMMSE equalization and DFE. Fig. **4-5** shows the BER performance of LMMSE equalization by Monte Carlo simulations. Even though the LMMSE can enhance the BER to some extent, it cannot enhance the BER for the τ =8 case.

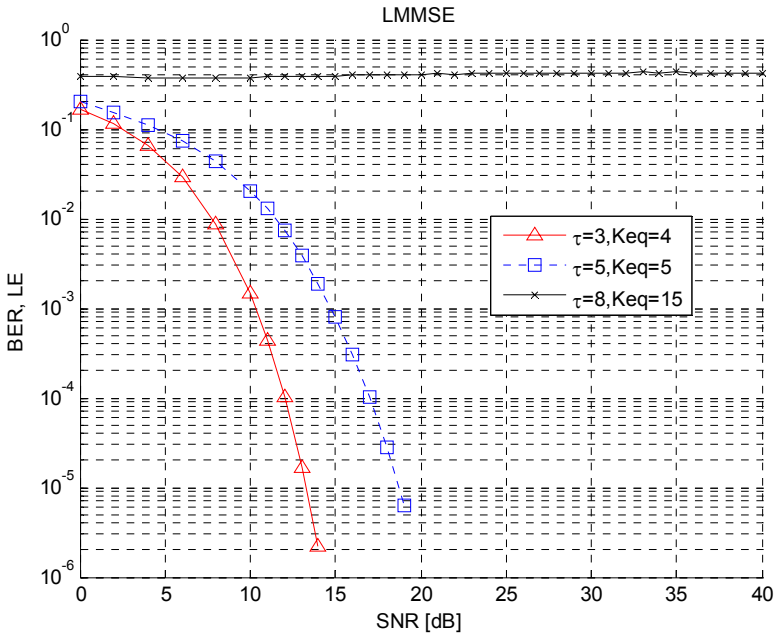

Fig. **4-5**: LMMSE equalization. τ = 3, 5, 8

In Fig. **4-6**, we show the DFE performance. We fixed N_{FB} (number of feedback taps) to be as long as the channel length, and set N_{FF} (number of feedforward taps) correspondingly, such that the performance of LE and DFE can be compared fairly with

equal tap numbers assumed. Unlike the LE BER curves of Fig. **4-5**, we can still decode reliably, even though high SNR values are needed.

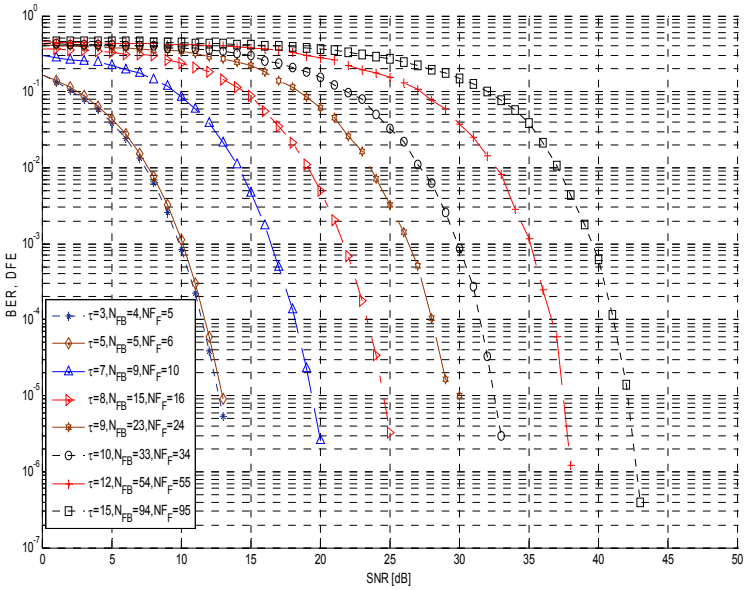

Fig. **4-6**: MMSE DFE, $\tau = 3 \sim 15$

4.4.3 Comparison in TEQ Optimality Criteria and Effective SCIR Length

In TEQ designs, first, it needs to be considered that the TEQ length T (or N_f) and the TIR length v+1 (or N_b) give rise to the computational complexity of the TEQ and the MLSD equalizer, respectively. Also, considering the MLSD stage following the TEQ and its memory requirements, v+1 should not exceed a reasonable length. In this context, we adopted an inequality constraint on T such as $T \le 100$, $T \le 200$, or $T \le 400$ depending on the optical thickness and an inequality constraint on v such as $v+1 \le 20$, and then searched through the quadratic MSE or the MSSNR_n space for the candidate points

consisting of T and v+1. Second, even though we set $v+1 \leq 20$, it does not always guarantee that the evaluated SCIR is of MLSD-equalizable length. In particular, if we have any residual SCIR taps which occur away from the main taps, many times we cannot implement a Viterbi equalizer, even though the main energy of the SCIR occurs within several main taps. Thus, we numerically calculated the effective SCIR length space by counting in only taps of 99.9% energy and masked the MSE or the $MSSNR_n$ space such that only the MLSD-equalizable points could be considered. In this thesis, we arbitrarily picked only SCIR's not exceeding 14 taps in a 99.9% energy criterion as Viterbi-equalizable SCIRs for its moderate level of complexity in the computing environment of Matlab on PCs.

4.4.3.1 Shortening by MMSE-UEC-TEQ

Fig. **4-7** shows the MMSE-UEC criterion TEQ's performance in a 3D MSE space, an effective SCIR length space in 99.9% energy criterion, a 3D MSE space with only Viterbi-equalizable points only, and the evaluated SCIR. We can make several observations. First, T naturally needs to be of a greater length than the CIR, and v+1 need to be of some reasonable value such that MSE can be enhanced. Second, the MSE space depends very sensitively on the combination of the T and v+1 values. Third, in Fig. **4-7** b), similar to our findings in Fig. **4-7** a), the effective length distribution depends on both T and v+1. If we have T and v+1 of beyond certain lengths, then the effective SCIR length increases linearly with v+1, but not as much with T. If we consider Fig. **4-7** a) and

b) simultaneously, we get Fig. **4-7** c). Out of the 77 equalizable points that we obtained from the 200 possible points in $T \le 100$, $v+1 \le 20$, we chose T = 60 and v+1 = 6 as the MMSE-UEC-TEQ setting for the BER evaluation, for its advantages in both MSE and effective SCIR length.

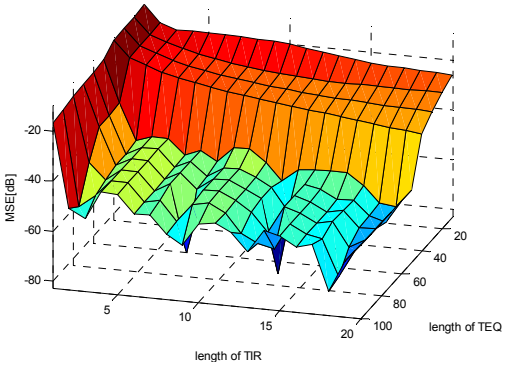

a) 3D MSE space

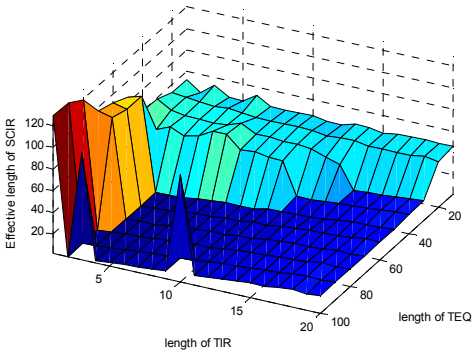

b) Distribution of 99.9% effective length of SCIR

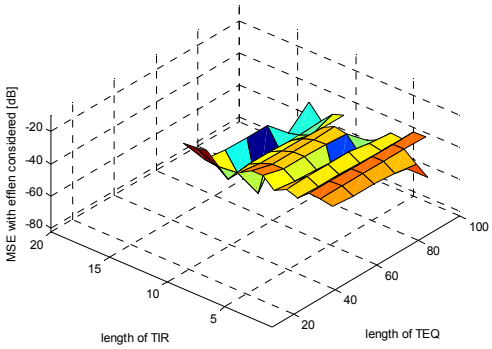

c)3D MSE space with Viterbi-equalizable points

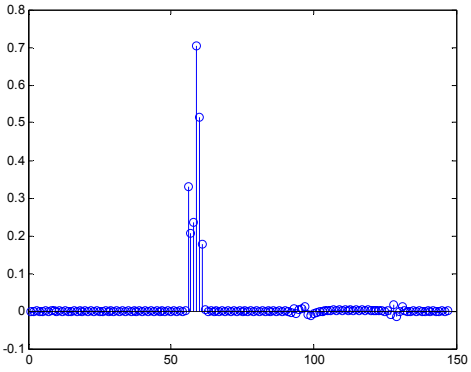

d) SCIR, T = 80, v+1 = 6

Fig. **4-7**: MMSE-UEC TEQ, τ = 10, SNR = 30dB, $T \le 100$, $v+1 \le 20$

4.4.3.2 Shortening by MSSNR$_n$-TEQ

Likewise, similar tests were performed using the MSSNR$_n$-TEQ algorithm, under the same constraints and conditions as before. We can make several observations. First, Fig. **4-8** a) shows that the 3D SSNR$_n$ space shows dependence on both T and v+1. Second, Fig. **4-8** a) shows that to some extent, the complexity in terms of T and v+1 are exchangeable. Third, Fig. **4-8** b) shows that in so far as T and v+1 are larger than certain values, the SCIR's effective length grows linearly with v+1 as expected, but almost independent of T. Fourth, Fig. **4-8** c) shows that out of a total of 200 points, we obtained 106 Viterbi-equalizable points. We chose T = 100 and v+1 = 15 as the point for the BER evaluation. But in fact, as Fig. **4-8** c) indicates, there are 105 other alternative MSSNR$_n$-TEQ points that can show a similar performance in the MSSNR$_n$ context.

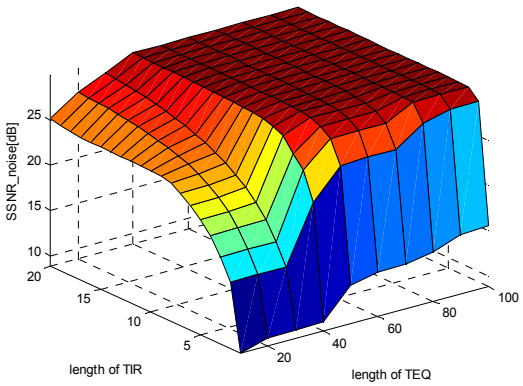

a) 3D $MSSNR_n$ space

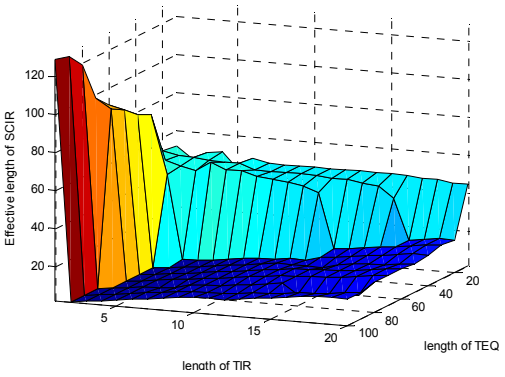

b) Distribution of 99.9% effective length of SCIR

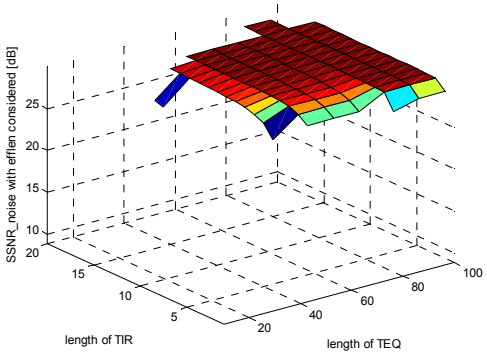

c) 3D $MSSNR_n$ space with Viterbi-equalizable points

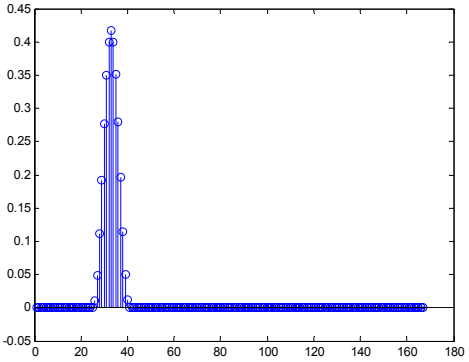

d) SCIR, T = 100, v+1 = 15

Fig. **4-8**: $MSSNR_n$ TEQ, τ = 10, SNR = 30dB, $T \le 100$, $v+1 \le 20$

Since we encounter even more dispersive channel conditions as the weather conditions change, we further considered the shortening performance of the TEQ in more dispersive channel conditions as below.

4.4.3.3 MMSE-UEC Shortening at More Dispersive Channel Conditions

At τ = 12, out of a total of 400 points, we could get 4 equalizable points of (T = 80, v+1 = 11), (T = 90, v+1 = 11), (T = 100, v+1 = 11), and (T = 110, v+1 = 11). The results are presented in Fig. **4-9**. For the τ values of 13 and higher, we could not get any equalizable point in a similar space.

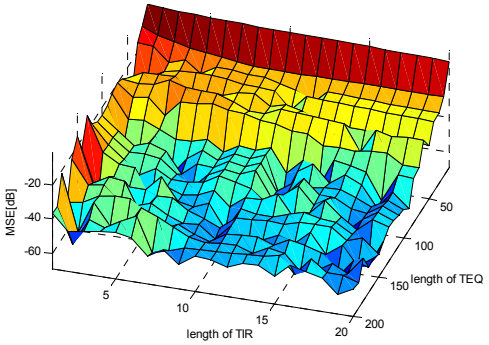

a) 3D MMSE space

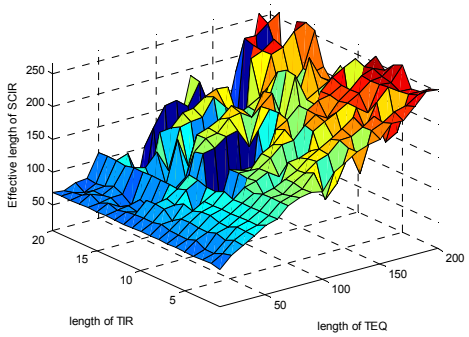

b) Distribution of effective SCIR length

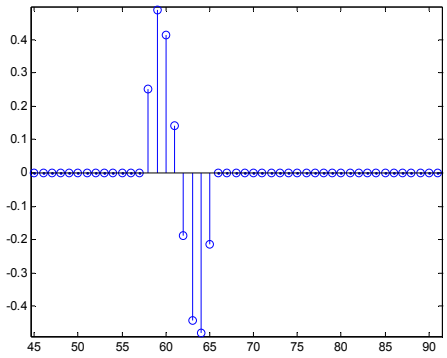

c) SCIR found with T = 170, v+1 = 8

Fig. **4-9**: MMSE-UEC TEQ, τ = 12, SNR = 30dB, $T \le 200$, $v+1 \le 20$

4.4.3.4 MSSNR$_n$ Shortening at More Dispersive Channel Conditions

At τ = 15, when the discrete channel spans about 112 taps in the 99.9% energy criterion, we get the results shown in Fig. **4-10** a) ~ d). Out of a total space of 400 points, we could obtain 67 equalizable points.

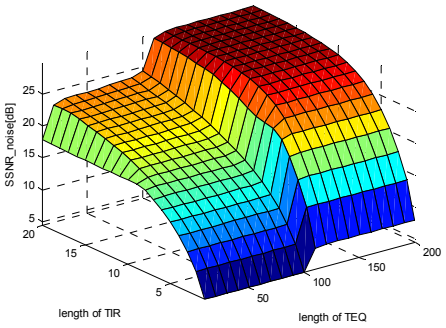

a) 3D MSSNR$_n$ space

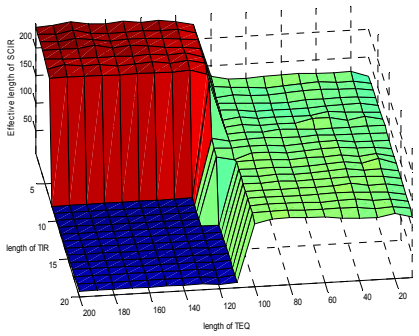

b) Distribution of SCIR's effective length

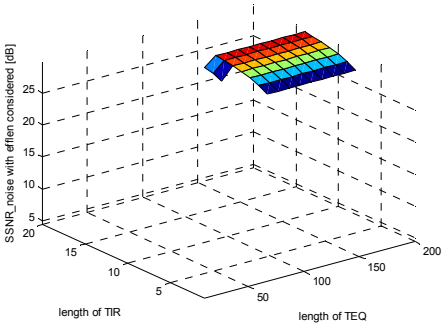

c) 3D MSSNR$_n$ space with Viterbi-equalizable points

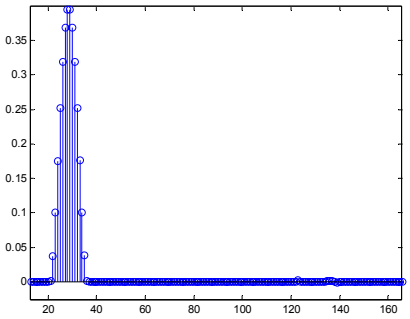

d) SCIR found with T = 200, v+1 = 13

Fig. **4-10**: MSSNR$_n$ TEQ, τ = 15, SNR = 30dB, $T \le 200$, $v+1 \le 20$

At an even higher optical thickness of τ = 20, however, out of 400 points in $T \le 400$ and $v+1 \le 20$, we could not get any equalizable point by the MSSNR$_n$ algorithm. To summarize, we can make several observations from Fig. **4-7** ~ Fig. **4-10**. We can use both the MMSE-UEC and the MSSNR$_n$ algorithms for τ = 10. But for τ =

15, $MSSNR_n$ is a better choice, since the MMSE-UEC algorithm does not yield Viterbi-equalizable SCIR, whereas the $MSSNR_n$ algorithm can still return SCIRs of moderate lengths.

4.4.4 Statistics on TEQ Shortening Capability

Below, Fig. **4-11** graphically shows the percentages of Viterbi-equalizable points (P_{VEP}), given spaces consisting of τ, T and v+1. For different τ values, we modified the T and v+1 ranges slightly such that each test case can be meaningful and such that we can make comparisons between the MMSE-UEC TEQ and the $MSSNR_n$ TEQ for the same testing conditions.

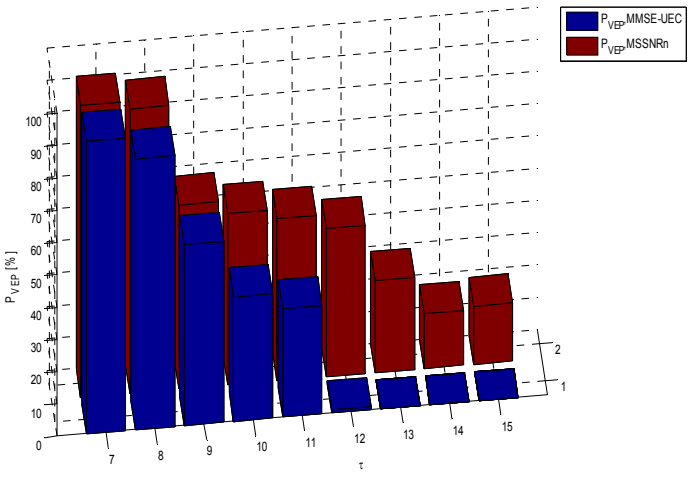

Fig. **4-11**: P_{VEP} for spaces consisting of τ, T, and v+1 values.

τ = 7 case: $\{T : 10 \le T \le 60\} \bigcap \{v : 1 \le v+1 \le 7\}$,
τ = 8 case: $\{T : 10 \le T \le 100\} \bigcap \{v : 1 \le v+1 \le 16\}$,
τ = 9, 10 cases: $\{T : 10 \le T \le 100\} \bigcap \{v : 1 \le v+1 \le 20\}$,
τ = 11, 12, 13 cases: $\{T : 10 \le T \le 200\} \bigcap \{v : 1 \le v+1 \le 20\}$,
τ = 14, 15 cases: $\{T : 20 \le T \le 200\} \bigcap \{v : 1 \le v+1 \le 20\}$

From Fig. **4-11**, we can make several observations. First, at lower τ values of 7 ~ 10, both algorithms work relatively well in so far as P_{VEP} is concerned, opening ways for the following MLSD algorithm to decode the received symbols correctly. Second, however, it cannot be guaranteed that we will always find Viterbi-equalizable points at higher τ values. In fact, at the τ values of 12 ~ 15, it is very hard to find any Viterbi-equalizable points for the MMSE-UEC algorithm. However, we still have $P_{VEP} > 0$ for the $MSSNR_n$ algorithm at the τ values of 12 ~ 15. The main reason that the MMSE-UEC algorithm fails for τ values of 12 ~ 15 is that we unavoidably end up having residual taps far from the main taps, and for this reason, we can to some extent shorten the CIR, but cannot use the MLSD algorithm.

4.4.5 BER Performance of the TEQ with the Viterbi Equalizer Scheme

With our previous discussion and results, we attached a Viterbi equalizer at the receiver. As for the choice of T and v+1 values, we first evaluated the 3D $MSSNR_n$ space or the MSE space, and then chose one of the points with a satisfactory performance. Fig. **4-12** and Fig. **4-13** show the BER curves for several τ values for the $MSSNR_n$ and the MMSE-UEC algorithms obtained from Monte Carlo simulations. We can make several observations. First, if we compare at the BER of 1E-4, even though both the algorithms show similar performance at the τ values of 5 and 7, the MMSE-UEC algorithm outperforms the $MSSNR_n$ algorithm at the higher τ values of 8, 10, and 12. This is due to the fact that the MMSE-UEC algorithm returned a shorter SCIR than the $MSSNR_n$ algorithm at these higher τ values. Second, since we cannot run the MMSE-

UEC algorithm for $\tau \geq 15$, we must conclude that both algorithms have highs and lows. Fourth, due to our limits in computational capability, we could not verify below the shown BER. In particular, for the τ values of 10 and 12, it is unclear whether the $MSSNR_n$ curves can still enhance or not by increasing SNR. However, if we compare at the BER of 1E-4, both the $MSSNR_n$ curves and the MMSE-UEC curves outperform the DFE curves, although this enhancement comes of course at the cost of a heavier computational complexity and memory requirements of the suggested transceiver architecture.

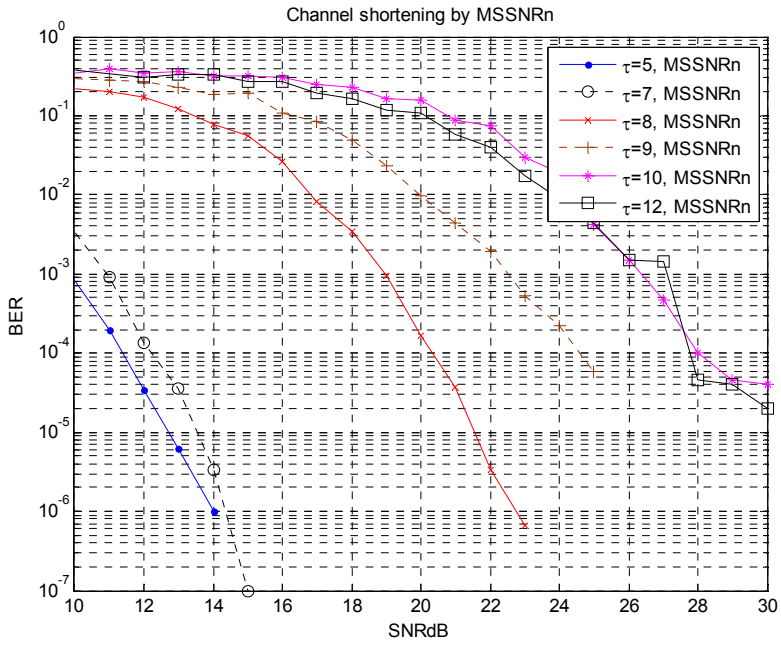

Fig. **4-12**. Error performance by MLSD with $MSSNR_n$-TEQ.

τ = 5 case: T = 40, v+1 = 1, τ = 7 case: T = 60, v+1 = 2, τ = 8 case: T = 100, v+1 = 10, τ = 9 case: T = 100, v+1 = 11, τ = 10 case: T = 100, v+1 = 15, τ =12 case: T = 200, v+1 = 16

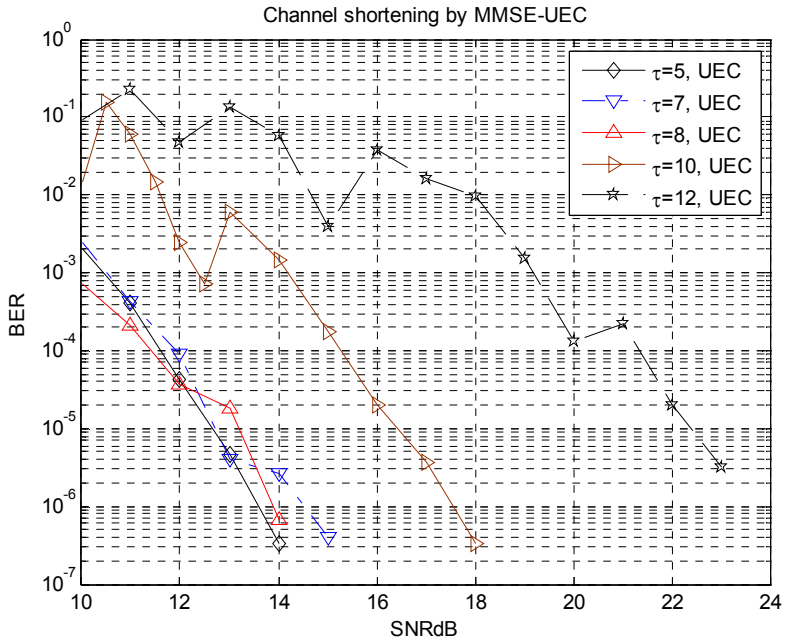

Fig. **4-13**: Error performance by MLSD with MMSE-UEC-TEQ.

τ = 5 case: T = 20, v+1 = 2, τ = 7 case: T = 20, v+1 = 2, τ = 8 case: T = 100, v+1 = 2, τ = 10 case: T = 80, v+1 = 6, τ = 12 case: T = 170, v+1 = 8

4.4.6 Performance in Channel Estimation Errors

So far, we have been assuming that we have a perfect CSI at the receiver. In reality, this is not always the case. First, after adapting the TEQ at a certain τ value, the true τ value may have changed after some time. This could be due to the mobility of the ground station or the aerial vehicle, or to the changing nature of the cloud medium itself. Second, even without consideration of mobility, there could have been channel estimation errors. For any of these cases, in a broad sense, we use the term 'channel estimation error' in this thesis.

In the TEQ-based receiver architecture, the effects of the channel estimation errors can be serious. In particular, by having a TEQ computed for wrong τ values, the SCIR may be beyond the Viterbi-equalizable length. In this section, we investigate the effects of channel estimation errors in both the effective SCIR length and the BER contexts.

4.4.6.1 Distribution of Effective Length of SCIR in the Presence of Channel Estimation Errors

In Fig. **4-14** and Fig. **4-15**, we have shown the effects of channel estimation errors on the P_{VEP}. We assumed that the TEQ was originally computed for respective τ values of 5, 7, 8, and 9, but that in fact the FSO link is communicating in $\tau + \Delta\tau$ (= τ offset), due to channel estimation errors. Since we employed slightly different N_f-N_b space setups for different τ values of 5, 7, 8, and 9, we cannot compare cases of different τ values in a strict sense, but we can still compare in a less strict sense, however. At least, we can track the pattern of P_{VEP} for each τ value as the $\Delta\tau$ values change.

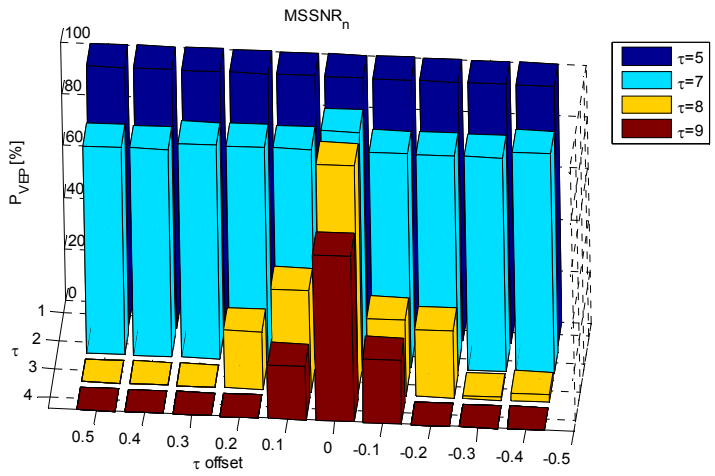

Fig. **4-14**: P_{VEP} for respective τ values of 5, 7, 8, and 9 under the presence of channel estimation error represented by $\Delta\tau$. $MSSNR_n$ algorithm used.

$\tau = 5$ case: $\{T : 2 \le T \le 22\} \bigcap \{v : 1 \le v+1 \le 3\}$,
$\tau = 7$ case: $\{T : 5 \le T \le 40\} \bigcap \{v : 1 \le v+1 \le 5\}$,
$\tau = 8$ case: $\{T : 5 \le T \le 95\} \bigcap \{v : 1 \le v+1 \le 13\}$,
$\tau = 9$ case: $\{T : 10 \le T \le 100\} \bigcap \{v : 1 \le v+1 \le 20\}$

From Fig. **4-14** and Fig. **4-15**, as τ approaches 9, we have narrower windows where $P_{VEP} > 0$. In particular, at these high τ values, comparing between the $MSSNR_n$ and the MMSE-UEC algorithm, the $MSSNR_n$ algorithm shows wider $\Delta\tau$ windows than the MMSE-UEC algorithm does. We recall that from Fig. **4-11**, the $MSSNR_n$ algorithm showed higher P_{VEP} than the MMSE-UEC algorithm even under the condition of a perfect channel estimation at the receiver.

For smaller τ values near 5, on the contrary, we have very wide $\Delta\tau$ windows for $P_{VEP} > 0$, for both the $MSSNR_n$ and the MMSE-UEC algorithms. From these results, we can conclude that, as τ becomes larger, we need very accurate τ estimation algorithms,

regardless of the TEQ algorithms used. Otherwise, in so far as we have wrong τ information at the receiver, even though we may try to find an appropriate equalizable N_f-N_b point by searching, it can be very difficult.

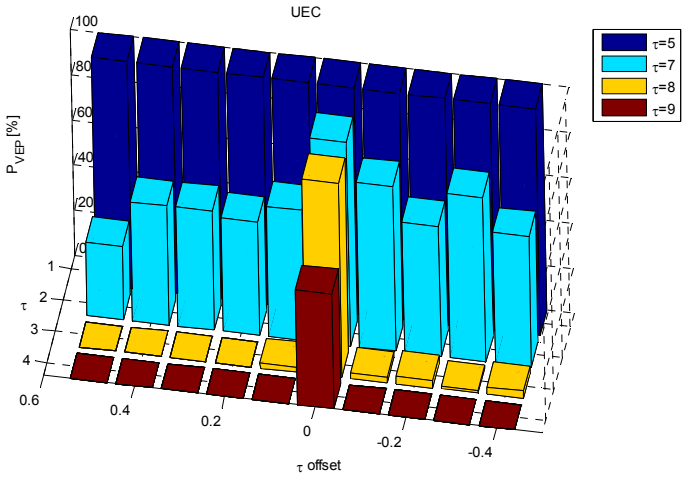

Fig. **4-15**: P_{VEP} for respective τ values of 5, 7, 8, and 9 under the presence of channel estimation error represented by $\Delta\tau$. MMSE-UEC algorithm used.

τ = 5 case: $\{T : 2 \le T \le 22\} \bigcap \{v : 1 \le v+1 \le 3\}$,
τ = 7 case: $\{T : 5 \le T \le 40\} \bigcap \{v : 1 \le v+1 \le 5\}$,
τ = 8 case: $\{T : 5 \le T \le 95\} \bigcap \{v : 1 \le v+1 \le 13\}$,
τ = 9 case: $\{T : 10 \le T \le 100\} \bigcap \{v : 1 \le v+1 \le 20\}$

To illustrate two points with $\Delta\tau = 0.5$ at $\tau = 7$ from Fig. **4-14** and Fig. **4-15**, we further investigated the effective SCIR length distribution as shown in Fig. **4-16**. In this specific case, we can deduce that the $MSSNR_n$ algorithm is more sensitive to channel estimation errors than the MMSE-UEC algorithm, once again confirming our findings from Fig. **4-14** and Fig. **4-15**.

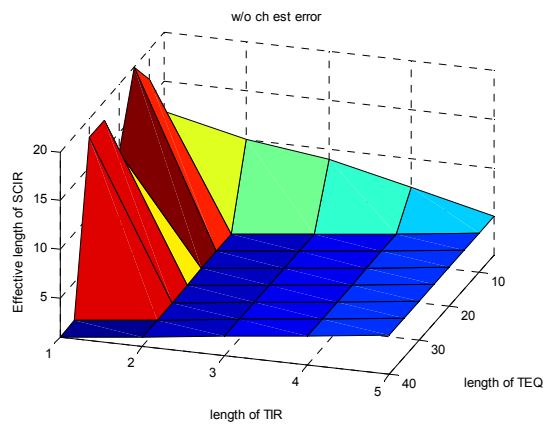

a) $MSSNR_n$ case without channel estimation errors

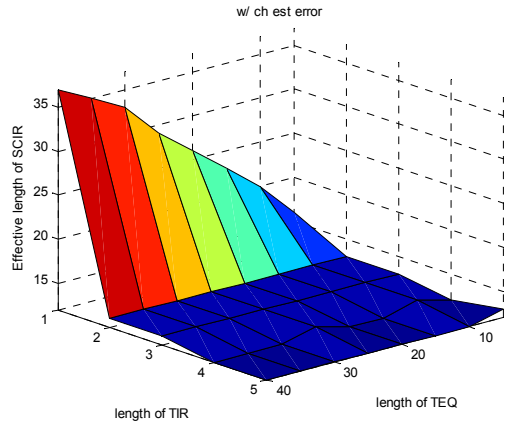

b) $MSSNR_n$ case with channel estimation errors

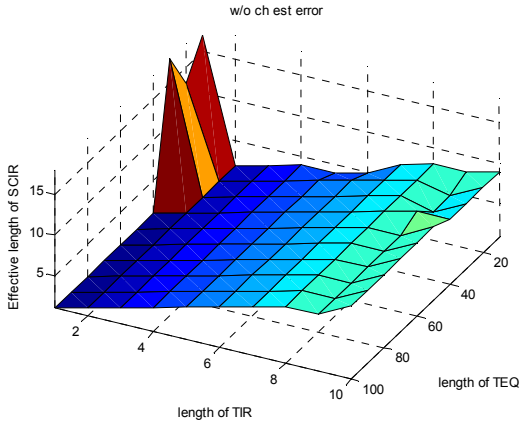

c) MMSE-UEC case without channel estimation errors

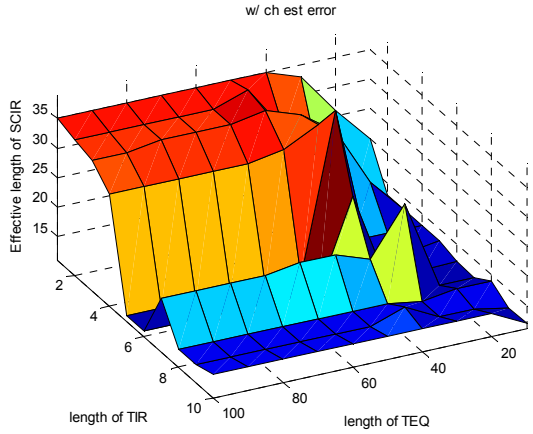

d) MMSE-UEC case with channel estimation errors

Fig. **4-16**: Distribution of the 99.9% effective length of SCIR in the presence of channel estimation errors.

The TEQ was set at τ =7 when the actual channel is of τ = 7.5

4.4.6.2 TEQ Adaptation Interval Design

In this section, we investigate the proper time interval for the TEQ adaptation. In the previous sections of this chapter, we could somehow achieve $P_{VEP} > 0$ in so far as we

set an appropriate N_f-N_b space. However, if we consider the BER, once the TEQ is set, the effects of channel estimation errors can be detrimental. The scenario that we are considering is as shown in Fig. **4-17**, where we assume that we have a cloud of an ideal shape and of a homogeneous physical nature, or k_{scat}. This scenario is a little different from our snapshots in Fig. **4-4**, since we considered different snapshots representing different k_{scat} values there. However, we do not have the distribution function of k_{scat} values in a very large geographic area. Instead, we can deal with the issues of the channel mobility and the TEQ adaptation interval by adopting a scenario as shown in Fig. **4-17**.

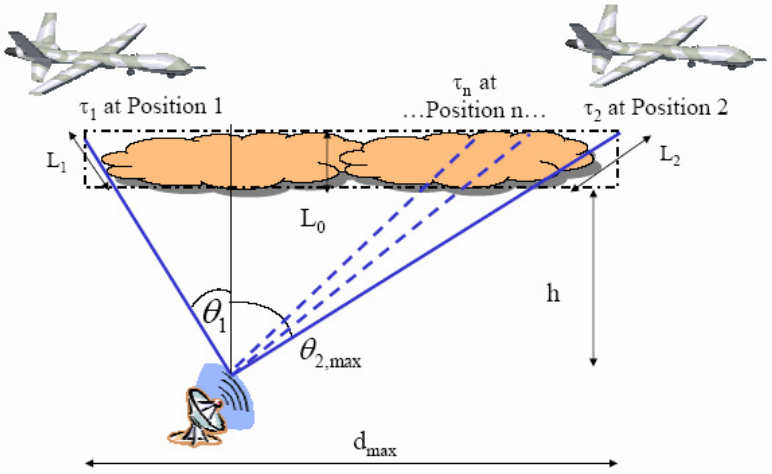

Fig. **4-17**: Problem setup to find the time interval for the TEQ computation.

Assumed that L_1 is fixed, while θ_1 keeps changing.

$\Delta\tau_{\max} \underset{=}{\Delta} \tau_2 - \tau_1$

h: cloud altitude, 10km

L_0, L_1, L_2: physical dimension of the cloud, defining optical thickness,

θ_1, θ_2: zenith angles, clockwise rotation regarded positive, counterclockwise rotation regarded negative. Assumed uniform distribution of [-60° ~ 60°]

v: Speed of the aerial vehicle. Assumed to be 688m/s.

In Fig. **4-17**, position 1 is where we initially estimate the channel's optical thickness, and the position n represents the location where we communicate based on the channel estimated from position 1, such that position 2 is the farthest place where channel estimated at position 1 can be used reliably but with some errors.

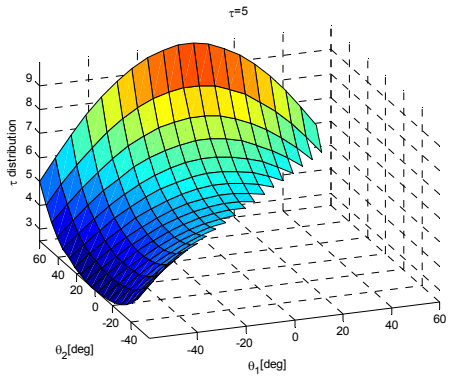

a) τ distribution as the vehicle moves away, τ_1 = 5 originally

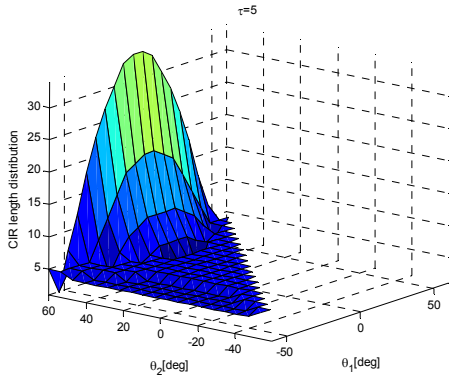

b) CIR length distribution as the vehicle moves away, τ_1 = 5 originally

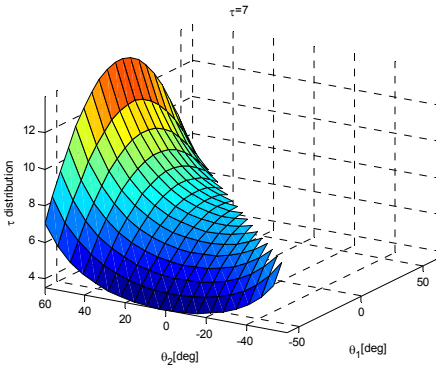

c) τ distribution as the vehicle moves away, τ_1 = 7 originally

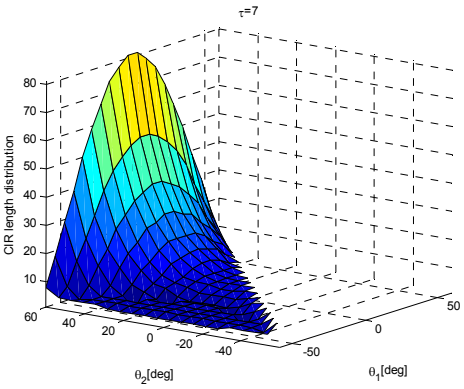

d) CIR length distribution as the vehicle moves away, τ_1 = 7 originally

Fig. **4-18**: τ distribution and CIR length distribution as a function of θ_1 and θ_2

(Between τ_1 =5 and τ_1 = 7, we assumed different K_{scat} values, but the same L_1 value at the initial point)

To evaluate changes in the cloud channel's τ values as the geometry between the ground station and the positions of the aerial vehicle change as in Fig. **4-17**, we

evaluated the changes to the channel in two respects, in CIR length and the intermediate τ_n values. In Fig. **4-18**, the 3D plots show that the channel worsening in terms of τ or the CIR length depends on both θ_1 and θ_2.

To gain more ideas about the location of position 2, in Fig. **4-19**, we showed 3D BER plots for two TEQ algorithms and for the two different τ values of 5 and 7 in the presence of channel estimation errors. We can make several observations here. At the τ value of 5, first, the $MSSNR_n$ algorithm shows stable performance for the $\Delta\tau$ values of, at least, -0.2 ~ 0.05, whereas the MMSE-UEC algorithm shows stable performance for the $\Delta\tau$ values of, at least, -0.5 ~ 0.3. Second, in some cases, the curves are shifted more toward $\Delta\tau < 0$, whereas other curves show symmetry around $\Delta\tau = 0$. This seems to be due to the fact that, if we move to areas of a thinner cloud, at least we still have more than enough TEQ taps, which is safe. Third, however, for a τ value of 7, we could obtain stable performance only for $-0.05 \leq \Delta\tau \leq 0.05$ in the case of the $MSSNR_n$ algorithm, and $-0.025 \leq \Delta\tau \leq 0.025$ for the UEC algorithm. Based on these results, we consider a scenario when the aerial vehicle moves away from the ground station and finally ends up with higher τ values than the original values, and also as a safer value, we take the intersection between the UEC algorithm's $\Delta\tau$ window and the $MSSNR_n$ algorithm's $\Delta\tau$ window. Thus, we chose a $\Delta\tau_{max}$ value of 0.05 at $\tau = 5$, and a $\Delta\tau_{max}$ value of 0.025 at $\tau = 7$ as the maximum $\Delta\tau$ values that the optical link can endure in our ensuing analysis.

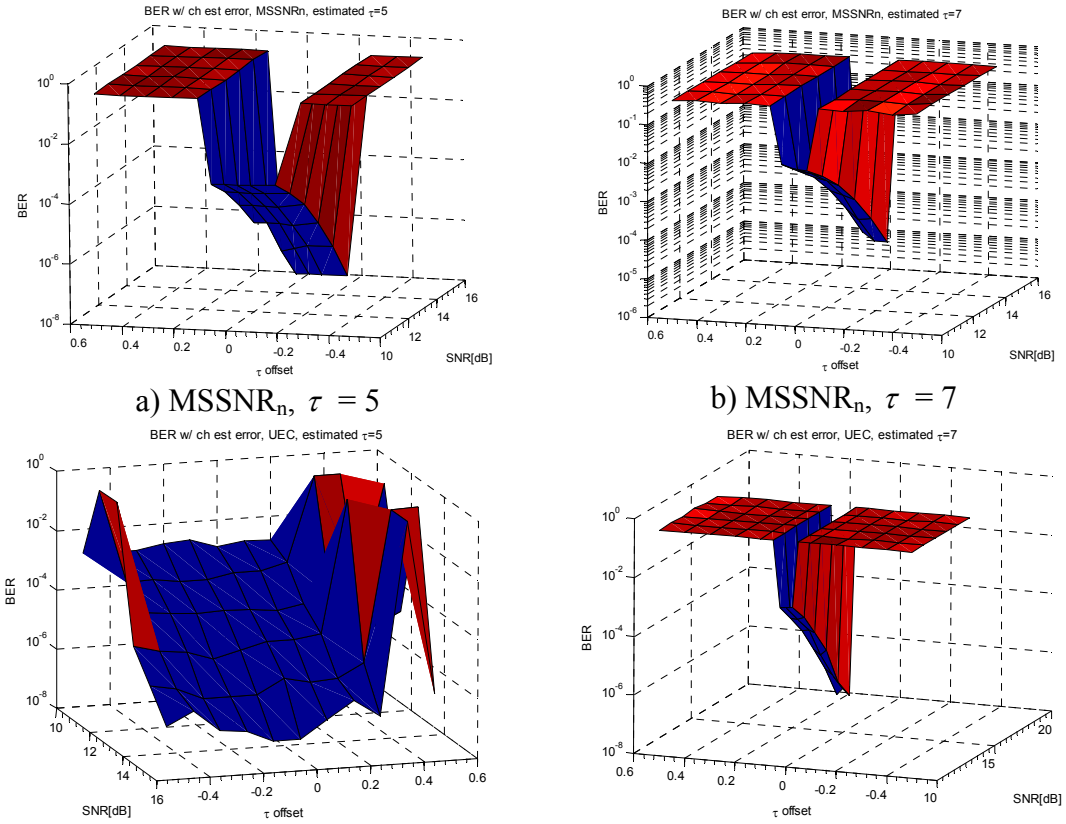

a) MSSNR$_n$, $\tau = 5$ b) MSSNR$_n$, $\tau = 7$

c) MMSE-UEC, $\tau = 5$ d) MMSE-UEC, $\tau = 7$

Fig. **4-19**: BER plots of TEQ with channel estimation errors

On the other hand, when we evaluate the performance of the DFE in the channel estimation errors as shown in Fig. **4-20**, it shows a relatively more stable performance than the TEQ-Viterbi scheme. While Fig. **4-19** shows relatively narrow windows, dependent on the initial τ value, Fig. **4-20** shows stable performances over wider windows. This difference can be contributed to the difference in the decoding algorithms. In the channel estimation errors, the TEQ will end up with longer-than-originally-desired SCIR tap length values, which are detrimental to the ensuing Viterbi equalizer, translated directly into a worsened BER. Also, the TEQ performance is more sensitive when

$\Delta\tau > 0$ than when $\Delta\tau < 0$, since our TEQ length and TIR length will be mostly insufficient under the $\Delta\tau > 0$ cases. However, the DFE can still decode most of the equalized signal, even though there may be channel estimation errors.

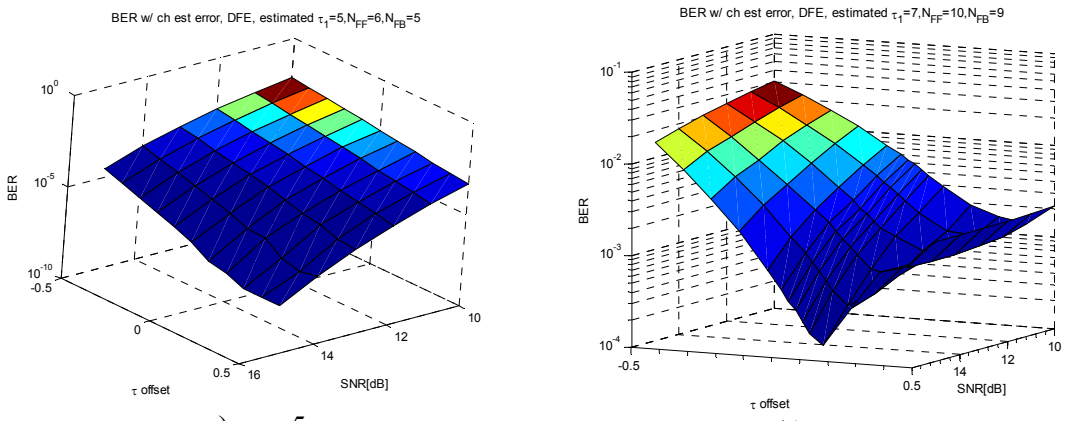

a) $\tau = 5$ b) $\tau = 7$

Fig. **4-20**: BER plots of DFE with channel estimation errors

Based on the BER results given in Fig. **4-19** and Fig. **4-20**, we further examined the issue of the TEQ adaptation interval design. For the problem setup, since we do not have a time-varying through-clouds channel model, we can assume a geo-stationary cloud channel model during some relatively short time period, and that the time-varying channel property is caused by the movement of the aerial vehicle. From Fig. **4-17**, we assume an ideal homogeneous rectangular-shaped cloud. For simplicity, we rule out any possibility of non-rectangular-shaped clouds. After adapting the TEQ at position 1 based on τ_1, now depending on the movement of the aerial vehicle, the propagating optical beam will see various new propagation lengths represented by the dotted lines of Fig. **4-17**, thus experiencing various new τ values. Adopting a safe $\Delta\tau$ value assuring a stable BER performance from Fig. **4-19**, finally we can find position 2 where we have

$\tau_2 = \tau_1 + \Delta\tau_{\max}$ and L_2. Once we found position 2, we can calculate $d_{\max}$ as in Eq. **4.56**. Furthermore, we could calculate the time interval Δt_{adapt} between position 1 and position 2 by dividing Eq. **4.56** by the velocity of the aerial vehicle. If we adapt the TEQ by intervals shorter than Δt_{adapt}, then the changes in τ will be very small, assuring a good BER performance. If the computation interval is longer than Δt_{adapt}, performance will suffer from changes in τ larger than $\Delta\tau$, and thus we cannot assure a good BER performance.

$$d_{\max} = (L_0 + h)(\tan\theta_1 + \tan\theta_2) \qquad \text{Eq. } \mathbf{4.56}$$

We evaluated the aforementioned algorithm and obtained $d_{\max}$ versus θ_1 and Δt_{adapt} versus θ_1, and showed the results in Fig. **4-21**. For the analysis in Fig. **4-21**, we considered the altitude of cirrus at 10km, because for our test cases of the cases of τ = 5 and 7, cirrus shows the closest K_{scat} value according to [15], and also because [63] shows a typical altitude of 10km for the cirrus. As we can expect, the Δt_{adapt}-distribution is dependent on θ_1. Initially when we start off from the case where $\theta_1 < 0$ and $\theta_2 > 0$, we have a long Δt_{adapt}. However, as θ_1 becomes positive, the Δt_{adapt} value becomes very small. For example, from Fig. **4-21** a) and b), we obtain $\Delta t_{adapt} \approx$ 32 sec and $d_{\max} \approx$ 22 km at θ_1 = -45.45 deg for both τ = 5 and 7 cases. However, if we start off from a position 1 with $\theta_1 > 0$, then we have a different situation. For example, if $\theta_1 = 20°$, we find $\Delta t_{adapt} \approx$ 0.48 sec and $d_{\max} \approx$ 329 m for the τ = 5 case, and $\Delta t_{adapt} \approx$ 0.17 sec and

$d_{\max} \approx 120$ m for the $\tau = 7$ case. For comparison, if we adopt $\Delta\tau_{\max}$ of 0.5 from the DFE cases with $\tau = 7$ of Fig. **4-20**, we get $\Delta t_{adapt} \approx 3$ sec and $d_{\max} \approx 2$km. Once the aerial vehicle finally arrives at position 2, we can iterate this procedure, using the newly estimated τ value as τ_1. However, actually, at τ of 7 or higher, the Δt_{adapt} values of the order of seconds are prohibitively small. Also, with the new τ_1 value, we will need a new $\Delta\tau$ value that assures a stable BER performance, meaning that we need to have a database of results similar to Fig. **4-19** performed for many τ_1 values. On the other hand, on the adaptive implementation, there have been efforts to find adaptive or blind TEQ algorithms as in [62]. However, considering the Δt_{adapt} ranges calculated in our problem setup, we may not have enough time to find the TEQ. Rather, we propose lookup table methods. Once θ_1 and τ_1 are known, the transmitter and the receiver can retrieve the proper TEQ tap values and the Δt_{adapt} value already stored in the lookup table, and after Δt_{adapt}, we can iterate the same procedure, rather than calculate TEQ taps each time.

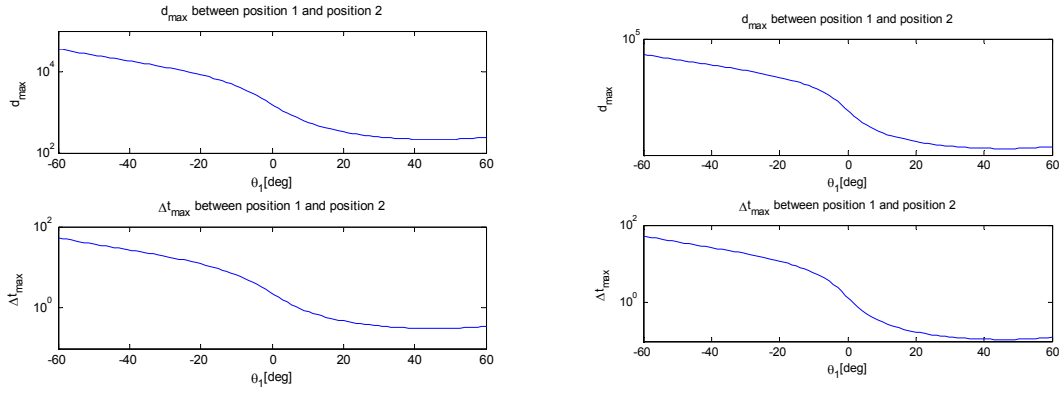

a) $\tau = 5,\ \Delta\tau_{\max} = 0.05$ b) $\tau = 7,\ \Delta\tau_{\max} = 0.025$

Fig. **4-21**: Δt calculation for two test cases at cloud altitude of 10km.

4.5 Optical Frequency-Domain Equalization

Alternatively, we can extend the frequency-domain equalization idea to FSO. There are various ways to implement FDE filters in the optical domain, but our interest lie more with the use of the pulse shaping apparatus idea in the frequency-domain equalization.

4.5.1 Pulse Shaping Apparatus

In [47], the authors suggested a modified technique for waveform synthesis, based on the well-understood frequency-domain processing schemes suggested in [41 - 46]. Fig. **4-22** shows a widely used pulse shaping apparatus based on the Fourier transform relationship between the spectrum and the temporal shape of a pulse. In the 4F system of Fig. **4-22**, the spectral components of an input ultra-short pulse are spatially dispersed by the first grating (FG) and then focused in the back focal plane (BFG) of the first lens (FL). We place a spatially varying amplitude mask (AM) and a spatially varying phase mask (PM) for filtering of the frequency components at BFG, followed by a second lens (SL) and a second grating (SG), recombining the amplitude/phase encoded spectrum. The role of the mask is to induce different phase retardations and amplitude changes to different frequency components, thus manipulating the spectral content of the pulse, so that the pulse' temporal shape is changed in a desired manner according to the Fourier transform relationship between the time and frequency domains.

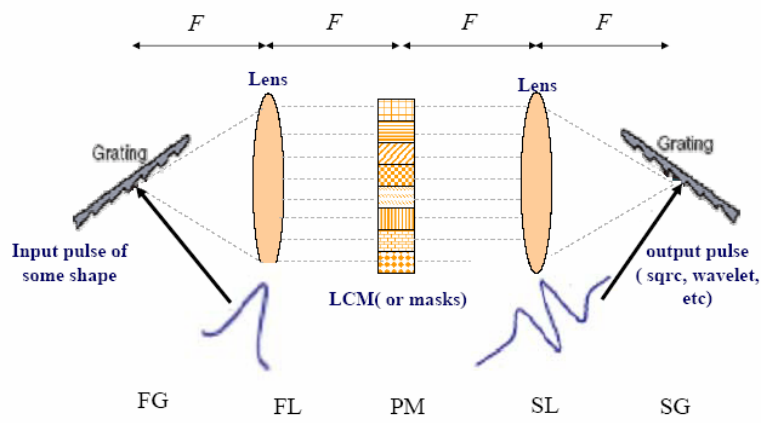

Fig. **4-22:** A pulse shaping apparatus using gratings, lenses, and a pulse shaping mask

There are certain conditions and considerations. First, owing to the pixilated nature of the mask and the finite spatial extent of each frequency component, the output waveform from the mask is shaped not only in time but also in space. Second, this spatial shaping of the individual components will in turn cause a space-time coupling of the output field characteristics. Third, while the ultra-short pulsed laser emission is composed of huge number of frequency components, the focal spot formed by each component onto the mask is of a finite size, not of an infinitesimal size. Hence, multiple frequency components contribute to the total field at a given point in the masking plane.

4.5.2 Waveform Generation in Ideal Conditions

Ideally, if each pixel in the PM contains only one frequency component of the input pulse spectrum, and if each frequency component's focused spot comes completely within the corresponding pixel, then the mask will behave like a non-pixilated mask without non-ideal effects. In a transmitter, a mode-locked laser pulse train can be

described by Eq. **4.57** and Eq. **4.58** in the time and the frequency domain, using Eq. **4.59**. If f_r is high, the separation of the spectral components $G(kf_r)\delta(f-kf_r)$ can be sufficiently large so that the individual comb lines can be resolved and their focal spots do not overlap in space. This is how we define ideal conditions.

$$x(t)=g(t)\otimes\sum_{k=-\infty}^{\infty}\delta(t-kT_r) \qquad \text{Eq. } \mathbf{4.57}$$

$$X(f)=\frac{1}{T_r}\sum_{k=-\infty}^{\infty}G(kf_r)\delta(f-kf_r) \qquad \text{Eq. } \mathbf{4.58}$$

$T_r=1/f_r$: pulse repetition period, f_r: pulse repetition rate, $g(t)$: some pulse shape — Eq. **4.59**

Now, with the ideal assumptions, the PM can be designed as a pixilated structure. The role of the PM is to bring different phase retardations and amplitude changes for different frequency components, thus controlling the spectral content of the pulse, so that the pulse temporal shape is changed in a certain way according to the Fourier transform relationship. We can design the PM such that the mask transmission properties are different among different comb lines, but within a single comb line, they are the same without any spatial extent. This additionally solves the space-time coupling problem, since each component is not filtered spatially. Moreover, the mask pixel edges are not illuminated, because there are no frequency components connecting two adjoining pixels. In this way, there is no diffraction off the PM and higher-order spatial modes are not present in the output waveform. Assuming a linear-filtering PM and a zero-dispersion pulse shaper, the output pulse train can be expressed as Eq. **4.60**, where $M(kf_r)$ is the complex transmission of the mask for the kth frequency component. The desired output from the pulse shaper is, due to the linear filtering properties, again a train of pulses as in

Eq. **4.61**, Eq. **4.62**, where $r(t)$ and $R(f)$ are the desired output pulse shape of our design. By comparison, $M(kf_r)$ can be calculated by Eq. **4.63**. For this implementation, in the case of simple inversion, we need $\overline{R} = [R(kf_r)]$ and $\overline{G} = [G(kf_r)]$.

$$X_{out}(f) = \frac{1}{T_r}\sum_{k=-\infty}^{\infty} G(kf_r)M(kf_r)\delta(f - kf_r) \quad \text{Eq. } \mathbf{4.60}$$

$$x_{out}^{des}(t) = r(t) \otimes \sum_{k=-\infty}^{\infty} \delta(t - kT_r) \quad \text{Eq. } \mathbf{4.61}$$

$$X_{out}^{des}(f) = \frac{1}{T_r}\sum_{k=-\infty}^{\infty} R(kf_r)\delta(f - kf_r) \quad \text{Eq. } \mathbf{4.62}$$

$$M(kf_r) = \frac{R(kf_r)}{G(kf_r)} \quad \text{Eq. } \mathbf{4.63}$$

4.5.3 Extension to the Frequency Domain Equalization

4.5.3.1 Mask Design Methods for the FEQ

We can denote a linear channel defined in the optical intensity domain by $c(t)$ or $C(f)$. When entering the MP of the pulse shaper (= frequency domain equalizer) on the receiver, the light signal can be described by Eq. **4.64** and Eq. **4.65**.

$$x_{rec}(t) = x_{out}(t) \otimes c(t) = w(t) \otimes \sum_{k=-\infty}^{\infty} \delta(t - kT), w(t) = r(t) \otimes c(t) \quad \text{Eq. } \mathbf{4.64}$$

$$X_{rec}(f) = \frac{1}{T_r}\sum_{k=-\infty}^{\infty} W(kf_r)\delta(f - kf_r),\ W(kf_r) = R(kf_r)C(kf_r) \quad \text{Eq. } \mathbf{4.65}$$

Assuming a linear mask filtering and zero-dispersion pulse shaper, the output pulse train from the FEQ can be expressed by Eq. **4.66** and Eq. **4.67**, where $q(t)$ or $Q(kf_r)$ represents the mask which functions as FEQ.

$$x_{rec}^{out}(t) = x_{rec}(t) \otimes q(t) = s(t) \otimes \sum_{k=-\infty}^{\infty} \delta(t - kT),\ s(t) = w(t) \otimes q(t) = r(t) \otimes c(t) \otimes q(t) \qquad \text{Eq. } \mathbf{4.66}$$

$$X_{rec}^{out}(f) = \frac{1}{T_r} \sum_{k=-\infty}^{\infty} S(kf_r)\delta(f - kf_r),\ S(kf_r) = W(kf_r)Q(kf_r) = R(kf_r)C(kf_r)Q(kf_r) \qquad \text{Eq. } \mathbf{4.67}$$

Now, a comparison between Eq. **4.67** and Eq. **4.62** shows that Eq. **4.68** holds.

$$R(kf_r) = R(kf_r)C(kf_r)Q(kf_r),\ Q(kf_r) = 1/C(kf_r) \qquad \text{Eq. } \mathbf{4.68}$$

4.5.3.2 Implementation Issues of the FEQ

Since masks are passive devices, their gains are less than 1. Therefore, we assume that the mask is preceded by an optical amplifier, such as an EDFA (Erbium-Doped Fiber Amplifiers), so that the combined action of the optical amplifier's gain and the optical masks can provide adequate compensation. Implementation of the FEQ solution in Eq. **4.68** is based on a channel inversion. Although it involves the estimated channel $\hat{C}(kf_r)$, assuming perfect channel estimation, we can replace $\hat{C}(kf_r)$ by $C(kf_r)$.

Analogous to discrete equalization problems, implementations based on channel inversion can cause problems if $C(kf_r)$ involves zero or infinitesimal frequency response components. This problem is best solved by adaptive algorithms. Adaptive algorithms simply adjust the parameters of each pixel of the mask iteratively until the error between the waveform generated and the desired waveform, e.g., a minimum-ISI pulse, is

minimized. A mask pattern can be realized for a real system by iterating through each pixel and dynamically adjusting parameters of each pixel in the pulse shaping system until the error between the output waveform and the desired waveform is minimized. A feedback loop between the output, a control unit, and the liquid crystal spatial light modulator (LC-SLM) can compare the output waveform to the desired waveform and determine whether a given change reduces or increases the error. Depending on the algorithm used, the new parameters of a pixel may be kept or removed based on the changes in error from the previous update. We can employ adaptive algorithms such as least-mean-square (LMS) or recursive-least-square (RLS), as is presented in Fig. **4-23**.

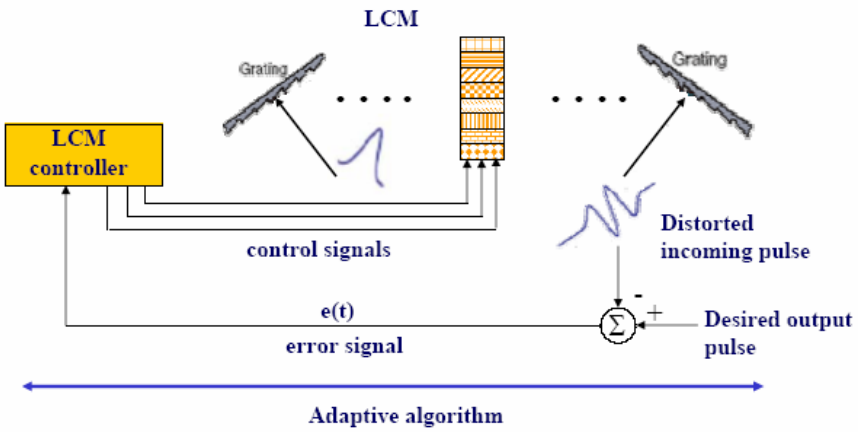

Fig. **4-23**: A FEQ based on a pulse shaping apparatus using gratings, lenses, and a pulse shaping mask.

4.5.4 Results

In this section, we adopted test conditions outlined in Table **4-1** and present some results. Test conditions are as described in Table **4-2**.

Table **4-1**: FEQ test conditions assumed

Channel-related assumptions	- Assumed that channel c(t) is known at the receiver - τ = 5
System assumptions	- data rate R_b = 666.625 Mbps
Mask design assumptions	- Number of mask pixels, N_p: 1024 or 1024×256 - Number of amplitude levels, N_{AL}: 16 (4-bit) or 256 (8-bit) - Ratio of maximum amplitude over minimum amplitude (= dynamic range of amplitudes expressible by mask): 4000 - Number of phase levels, N_{PL}: 16 (4-bit) or 256 (8-bit)
Others	Waveform generation in ideal conditions assumed

Table **4-2**: Test cases of FDE

	Number of mask pixels, N_P	Number of amplitude levels, N_{AL}	Number of phase levels, N_{PL}
Test 1	1024	16	16
Test 2	1024	256	256
Test 3	1024×256	256	256

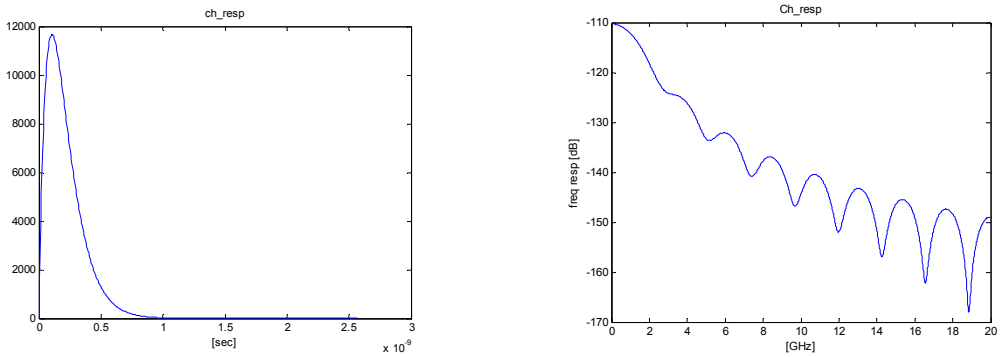

a) b)

Fig. **4-24**: a) Optical channel in the time domain, $\tau = 5$ b) Optical channel's frequency response, $\tau = 5$

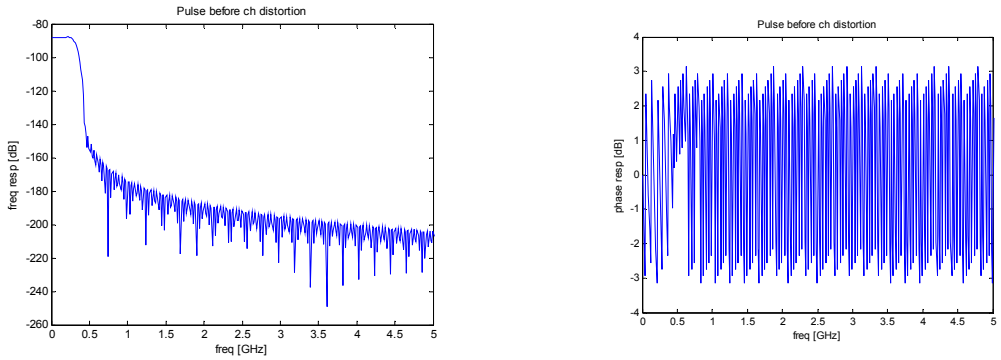

Fig. **4-25**: Raised cosine pulse a) frequency response b) phase response

Given a channel model as in Fig. **4-24**, and a raised cosine pulse as in Fig. **4-25**, if we used an FDE with infinite bin size both in amplitude and phase, we would of course be able to ideally compensate for channel distortion. For a finite bin size FDE, however, this is not always possible.

Comparing between the optical equalization and the digital equalization, we can make several arguments. First, in our specific channel model case, with an R_b of

666.625Mbps, our raised cosine pulse will show a 3dB bandwidth of approximately 333 MHz. Our FSO channel will cause distortion not only within the 3dB band but also within the beyond-3dB band. We can see this by comparing Fig. **4-25** with Fig. **4-26** where the channel distortion in the frequency response occurs across the whole optical spectrum. On the contrary, in the DSP case, we would have sampled at rates multiple of 666.625MHz, thus giving up chances to equalize beyond the sampling frequency, depending on the sampling frequency. This explains the difference between the analog optical equalization idea and the digital equalization idea. Second, however, regardless of the equalization methods, we will in the end sample at some multiple number of R_b before the decision device and therefore, it is also meaningless to try to equalize over the whole optical band. Third, we do not usually transmit signals beyond the 3dB bandwidth of the channel c(t). Therefore, before we further continue, our discussion about optical equalization is meaningful more in the sense that we can use the pulse shaping apparatus in FDE sense.

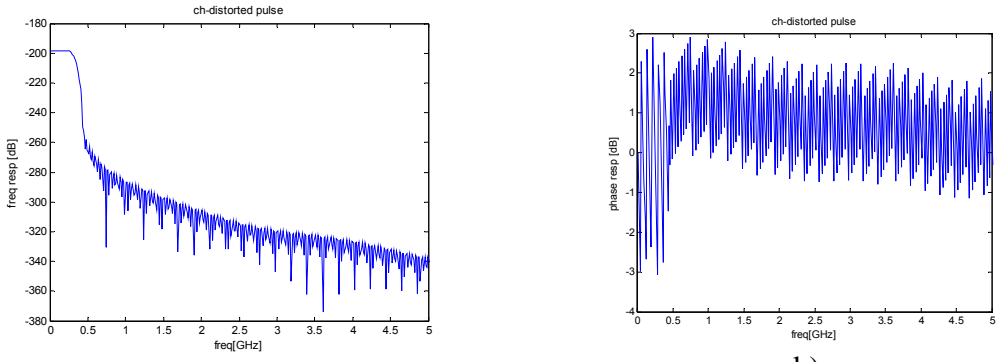

a) b)

Fig. **4-26**: Pulse after channel distortion a) Frequency response b) Phase response

Fig. **4-27** shows various aspects of our FDE of test 1. Due to the limited resolutions in frequency, amplitude, and phase, compensation is on the bad side. Fig. **4-27** e) shows that the limitations in frequency, amplitude, and phase resolution result in unwanted imaginary components.

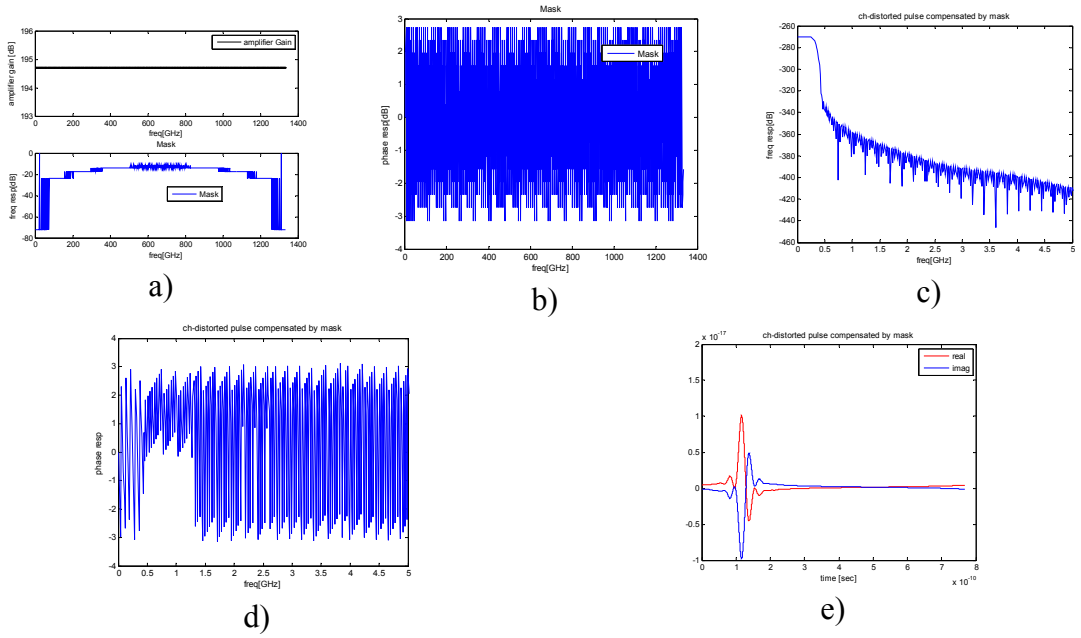

Fig. **4-27**: Test 1 a) frequency response of mask b) phase response of mask c) channel-distorted pulse after mask-compensation, frequency response d) channel-distorted pulse after mask-compensation, phase response e) channel-distorted pulse after mask-compensation in time-domain

Fig. **4-28** shows results of test 2, where we increased N_{AL} and N_{PL} to 256 and checked if this increase can contribute to any enhancement. Comparing between Fig. **4-27** c) and e), the imaginary components have been decreased considerably, but there is still a significant level of imaginary components.

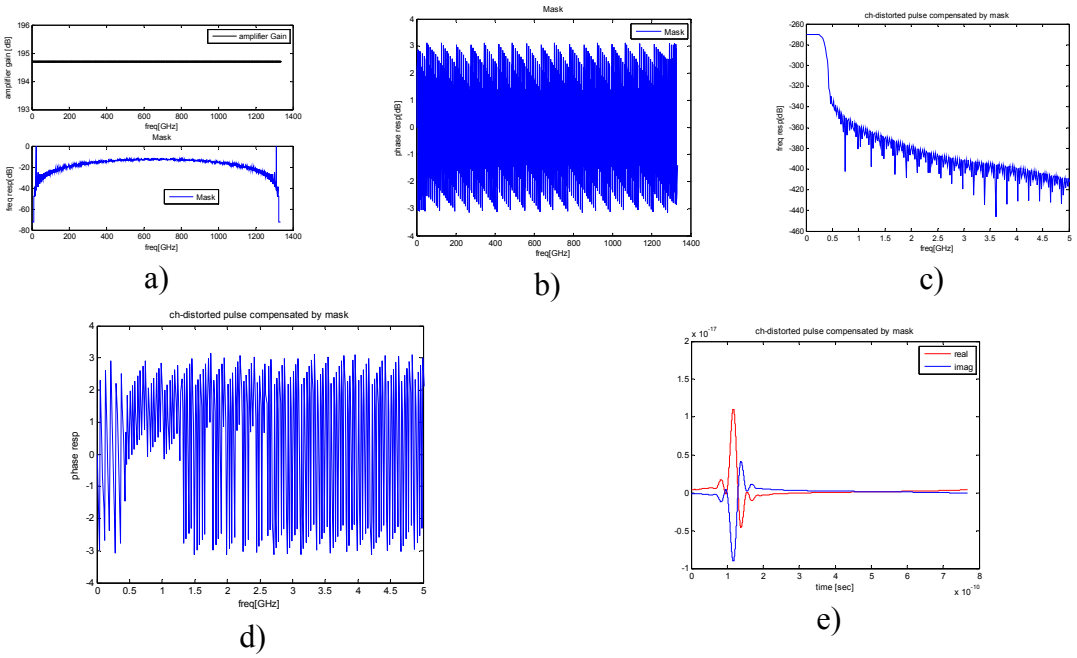

Fig. **4-28**: Test 2 a) frequency response of mask b) phase response of mask c) channel-distorted pulse after mask-compensation, frequency response d) channel-distorted pulse after mask-compensation, phase response e) channel-distorted pulse after mask-compensation in time-domain

In Fig. **4-29**, we adopted $N_p = 1024 \times 256$, $N_{AL} = 256$, and $N_{PL} = 256$. Fig. **4-29** e) clearly says that our desired waveform, or raised cosine pulse shape has been almost perfectly recovered, with negligible imaginary components. However, the requirement of a 1024×256 pixel size can be difficult to realize in terms of implementation, in particular if we use a large bin size in the amplitude or the phase domain.

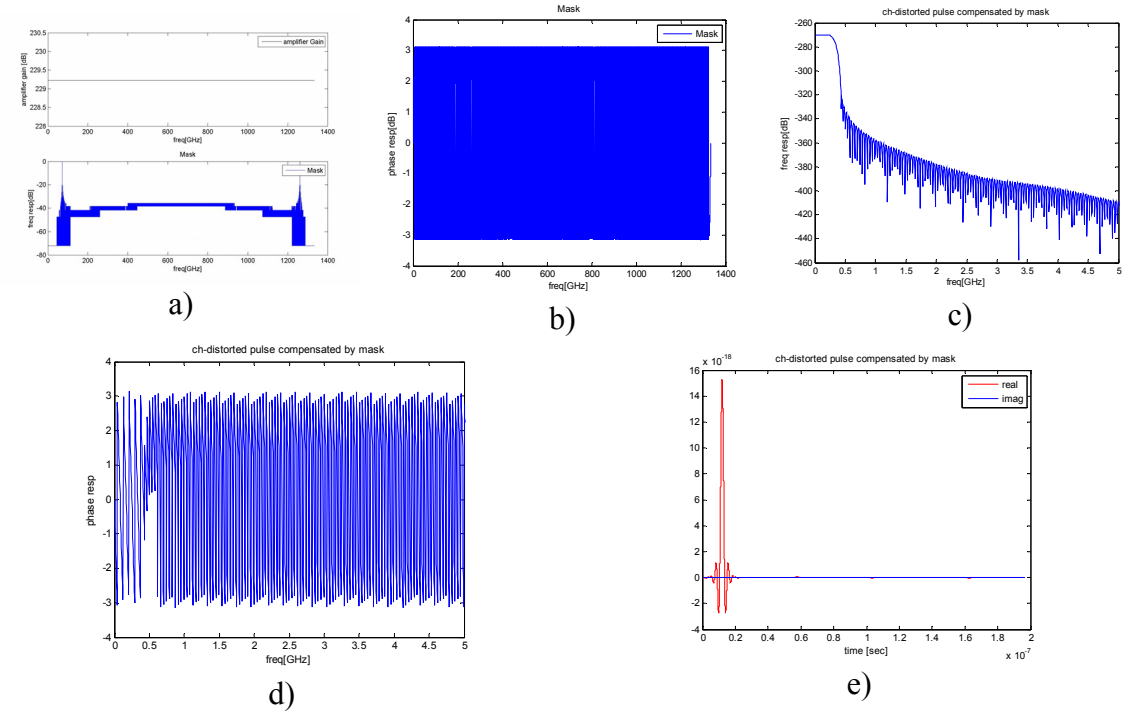

Fig. **4-29**: Test 3 a) frequency response of mask b) phase response of mask c) channel-distorted pulse after mask-compensation, frequency response d) channel-distorted pulse after mask-compensation, phase response e) channel-distorted pulse after mask-compensation in time-domain

We conclude this section by making several arguments. First, as we pointed out already, knowing the Nyquist theorem concept, signal processing in the beyond 3-dB bandwidth is unusual in the communications context, while this optical FDE unavoidably encounters signal processing in the beyond 3-dB bandwidth. Second, then, if we can somehow adaptively adjust the frequency domain resolution such that unequal frequency-domain spacing is feasible, we can further justify the optical FDE. Third, even though we could compensate for channel distortion almost perfectly by increasing the bin size in the frequency, phase, or amplitude domain, this required high complexity. Fourth, however, knowing the noise enhancement problem of digital equalization either in the frequency or

the time domain once the optical signal is photo-detected, this optical FDE can be a way around, affected only by ambient light, etc.

4.6 Summary and Conclusions

In this chapter, we presented theories and results of FSO equalizations. In the time domain, we further extended the TEQ concept, which was originally used in landline DSL communications, to FSO. We introduced the TEQ design algorithms of MSSNR, $MSSNR_n$, and MMSE by quoting from existing references and modified them such that the TEQ can be placed in the transmitter, avoiding colored noise in the receiver. We made extensive efforts to compare performance in various criteria. We presented conceptual meanings of these performance criteria. We also attached a Viterbi equalizer after the TEQ and verified that this fully electrical signal processing scheme can work well for low-to-mid range of optical thickness values. In wireless airborne links, issues of mobility-induced channel estimation errors can also arise. We suggested a method to model the channel estimation errors, and then evaluated the TEQ performance in the presence of channel estimation errors. Based on these data, we proposed proper TEQ adaptation intervals. We also presented results from initial research efforts of the optical FDE, and considering its highs and lows of the optical FDE, we need further investigations on the performance of optical FDE.

Chapter 5

Equalization of RF Links

In this chapter, we will investigate RF equalization schemes. Since the advent of MIMO, there has been increasing research interest and efforts in MIMO equalization, because demands for higher capacity triggered not only MIMO approaches but also broadband approaches.

As in [**3**][50], there has been research interest in the MIMO DFE for single-carrier modulation based systems. In [**85**], the authors approached MIMO equalization techniques for single-carrier based space-time transmit-receive systems, but in the frequency-domain. In [**86**], the authors extended the FDE concepts of [**85**] to various FDE techniques including DFE and turbo equalizations in the single-carrier based space-time diversity systems. In [**88**], the authors approached the Alamouti-type space-time MIMO system in the time domain. MIMO layered spaced-time equalization architectures were investigated in [**89**]. Reference [**87**] approached MIMO equalizations from the beamforming perspective.

In the case of OFDM-based MIMO systems, efforts were made to find a combined structure of a TEQ and an FDE, or called a per-tone equalizer (PTEQ), in MIMO systems as in [**90**]. In [**91**], research efforts were made to employ a TEQ and an FDE in an uplink MIMO-OFDM to solve issues of uplinks, such as cochannel interference and asynchronism. As for the MIMO channel shortening TEQ, investigations

on MIMO MMSE TEQ were made in [30], and the SISO MSSNR concept [**5**] was extended to MIMO in [**92**].

As an extension to the shortening filter applied to the FSO links as presented in the previous chapter, we will focus on MIMO-TEQ in this chapter. Even though the core signal processing scheme is the same between the FSO and the RF links, there are certain differences. Similar to the DSL channel, our FSO channel is extremely dispersive, where we mostly benefit from using the TEQ. On the other hand, in most RF wireless links, the channel is not severely dispersive, and there is fading. Thus it is unclear whether we can benefit from the TEQ in the wireless channels. The author of this thesis claims that, to the author's best knowledge, there have been previous research efforts on space-time codes combined with the MIMO TEQ, but have not been any papers approaching the performance issues from the correlation matrix perspective.

5.1 SISO Frequency-Domain Equalization

An alternative approach to time domain RF equalization is frequency domain equalization, not only for multi-carrier modulated systems but also for single-carrier modulated systems [21]. In an OFDM receiver, given the FFT output vector $\widetilde{\mathbf{y}}_{k,N} = [\widetilde{y}_{k,0} \ldots \widetilde{y}_{k,N-1}]^T$, we can devise a very simple equalization, where each tone is scaled by the inverse of the discrete channel frequency response as in Eq. **5.1** and Eq. **5.2**.

$$\hat{\widetilde{x}}_{k,n} = \widetilde{d}_n \widetilde{y}_{k,n} = \widetilde{h}_n^{-1}(\widetilde{h}_n \widetilde{x}_{k,n} + \widetilde{n}_{k,n}) = \widetilde{x}_{k,n} + \widetilde{h}_n^{-1}\widetilde{n}_{k,n} \qquad \text{Eq. } \mathbf{5.1}$$

$$\widetilde{\mathbf{d}}_n = [\widetilde{d}_0 \ldots \widetilde{d}_{N-1}]^T, \text{ where } \widetilde{d}_n = \widetilde{h}_n^{-1} \qquad \text{Eq. } \mathbf{5.2}$$

Given an FFT-processed sample vector at the receiver, an estimate for a symbol at the k[th] instant for the n[th] tone can be made by Eq. **5.3**, where $\widetilde{h}_n^{-1}$ is a 1-tap equalizer per tone index n, found from the inverse of the channel estimation per tone.

$$\hat{\widetilde{x}}_{k,n} = \widetilde{d}_n \widetilde{y}_{k,n,\mathbf{w}} = \widetilde{h}_n^{-1}(\widetilde{h}_n \widetilde{x}_{k,n} + \widetilde{n}_{k,n}) = \widetilde{x}_{k,n} + \widetilde{h}_n^{-1}\widetilde{n}_{k,n} \qquad \text{Eq. } \mathbf{5.3}$$

There are two things to note. First, $\widetilde{y}_{k,n} = (\widetilde{h}_n \widetilde{x}_{k,n} + \widetilde{n}_{k,n})$ of **Eq. 5.1** holds only when we have enough guard sequence length. Therefore, naturally, our FDE is valid only when we have enough guard sequence length. Second, the performance of FDE is equivalent to the operation of symbol-by-symbol detection when the CSI is known at the receiver.

On the other hand, in single-carrier modulated systems, we will have an FFT device at the receiver first, followed by one-tap FDE, IFFT device, and a detector [21].

5.2 SISO Per-Tone Equalization

An equalizer design alternative to the TEQ is the per-tone equalizer. In short, this is an effort to combine a TEQ and an FDE. As for its advantages, the PTEQ is known to perform at least as well as the TEQ, and its complexity is of a similar level to that of the TEQ. Conceptually, the principles of the PTEQ can be explained by Eq. **5.4**, where the n[th] tone component is given by Eq. **5.5**. Transmitted symbols can be further frequency-domain equalized as in Eq. **5.6**, and then can be decided on.

$$\tilde{\mathbf{y}}_{k,N,\mathbf{w}} = F_N(\mathbf{Y}_k\mathbf{w}) = (F_N\mathbf{Y}_k)\mathbf{w}\ ,\ \mathbf{w}:\text{TEQ} \qquad \text{Eq. } \mathbf{5.4}$$

$$\tilde{y}_{k,n,\mathbf{w}} = F_n(\mathbf{Y}_k\mathbf{w}) = (F_n\mathbf{Y}_k)\mathbf{w}\ ,\ \mathbf{w}:\text{TEQ} \qquad \text{Eq. } \mathbf{5.5}$$

$$\hat{\tilde{x}}_{k,n} = \tilde{d}_n\tilde{y}_{k,n,\mathbf{w}} = \tilde{d}_n(F_n\mathbf{Y}_k)\mathbf{w}\ , \qquad \text{Eq. } \mathbf{5.6}$$

Since $\tilde{d}_n$ is a 1-by-1 element, we can further re-arrange the terms of Eq. **5.6** and obtain Eq. **5.7**. Thus, a T-by-1 vector TEQ $\mathbf{w}$, common for all frequency components, can be multiplied by the frequency-specific FEQ $\tilde{d}_n$ of the nth tone to obtain a T-by-1 vector PTEQ (per-tone equalizer) $\mathbf{w}_n$.

$$\hat{\tilde{x}}_{k,n} = F_n\mathbf{Y}_k\tilde{d}_n\mathbf{w} = F_n\mathbf{Y}_k\mathbf{w}_n = \tilde{\mathbf{y}}_{k,n}\mathbf{w}_n\ ,$$
$$\text{where } \mathbf{w}_n \underset{=}{\Delta} \tilde{d}_n\mathbf{w} \text{ and } \tilde{\mathbf{y}}_{k,n} \underset{=}{\Delta} F_n\mathbf{Y}_k\ ,\ \tilde{\mathbf{y}}_{k,n}:\text{1-by-T},\ \mathbf{w}_n:\text{T-by-1} \qquad \text{Eq. } \mathbf{5.7}$$

As was investigated in [1], there are simpler methods of obtaining $\tilde{\mathbf{y}}_{k,n}$ by a recursive method, rather than depending on DFT calculations. Thus, as in Eq. **5.8** , we can calculate a vector $\tilde{\mathbf{y}}_{k,n}$ at time t based on the vector $\tilde{\mathbf{y}}_{k,n}$ calculated at time t-1. The PTEQ can be understood as a scheme combining a TEQ and an FDE.

$$\tilde{\mathbf{y}}_{k,n}(t) = \alpha_n\tilde{\mathbf{y}}_{k,n}(t-1) + \Delta y_{k,-t}, \Delta y_{k,-t} \underset{=}{\Delta} y_{k,-t} - y_{k,N-t}\ ,$$
$$\alpha_n \underset{=}{\Delta} \exp\left(-j2\pi(n-1)/N\right)/\sqrt{N} \qquad \text{Eq. } \mathbf{5.8}$$

5.3 MIMO MMSE Channel Shortening Equalization

A good choice of MIMO equalization can be found by extending SISO MMSE channel shortening filters to a MIMO configuration. Table **5-1** shows a summary of notations for the vectors and the matrices to be used for the formulas in this chapter as

well as their matrix sizes for better understanding. We refer to the algorithm of [30], re-formulated partially for better understanding, and present them in this chapter.

Table **5-1**: Matrices and notations used in MIMO-TEQ formulas

Notation	Description
N_i	Number of transmit antennas
N_o	Number of receive antennas
v	Channel memory length such that total channel length = v+1
l	Temporal oversampling factor
N_f	a block length
$\mathbf{W}_k$	$[N_i \times N_o l]$, a MIMO-TEQ matrix at the kth instant
$\mathbf{W}$	MIMO-TEQ matrix with submatrices $\mathbf{W}_k$, k = 0…N_{f-1}
$\mathbf{H}_m$	$[lN_o \times N_i]$, a matrix composed of $\mathbf{h}_m^{(i,j)}$
$\mathbf{H}_{p,eq}$	$[N_i \times N_i]$, a shortened channel matrix
$\mathbf{H}$	Channel matrix, $[lN_o N_f \times N_i(N_f + v)]$
$\mathbf{B}_k$	Target impulse response at the kth instant, $[N_i \times N_i]$, k = 0…N_b , N_b <<v
$\mathbf{B}$	Target impulse response matrix, $[N_i(N_b+1) \times N_i]$
$\mathbf{R}_\Delta$	$[N_i(N_b+1) \times N_i(N_b+1)]$
$\mathbf{R}^\perp$	$[N_i(N_f+v) \times N_i(N_f+v)]$
$\mathbf{E}_k$	Error vector at the kth instant, $[N_i \times 1]$
$\mathbf{U}$	Eigenvector matrix, $[N_i(N_b+1) \times N_i(N_b+1)]$
$\mathbf{\Sigma}$	Eigenvalue matrix, $[N_i(N_b+1) \times N_i(N_b+1)]$

Samples at the jth Rx antenna at the kth time instant can be given by Eq. **5.9** where column vector notations have been given in order to denote general cases of symbols oversampled by an oversampling factor of l.

$$\mathbf{y}_k^{(j)} = \sum_{i=1}^{n_i} \sum_{m=0}^{v(i,j)} \mathbf{h}_m^{(i,j)} x_{k-m}^{(i)} + \mathbf{n}_k^{(j)},$$

$\mathbf{h}_m^{(i,j)}$: column vector of CIR from the i^{th} transmitter to the j^{th} receiver, [l-by-1]

$x_{k-m}^{(i)}$: transmit symbol at the (k-m)$^{\text{th}}$ instant from the i$^{\text{th}}$ transmitter Eq. **5.9**

$\mathbf{n}_k^{(j)}$: column vector of noise at the j$^{\text{th}}$ receiver at the k$^{\text{th}}$ instant, [l-by-1]

$\mathbf{y}_k^{(j)}$: a column vector of l-times oversampled received samples at the k$^{\text{th}}$ instant at the j$^{\text{th}}$ receiver, [l-by-1]

Putting $\mathbf{y}_k^{(j)}$, $1 \le j \le N_o$ together, we obtain an expression of Eq. **5.10**, using Eq. **5.11** and Eq. **5.12**.

$$\mathbf{y}_k = \sum_{m=0}^{v} \mathbf{H}_m \mathbf{x}_{k-m} + \mathbf{n}_k$$

$\mathbf{H}_m$: a $[lN_o \times N_i]$ matrix composed of $\mathbf{h}_m^{(i,j)}$

$\mathbf{x}_{k-m}$: a column vector of transmit symbols, $[N_i \times 1]$ Eq. **5.10**

$v = \max_{i,j} v^{(i,j)}$

$\mathbf{n}_k$: a column noise vector at receiver, $[lN_o \times 1]$

$\mathbf{y}_k$: a column vector of received samples at receiver, $[lN_o \times 1]$

$$\mathbf{H}_m = \begin{bmatrix} \ddots & \cdots & \iddots \\ \vdots & \mathbf{h}_m^{(i,j)} & \vdots \\ \iddots & \cdots & \ddots \end{bmatrix}, 1 \le i \le N_i, 1 \le i \le N_o \qquad \text{Eq. } \mathbf{5.11}$$

$$\mathbf{y}_k = \begin{bmatrix} \vdots \\ \mathbf{y}_k^{(j)} \\ \vdots \end{bmatrix}, 1 \le j \le N_o \qquad \text{Eq. } \mathbf{5.12}$$

Observing Eq. **5.10** over many symbol periods at the receiver, say N_f, we can further expand Eq. **5.10** to Eq. **5.13** which can be alternatively described by Eq. **5.14**.

$$\mathbf{y}_{k+N_f-1:k} = \mathbf{H}\mathbf{x}_{k+N_f-1:k-v} + \mathbf{n}_{k+N_f-1:k} \qquad \text{Eq. } \mathbf{5.13}$$

$$\begin{bmatrix} \mathbf{y}_{k+N_f-1} \\ \vdots \\ \mathbf{y}_k \end{bmatrix} = \begin{bmatrix} \mathbf{H}_0 & \mathbf{H}_1 & \cdots & \mathbf{H}_v & \mathbf{0} & \cdots & \mathbf{0} \\ \mathbf{0} & \mathbf{H}_0 & \mathbf{H}_1 & \cdots & \mathbf{H}_v & \ddots & \vdots \\ \vdots & \ddots & \ddots & \ddots & \ddots & \ddots & \mathbf{0} \\ \mathbf{0} & \cdots & \mathbf{0} & \mathbf{H}_0 & \mathbf{H}_1 & \cdots & \mathbf{H}_v \end{bmatrix} \begin{bmatrix} \mathbf{x}_{k+N_f-1} \\ \vdots \\ \mathbf{x}_{k-v} \end{bmatrix} + \begin{bmatrix} \mathbf{n}_{k+N_f-1} \\ \vdots \\ \mathbf{n}_k \end{bmatrix} \qquad \text{Eq. } \mathbf{5.14}$$

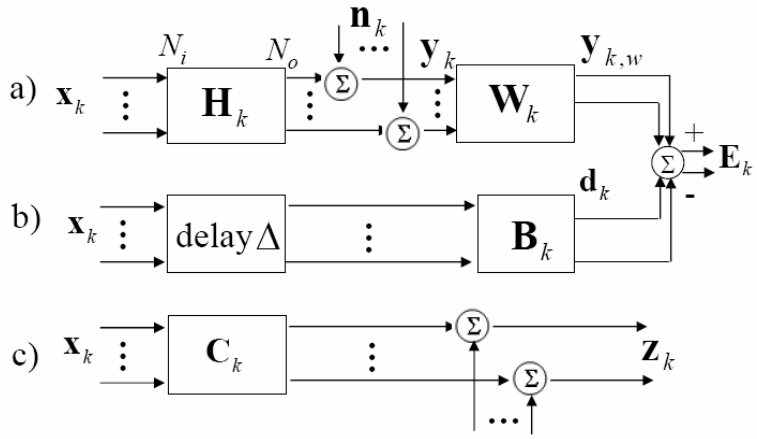

Fig. **5-1**: Block diagram for MIMO-MMSE-TEQ a) A discrete-time model with TEQ b) delay and TIR c) equivalent equalized channel

Our discussion above on the receiver structure and the MIMO-MMSE-TEQ can be described as in Fig. **5-1** by extending a SISO MMSE TEQ given in chapter 4. MIMO shortening can be explained by Eq. **5.15**. We aim at comparing Eq. **5.15** with the TIR-filtered input symbol vector $\mathbf{d}_k$ of Eq. **5.16**, and at minimizing the error signal vector $\mathbf{E}_k$ of Eq. **5.17** in the MMSE sense. Eq. **5.17** can also be expressed by Eq. **5.18**.

$\mathbf{H}_{p,eq} = \sum_n \mathbf{W}_n \mathbf{H}_{p-n}$, $\mathbf{H}_{p,eq}$: shortened channel matrix,
$\mathbf{W}_n$: MIMO-MMSE-TEQ matrix at the k^{th} instant — Eq. **5.15**

$$\mathbf{d}_k = \sum_n \mathbf{B}_n \mathbf{x}_{k-n-\Delta} \quad \text{Eq. 5.16}$$

$$\mathbf{E}_k = \mathbf{d}_k - \mathbf{y}_{k,w} \quad \text{Eq. 5.17}$$

$$\mathbf{E}_k = \mathbf{d}_k - \mathbf{y}_{k,w} = \sum_n \mathbf{B}_n \mathbf{x}_{k-n-\Delta} - \sum_n \mathbf{W}_n \mathbf{y}_{k-n} \quad \text{Eq. 5.18}$$

Alternatively, Eq. **5.17** can be expressed by Eq. **5.19** where the definitions of Eq. **5.20** and Eq. **5.21** are used.

$$\mathbf{E}_k = \sum_{m=0}^{N_b} \mathbf{B}_m^H \mathbf{x}_{k+N_f-1-\Delta-m} - \sum_{n=0}^{N_f-1} \mathbf{W}_n^H \mathbf{y}_{k+N_f-1-n} = \widetilde{\mathbf{B}}^H \mathbf{x}_{k+N_f-1:k-v} - \mathbf{W}^H \mathbf{y}_{k+N_f-1:k} \quad \text{Eq. 5.19}$$

$$\widetilde{\mathbf{B}}^H \underset{=}{\Delta} \left[\mathbf{0}_A \ \mathbf{B}^H \ \mathbf{0}_B\right]^t,$$

$$\mathbf{0}_A : \text{a } \left[N_i - by - N_i\Delta\right] \text{ zero matrix, } \mathbf{0}_B : \text{a } \left[N_i - by - N_i s\right] \text{ zero matrix,} \quad \text{Eq. 5.20}$$

$$\Delta : \text{a decision delay, } 0 \le \Delta \le N_f + v - N_b - 1, \ s \underset{=}{\Delta} N_f + v - N_b - \Delta - 1$$

$$\mathbf{B} \underset{=}{\Delta} \left[\mathbf{B}_0 \cdots \mathbf{B}_{N_b}\right]^t, \ \left[N_i(N_b+1) - by - N_i\right] \quad \text{Eq. 5.21}$$

As we minimize the MMSE for a SISO MMSE equalization, we similarly minimize a trace of the error vector's autocorrelation matrix [3] defined by Eq. **5.22** ~ Eq. **5.26** where Eq. **5.27** ~ Eq. **5.35** are used.

$$\mathbf{R}_{ee} \underset{=}{\Delta} = E\left[\mathbf{E}_k \mathbf{E}_k^H\right] \quad \text{Eq. 5.22}$$

$$= E\left[[\widetilde{\mathbf{B}}^H \mathbf{x}_{k+N_f-1:k-v} - \mathbf{W}^H \mathbf{y}_{k+N_f-1:k}][\widetilde{\mathbf{B}}^H \mathbf{x}_{k+N_f-1:k-v} - \mathbf{W}^H \mathbf{y}_{k+N_f-1:k}]^H\right] \quad \text{Eq. 5.23}$$

$$= E\left[[\widetilde{\mathbf{B}}^H \mathbf{x}_{k+N_f-1:k-v} - \mathbf{W}^H \mathbf{y}_{k+N_f-1:k}][\mathbf{x}_{k+N_f-1:k-v}^H \widetilde{\mathbf{B}} - \mathbf{y}_{k+N_f-1:k}^H \mathbf{W}]\right] \quad \text{Eq. 5.24}$$

$$\begin{aligned} &= E\left[\widetilde{\mathbf{B}}^H \mathbf{x}_{k+N_f-1:k-v} \mathbf{x}_{k+N_f-1:k-v}^H \widetilde{\mathbf{B}}\right] - E\left[\widetilde{\mathbf{B}}^H \mathbf{x}_{k+N_f-1:k-v} \mathbf{y}_{k+N_f-1:k}^H \mathbf{W}\right] \\ &- E\left[\mathbf{W}^H \mathbf{y}_{k+N_f-1:k} \mathbf{x}_{k+N_f-1:k-v}^H \widetilde{\mathbf{B}}\right] + E\left[\mathbf{W}^H \mathbf{y}_{k+N_f-1:k} \mathbf{y}_{k+N_f-1:k}^H \mathbf{W}\right] \end{aligned} \quad \text{Eq. 5.25}$$

$$= \widetilde{\mathbf{B}}^H \mathbf{R}_{xx} \widetilde{\mathbf{B}} - \widetilde{\mathbf{B}}^H \mathbf{R}_{xy} \mathbf{W} - \mathbf{W}^H \mathbf{R}_{yx} \widetilde{\mathbf{B}} + \mathbf{W}^H \mathbf{R}_{yy} \mathbf{W} \quad \text{Eq. 5.26}$$

$$\mathbf{R}_{xx} \underset{=}{\Delta} = E\left[\mathbf{x}_{k+N_f-1:k-v} \mathbf{x}_{k+N_f-1:k-v}^H\right] \quad \text{Eq. 5.27}$$

$$\mathbf{R}_{xy} \underset{=}{\Delta} = E\left[\mathbf{x}_{k+N_f-1:k-v} \mathbf{y}_{k+N_f-1:k}^H\right] \quad \text{Eq. 5.28}$$

$$= E\left[\mathbf{x}_{k+N_f-1:k-v} \left[\sum_{m=0}^{L} \mathbf{H}_m \mathbf{x}_{k+N_f-1-m:k-m} + \mathbf{n}_{k+N_f-1:k}\right]^H\right] \quad \text{Eq. 5.29}$$

$$= \sum_{m=0}^{L} E\left[\mathbf{x}_{k+N_f-1:k-v} \mathbf{x}_{k+N_f-1-m:k-m}^H\right] \mathbf{H}_m^H = \mathbf{R}_{xx} \mathbf{H}^H \quad \text{Eq. 5.30}$$

$$\mathbf{R}_{yy} \underset{=}{\Delta} = E\left[\mathbf{y}_{k+N_f-1:k}\mathbf{y}_{k+N_f-1:k}^{H}\right] \quad \text{Eq. 5.31}$$

$$= E\left[\left[\sum_{m=0}^{L}\mathbf{H}_m\mathbf{x}_{k+N_f-1-m:k-m} + \mathbf{n}_{k+N_f-1:k}\right]\left[\sum_{p=0}^{L}\mathbf{H}_p\mathbf{x}_{k+N_f-1-p:k-p} + \mathbf{n}_{k+N_f-1:k}\right]^{H}\right] \quad \text{Eq. 5.32}$$

$$= E\left[\left[\sum_{m=0}^{L}\mathbf{H}_m\mathbf{x}_{k+N_f-1-m:k-m} + \mathbf{n}_{k+N_f-1:k}\right]\left[\sum_{p=0}^{L}\mathbf{H}_p\mathbf{x}_{k+N_f-1-p:k-p} + \mathbf{n}_{k+N_f-1:k}\right]^{H}\right] \quad \text{Eq. 5.33}$$

$$= \sum_{m=0}^{L}\sum_{p=0}^{L}\mathbf{H}_m E\left[\mathbf{x}_{k+N_f-1-m:k-m}\mathbf{x}_{k+N_f-1-p:k-p}^{H}\right]\mathbf{H}_p^{H} + E\left[\mathbf{n}_{k+N_f-1:k}\mathbf{n}_{k+N_f-1:k}^{H}\right] \quad \text{Eq. 5.34}$$

$$= \mathbf{H}\mathbf{R}_{xx}\mathbf{H}^{H} + \mathbf{R}_{nn} \quad \text{Eq. 5.35}$$

An optimal MIMO-MMSE-TEQ solution minimizing $trace(\mathbf{R}_{ee})$ can be found by applying the orthogonality principle [2] as in Eq. **5.36**, Eq. **5.37** and Eq. **5.38**. Thus an optimal MIMO-MMSE-TEQ of Eq. **5.39** is finally found.

$$E\left[\mathbf{E}_k\mathbf{y}_{k+N_f-1:k}^{H}\right] = \mathbf{0}_{[lN_o\times N_f lN_o]} \quad \text{Eq. 5.36}$$

$$E\left[[\widetilde{\mathbf{B}}_{opt}^{H}\mathbf{x}_{k+N_f-1:k-v} - \mathbf{W}_{\text{opt}}^{\text{H}}\mathbf{y}_{k+N_f-1:k}]\mathbf{y}_{k+N_f-1:k}^{H}\right] = \mathbf{0}_{[lN_o\times N_f lN_o]} \quad \text{Eq. 5.37}$$

$$\widetilde{\mathbf{B}}_{opt}^{H}\mathbf{R}_{xy} = \mathbf{W}_{\text{opt}}^{\text{H}}\mathbf{R}_{yy} \quad \text{Eq. 5.38}$$

$$\mathbf{W}_{\text{opt}}^{\text{H}} = \widetilde{\mathbf{B}}_{opt}^{H}\mathbf{R}_{xy}\mathbf{R}_{yy}^{-1} = \widetilde{\mathbf{B}}_{opt}^{H}\mathbf{R}_{xx}\mathbf{H}^{H}\left(\mathbf{H}\mathbf{R}_{xx}\mathbf{H}^{H} + \mathbf{R}_{nn}\right)^{-1} \quad \text{Eq. 5.39}$$

Also, since we obtained $\mathbf{W}_{\text{opt}}$, we can substitute Eq. **5.39** into Eq. **5.22** to obtain Eq. **5.40** ~ Eq. **5.42** where Eq. **5.44** ~ Eq. **5.46** has been used, or into Eq. **5.43** where Eq. **5.47** ~ Eq. **5.48** have been used.

$$\mathbf{R}_{ee,opt} = \widetilde{\mathbf{B}}_{opt}^{H}\mathbf{R}_{xx}\widetilde{\mathbf{B}}_{opt} - \widetilde{\mathbf{B}}_{opt}^{H}\mathbf{R}_{xy}\mathbf{W}_{opt} - \mathbf{W}_{opt}^{H}\mathbf{R}_{yx}\widetilde{\mathbf{B}}_{opt} + \mathbf{W}_{opt}^{H}\mathbf{R}_{yy}\mathbf{W}_{opt} \quad \text{Eq. 5.40}$$

$$\begin{aligned}= {} & \widetilde{\mathbf{B}}_{opt}^{H}\mathbf{R}_{xx}\widetilde{\mathbf{B}}_{opt} - \widetilde{\mathbf{B}}_{opt}^{H}\mathbf{R}_{xy}\left(\mathbf{R}_{yy}^{-H}\mathbf{R}_{yx}\widetilde{\mathbf{B}}_{opt}\right) - \left(\widetilde{\mathbf{B}}_{opt}^{H}\mathbf{R}_{xy}\mathbf{R}_{yy}^{-1}\right)\mathbf{R}_{yx}\widetilde{\mathbf{B}}_{opt} \\ & + \left(\widetilde{\mathbf{B}}_{opt}^{H}\mathbf{R}_{xy}\mathbf{R}_{yy}^{-1}\right)\mathbf{R}_{yy}\left(\mathbf{R}_{yy}^{-H}\mathbf{R}_{yx}\widetilde{\mathbf{B}}_{opt}\right) = \widetilde{\mathbf{B}}_{opt}^{H}\left(\mathbf{R}_{xx} - \mathbf{R}_{xy}\mathbf{R}_{yy}^{-1}\mathbf{R}_{yx}\right)\widetilde{\mathbf{B}}_{opt}\end{aligned} \quad \text{Eq. 5.41}$$

$$= \widetilde{\mathbf{B}}_{opt}^{H}\mathbf{R}^{\perp}\widetilde{\mathbf{B}}_{opt} \quad \text{Eq. 5.42}$$

$$= \mathbf{B}_{opt}^{H}\mathbf{R}^{\Delta}\mathbf{B}_{opt} \quad \text{Eq. 5.43}$$

$$\mathbf{R}^{\perp} = \mathbf{R}_{xx} - \mathbf{R}_{xy}\left(\mathbf{R}_{yy}^{-H}\mathbf{R}_{yx}\right) - \left(\mathbf{R}_{xy}\mathbf{R}_{yy}^{-1}\right)\mathbf{R}_{yx} + \left(\mathbf{R}_{xy}\mathbf{R}_{yy}^{-1}\right)\mathbf{R}_{yy}\left(\mathbf{R}_{yy}^{-H}\mathbf{R}_{yx}\right) \quad \text{Eq. } \mathbf{5.44}$$

$$= \left(\mathbf{R}_{xx} - \mathbf{R}_{xy}\mathbf{R}_{yy}^{-H}\mathbf{R}_{yx} - \mathbf{R}_{xy}\mathbf{R}_{yy}^{-1}\mathbf{R}_{yx} + \mathbf{R}_{xy}\mathbf{R}_{yy}^{-1}\mathbf{R}_{yy}\mathbf{R}_{yy}^{-H}\mathbf{R}_{yx}\right) \quad \text{Eq. } \mathbf{5.45}$$

$$= \left(\mathbf{R}_{xx} - \mathbf{R}_{xy}\mathbf{R}_{yy}^{-1}\mathbf{R}_{yx}\right) \quad \text{Eq. } \mathbf{5.46}$$

$$\mathbf{R}_{\Delta} = \mathbf{I}_{\Delta}\mathbf{R}^{\perp}\mathbf{I}_{\Delta}^{H} \quad \text{Eq. } \mathbf{5.47}$$

$$\mathbf{I}_{\Delta} \underline{\underline{\Delta}} \left[\mathbf{0}_{(N_b+1)\times\Delta}\ \mathbf{I}_{N_b+1}\ \mathbf{0}_{(N_b+1)\times s}\right] \quad \text{Eq. } \mathbf{5.48}$$

Similar to the various constraints such as unit-energy constraint or unit-tap constraint we discussed in chapter 4, we introduce two constraints suggested as in [30].

5.3.1 MIMO-MMSE-UTC-TEQ

Similar to the 'Unit-Tap Constraint on TIR' condition in the SISO context in chapter 4, we can adopt a unit-tap constraint on $\mathbf{B}$ in the MIMO context as is presented in Eq. **5.49** using Eq. **5.50**. In Eq. **5.49**, the constraint of $\mathbf{B}^{H}\mathbf{\Phi} = \mathbf{I}_{N_i}$ means that out of $\mathbf{B}$, at least the $(m+1)^{th}$ instant's MIMO taps constitute an identity matrix of size N_i-by-N_i, even though the taps at other instants do not. A MIMO-MMSE-UTC-TEQ solution can be given by Eq. **5.51** and Eq. **5.52** [30].

$$\mathbf{B}_{opt}^{UTC} = \underset{B}{\operatorname{argmin}}\, trace(\mathbf{R}_{ee}) \text{ subject to } \mathbf{B}^{H}\mathbf{\Phi} = \mathbf{I}_{N_i} \quad \text{Eq. } \mathbf{5.49}$$

$$\mathbf{\Phi}^{H} = \left[\mathbf{0}_{N_i\times N_i m}\ \mathbf{I}_{N_i}\ \mathbf{0}_{N_i\times N_i(N_b-m)}\right],\ \left[N_i \times N_i(N_b+1)\right] \quad \text{Eq. } \mathbf{5.50}$$

$$\mathbf{B}_{opt}^{UTC} = \mathbf{R}_{\Delta}^{-1}\mathbf{\Phi}\left(\mathbf{\Phi}^{H}\mathbf{R}_{\Delta}^{-1}\mathbf{\Phi}\right)^{-1} \quad \text{Eq. } \mathbf{5.51}$$

$$\mathbf{R}_{ee,opt}^{UTC} = \left(\mathbf{\Phi}^{H}\mathbf{R}_{\Delta}^{-1}\mathbf{\Phi}\right)^{-1} \quad \text{Eq. } \mathbf{5.52}$$

For computation, we can follow the flow of the algorithm outlined in Table **5-2**.

Table **5-2**: An algorithm for the MIMO-MMSE-UTC-TEQ calculation

- Assumption: The channel is either known at the receiver, or has been estimated by the receiver
- For $0 \le \Delta \le N_f + \nu - N_b - 1$ and for $0 \le m \le N_b$,

  Step 1: Calculate $\mathbf{R}_{xx}$, $\mathbf{R}_{xy}$, $\mathbf{R}_{xy}$ by Eq. **5.27** ,Eq. **5.30**, Eq. **5.35** , respectively

  Step 2: Calculate $\mathbf{\Phi}$

  Step 3: Calculate $\mathbf{R}^{\perp}$ by Eq. **5.44** ~ Eq. **5.46**

  Step 4: Calculate $\mathbf{R}_{\Delta}$ by Eq. **5.47**

  Step 5: Find $\mathbf{B}_{opt}^{UTC}$ by Eq. **5.51**

  Step 6: Find $\mathbf{R}_{ee,opt}^{UTC}$ by Eq. **5.52**

- Find Δ and m which minimize $\mathbf{R}_{ee,opt}^{UTC}$

- At the found Δ and m, find $\mathbf{W}_{\text{opt}}^{\text{H}}$ by Eq. **5.39**.

5.3.2 MIMO-MMSE-UEC-TEQ

Similar to the 'Unit-Energy Constraint on the TIR Solution' in the SISO case which we introduced in chapter 4, we can extend the same concept to MIMO, which is called MIMO-MMSE-UEC-TEQ. The optimization problem can be set up as in **Eq. 5.53**.

$$\mathbf{B}_{opt}^{UNC} = \underset{B}{\operatorname{argmin}}\, trace(\mathbf{R}_{ee}) \text{ subject to } \mathbf{B}^H\mathbf{B} = \mathbf{I}_{N_i} \qquad \textbf{Eq. 5.53}$$

By defining an eigen-decomposition as in Eq. **5.54** using Eq. **5.55**, we can find the optimal MIMO-MMSE-UEC-TEQ by Eq. **5.56** and Eq. **5.57**.

$$\mathbf{R}_{\Delta} = \mathbf{U}\mathbf{\Sigma}\mathbf{U}^H,\ \mathbf{R}_{\Delta} : [N_i(N_b+1)\times N_i(N_b+1)],\ \mathbf{U} : [N_i(N_b+1)\times N_i(N_b+1)] \qquad \text{Eq. } \textbf{5.54}$$

$$\mathbf{\Sigma} = \begin{bmatrix} \sigma_0 & 0 & 0 \\ 0 & \ddots & 0 \\ 0 & 0 & \sigma_{N_i(N_b+1)-1} \end{bmatrix}, \ \sigma_0 \geq \sigma_0 \geq \cdots \geq \sigma_{N_i(N_b+1)-1}, \qquad \text{Eq. } \mathbf{5.55}$$

$$[N_i(N_b+1) \times N_i(N_b+1)]$$

$$\mathbf{B}_{opt}^{UNC} = \mathbf{U}[\mathbf{e}_{N_i N_b} \cdots \mathbf{e}_{N_i(N_b+1)-1}] \qquad \text{Eq. } \mathbf{5.56}$$

$$\mathbf{e}_m \underset{=}{\Delta} \left[e_{m,0} \ldots e_{m,n} \ldots e_{m,N_i(N_b+1)-1}\right]^T, \text{ where } \begin{cases} e_{m,n} = 0, m \neq n \\ e_{m,n} = 1, m = n \end{cases} \qquad \text{Eq. } \mathbf{5.57}$$

Furthermore, the MMSE is given by Eq. **5.58**.

$$\mathbf{R}_{ee,opt}^{UEC} = diag(\sigma_{N_i N_b} \ldots \sigma_{N_i(N_b+1)-1}) \qquad \text{Eq. } \mathbf{5.58}$$

Our current discussion is similar to what we observed in chapter 4 for the UEC on TIR solution. There we obtained SISO TIR **b** as the eigenvector corresponding to the smallest eigenvalue of $\mathbf{A} = \mathbf{R}_{xx} - \mathbf{R}_{xy}\mathbf{R}_{yy}^{-1}\mathbf{R}_{xy}^{T}$. Here, likewise, now we have a MIMO TIR $\mathbf{B}$, and we obtain $\mathbf{B}_{opt}^{UNC}$ as the eigenvector corresponding to the smallest eigenvalue of $\mathbf{R}_{\Delta} = \mathbf{I}_{\Delta}\mathbf{R}^{\perp}\mathbf{I}_{\Delta}^{H}$ where $\mathbf{R}^{\perp} = \left(\mathbf{R}_{xx} - \mathbf{R}_{xy}\mathbf{R}_{yy}^{-1}\mathbf{R}_{yx}\right)$. Thus we see similarities between the SISO and MIMO cases, as we predicted before deriving the MIMO formula. For computations, the flow outlined in Table 5-3 can be used.

Table **5-3**: An algorithm for the MIMO-MMSE-UEC-TEQ calculation

- Assumption: The channel is either known at the receiver, or has been estimated by the receiver
- For $0 \le \Delta \le N_f + \nu - N_b - 1$ and for $0 \le m \le N_b$,

  Step 1: Calculate $\mathbf{R}_{xx}$, $\mathbf{R}_{xy}$, $\mathbf{R}_{xy}$ by Eq. **5.27** ,Eq. **5.30**, Eq. **5.35** , respectively

  Step 2: Calculate $\mathbf{\Phi}$

  Step 3: Calculate $\mathbf{R}^{\perp}$ by Eq. **5.44** ~ Eq. **5.46**

  Step 4: Calculate $\mathbf{R}_{\Delta}$ by Eq. **5.47**

  Step 5: Perform eigen-decomposition on $\mathbf{R}_{\Delta}$ as in Eq. **5.54** and find $\mathbf{U}$, $\mathbf{\Sigma}$

  Step 6: Find $\mathbf{B}_{opt}^{UNC}$ by Eq. **5.56**

  Step 7: Find $\mathbf{R}_{ee,opt}^{UNC}$ by Eq. **5.58**

- Find Δ and m which minimize $\mathbf{R}_{ee,opt}^{UNC}$
- At the found Δ and m, find $\mathbf{W}_{\text{opt}}^{\text{H}}$ by Eq. **5.39**.

5.4 Results of MIMO Equalization

In this section, the results from the MIMO shortening equalizations will be presented. Using the same context as explained in chapter 4, we usually optimize an equalizer to minimize some criterion of our choice. In the MIMO equalizer, usually we favor the MMSE equalizer, and the criterion we aim to minimize is thus the trace of $\mathbf{R}_{ee} \underset{=}{\Delta} E\left[\mathbf{E}_k \mathbf{E}_k^H\right]$. Even though the ultimate performance metric of equalization is the BER, it is difficult to verify the optimality of an equalizer by extensive BER analysis. Thus, we are usually satisfied instead with some performance criterion with lower computational complexity, in the hope that maximizing (or minimizing) this criterion will be commensurate with optimality in BER sense.

One performance criterion is arithmetic SNR (ASNR) [50] defined by Eq. **5.59**. With this criterion, we check the ratio of the transmitted power over the MMSE with an additional normalization by the total TEQ length N_f + the largest channel length v. ASNR can be justified in the sense that N_f is a cost, and a larger v means a badly shortened CIR.

$$ASNR \underset{=}{\Delta} \frac{\frac{1}{N_i(N_f+v)} trace(\mathbf{R}_{xx})}{\frac{1}{N_i} trace(\mathbf{R}_{ee}, \min)} \qquad \text{Eq. } \mathbf{5.59}$$

Another criterion is the geometric SNR (GSNR) [50] defined in Eq. **5.60**. Here, intuitively, the GSNR criterion is proportional to the input auto-correlation matrix's determinant, and is inversely proportional to the error auto-correlation matrix's determinant. Furthermore, the input auto-correlation matrix's determinant has been normalized in the power domain by the TEQ length N_f + the largest channel length v. Likewise, the error auto-correlation matrix' determinant has been normalized by N_i.

$$GSNR \underset{=}{\Delta} \frac{\left|\mathbf{R}_{xx}\right|^{1/N_i(N_f+v)}}{\left|\mathbf{R}_{ee}, \min\right|^{1/N_i}} \qquad \text{Eq. } \mathbf{5.60}$$

5.4.1 MIMO TEQ versus Number of Antennas

In this section, the MIMO TEQ performance will be investigated in the context of performance versus number of antennas. Since performance in the context of the BER will be too expensive to compute, we will adopt alternative design criteria first and compare performance based on these criteria.

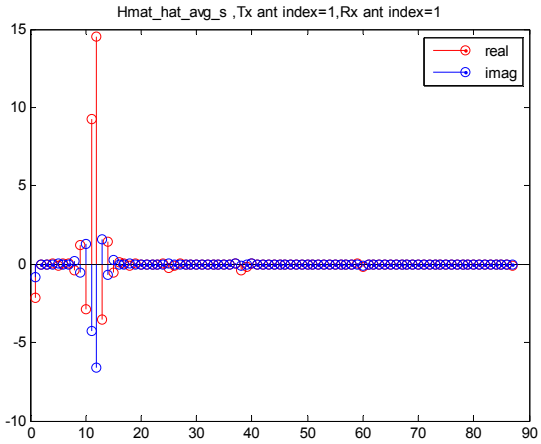

Fig. **5-2**: A SISO channel model before shortening. Suburban macro cell system scenario, channel type = vehicular A, channel sampling frequency = 34.21 MHz, mobile speed = 30km/h, downlink.

Channel snapshots were generated for 30 times T_c, and then the average was obtained

Fig. **5-2** shows a snapshot of the SISO discrete-time channel model based on the IEEE 802.20 channel model, and the channel generation conditions are fully given in Fig. **5-2**. Since we had a random and time-varying channel, we generated a certain number of snapshots for 30 ~ 100 times T_c (coherent time), and used the averaged channel for equalization testing purposes in the context of R_{ee}, ASNR and GSNR. We used this averaged channel snapshot in Fig. **5-2** ~ Fig. Error! Reference source not found. for convenience.

Fig. **5-3** shows the performance of the SISO UEC TEQ. Likewise, Fig. **5-4** shows performance of SISO UTC TEQ. We can make several observations. First, Fig. **5-3** and Fig. **5-4** show more or less the same patterns. Second, if we have large N_f and N_b values, the SISO UEC TEQ shows better results than the SISO UTC TEQ, although the enhancement is very small. However, if we have constraints on N_f and N_b, since the UTC algorithm shows a performance more or less independent of N_f and N_b, it may be more

beneficial to use the UTC TEQ than the UEC TEQ to achieve a certain performance. Third, from Fig. **5-3**, even though we can maximize the ASNR by adopting large-enough N_b value, this conflicts with our original idea of channel shortening. On the other hand, if we adopt smaller N_b value, then we can make the CIR shorter than the original length, but there is unavoidably loss in the signal power. Fourth, between a system without a TEQ and a system with a TEQ, it is a little hard to predict the accurate trend of the BER performance changes. If we pick certain N_f and N_b values, then we will have some SNR degradation from the TEQ. However, this does not mean that the BER without a TEQ will be parallel to the BER with a TEQ except for several dB's shift, since the TEQ causes our channel snapshot to be changed. This means, in the case of a single-carrier modulated system, that the distribution of ISI will be changed. In the case of frequency-domain-based modulations, the presence of a TEQ means that the distribution of subchannel SNR will be changed respectively.

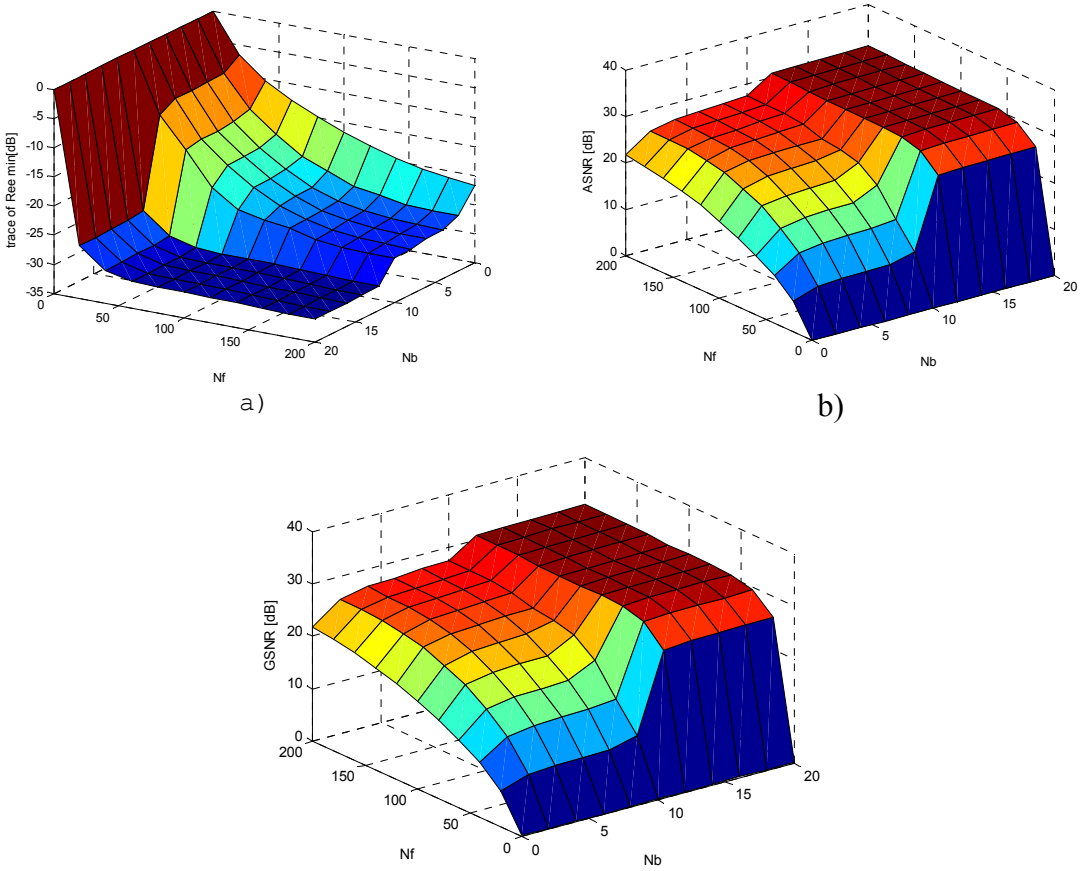

Fig. **5-3**: Performance of the SISO UEC TEQ at 30dB SNR a) trace of R_{ee} b) ASNR c) GSNR

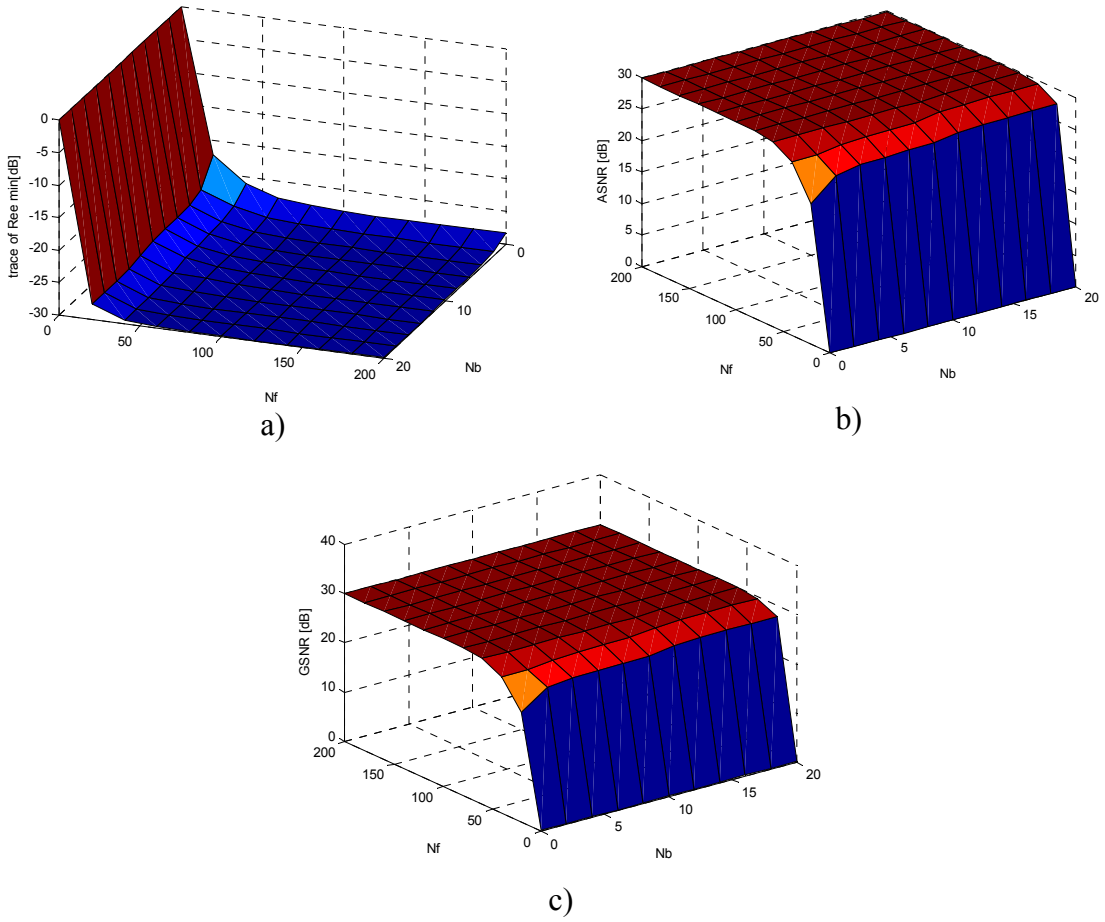

Fig. **5-4**: Performance of the SISO UTC TEQ at 30dB SNR a) trace($\mathbf{R}_{ee}$) b) ASNR c) GSNR

From the SCIR of Fig. **5-5**, we can make several observations. First, while the significant components of the CIR span up to 20 taps before the TEQ stage, Fig. **5-5** shows that the SCIR is now only 11 taps. Second, between Fig. **5-5** a) and b), even though we increased N_f, we see similar SCIRs, as Fig. **5-4** suggests. Likewise, between Fig. **5-5** c) and d), we have similar observations. If we want to use a) instead of c) of Fig. **5-5**, we can do so, but then the 3D space of Fig. **5-3** shows that we will have about 2 ~ 3 dB's loss. Third, as the names UEC and UTC imply, Fig. **5-5**'s c) and d) show SCIRs

whose center taps are close to one, whereas Fig. **5-5** a) and b) show SCIRs whose energy is one, regardless of the center tap height. In the rest of this thesis, we will focus only on the UEC TEQ algorithm, since we are interested in the effects of both N_f and N_b on performance. Also, since ASNR and GSNR are both similar in the end, we will use only ASNR and discard GSNR criterion.

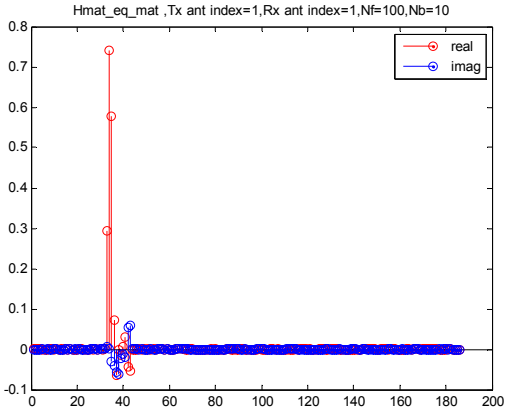

a) UEC, $N_f = 100, N_b = 10$

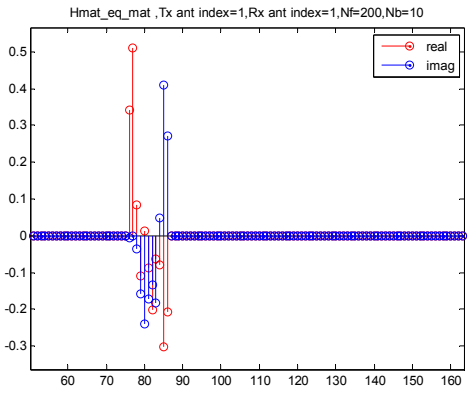

b) UEC, $N_f = 200, N_b = 10$

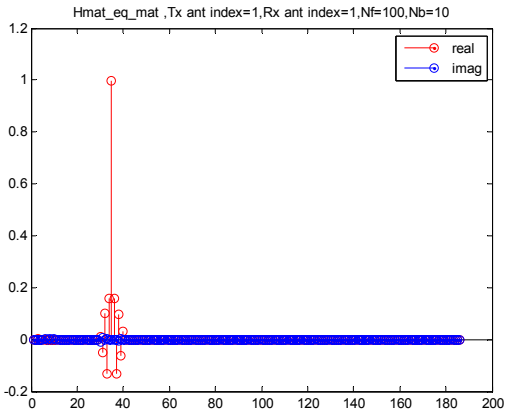

c) UTC, $N_f = 100, N_b = 10$

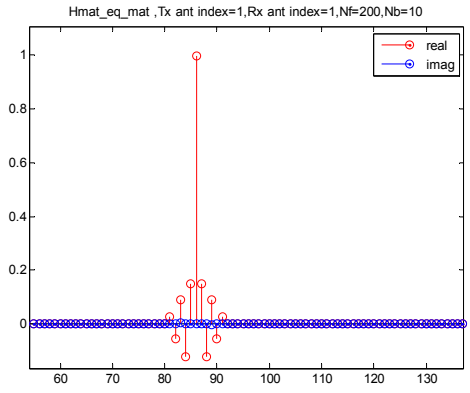

d) UTC, $N_f = 200, N_b = 10$

Fig. **5-5**: SISO channels shortened by the UEC ands UTC algorithms

Now, as a way to further verify the performance of TEQ, we further expanded our channel model to a 2-by-2 MIMO channel case and applied the MIMO UEQ TEQ algorithm. The MIMO channel snapshots are provided in Fig. **5-6**.

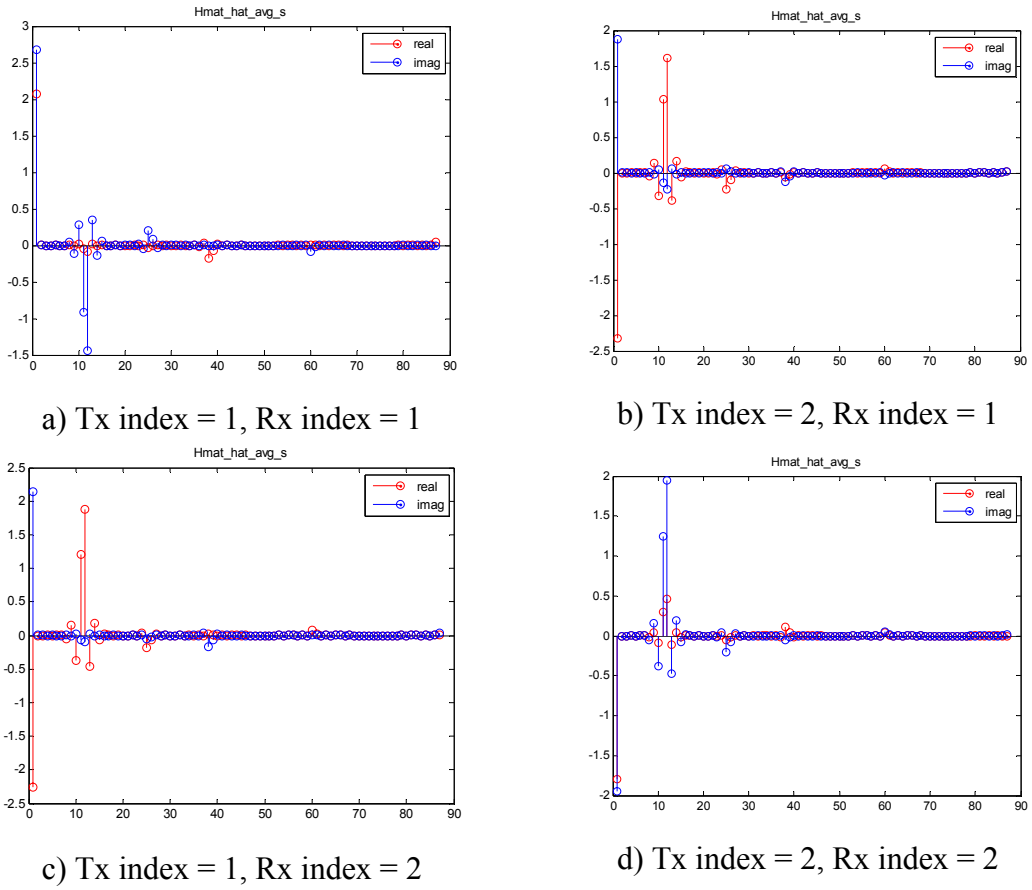

a) Tx index = 1, Rx index = 1

b) Tx index = 2, Rx index = 1

c) Tx index = 1, Rx index = 2

d) Tx index = 2, Rx index = 2

Fig. **5-6**: A 2-by-2 MIMO channel model before shortening. Suburban macro cell system scenario, channel type = vehicular A, channel sampling frequency = 34. 21 MHz, mobile speed = 30km/h, downlink.

Channel snapshots were generated for 30 times T_c, and then the average was obtained

What is interesting is that Fig. **5-7** a) and b) show stepwise dependencies on N_b. This means that N_b can work as if a threshold such that over this threshold we have enough SNR but the TEQ cannot shorten the channel, whereas below this threshold we have SNR loss but the TEQ can shorten the channel.

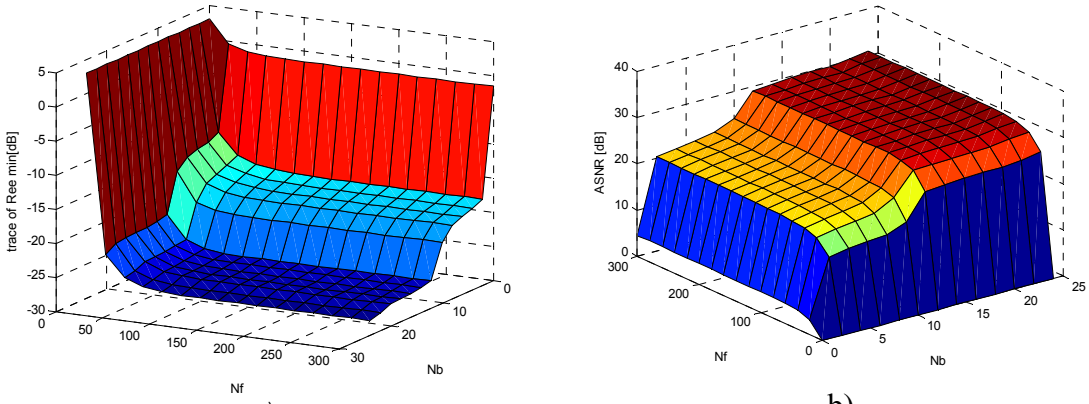

a) b)

Fig. **5-7**: Performance of a 2-by-2 MIMO UEC TEQ at 30dB SNR a) trace($\mathbf{R}_{ee}$) b) ASNR

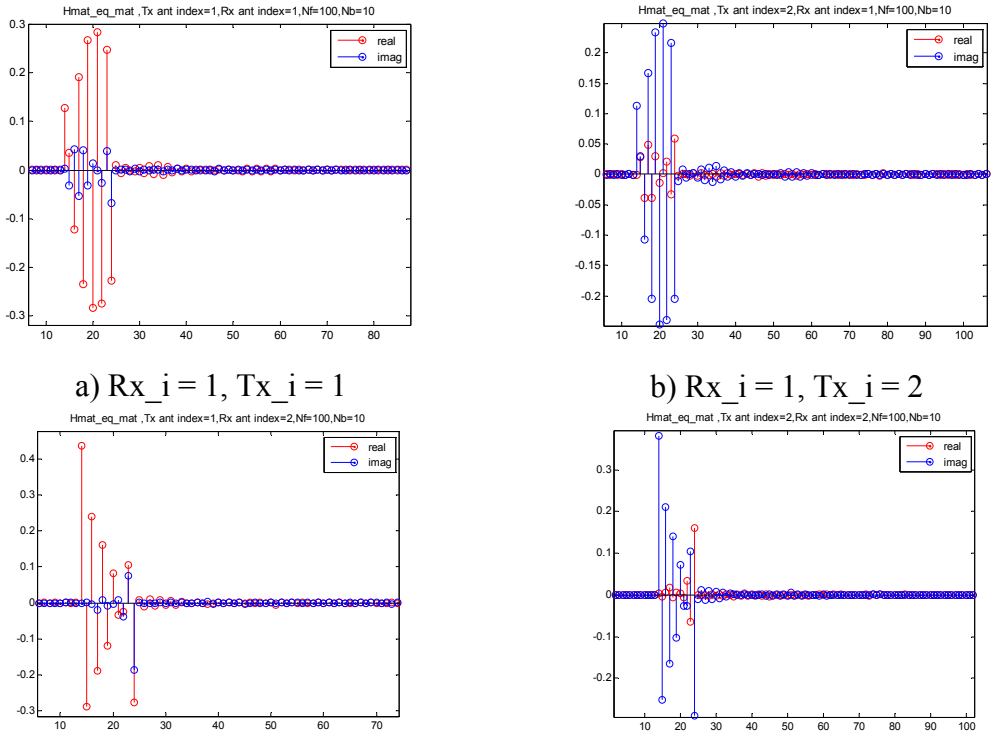

a) Rx_i = 1, Tx_i = 1

b) Rx_i = 1, Tx_i = 2

c) Rx_i = 2, Tx_i = 1

d) Rx_i = 2, Tx_i = 2

Fig. **5-8**: A 2-by-2 MIMO channel shortened by UEC criterion, $N_f = 100$, $N_b = 10$

Fig. **5-8** shows the SCIRs by the UEC TEQ algorithm. Fig. **5-8** shows that the MIMO CIR can be successfully shortened to N_b+1, except for the residual ISI beyond the window of N_b+1 length.

We also evaluated the BER for typical test cases. Considering the fact that our overall system, in particular the TEQ operation, is hard to analytically investigate, we have adopted Monte Carlo simulations.

5.4.1.1 BER Evaluations of SISO TEQ Cases

We start by investigating the SISO TEQ and its effects on the BER. As outlined in Table **5-4**, we chose a data rate of 50Mbps in a vehicular A type link model and a suburban macro cellular type system. We chose 8-PSK here since, later when we consider space-frequency block codes, we will consider the symbol rate R_s normalized by space-frequency code's rate R. Since we will consider space-frequency block codes of rate R = ½, ¾, and 1, if we aim at space-frequency block codes with spectral efficiency of 3bits/s/tone, then we will need 8-PSK for the case of SISO (R = 1).

In Fig. **5-9**, we can make several observations. First, knowing the CSI at the receiver, if we could keep on increasing the number of subcarriers, then it means that each subchannel would be more and more like a Gaussian channel, the linear summation of the subchannels behaving more similar to a Gaussian channel performance. However, this is impossible in truth, since increasing the number of subcarriers means increasing the fft size, which is limited even with the state-of-the-art DSP technology. Thus, with the FFT size of 4096, we cannot expect a near Gaussian performance, even with a perfect

CSI at the receiver. Second, if we change from condition A1 to A3 by decreasing the guard interval length, then we see a worsened BER performance. What is even worse is that A3 starts to show a BER floor, meaning that the BER performance depends more on ISI than on SNR, nullifying the increase in SNR. Third, if we adopt TEQ with various conditions as outlined in A4 ~ A8, some of them, such as A6, A7 and A8 start to outperform A3 at respective SNRs. This is due to the fact that the A3's ISI power at certain points starts to exceed the SNR loss of the TEQs of A5, A6 or A7 at very high SNRs. Thus, at high SNRs, in so far is the CIR is shortened to a proper length to prevent ISI, the TEQ will work fine. Fourth, at high SNRs, some curves with TEQs may cross A1, but there is no guarantee though, with our limited simulation capability. One possibility is that, considering the constraints in FFT size and our wide system bandwidth, our subchannels cannot see purely Gaussian subchannels. In this situation then, we may be able to flatten the channel to some extent with the aid of the TEQ, which may further enhance the BER performance. Fifth, even though we could enhance the OFDM spectral efficiency from 0.958 to 0.993, this comes at the cost of more DSP power and a higher SNR requirement. Thus, whether we design an OFDM link following the traditional method of enough guard length, or whether we use a TEQ up front, it is totally a matter of optimization with the cost of DSP power and SNR considered.

Table **5-4**: SISO test cases

No	η	TEQ	Occupied Bandwidth (double sided)
A1	0.958	Not used	17.395020MHz
A2	Gaussian channel		
A3	0.993	Not used	16.772461MHz
A4	0.993	Used, $N_f = 100$, $N_b = 4$	16.772461MHz
A5	0.993	Used, $N_f = 100$, $N_b = 9$	16.772461MHz
A6	0.993	Used, $N_f = 100$, $N_b = 14$	16.772461MHz
A7	0.993	Used, $N_f = 100$, $N_b = 19$	16.772461MHz
A8	0.993	Used, $N_f = 100$, $N_b = 24$	16.772461MHz

- R_b = 50Mbps, modulation: 8-PSK,
- SFBC spectral efficiency = 3 b/s/tone, fft size = 4096,
- number of subcarriers = 2008
- Perfect channel estimation at the receiver assumed

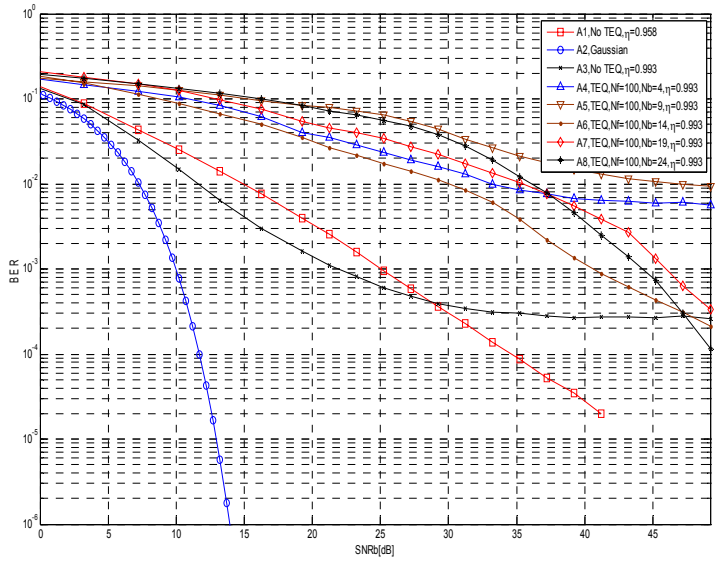

Fig. **5-9**: BER curves for 8 different SISO test cases of Table **5-4**

5.4.1.2 BER Evaluations of 2-by-2 MIMO TEQ Cases

In this section, we further expanded our previous discussion on the SISO TEQ to 2-by-2 MIMO cases using Alamouti's diversity scheme [33]. The test conditions are outlined in Table **5-5**.

Table **5-5**: 2-by-2 MIMO test cases

No	OFDM spectral efficiency	TEQ	Occupied Bandwidth (double sided)
B1	0.958	Not used	17.395020MHz
B2	Gaussian channel		
B3	0.993	Used, $N_f = 100$, $N_b = 4$	16.772461MHz
B4	0.993	Used, $N_f = 100$, $N_b = 9$	16.772461MHz
B5	0.993	Used, $N_f = 100$, $N_b = 14$	16.772461MHz
B6	0.993	Used, $N_f = 100$, $N_b = 19$	16.772461MHz
B7	0.993	Used, $N_f = 100$, $N_b = 24$	16.772461MHz

- R_b = 50Mbps, modulation: 8-PSK
- Spectral efficiency = 3 b/s/tone, fft size = 4096
- number of subcarriers = 2008
- Perfect channel estimation at the receiver assumed
- BS spacing = 10λ

In Fig. **5-10**, among our TEQ test cases, B7 ($N_f = 100$ and $N_b = 24$) and B5 ($N_f = 100$ and $N_b = 14$) shows a relatively good performance. Comparing between B7 ($N_f = 100$ and $N_b = 24$) and B1 (no TEQ, sufficient guard sequence), however, when a design without a TEQ works already fine, the TEQ brings a gain in terms of bandwidth efficiency but at the cost of the requirement for a higher SNR.

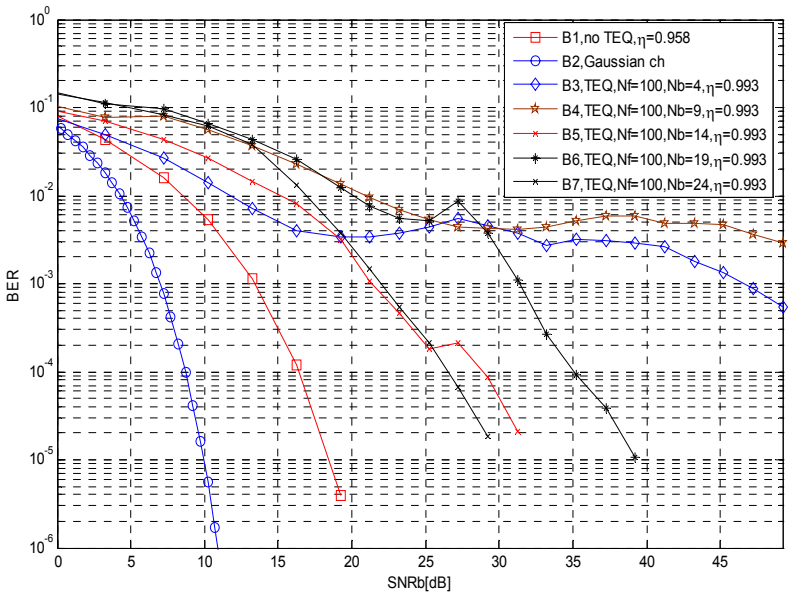

Fig. **5-10**: BER curves for 6 different 2-by-2 MIMO test cases of Table **5-5**

5.4.2 MIMO TEQ versus Antenna Spacing

We also considered the issue of the MIMO TEQ versus antenna spacing. For three antenna spacing values of $0.5\,\lambda$, $4\,\lambda$ and $10\,\lambda$, we evaluated the MIMO TEQ performance by $tr(\mathbf{R}_{ee})$ criterion, and presented the results in Fig. **5-11**. In Fig. **5-11**, we have lower $tr(\mathbf{R}_{ee})$ in the order of $10\,\lambda$, $4\,\lambda$ and $0.5\,\lambda$, with the $10\,\lambda$ case showing the lowest $tr(\mathbf{R}_{ee})$. For the $10\,\lambda$ case, $tr(\mathbf{R}_{ee})$ goes down close to -35dB. For the $4\,\lambda$ and $0.5\,\lambda$ cases, $tr(\mathbf{R}_{ee})$ goes down to -30dB, but with insufficient N_b, the $4\,\lambda$ case is a little better.

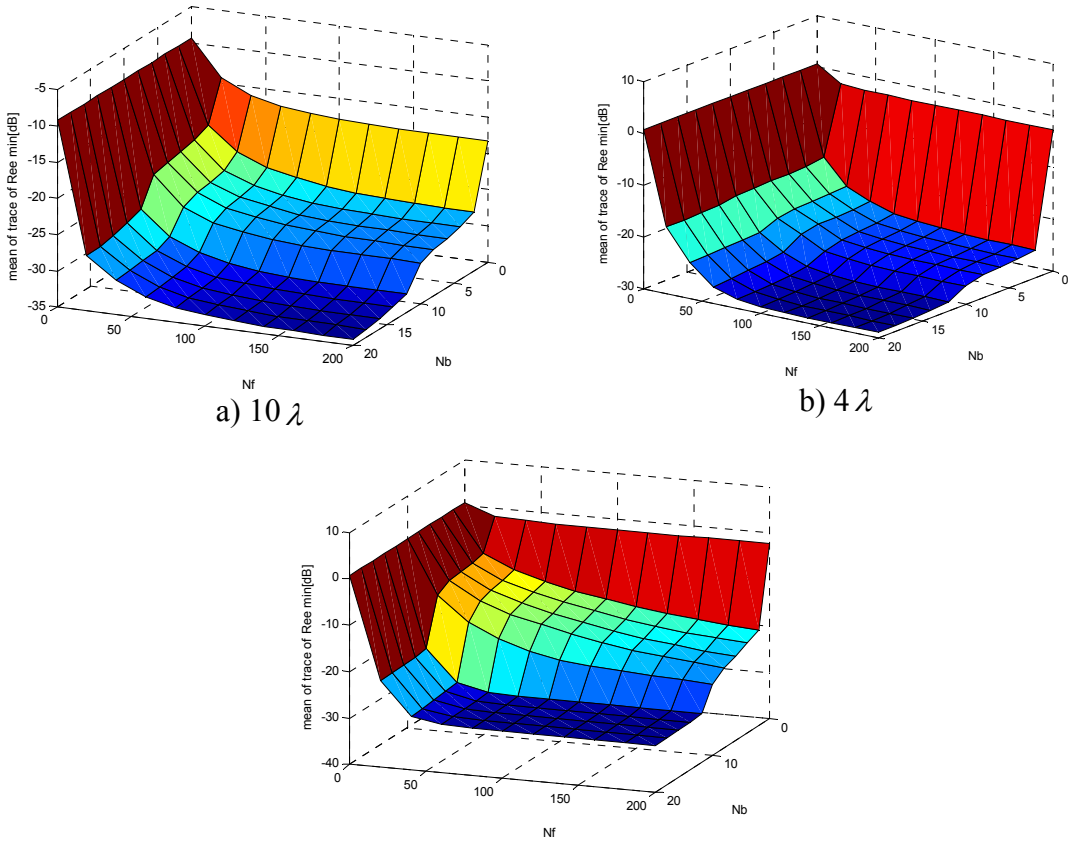

Fig. **5-11**: $tr(\mathbf{R}_{ee})$ versus antenna spacing tested at SNR = 30dB, spectral efficiency = 0.993

However, since $tr(\mathbf{R}_{ee})$ itself may have started from different points initially without the MIMO-TEQ, resulting from the different channel properties, we projected figures of Fig. **5-11** onto the $N_f = 0$ plane and the $N_b = 0$ plane, as given in Fig. **5-12** and Fig. **5-13**. We can make two observations. First, with $N_f = 0$ or $N_b = 0$, we see the lowest $tr(\mathbf{R}_{ee})$ for the case of the antenna spacing = 10λ, which indeed makes sense. Second, however, if we use the MIMO-TEQ and vary N_f and/or N_b, and if we measure $\Delta[tr(\mathbf{R}_{ee})]$, we see about 25dB, 29dB, and 30.5dB enhancements from Fig. **5-12** a), b) and c),

respectively. Fig. **5-13** will show the same levels of enhancement. This observation means that we can expect the largest enhancement for the highly correlated case. For less correlated channels, on the other hand, the N_Tx-by-M_Rx MIMO subchannels have different taps at different time instants, whereas for a highly correlated channel, the MIMO subchannels have similar taps at similar time instants. Thus, of course, the highly correlated channel case may be easier to equalize.

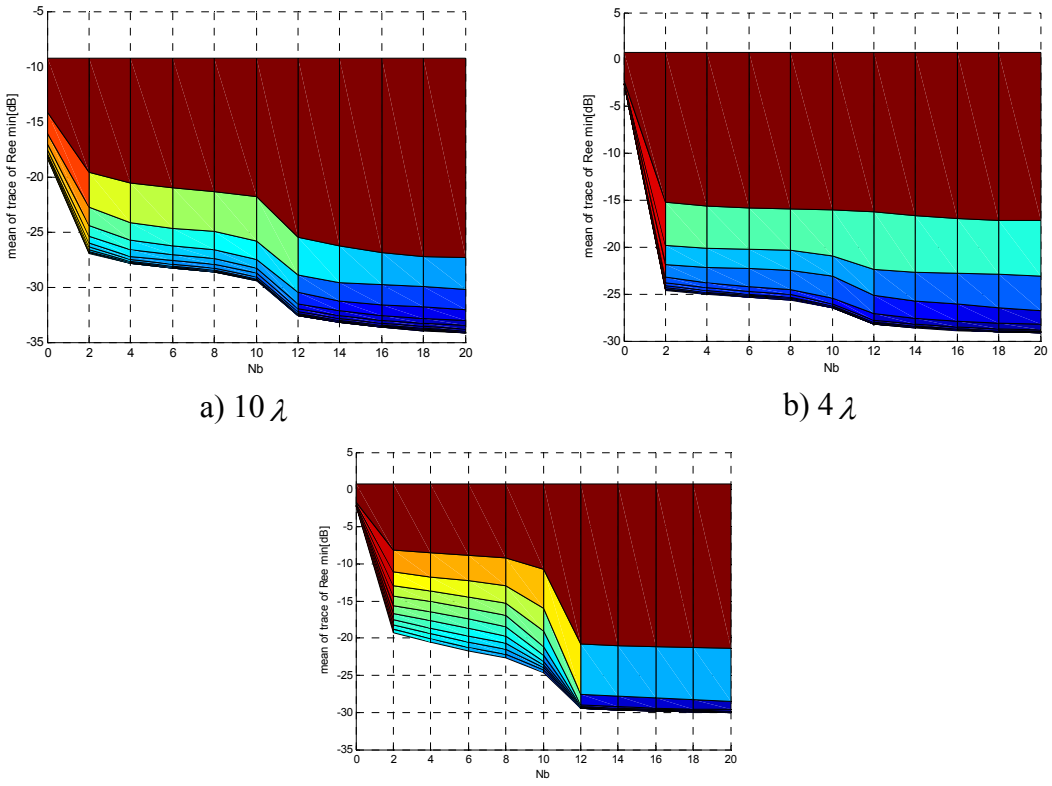

a) 10 λ b) 4 λ

c) 0.5 λ

Fig. **5-12**: $tr(\mathbf{R}_{ee})$ versus antenna spacing tested at SNR = 30dB, spectral efficiency = 0.993, projected onto $N_f = 0$ plane.

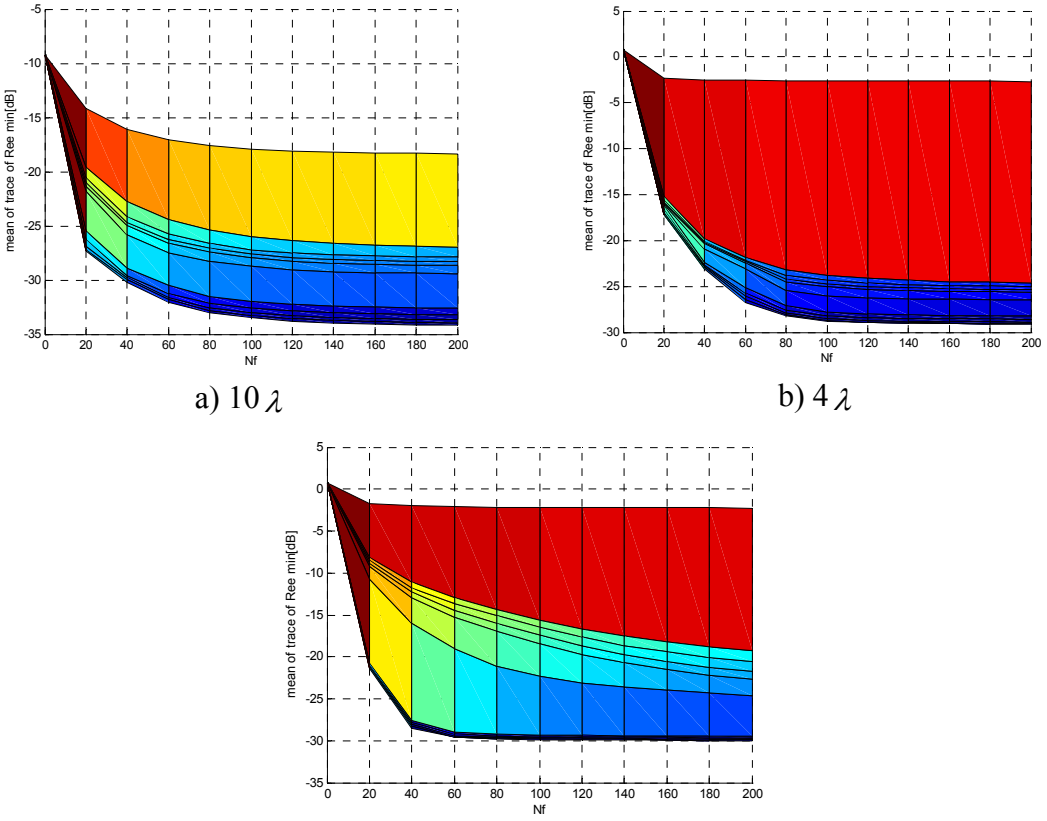

a) 10 λ b) 4 λ

c) 0.5 λ

Fig. **5-13**: $tr(\mathbf{R}_{ee})$ versus antenna spacing tested at SNR = 30dB, spectral efficiency = 0.993, projected onto $N_b = 0$ plane.

To further verify our observations of Fig. **5-11**~ Fig. **5-13**, we evaluated the BER for test conditions outlined in Table **5-6** and show the results in Fig. **5-14**.

Table **5-6**: Test cases for BER versus antenna spacing

No	OFDM spectral efficiency	TEQ	Occupied Bandwidth (double sided)	Antenna spacing at the BS
C1	0.958	Not used	17.395020 MHz	10 λ
C2	0.993	Used, N_f = 100, N_b = 24	16.72461 MHz	10 λ
C3	0.958	Not used	17.395020 MHz	4 λ
C4	0.993	Used, N_f = 100, N_b = 24	16.72461 MHz	4 λ
C5	Gaussian channel			
C6	0.958	Not used	17.395020 MHz	0.5 λ
C7	0.993	Used, N_f = 100, N_b = 24	16.72461 MHz	0.5 λ

- R_b = 50Mbps, modulation : 8-PSK,
- Spectral efficiency = 3 b/s/tone, fft size = 4096,
- number of subcarriers = 2048
- Perfect channel estimation at the receiver assumed
- N_Tx = 2, M_Tx = 2, SFBC: Alamouti code

From Fig. **5-14**, we can make several observations. First, among the cases without the TEQs, performance is in the order of C1, C3 and C6, with C1 showing the best BER. This observation is in agreement with our knowledge that the Alamouti scheme works best with farther antenna spacing. Second, even among the MIMO TEQ cases, performance is in the order of C2, C4 and C7, once again in agreement with our previous observation from Fig. **5-11** that the less correlated scenarios returned the better ASNR results.

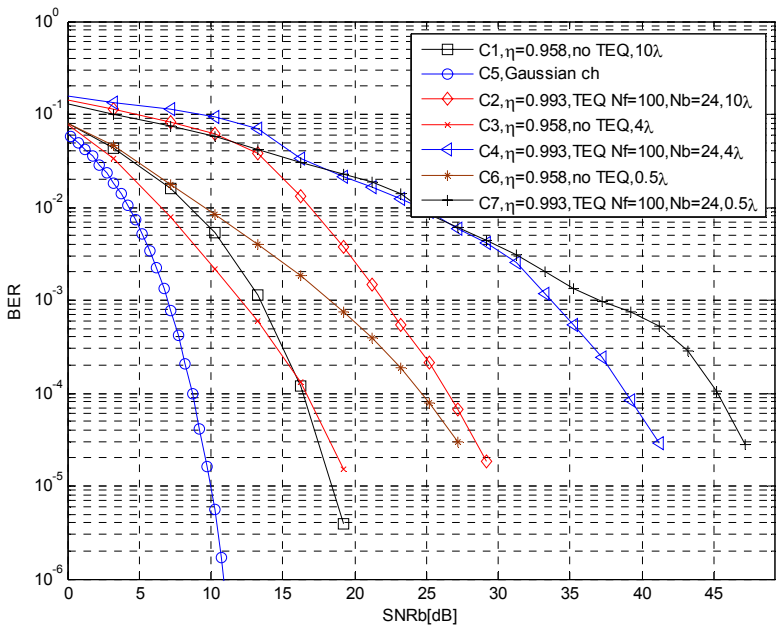

Fig. **5-14**: BER curves for 6 different 2-by-2 MIMO test cases with/without TEQ and various antenna spacing conditions outlined in Table **5-6**

5.5 Summary and Conclusions

In this chapter, we extended the SISO TEQ concept to the MIMO TEQ, showed its formulas, and evaluated its performance in various metrics. We can use either the SISO MLSD or the MIMO MLSD [29] after the SISO or MIMO TEQ. Or, we can use the TEQ to enhance the spectral efficiency of OFDM links. In the case where the OFDM links are constrained by the FFT size, the MIMO TEQ may not only enhance the spectral efficiency but also enhance the BER. In this context, we examined the SISO/MIMO TEQ performance in the MIMO-OFDM links. The performance depends on many factors and mostly the channel's time domain shape itself. Among the test cases examined in this

chapter, we could not find a case where we can enhance both the spectral efficiency and the BER. In the case of SISO links, there were cases where the TEQ-equalized BER curves started to show steeper slopes than the standard BER curve without a TEQ, but we couldn't verify if the standard BER curve will be in the end outperformed by the TEQ-equalized cases, due to our limited computational capability. However, at least, the SISO/MIMO TEQ cases worked as an alternative design at the cost of SNR, gaining in spectral efficiency. This can be understood as due to characteristics of the RF channel, which is not very heavily disturbed, unlike the FSO channel or DSL channel.

Chapter 6

Space-Frequency Block Codes

Another way to further improve the link quality and thus provide QoS (Quality-of-Service) in a MIMO system is through spatial diversity codes which benefit from rich-scattering medium properties. One important motivation for investigating the spatial diversity codes is that, as we mentioned in chapter 3, the channel shortening equalizer can change the average channel correlation properties. If then, we may ask if a MIMO TEQ combined with a spatial diversity code can give us any benefit or not.

In MIMO, traditionally three kinds of diversity coding have been of interest: space-time block codes (STBC), space-time trellis codes (STTC), and layered space-time codes (LSTC). Whereas time-domain modulations go well with the STBC, frequency-domain modulations such as OFDM go well with STBC's frequency-domain counterpart or SFBC (space-frequency block coding).

In this thesis, we focus more on STBC (or SFBC) for its simple implementation via ML detector. In this chapter, we slightly change our previous notations of MIMO, and represent the overall system by a narrow-band MIMO model given in Eq. **6.1** where n is the Tx antenna index, m is the Rx antenna index, t is the time, $\mathbf{C}_{t,n}$ is the transmitted signal (in this chapter, codewords), $\alpha_{n,m}$ is the path gain of the narrowband MIMO model, and $r_{t,m}$ is the received signal. In matrix forms, we will have Eq. **6.2**, using Eq. **6.3**, Eq. **6.4** and Eq. **6.5**.

$$r_{t,m} = \sum_{n=1}^{N} \alpha_{n,m} \mathbf{C}_{t,n} + n_{t,m} \qquad \text{Eq. } \mathbf{6.1}$$

$$\mathbf{r} = \mathbf{C} \cdot \mathbf{H} + \mathbf{N} \qquad \text{Eq. } \mathbf{6.2}$$

$$\mathbf{r} = \begin{bmatrix} \ddots & \cdots & \\ & r_{t,m} & \\ & \cdots & \ddots \end{bmatrix}, \ \mathbf{r}\text{: T-by-M} \qquad \text{Eq. } \mathbf{6.3}$$

$$\mathbf{H} = \begin{bmatrix} \ddots & \cdots & \\ & H_{n,m} & \\ & \cdots & \ddots \end{bmatrix}, \ H_{n,m} = \alpha_{n,m}, \text{ H: N-by-M} \qquad \text{Eq. } \mathbf{6.4}$$

$$\mathbf{C} = \begin{bmatrix} \ddots & \cdots & \\ & \mathbf{C}_{t,n} & \\ & \cdots & \ddots \end{bmatrix}, \ \mathbf{C}\text{: T-by-N} \qquad \text{Eq. } \mathbf{6.5}$$

We can think of several code design criteria and try to minimize the thus-selected criterion in our code design. Typical ones are rank criterion, determinant criterion, trace criterion, maximum mutual information criterion, etc [32].

6.1 Theory of Space-Time Block Codes

We begin with a brief introduction to the theory of orthogonal SFBCs in this chapter. One good example of SFBCs is the codes by Alamouti, but we will discuss more generalized cases in this chapter. A low-complexity joint maximum-likelihood (ML) decoding rule can be given by Eq. **6.6** using Eq. **6.1** ~ Eq. **6.5**. Eq. **6.6** can be further simplified to Eq. **6.7**.

$$\hat{\mathbf{C}} = \arg\min_{\mathbf{C}} tr\left[\left(\mathbf{r} - \mathbf{C} \cdot \mathbf{H}\right)^{H} \left(\mathbf{r} - \mathbf{C} \cdot \mathbf{H}\right)\right] \qquad \text{Eq. } \mathbf{6.6}$$

$$\hat{\mathbf{C}} = \arg\min_{\mathbf{C}} \left\{ \sum_{m=1}^{M} \left[\mathbf{H}_m^{H} \cdot \mathbf{C}^{H} \cdot \mathbf{C} \cdot \mathbf{H}_m - 2R\left(\mathbf{H}_m^{H} \cdot \mathbf{C}^{H} \cdot \mathbf{r}_m\right) \right] \right\} \qquad \text{Eq. } \mathbf{6.7}$$

We start our discussion with the case of real orthogonal designs, but we are in the end interested in complex orthogonal designs. A generator matrix for the real orthogonal design case is a T-by-N matrix $\mathbf{g}$ with real entries $x_1,-x_1,...,x_K,-x_K$ which satisfies $\mathbf{g}^T\mathbf{g} = \kappa(x_1^2 + ...x_K^2)\mathbf{I}_N$, where $\mathbf{I}_N$ an N-by-N identity matrix is and κ is a constant. We use a matrix $\mathbf{\Omega}_R$ such that, for example, in the case of Alamouti's code, when we have a received vector $r_1 = \alpha_1 s_1 + \alpha_2 s_1 + \eta_1$ and $r_2 = -\alpha_1 s_2^* + \alpha_2 s_1^* + \eta_2$, we can re-formulate it by Eq. **6.8**. We define matrix $\mathbf{\Omega}_R$ per each receive antenna as defined in typical examples of Eq. **6.9**, Eq. **6.10** or Eq. **6.11**. On the other hand, given an STBC codeword $\mathbf{C}$, we can also define a generator matrix for the STBC, as we define a generator matrix for the linear block codes.

$$\begin{bmatrix} r_1 & r_2^* \end{bmatrix} = \begin{bmatrix} s_1 & s_2 \end{bmatrix} \Omega_R + \begin{bmatrix} \eta_1 & \eta_2^* \end{bmatrix} \qquad \text{Eq. } \mathbf{6.8}$$

$$\Omega_R(\alpha_{1,m},\alpha_{2,m}) = \begin{bmatrix} \alpha_{1,m} & \alpha_{2,m} \\ \alpha_{2,m} & -\alpha_{1,m} \end{bmatrix}, \text{ K-by-T, K = 2, T = 2, m = 1…M} \qquad \text{Eq. } \mathbf{6.9}$$

$$\Omega_R(\alpha_{1,m},\alpha_{2,m},\alpha_{3,m},\alpha_{4,m}) = \begin{bmatrix} \alpha_{1,m} & \alpha_{2,m} & \alpha_{3,m} & \alpha_{4,m} \\ \alpha_{2,m} & -\alpha_{1,m} & -\alpha_{4,m} & \alpha_{3,m} \\ \alpha_{3,m} & \alpha_{4,m} & -\alpha_{1,m} & -\alpha_{2,m} \\ \alpha_{4,m} & -\alpha_{3,m} & \alpha_{2,m} & -\alpha_{1,m} \end{bmatrix}, \qquad \text{Eq. } \mathbf{6.10}$$

K-by-T,K = 4, T = 4, m = 1…M

$$\Omega_R(\alpha_{1,m},\alpha_{2,m},\alpha_{3,m},\alpha_{4,m},\alpha_{5,m},\alpha_{6,m},\alpha_{7,m},\alpha_{8,m})$$

$$= \begin{bmatrix} \alpha_{1,m} & \alpha_{2,m} & \alpha_{3,m} & \alpha_{4,m} & \alpha_{5,m} & \alpha_{6,m} & \alpha_{7,m} & \alpha_{8,m} \\ \alpha_{2,m} & -\alpha_{1,m} & -\alpha_{4,m} & \alpha_{3,m} & -\alpha_{6,m} & \alpha_{5,m} & \alpha_{8,m} & -\alpha_{7,m} \\ \alpha_{3,m} & \alpha_{4,m} & -\alpha_{1,m} & -\alpha_{2,m} & \alpha_{7,m} & \alpha_{8,m} & -\alpha_{5,m} & -\alpha_{6,m} \\ \alpha_{4,m} & -\alpha_{3,m} & \alpha_{2,m} & -\alpha_{1,m} & \alpha_{8,m} & -\alpha_{7,m} & \alpha_{6,m} & -\alpha_{5,m} \\ \alpha_{5,m} & \alpha_{6,m} & -\alpha_{7,m} & -\alpha_{8,m} & -\alpha_{1,m} & -\alpha_{2,m} & \alpha_{3,m} & \alpha_{4,m} \\ \alpha_{6,m} & -\alpha_{5,m} & -\alpha_{8,m} & \alpha_{7,m} & \alpha_{2,m} & -\alpha_{1,m} & -\alpha_{4,m} & \alpha_{3,m} \\ \alpha_{7,m} & -\alpha_{8,m} & \alpha_{5,m} & -\alpha_{6,m} & -\alpha_{3,m} & \alpha_{4,m} & -\alpha_{1,m} & \alpha_{2,m} \\ \alpha_{8,m} & \alpha_{7,m} & \alpha_{6,m} & \alpha_{5,m} & -\alpha_{4,m} & -\alpha_{3,m} & -\alpha_{2,m} & -\alpha_{1,m} \end{bmatrix} \qquad \text{Eq. } \mathbf{6.11}$$

,K-by-T, K = 8, T = 8, m = 1…M

For decoding, we can think of the received vector of Eq. **6.2** with M = 1 without loss of generality as in Eq. **6.12,** Eq. **6.13,** Eq. **6.14**, and Eq. **6.15.** We first do the linear processing given in Eq. **6.16,** using the property of Eq. **6.17** [32], verifying that our transmitted symbols $(s_1,...,s_K)$ can be decoded by the ML rule, respectively. Real orthogonal designs exist only for N = 2, 4, and 8 [32].

$$\mathbf{r}^T = \mathbf{H}^T \cdot \mathbf{C}^T + \mathbf{N}^T,\ \mathbf{r}^T \text{:1-by-T},\ \mathbf{H}^T \text{: 1-by-N},\ \mathbf{C}^T \text{: N-by-T} \qquad \text{Eq. } \mathbf{6.12}$$

$$= \mathbf{H}^T \sum_{k=1}^{K} s_k \mathbf{E}_k^T + \mathbf{N}^T,\ \mathbf{E}_k^T \text{: N-by-T} \qquad \text{Eq. } \mathbf{6.13}$$

$$= \sum_{k=1}^{K} s_k \mathbf{\Omega}_{R,k} + \mathbf{N}^T,\ \mathbf{\Omega}_{R,k} \text{: 1-by-T, the k}^{\text{th}} \text{ row of the matrix } \mathbf{\Omega}_R \qquad \text{Eq. } \mathbf{6.14}$$

$$= (s_1,...,s_K) \cdot \mathbf{\Omega}_R + \mathbf{N}^T,\ \mathbf{\Omega}_R \text{: K-by-T} \qquad \text{Eq. } \mathbf{6.15}$$

$$\mathbf{r}^T \cdot \mathbf{\Omega}_R^T = (s_1,...,s_K) \cdot \mathbf{\Omega}_R \cdot \mathbf{\Omega}_R^T + \mathbf{N}^T \cdot \mathbf{\Omega}_R^T$$

$$= \left(\sum_{n=1}^{N} \alpha_n^2 \right) \cdot (s_1,...,s_K) + \mathbf{N}^T \cdot \mathbf{\Omega}_R^T \qquad \text{Eq. } \mathbf{6.16}$$

$$\mathbf{\Omega}_R \cdot \mathbf{\Omega}_R^T = \left(\sum_{n=1}^{N} \alpha_n^2 \right) \mathbf{I}_K \qquad \text{Eq. } \mathbf{6.17}$$

In order to further develop complex orthogonal designs, first, given a real orthogonal generator matrix of rate R and size T-by-N, its complex orthogonal version can be generated by Eq. **6.18**. Eq. **6.18** explains how a codeword can be generated, given a vector of symbols. We can modify the received vector formula of the real orthogonal case and express it by Eq. **6.19.** We can also define another conceptual vector $\mathbf{r}'$ as in Eq. **6.20**. Similar to $\mathbf{\Omega}_R$, we can define $\mathbf{\Omega}$ as in Eq. **6.21**.

$$\mathbf{g}_c = \begin{bmatrix} \mathbf{g} \\ \mathbf{g}^H \end{bmatrix} = \begin{bmatrix} \sum_{k=1}^{K} x_k \mathbf{E}_k \\ \sum_{k=1}^{K} x_k^* \mathbf{E}_k \end{bmatrix}, \text{ 2T-by-N} \qquad \text{Eq. } \mathbf{6.18}$$

$$\mathbf{r} = [r_1,...,r_T, r_{T+1},...r_{2T}]^T = \mathbf{C}\cdot\mathbf{H} + \mathbf{N} = \begin{bmatrix} \mathbf{C}_R \cdot \mathbf{H} \\ \mathbf{C}_R^H \cdot \mathbf{H} \end{bmatrix} + \begin{bmatrix} \mathbf{N}_1 \\ \mathbf{N}_2 \end{bmatrix}, \ \mathbf{r} : \text{2T-by-1} \qquad \text{Eq. } \mathbf{6.19}$$

$$\mathbf{r}' \underset{=}{\Delta} [r_1,...,r_T, r_{T+1}^*,...r_{2T}^*]^T = \begin{bmatrix} \mathbf{C}_R \cdot \mathbf{H} \\ \mathbf{C}_R \cdot \mathbf{H}^H \end{bmatrix} + \begin{bmatrix} \mathbf{N}_1 \\ \mathbf{N}_2^H \end{bmatrix}, \ \mathbf{r}' : \text{2T-by-1} \qquad \text{Eq. } \mathbf{6.20}$$

$$\mathbf{\Omega} = \cdot[\mathbf{\Omega}_R(\alpha_{1,m},...,\alpha_{N,m}), \mathbf{\Omega}_R(\alpha_{1,m}^*,...,\alpha_{N,m}^*)], \text{ K-by-2T} \qquad \text{Eq. } \mathbf{6.21}$$

Eq. **6.20** can be further expressed by Eq. **6.22** using Eq. **6.23.** Finally, using Eq. **6.24**, we obtain Eq. **6.25** which clearly shows, as was verified by Eq. **6.16** for the case of real orthogonal designs, that our transmitted symbols $(s_1,...,s_K)$ can be decoded respectively by ML.

$$\begin{aligned} \mathbf{r}'^T &= \left[(\alpha_{1,m},...,\alpha_{N,m})\cdot\mathbf{C}_R^T, (\alpha_{1,m}^*,...,\alpha_{N,m}^*)\cdot\mathbf{C}_R^T \right] + \begin{bmatrix} \mathbf{N}_1^T & \mathbf{N}_2^H \end{bmatrix} \\ &= (s_1,....,s_K)\cdot\mathbf{\Omega} + \begin{bmatrix} \mathbf{N}_1^T & \mathbf{N}_2^H \end{bmatrix}, \text{ m} = 1\ldots\text{M} \end{aligned} \qquad \text{Eq. } \mathbf{6.22}$$

$$\mathbf{H}^T \cdot \mathbf{C}_R^T = (s_1,....s_K)\cdot\mathbf{\Omega}_R \qquad \text{Eq. } \mathbf{6.23}$$

$$\mathbf{\Omega}\cdot\mathbf{\Omega}^H = 2\left(\sum_{n=1}^{N} \left|\alpha_{n,m}\right|^2 \right)\mathbf{I}_K \qquad \text{Eq. } \mathbf{6.24}$$

$$\mathbf{r}'^T \cdot \mathbf{\Omega}^H = 2\sum_{n=1}^{N} \left|\alpha_{n,m}\right|^2 (s_1,....s_K) + \begin{bmatrix} \mathbf{N}_1^T & \mathbf{N}_2^H \end{bmatrix}\cdot\mathbf{\Omega}^H, \text{ m} = 1\ldots\text{M} \qquad \text{Eq. } \mathbf{6.25}$$

The general ML decision metric for the case of M Rx antennas, N Tx antennas and K symbols over a period of 2T can be found by Eq. **6.26** where $\mathbf{r}_m'^T$ refers to the mth row vector from the M-by-2T matrix $\mathbf{r}'^T$,and $\mathbf{\Omega}_{k,m}^H$ refers to the kth column vector from the 2T-by-K matrix $\mathbf{\Omega}^H$ at the mth Rx antenna.

$$\hat{s}_k = \underset{s_k}{\operatorname{argmin}}\left\{\left| s_k - \sum_{m=1}^{M} \mathbf{r}_m'^{T} \cdot \mathbf{\Omega}_{k,m}^{H} \right|^2 + (-1 + 2\sum_{m=1}^{M}\sum_{n=1}^{N} |\alpha_{n,m}|^2)|s_k|^2 \right\} \qquad \text{Eq. } \mathbf{6.26}$$

In this research, we study 6 different SFBC cases shown in [31] and [32]. We tabulated these 6 different cases in Table **6-1**. Of course, MIMO cases with Tx or Rx antenna numbers larger than 4 are of little practical significance unless considered in very high frequency ranges, and are shown here only from academic interest.

Table **6-1**: SFBC cases considered

Case No.	N_Tx	M_Rx	K_{SFBC}	T_{SFBC}	Encoder g_{NKT}	Rate R = K_{SFBC}/T_{SFBC}	Modulation
H1	4	4	4	8	g448	1/2	64-PSK
H2	8	8	8	16	g8816	1/2	64-PSK
H3	8	8	4	8	g848	1/2	64-PSK
H4	3	3	4	8	g348	1/2	64-PSK
H5	3	3	3	4	h334	3/4	16-PSK
H6	2	2	2	2	g222	1	8-PSK

- Rate of SFBC: ratio of the number of symbols the SFBC encoder takes as its input over the number of space-frequency coded symbols transmitted from each antenna. R = K_{SFBC}/T_{SFBC}
- g222: Alamouti code
- Since we have different rates, we employed different symbol rates (that is, different M-ary modulation) such that we have the same transmission rate of 3 bps/tone

6.2 Results

In this section, we show some SFBC results where we employ N_Tx >2 and M_Rx > 2 antennas with and without MIMO-TEQ. In Fig. **6-1**, we compared the BER performance of 6 SFBC cases outlined in Table **6-1**.

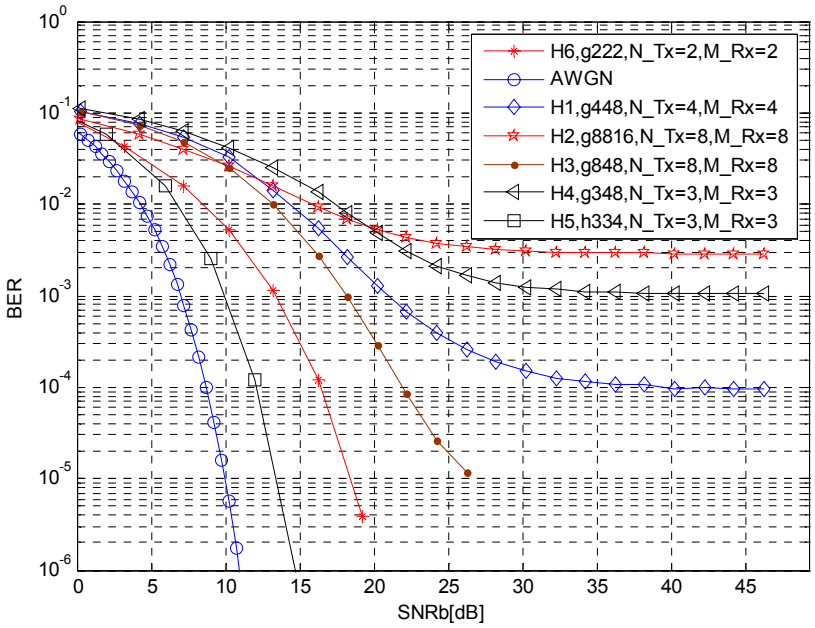

Fig. **6-1**: BER performance of 6 SFBC test cases with BS spacing = 10 λ, mobile speed = 30km/s, $\eta = 0.953$

We can make several observations here. First, usually we are in a less favorable condition if we have higher T_{SFBC} values. That is, our maximum-likelihood decoder depends on the channel estimate for accurate decoding. Thus, it needs to be satisfied that the channel's frequency response does not change during the T_{SFBC} period, but this condition is harder to fulfill if we have higher T_{SFBC} values. Thus, T_{SFBC} needs to be constrained within some practical size, depending on the channel. In our test cases, g8816 with $T_{SFBC} = 16$ shows the worst performance for this reason. For the $T_{SFBC} = 8$ cases such as g448 and g348, we also have bad performance. On the other hand, the g848 case also has $T_{SFBC} = 8$, but benefits from spatial domain diversity with 8 transmit antennas, and thus shows relatively good performance. Second, however, if T_{SFBC} gets smaller, then our diversity order in the space-frequency domain is limited, too. That is why g222 is

somewhere in the middle among different curves. Third, according to the above-mentioned reasons, T_{SFBC} should be of moderate values, which will in turn restrict the antenna dimension to within some values. Indeed, among our test cases, SFBC h334, g222, and g848 show a relatively good BER performance. Below, we present some BER results from MIMO receivers with MIMO-TEQs combined with SFBCs.

6.2.1 SFBC g8816

Table **6-2**: 8-by-8 MIMO test cases with g8816

No	η	TEQ	Occupied Bandwidth (double sided)
D1	0.958	Not used	17.46MHz
D2	Gaussian Channel		
D3	0.993	Used, $N_f = 100$, $N_b = 3$	16.83MHz
D4	0.993	Used, $N_f = 100$, $N_b = 6$	16.83MHz
D5	0.993	Used, $N_f = 100$, $N_b = 24$	16.83MHz

- R_b = 50Mbps, modulation: 64-PSK
- Spectral efficiency = 3 b/s/tone, fft size = 4096
- number of subcarriers = 2016
- Perfect channel estimation at the receiver assumed
- BS spacing = 10λ

We tested different SFBC g8816 cases outlined in Table **6-2.** From Fig. **6-2**, whereas we had a very poor BER performance before adopting a TEQ, we gained significantly from the TEQ. In particular, as can be seen from the curve D4, at a certain SNR threshold, it begins to significantly enhance the BER. We can explain this by a couple of analytical answers. First, now the MIMO channel has been shortened to a few taps. Second, simultaneously, in the frequency domain, if this can somehow provide a

frequency response that does not change significantly during the coding/decoding block of size T_{SFBC} = 16, then the BER can be enhanced. If then, our T_{SFBC} = 16 is not prohibitive any more.

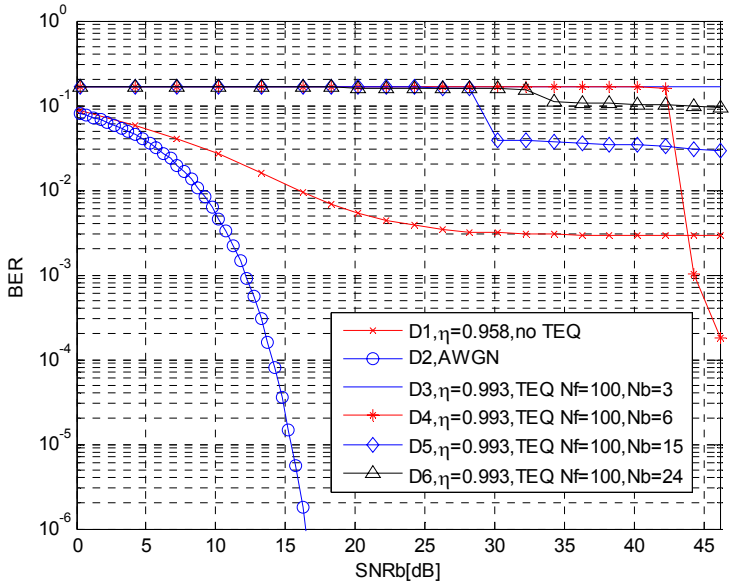

Fig. **6-2**: BER curves of SFBC g8816 test cases

In Fig. **6-3** and Fig. **6-4**, we show the 3D correlation matrix's in the frequency domain. Between Fig. **6-3** b) and Fig. **6-4** b), comparing the main lobes, it is not evident that our g8816 test cases can benefit from the second explanation, though. Fig. **6-3** b) and Fig. **6-4** b) show more or less similar correlation properties, actually. Third, in so far as we can somehow decode successfully with T_{SFBC} = 16, then we can benefit from 8 Rx antennas. Looking at Fig. **6-3** c), there is significant cross-correlation power between the Rx antennas, while the MIMO-TEQ renders the cross-correlation term to be significantly reduced. Conclusively, the author claims that the combined effects of the MIMO-TEQ, in the case of g8816, work to enhance the BER performance significantly at high SNRs.

One additional fact to be noticed is that, from the frequency-domain correlation plot without the TEQ, as shown in Fig. **6-3** b), it may be a little hard to have frequency-domain diversity, since the correlation is quite high, unless we deviate hundreds of tones from the central tone. Of course,

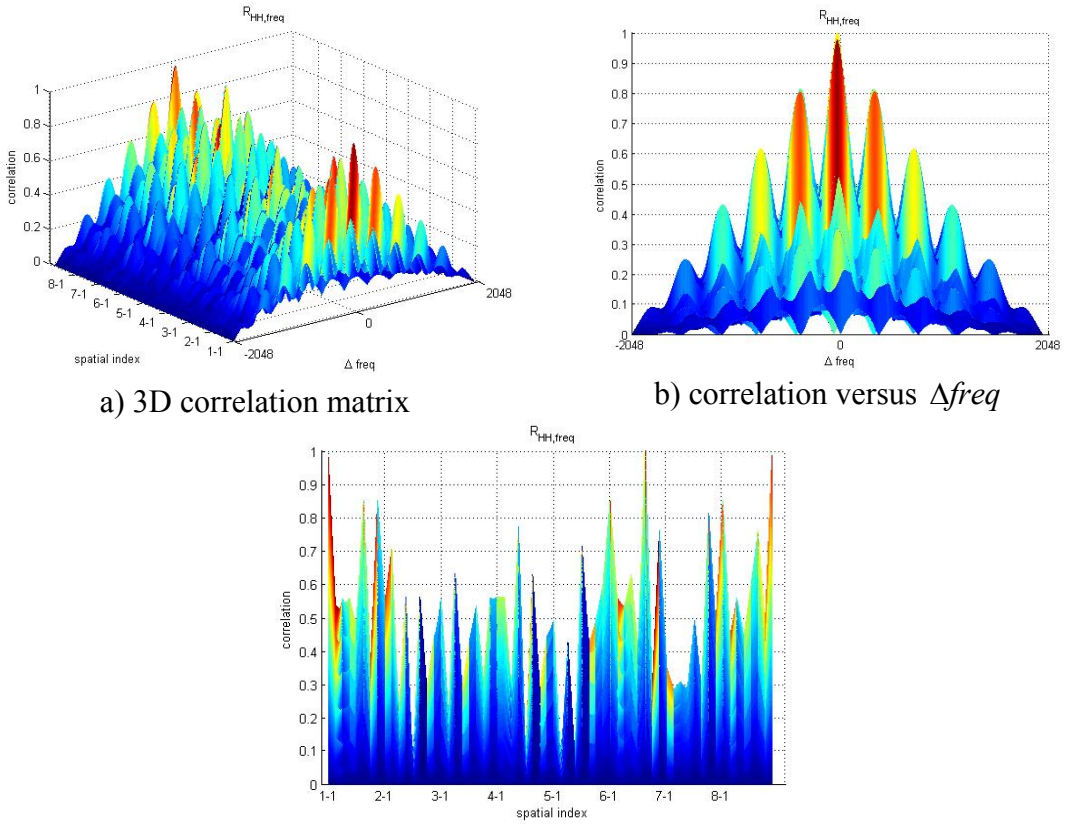

a) 3D correlation matrix

b) correlation versus $\Delta freq$

c) correlation versus space

Fig. **6-3**: 3D correlation matrix before equalization, g8816 used, η = 0.993

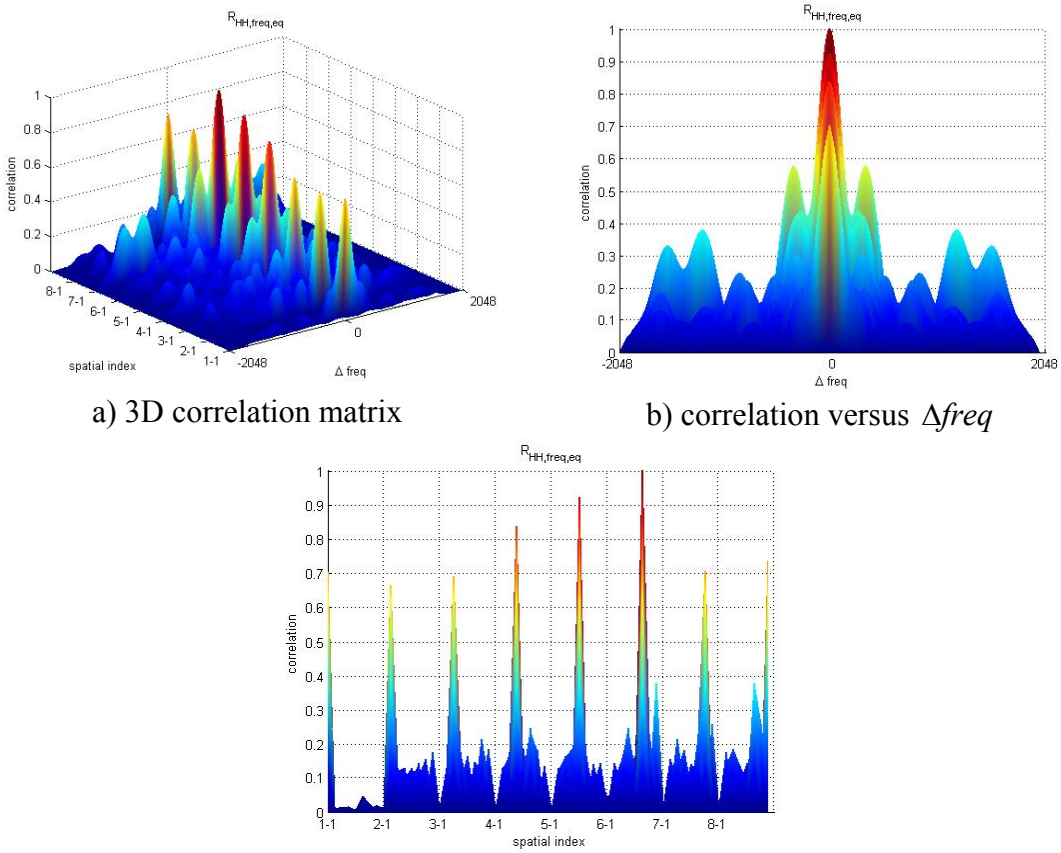

a) 3D correlation matrix

b) correlation versus $\Delta freq$

c) correlation versus space

Fig. **6-4**: 3D correlation after equalization, g8816 used, η = 0.993, D4, N_f = 100, N_b = 6

6.2.2 SFBC g848

We continued to evaluate the g848 test cases outlined in Table **6-3**. As shown in Fig. **6-5**, similar to our observations in Fig. **6-2**, curves E5 and E6 work with thresholds in SNR. Due to our limited computational capability, we could not verify if E5 or E6 could meet across E1, but after certain thresholds, E5 and E6 works very well, and the curves begin to show drastic enhancement.

Table **6-3**: 8-by-8 MIMO test cases with g848

No	η	TEQ	Occupied Bandwidth (double sided)
E1	0.958	Not used	17.39MHz
E2	Gaussian Channel		
E3	0.993	Used, $N_f = 100$, $N_b = 6$	16.77MHz
E4	0.993	Used, $N_f = 100$, $N_b = 9$	16.77MHz
E5	0.993	Used, $N_f = 100$, $N_b = 12$	16.77MHz
E6	0.993	Used, $N_f = 100$, $N_b = 15$	16.77MHz
E7	0.993	Used, $N_f = 100$, $N_b = 21$	16.77MHz

- R_b = 50Mbps, modulation: 64-PSK
- Spectral efficiency = 3 b/s/tone, fft size = 4096
- number of subcarriers = 2008
- Perfect channel estimation at the receiver assumed
- BS spacing = 10 λ

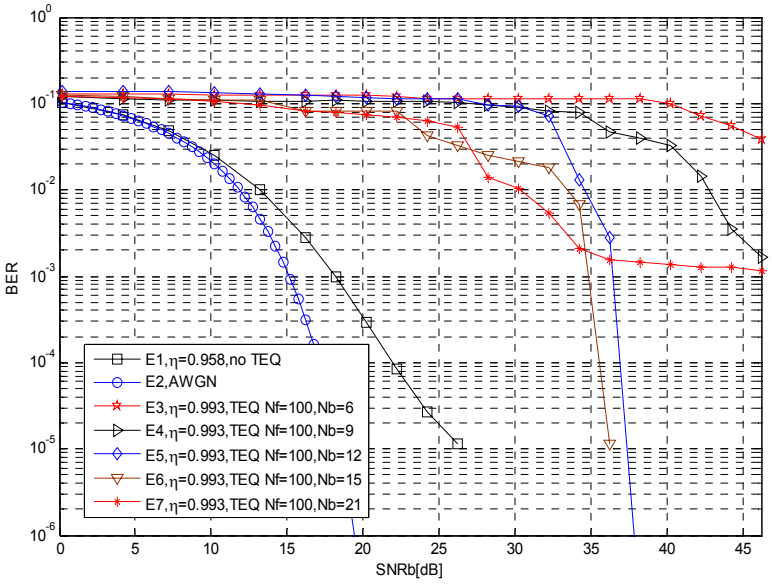

Fig. **6-5**: BER curves of 6 test cases with SFBC g848

To interpret the observations of Fig. **6-5**, we evaluated the 3D correlation matrices as in Fig. **6-6** and Fig. **6-7**. From Fig. **6-6** b) and Fig. **6-7** b), the correlation matrices change little in the frequency domain, and it will not give us any frequency-domain diversity gain. Rather, from Fig. **6-6** c) and Fig. **6-7** c), we have enhanced correlation in the spatial domain.

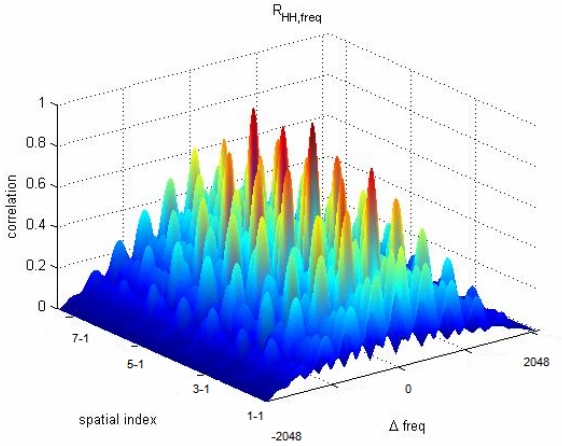

a) 3D correlation matrix

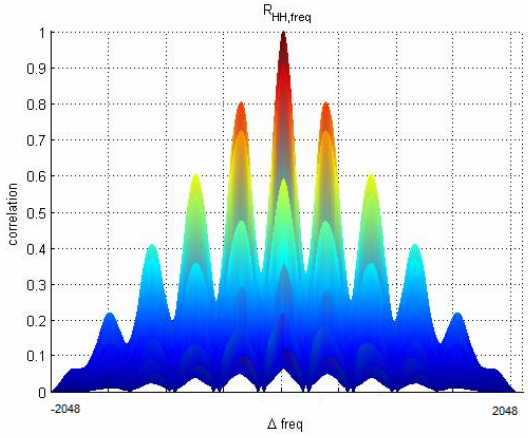

b) correlation versus Δ*freq*

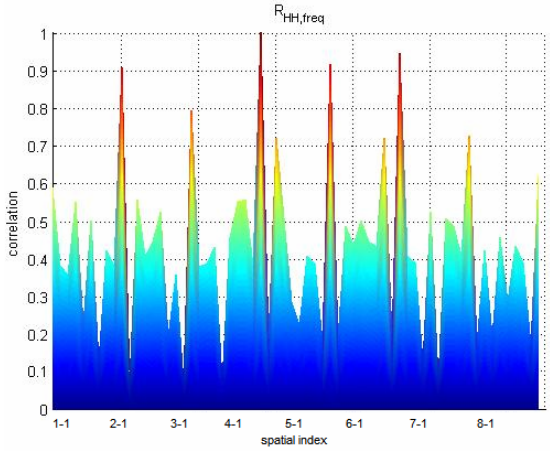

c) correlation versus space

Fig. **6-6**: 3D correlation matrix before equalization, g848 used, $\eta = 0.993$

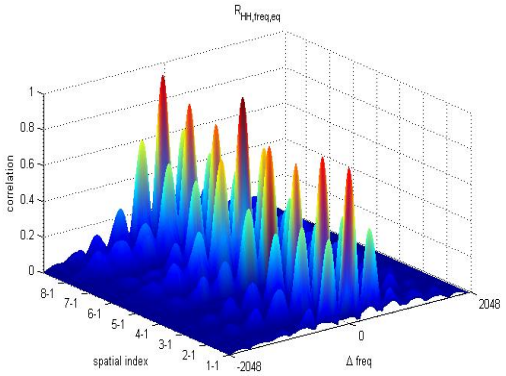

a) 3D correlation matrix

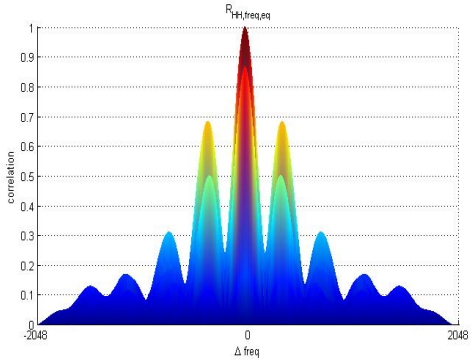

b) correlation versus $\Delta freq$

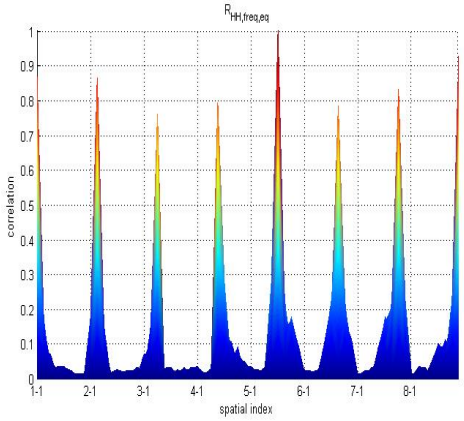

c) correlation versus space

Fig. **6-7**: 3D correlation after equalization, g848 used, η = 0.993, E6, N_f = 100, N_b = 15

6.2.3 SFBC g348

Similarly, we evaluated the BER performance for the test cases of g348 outlined in Table **6-4**. As in Fig. **6-8**, curves show performance with thresholds, and in this case, we gained significantly from having a TEQ, in particular, in F4 case.

Table **6-4**: 3-by-3 MIMO cases with g348

No	η	TEQ	Occupied Bandwidth (double sided)
F1	0.958	Not used	17.39MHz
F2	Gaussian Channel		
F3	0.993	Used, $N_f = 100$, $N_b = 6$	16.77MHz
F4	0.993	Used, $N_f = 100$, $N_b = 12$	16.77MHz
F5	0.993	Used, $N_f = 100$, $N_b = 15$	16.77MHz
F6	0.993	Used, $N_f = 100$, $N_b = 18$	16.77MHz
F7	0.993	Used, $N_f = 100$, $N_b = 21$	16.77MHz

- R_b = 50Mbps, modulation: 64-PSK
- Spectral efficiency = 3 b/s/tone, fft size = 4096
- number of subcarriers = 2008
- Perfect channel estimation at the receiver assumed
- BS spacing = 10 λ

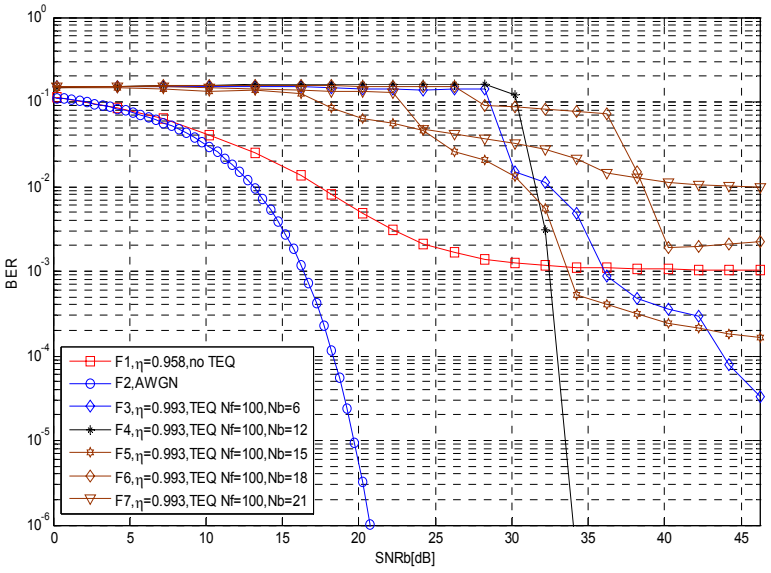

Fig. **6-8**: BER curves of 6 test cases with SFBC g348

Below in Fig. **6-9** Fig. **6-10**, we further investigated a specific case of the MIMO TEQ when we used N_f of 100 and N_b of 12. Similar to our previous observations, the MIMO TEQ enhances the correlation matrix mostly in the spatial domain.

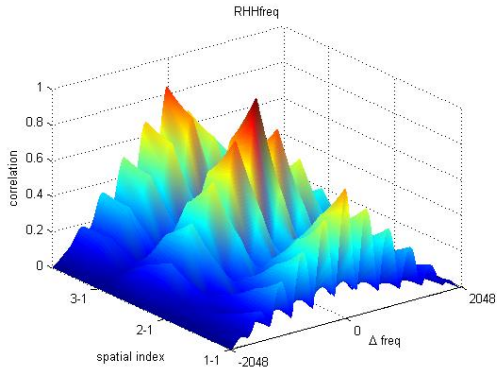

a) 3D correlation matrix

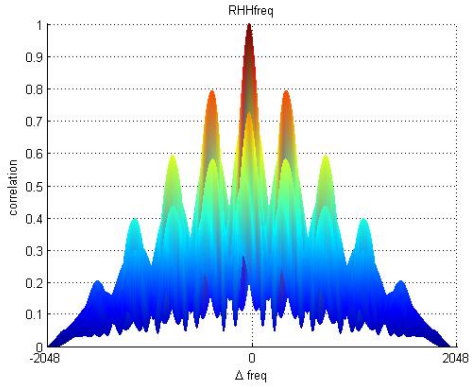

b) correlation versus $\Delta freq$

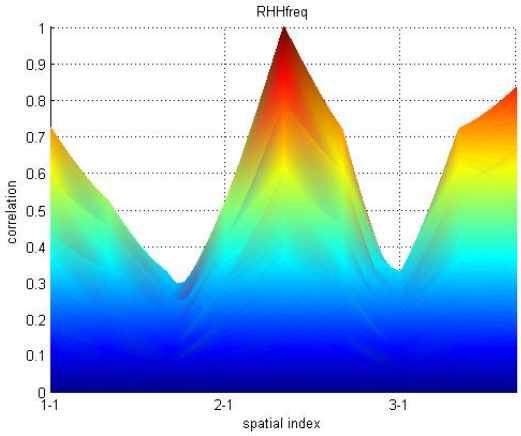

c) correlation versus space

Fig. **6-9**: 3D correlation matrix before equalization, g348 used, η = 0.993

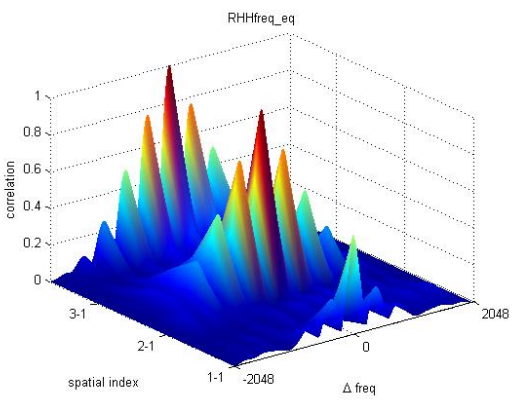

a) 3D correlation matrix

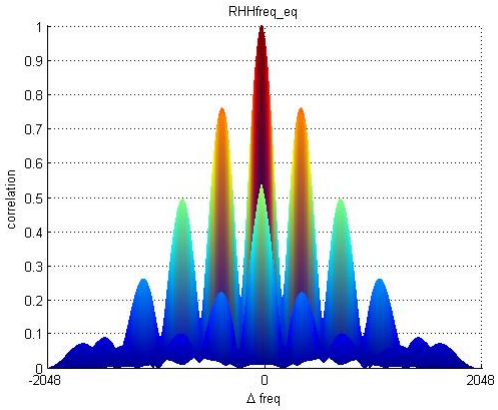

b) correlation versus $\Delta freq$

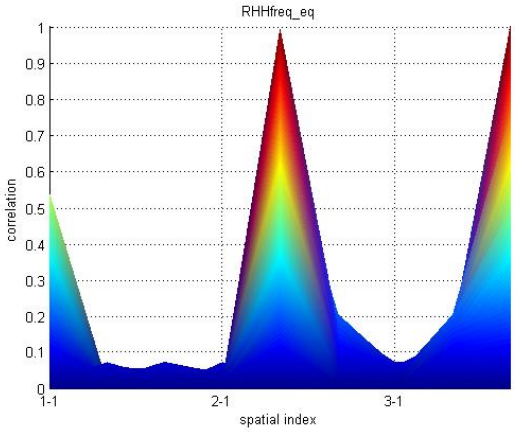

c) correlation versus space

Fig. **6-10**: 3D correlation after equalization, g348 used, η = 0.993, F4, N_f = 100, N_b = 12

6.2.4 SFBC h334

We evaluated test cases of h334 as outlined in Table **6-5**. In this case, G1 with sufficient guard interval already performs well enough, and naturally, having TEQs can only enhance spectral efficiency at the cost of SNR.

Table **6-5**: 3-by-3 MIMO cases with h334

No	η	TEQ	Occupied Bandwidth (double sided)
G1	0.958	Not used	17.39MHz
G2	Gaussian Channel		
G3	0.993	Used, $N_f = 100$, $N_b = 6$	16.77MHz
G4	0.993	Used, $N_f = 100$, $N_b = 9$	16.77MHz
G5	0.993	Used, $N_f = 100$, $N_b = 15$	16.77MHz
G6	0.993	Used, $N_f = 100$, $N_b = 21$	16.77MHz
G7	0.993	Used, $N_f = 100$, $N_b = 24$	16.77MHz

- R_b = 50Mbps, modulation: 16-PSK
- Spectral efficiency = 3 b/s/tone, fft size = 4096, number of subcarriers = 2008
- Perfect channel estimation at the receiver assumed, BS spacing = 10 λ

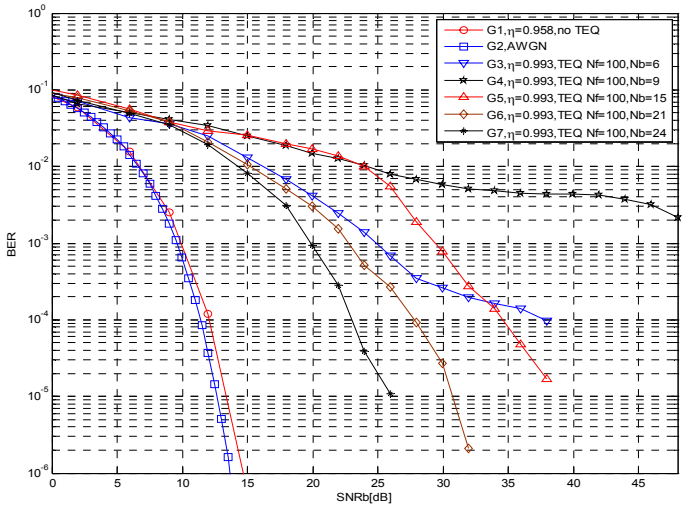

Fig. **6-11**: BER curves of 6 test cases with SFBC h334

6.3 Diversity on the GPS

Recently, there has been growing interest in navigational systems aiding or combined with wireless communication terminals. We begin our discussion with a brief tutorial on the Global Positioning System or GPS. GPS is a system for determining the location of terminals by signal broadcast from up to 29 satellites. Usually, a receiver sees 6 ~ 12 satellites simultaneously. Each satellite of the GPS systems sends data such that the receiver can determine its self-location. Among the data, the satellites send information about their location by sending almanac/ephemeris information such that the receiver can obtain both coarse and precise satellite information. Ephemeris data, showing the orbital information for the sender satellite and for every other satellite in the system, tell the GPS receiver where each GPS satellite should be at any time throughout the day. The almanac data contain information about the health status of the satellite, date and time. The data also include a propagation delay correction model and timing information, etc.

GPS satellites sends low power signals at L1 and L2 carriers, and the civilian GPS uses the L1 frequency at 1575.42 MHz. The GPS satellites send signals by BPSK modulation followed by a pseudo-random noise code and by the addition of navigation data messages. Signal spreading is done by two families of PN codes, either P (for precision) code or C/A (coarse/acquisition) code, where each distinctive PN code properties per satellite can be used to identify different satellites. Civilian applications use L1 and C/A code.

A GPS receiver typically consists of a GPS antenna, a BPF (bandpass filter), front-end LNA (low-noise amplifier), down-mixer, an LPF (low-pass filter), an ADC, followed by a digital baseband processor which incorporates a de-spreading device. In the acquisition mode, typical GPS receivers correlate the de-spread signal with a locally generated signal for one code period. By correlating with a number of correlators, the receiver decides on the code used and the Doppler.

A GPS terminal is basically a receiver, and the transmitters or satellites are all already fixed in terms of the system construction. Thus, our main interest lies only in the receiver sensitivity. We define the receiver sensitivity as the minimum signal power measured at the input to the bank of correlators such that a given SNR is obtained at the receiver output. Usually, GPS receivers work based on outage at certain SNR or C/No.

The satellite signals travel by LOS, penetrating through clouds, glass and plastic, but will not pass through most solid objects such as buildings, mountains, etc. There are signal-degrading channel impairments such as ionosphere and troposphere delays, signal multipath, receiver clock errors, orbital errors, etc. GPS sensitivity is usually bad in indoor environments or in urban canyons where buildings work as obstructions. To circumvent these problems, in the case of commercial applications such as GPS-equipped cell phones, there are techniques to either increase the correlator's integration time or to depend on frequency-domain signal processing schemes [56], but of course these techniques depends on the aiding data provided by the cellular network. Considering Fig. **1-1** and Fig. **1-2** again, it is more probable that our mobile military platform such as UAV and ground vehicles depend on the GPS system than the commercial applications of Fig. **1-2**. Indeed, the military depends on the GPS system for target tracing,

missile/bomb guidance, etc. In particular, when we consider an FSO/RF hybrid system as in Fig. **1-1**, we need the position information of each vehicle in order to establish optical links between the nodes. Even though there are RF links which can aid in the optical link acquisition, even the RF links need to somehow deliver position information between nodes. In order to seek higher GPS availability to meet the military specifications, one idea is to apply the MIMO concept to the GPS receivers. Of course, similar efforts have already been published, but most of them are focusing on either two-way NGO (non-geostationary orbit) satellite communications using LEO (low earth orbit) such as Globalstar satellites or Iridium satellites [**57**], or on satellite broadcasting systems [**58** - **59**]. In this section, our main concern is in combining a practical GPS channel model with diversity schemes without in-depth consideration of GPS signal processing methods. In the area of diversity for GPS, to the author's best knowledge, there are no significant research efforts, except for a US patent [**60**].

There are many channel models for GPS, but some times the GPS channels are regarded as a land mobile satellite (LMS) channel. Existing available statistical channel models for a narrowband LMS can be divided into two groups. In the single models, the channel is described by only one statistical distribution, whereas the mixture models use a weighted sum of several distinct distributions. Single models are usually used for stationary channel cases, whereas the mixture model is used for nonstationary cases. In the LMS channels, we encounter multipath fading (consists of a LOS component plus non-LOS scatter components) and shadow fading (either LOS shadow fading or multiplicative shadow fading). As we know, multipath fading occurs as a Rician

distribution. LOS shadow fading results from LOS blockage caused by buildings, trees, etc.

On the other hand, there are not many papers explicitly addressing the GPS channel fading model, except for [**61**], where the authors used one stationary reference receiver and one rover receiver to measure the GPS signal fading in C/No (carrier-to-noise ratio). Furthermore, given the measured fading data, the authors of [**61**] adopted the three-state fading model of Akturan and Vogel and suggested a GPS channel model represented by Eq. **6.27** and Eq. **6.28**.

$$f_v(v,\alpha) = C(\alpha) f_{Rice}(v) + S(\alpha) f_{Loo,shadowed}(v) + B(\alpha) f_{Loo,Blocked}(v),$$

α: elevation angle of satellite, v: received signal relative to the clear path signal Eq. **6.27**

$$f_{Loo}(v) = \frac{v}{b_0\sqrt{2\pi d_0}} \int_0^\infty \frac{1}{z} \exp\left[\frac{-(\log z - \mu)^2}{2d_0} - \frac{v^2 + z^2}{2b_0} \right] I_0(vz/b_0) dz \qquad \text{Eq. } \mathbf{6.28}$$

Of the published channel model results, we chose Eq. **6.27** ~ Eq. **6.28** as our reference channel model. There were several reasons for adopting this channel model. First, even though we can use two commercially available GPS receivers to evaluate the channel in either the C/No or the SNR sense, it needs significant data processing to subtract the clear-path signal portion from the overall received multipath faded signal. Second, there are many good results on satellite channels, but not specifically on GPS channels.

We chose two simple well-known receiver diversity schemes, or, selective combining and switched combining [**29**] for several reasons. First, since the GPS system is already deployed, there are not many options to modify the transmitter side, except for improving the receiver side. Second, for the maximal ratio combining or the equal gain combining scheme, it needs relatively accurate channel information estimation, whereas

the selective combining or the switched combining scheme offers easier performance enhancement methods.

One thing to note is that, given the C/No-based channel model of [**61**], we expect that this channel model is commensurate with the C/No values somewhere after the de-spreader and the correlator. Then, this C/No-based channel fade values are in direct relation to the GPS sensitivity. Also, since the C/No-based channel model is independent of the manufacturer-specific settings such as the correlator's integration time, etc, we expect that C/No is a fair metric to compare GPS receivers.

In Fig. **6-12**, we show the complementary cdf of the GPS channel model obtained from average of measurements made in Calgary and Vancouver with a satellite elevation angle of 35 degrees.

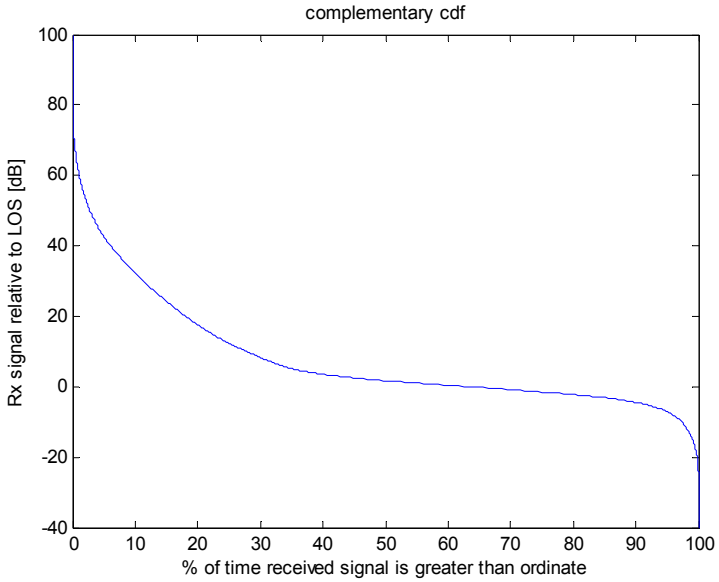

Fig. **6-12**: Complementary cdf of received signal level v

In Fig. **6-13**, we show selective combining results based on Fig. **6-12**, and we can see that compared with the L = 1 case, at cdf of 0.999, we have enhancements of approximately 3dB with L = 2, 4dB with L = 3, and 4.5dB with L = 4. We can say that a diversity GPS receiver with L = 2 and/or L = 3 will help.

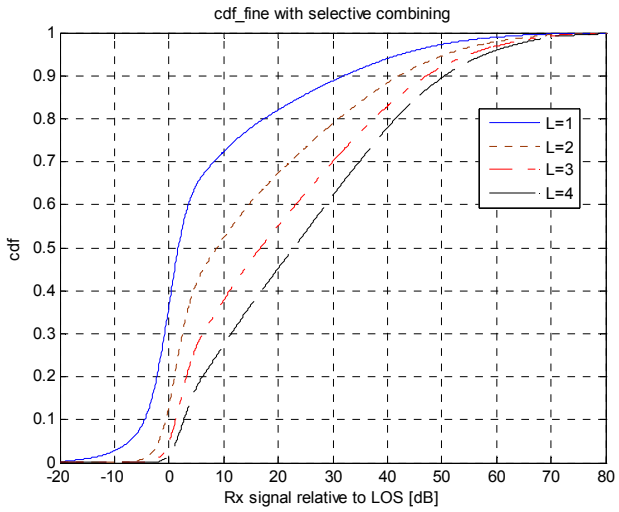

Fig. **6-13**: Selective combining scheme after GPS correlator bank. L: diversity order

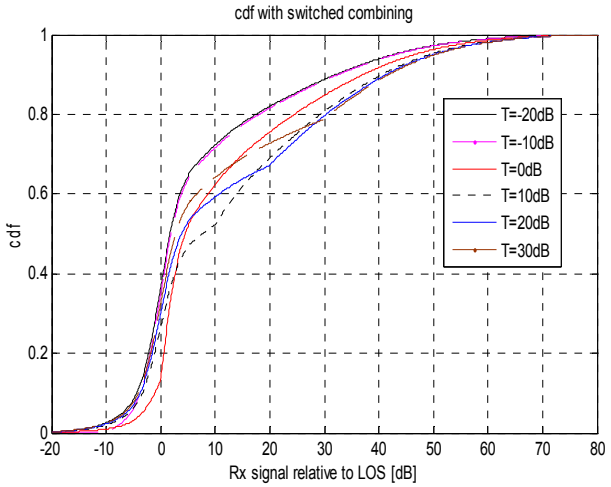

Fig. **6-14**: Switched combining scheme after GPS correlator bank. L: diversity order

In Fig. **6-14**, we show results of the switched combining scheme with various thresholds and with L = 2. At cdf of 0.999, we see an enhancement of 1.4dB from T = -20dB to 0dB, and 2.3dB from T = -20dB to 10dB.

6.4 Summary and Conclusions

In this chapter, as an extension of our previous investigations on the SISO/MIMO TEQ, we investigated the cases of higher order MIMO TEQ combined with space-frequency codes. Performance of the MIMO TEQ plus space-frequency coding depends on many factors. But unlike the case of 2-by-2 MIMO where it was not always easy to justify the use of MIMO TEQ, there are cases such as g8816, g848, and g348 where MIMO TEQ not only saves bandwidth, but also offers BER enhancement with thresholds in SNR. For other cases such as h334, we save bandwidth, but at the cost of higher SNR. In order to explain the simultaneous enhancement of BER and bandwidth, we presented 3D correlation matrices, and explained the new performance in terms of the changes in the correlation properties by channel shortening. However, since our MIMO-TEQ design was not derived with these channel correlation properties considered, we need more sophisticated analytical approaches where more factors are taken into account, in order to expect direct BER enhancement.

Chapter 7

FSO Filterbank Transceiver

In this chapter, we will extend the filterbank transceiver theory to optical implementations. We know that the filterbank transceiver concept originated in RF communications for its advantages related to subchannel approaches and capacity achievement. In contrast, FSO systems traditionally depend on single-carrier approaches, relying more on breakthroughs in optical enabling technologies than on DSP technologies. We can justify the use of multi-carrier or filterbank concepts in FSO in a couple of ways. One justification is resource efficiency. Even though the channel bandwidth is near infinite in FSO, the use of a truly wide bandwidth means implementation costs, too. Thus, even in FSO, we need some sort of resource efficiency. Another justification is the multi-rate diversity where streams of the same information but at different rates are transmitted as a means of diversity in the wavelet-packet modulation system [**15**][**38**][**51**][**64 - 66**]. Even though most existing wireless communications depend on real-time adaptation at the transmitter/receiver, blind equalization, and availability of channel information by channel estimation techniques, this is not always the best answer in military long-haul transmissions consisting of aerial vehicles and/or satellites, since techniques such as blind equalization and channel estimation are always accompanied by some errors. In particular, in military applications of future warfare, we not only need high throughput data transmission capability but also higher reliability than was ever possible. If we expect reliability beyond what is offered by current techniques of channel estimation and/or

blind equalization, we can justify the use of the feedforward multi-rate diversity system. Furthermore, given streams of different rates, we can pursue some sort of combining scheme. Streams of different rates can work equivalent to equalization.

In this chapter, we present a WPT filterbank-based FSO transceiver that depends on electro-optical and optical-electro conversions. In this design, the idea is that we use the divide-and-conquer rule in the FSO spectrum, as a way to better use the resources. Thus, each subchannel carries different information. In this chapter, we extended the algorithm proposed in [**34**] to FSO wireless communications.

7.1 General N-Subchannel Filterbank Transceiver Theory

Fig. **7-1** and its frequency-domain representation of Fig. **7-2** have been given to better represent the N-subchannel filterbank transceiver theory. Synthesis filters $G_i(z), i = 0...N-1$ are chosen to properly separate a subchannel spectrum such that it can be separated at the receiver using their matching analysis filters $F_i(z), i = 0...N-1$. Given N independent data streams $x_i[n], i = 0,..., N-1$, upsampling operation (or interpolation) by a ratio of M can be mathematically described by Eq. **7.1** in the time domain, and by Fig. **7-2** b) in the frequency domain. After addition of a noise term, filtering by $f_i[n]$, which has been designed to occupy the same band as $g_i[n]$, picks the subchannel signal $r_i[n]$ as in Eq. **7.3** or Fig. **7-2** c). Then, the downsampling or decimation operation can be expressed by Eq. **7.4** to yield $\hat{x}_i[n]$.

$$x_i^{\uparrow M}[n] = \begin{Bmatrix} x_i[n/M], n = 0, \pm M, \pm 2M, \ldots \\ 0, otherwise \end{Bmatrix}, i = 0, \ldots, N-1 \quad \text{Eq. } \mathbf{7.1}$$

$$x[n] = \sum_{i=1}^{NoSch} x_i^{\uparrow M}[n], \text{ NoSch: Number of subchannels} \quad \text{Eq. } \mathbf{7.2}$$

$$r_i[n] = (x[n] + n[n]) \otimes f_i[n] \quad \text{Eq. } \mathbf{7.3}$$

$$\hat{x}_i[n] = r_i[Mn] \quad \text{Eq. } \mathbf{7.4}$$

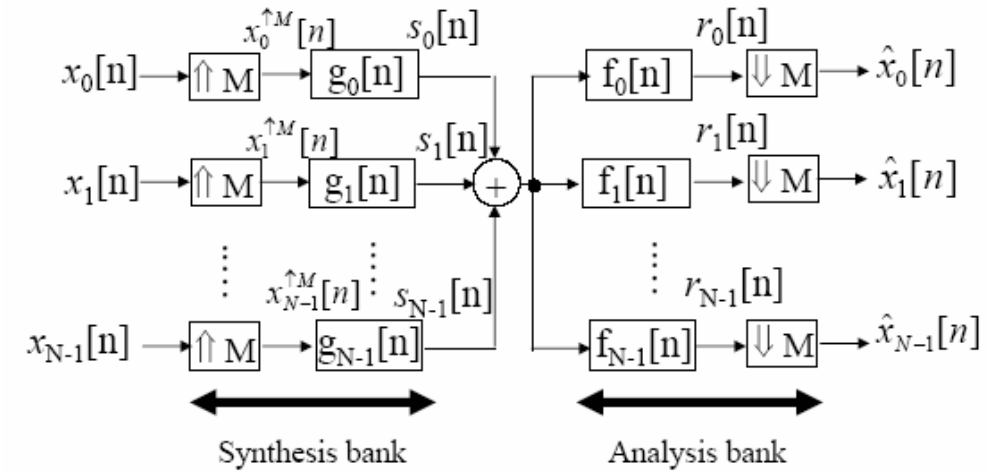

Fig. **7-1**: An N-subchannel filterbank transceiver, ⇑ M: upsampler, ⇓ 2: downsampler

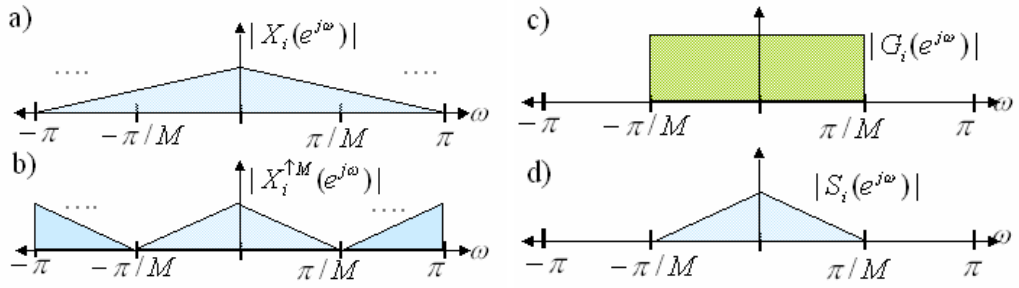

Fig. **7-2**: Representation of the synthesis bank's operations in the frequency domain a) transmit signal stream along the i[th] subchannel b) signal of a) upsampled by ratio of M c) transmit filter for the i[th] subchannel d) transmitted data on the i[th] subchannel

M does not have to be the same as N, but a system with M = N is said to be minimally interpolated and yields maximum spectral efficiency. Assuming an ideal AWGN channel, perfect reconstruction (PR) conditions are met by designing synthesis and analysis filters by Eq. **7.5**, which can actually be understood as a discrete-time convolution between $g_i[n]$ and $f_j[n]$ evaluated at kM .

$$\sum_n g_i[n] f_j[-n + kM] = M\delta[i - j]\delta[k], \qquad \text{Eq. 7.5}$$

n, k: integer, δ : Kronecker's delta function

Letting $f_i[n] = g_i^*[-n]$ as a discrete time matched filter, Eq. 7.5 can be further simplified to Eq. 7.6, which can be understood as a cross-correlation sequence between $g_i[n]$ and $g_j[n]$ at lag of kM . Eq. 7.6 tells that the synthesis filters are orthogonal to each other across both the subchannel index (unitary) and the time-shift of itself by kM . This orthogonality provides the basis of filterbank transmission.

$$\sum_n g_i[n] g_j^*[n - kM] = M\delta[i - j]\delta[k], \qquad \text{Eq. 7.6}$$

7.2 Wavelet Packet Tree Theory for Nonuniformly Spaced Filterbank Transceiver

Now, we can further extend our previous discussion to a more generalized case of a nonuniformly spaced filterbank transceiver. We can use a two-channel PR transmultiplexer structure, as a special form of Fig. 7-1, iteratively both in the transmitter and the receiver to form an arbitrary PR wavelet packet tree (WPT) as in Fig. 7-3. This means that there should be some mechanism of synchronization between the transmitter and the receiver in the sense of the filterbank structure.

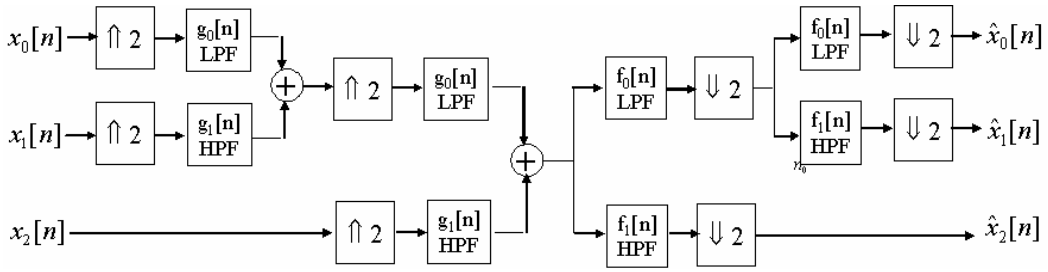

Fig. **7-3**: A 3-subchannel nonuniformly spaced filterbank transceiver formed by iterations of 2-subchannel transmultiplexer, D = 2

Whenever a subchannel is split, we have two more subchannels with half the original data rate. Fig. 7-4 is presented as an example of iteration. For better understanding, the synthesis filterbank of Fig. 7-4 has been given with more details in Fig. 7-5, with the upsamplers, LPFs and HPFs shown.

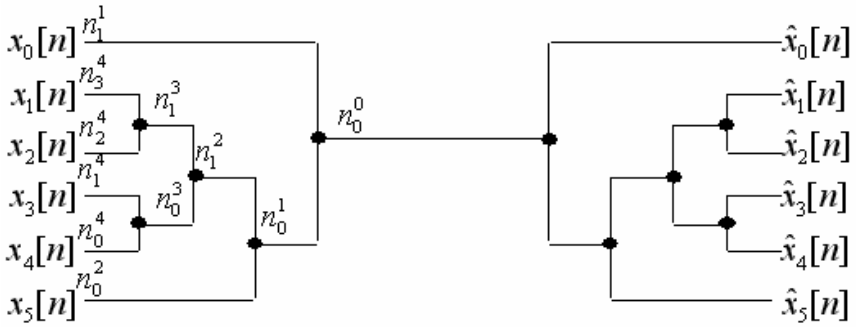

Fig. **7-4**: A 6-subchannel WPT transmultiplexer with D = 4

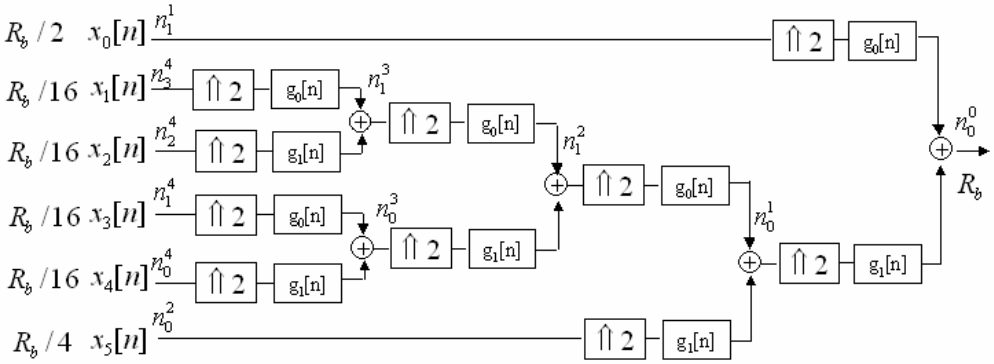

Fig. **7-5**: Synthesis filterbank of Fig. **7-4** with upsamplers and filters. $g_0[n]$: LPF, $g_1[n]$: HPF

Letting m be the total number of nodes, we can find the total number of rooted ordered binary trees on m nodes by Eq. 7.7.

$$b_m = \frac{1}{m+1}\binom{2m}{m} \qquad \text{Eq. } \mathbf{7.7}$$

Another factor to consider is maximum depth of iteration D, since it is related to the maximum system delay through the transmultiplexer, and specifies the maximum sampling rate needed. Now, with D as the constraint, we can find the cardinality γ_D defined as the size of the set Θ_D iteratively by Eq. 7.8. That is, given a complete WPT of depth D, we can find the size of all possible subtrees or WPTs of depth smaller than or equal to D. Table **7-1** has been provided for better understanding of the concepts of WPT.

$$\gamma_j = \gamma_{j-1}^2 + 1, \gamma_0 = 1 \qquad \text{Eq. } \mathbf{7.8}$$

Table **7-1**: Definitions for WPT

Term	Description
Node n_i^j	point of branch interconnection, j: scale or depth, $0 \le j \le D$, i: index assigned from top to bottom,
N	number of subchannels
M	number of nodes, m = N-1
Branch	one of the arms at any division points
D	maximum depth of iteration
θ_D	a single complete WPT of depth D
Θ_D	the set of all subtrees of a specific θ_D, with elements τ

7.3 Equivalent Branch Filters

In Fig. **7-4**, we iteratively employed upsampler/downsampler and filters to obtain a WPT by some optimality criterion. Another way to represent the WPT in a simpler way is by the equivalent branch filter concept as shown in Fig. **7-6**. In order to simplify WPT, we need to use the Noble identities. The Noble identities basically show how it is possible in digital signal processing to switch the location between an upsampler/downsampler and a filter. An example of the Noble identities has been shown graphically in Fig. **7-7** to move the sampler/downsampler back and forth.

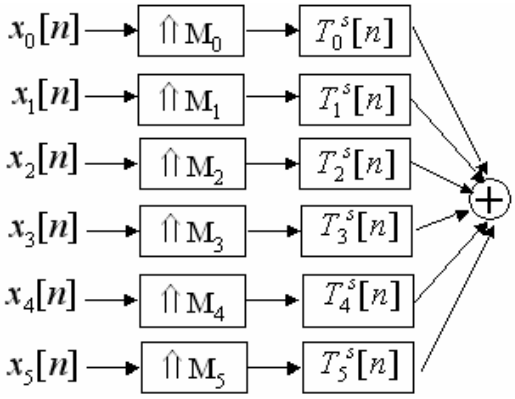

Fig. **7-6**: An alternative presentation of the synthesis filterbank part of Fig. **7-4** using equivalent branch filters

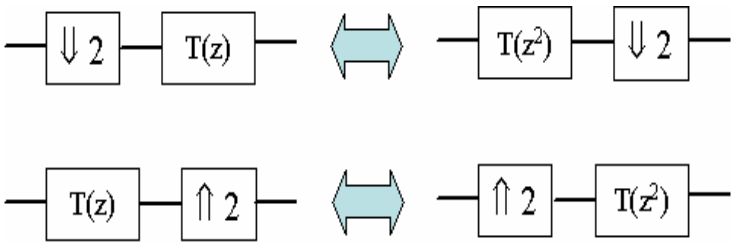

Fig. **7-7**: Noble identities

From Fig. **7-5**, we can see that data streams of different bit rates are assigned to subchannels. Assume that the sequence of synthesis filters from the root node n_0^0 to a specific node $n_i^j, 0 \le j \le D$ is given sequentially in the z-transform domain by $G^{i,k}(z)$, $0 \le k \le j-1$, $G^{i,k}(z) \in \{G_0(z), G_1(z)\}$. Then, we can apply the Noble identity to each subchannel iteratively to find the equivalent branch filter and the upsampler spanning n_0^0 through $n_i^j, 0 \le j \le D$ by Eq. **7.9.**

$$T_i^s(z) = \prod_{k=0}^{j-1} G^{ik}(z)(z^{2^k}),\ M_i = 2^j,\ 0 \le i \le N-1 \qquad \text{Eq. } \mathbf{7.9}$$

As an example, $T_5^s(z)$ of Fig. **7-6** can be found by following the steps of Fig. **7-8**, in accordance with Eq. **7.9**.

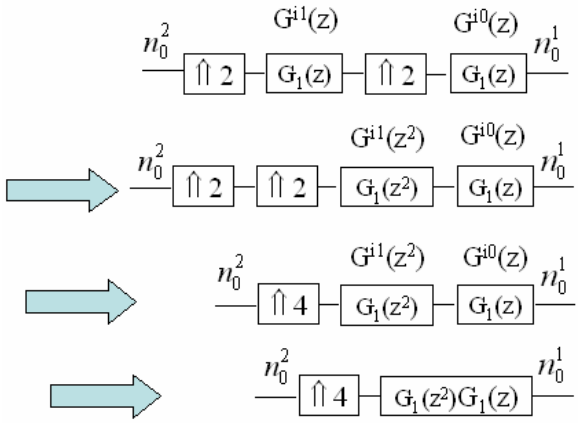

Fig. **7-8**: Noble identities applied to the fifth subchannel of Fig. **7-4** and Fig. **7-5**

7.4 Optical Wavelet Packet Modulation with Signal to Interference plus Noise Ratio Criterion

With this knowledge, now we need to somehow structure the transmultiplexer by some optimality criterion. Considering that cardinality γ_D calculated by Eq. 7.8 is huge, we need a computation algorithm to reasonably minimize some selected criterion with reasonable computational complexity to find τ_{opt}. The criterion of our choice is signal to interference plus noise ratio (SINR) [**34**]. At the receiver, after the receiver filterbank but before the decision devices, $\hat{X}_i[n]$ is interfered by 1) ISI from $\hat{X}_i[k], k \neq n$ 2) ICI from $\hat{X}_j[n], j \neq i$ and 3) additive noise $n[n]$. SINR is defined by Eq. 7.10, where the

definitions in Eq. 7.11 and Eq. 7.12 are used. Based on Eq. 7.10, the average SINR across subchannels can be found as in Eq. 7.13.

$$SINR_i = \sigma_{X_i}^2 / \sigma_{I_i}^2 \ , i = 0...N-1 \qquad \text{Eq. } \mathbf{7.10}$$

$$\sigma_{I_i}^2 = E\left[\left|\hat{X}_i[n] - X_i[n]\right|^2\right] \qquad \text{Eq. } \mathbf{7.11}$$

$\sigma_{X_i}^2$: transmit symbol power on the ith subchannel Eq. **7.12**

$$SINR_{av} = \frac{1}{N}\sum_{i=0}^{N-1} SINR_i \qquad \text{Eq. } \mathbf{7.13}$$

We can employ a tree structuring algorithm based on random OOK training sequence. Training sequences of proper lengths are launched on subchannels, and $SINR_{av}$ is evaluated as in Table **7-2**.

Table **7-2**: Tree structuring algorithm [**34**]

Step 1: Let $\tau = \theta_0$. Measure $SINR_{av}$ by transmitting a random training sequence.

Step 2: For each terminal node of current τ, $n_i^j, j < D, i = 0....$, perform node splitting one by one to obtain $\tau'_{i,j}$. Measure $SINR'_{av\,i,\,j}$ for each case.

- $_{i,j}$: denotes the node position where splitting occurs tentatively
- $'$: denotes 'tentative'

Step 3: Calculate $\Delta SINR_{av\,i,j} \underset{=}{\Delta} SINR'_{av\,i',\,j+1} - SINR_{av\,i,\,j}$ for each terminal node

Step 4: Find $n_i^j, j < D, i = 0....$ where the splitting gives maximum $\Delta SINR_{av\,i,j}$ over i,j. Update as $\tau \leftarrow \tau'_{i,j}$ and $SINR_{av} \leftarrow SINR'_{av\,i,\,j}$

- If more than one terminal node give maximum increase of SINR when split, then split all such terminal nodes
- If $\Delta SINR_{av\,i,j} \le 0$, exit the algorithm

Step 5: Go to Step 2

Conceptually, we can explain the WPT algorithm by its analogy to the water-filling theorem [**26**]. In water-filling, the transmitter needs CSI. Water-filling then assigns

more power to the subchannels with higher GNR (gain-to-noise ratio). Likewise, in a WPT, we re-structure both the synthesis filterbank and the analysis filterbank iteratively, in the direction of higher $SINR_{av}$. In the same way that assigning more power to subchannels with higher GNR gives higher capacity, increased $SINR_{av}$ gives enhanced overall BER.

There are also dissimilarities, however. We know that the water-filling of subchannels is mostly understood in its relation to the OFDM technology, since the OFDM with an infinite number of subchannels is approaching the channel capacity. Now, the water-filling theorem never considers the existence of ISI and ICI in the OFDM systems. In particular, when there is frequency offsets, there is ICI, even though we used a subchannel orthogonality property. In addition, when the guard sequence length is not sufficient for any reason, we do have ISI in OFDM as well. In this sense, the WPT algorithm is an algorithm that offers not the theoretical performance bound, but a practical method to mimic the water-filling operation by filterbank operations.

Another difference is that the OFDM technique with a sufficient guard sequence is ISI-resistant, whereas the WPT technique is not. Therefore, the WPT algorithm may need equalization.

The presence of ICI and ISI in WPT is evident from the following explanation. Mathematically, from Fig. **7-9**, using Eq. **7.14**, the received signal after the filterbank can be given by Eq. **7.15** and Eq. **7.16**. From Eq. **7.15**, the first term represent the desired term, the second term ISI, the third term ICI, and the fourth one the noise term. We can further simplify the third part of Eq. **7.16** to Eq. **7.17**, where χ represents the

combined power of ICI and ISI. Eq. **7.17** can be further decimated. Eq. **7.18** describes the downsampling operation.

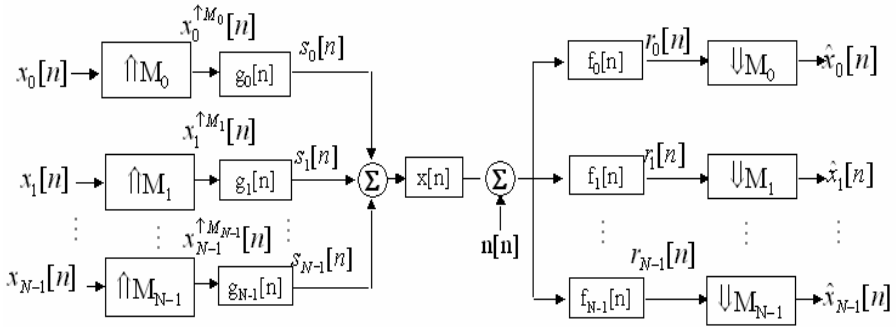

Fig. **7-9**: An N-subchannel WPT with nonuniform spectral decomposition, dispersive channel, and additive noise

$$gxf_{ij} \underset{=}{\Delta} g_i[n] * x[n] * f_j[n], i = 0...N-1 \qquad \text{Eq. } \mathbf{7.14}$$

$$\begin{aligned} r_i[n] &= \sum_{k=0}^{N-1} (x_k^{\uparrow M_k}[n] * gxf_{ki}[n]) + v[n] \\ &= x_i^{\uparrow M_i}[n] * gxf_{ii}[n] + \sum_{k=0,k\neq i}^{N-1} x_k^{\uparrow M_k}[n] * gxf_{ki}[n] + n[n] * f_i[n] \\ &= \sum_{k=0}^{N-1} \sum_m x_k^{\uparrow M_k}[n-m] gxf_{ki}[m] + v[n] \\ &= \sum_m x_i^{\uparrow M_i}[n-m] gxf_{ii}[m] + \sum_{k=0,k\neq i}^{N-1} \sum_p x_k^{\uparrow M_k}[n-p] gxf_{ki}[p] + n[n] * f_i[n] \\ &= x_i^{\uparrow M_i}[n] gxf_{ii}[0] + \sum_{m\neq 0} x_i^{\uparrow M_i}[n-m] gxf_{ii}[m] \\ &+ \sum_{k=0,k\neq i}^{N-1} \sum_p x_k^{\uparrow M_k}[n-p] gxf_{ki}[p] + n[n] * f_i[n] \end{aligned} \qquad \text{Eq. } \mathbf{7.15}, \text{ Eq. } \mathbf{7.16}$$

$$r_i[n] = x_i^{\uparrow M_i}[n] gxf_{ii}[0] + \chi + v[n] \qquad \text{Eq. } \mathbf{7.17}$$

$$\hat{x}_i[n] = r_i[M_i n] \qquad \text{Eq. } \mathbf{7.18}$$

7.5 Results

In this section, we used a channel model presented in chapter 2. Using this channel model, referring to the methods of [**34**], we tested the algorithm outlined in Table **7-2** to find the best tree under D = 3 constraint, using the biorthogonal wavelet as the basis of WPT. Besides, we also obtained results from the direct application of all possible tree structures under D = 3 constraints presented in Fig. **7-12**. This result was found to match those in Fig. **7-10** Thus, we assume that the algorithm in Table **7-2** has been validated in FSO to some extent, too. The WPT results in Fig. **7-10** show that the subchannel 1 of a lower magnitude but of a wider bandwidth is assigned for ω of up to 1, which is characterized by high distortion but less attenuation. However, for ω>1, which is characterized by severer attenuation but a relatively flat frequency response, subbands 2 ~ 5 of equal widths are assigned. Now, we also further released the constraint from D = 3 to D = 5 under the same channel condition to obtain the results shown in Fig. **7-13** and Fig. **7-14**. Compared with Fig. **7-11**, we can say that the band of higher frequency has been subdivided into narrower subchannels.

However, the WPT results so far are hard to be analytically explained. As we pointed out earlier, the algorithm itself drives seeking to minimize the combined power of ISI and ICI. Given ISI, the algorithm runs toward more splitting, thus decreasing the ISI power but simultaneously increasing the ICI power. Finally, at a certain point, the combined power of ISI and ICI neither increases nor decreases, thus terminating the algorithm. One thing to note is that, as the authors of [**34**] pointed out, we can compare

the results of the WPT algorithm with the manual splitting results of D=3, and be assured to some extent that the WPT algorithm works. But in a strict sense, it is more probable that we need a more sophisticated algorithm with memory which traces the trellis, similar to the Viterbi algorithm.

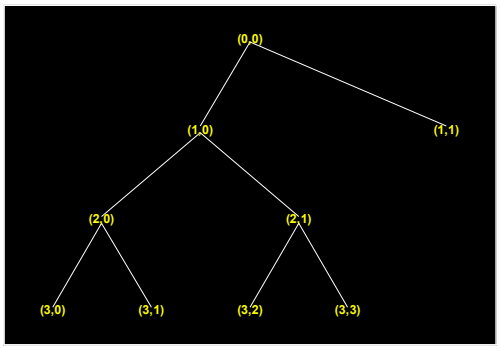

Fig. **7-10**: Tree structure obtained from optimal tree structuring algorithm with D = 3, τ = 10, link length = 1000m. Left: highfrequency domain frequency. Right: low frequency

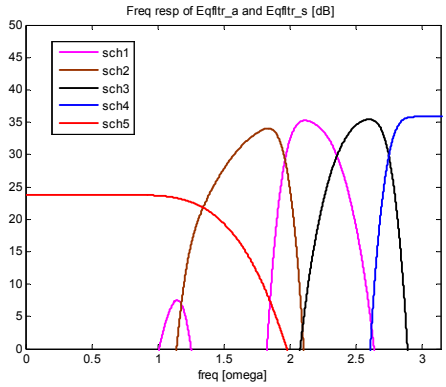

Fig. **7-11**: Optimal WPT with D = 3 in the

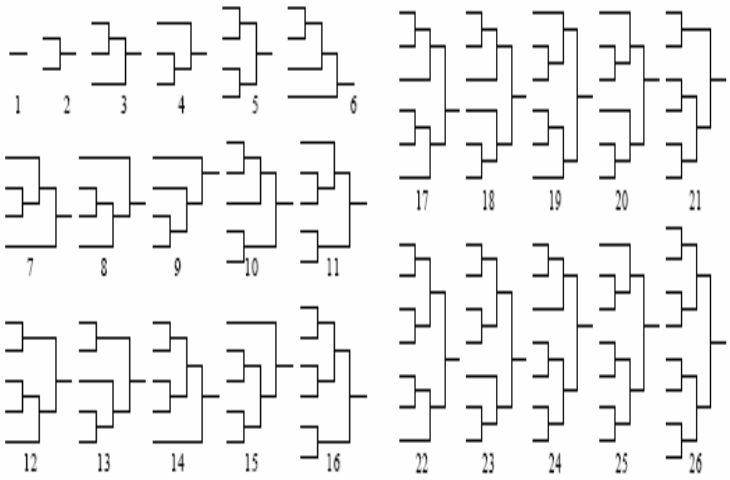

Fig. **7-12**: Trees Θ_3 with D = 3

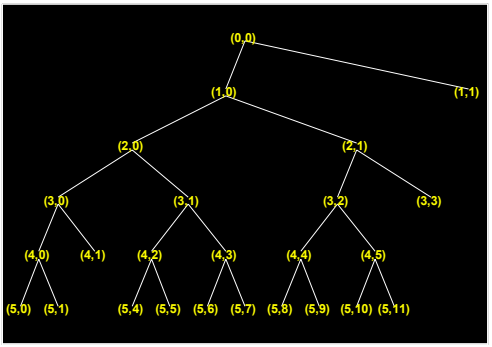

Fig. **7-13**: Tree structure obtained from optimal tree structuring algorithm with D = 5, τ = 10, link length = 1000m

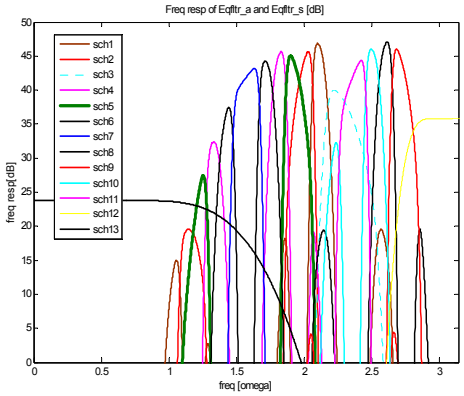

Fig. **7-14**: Optimal WPT with D = 5 in the frequency domain.

7.6 Summary and Conclusions

In this chapter, we introduced and justified the concept of filterbank transceivers in FSO. Similar to the RF OFDM technique, we applied the theories of filterbank transceiver and nonuniformly-spaced WPT to the FSO. We verified that the WPT algorithm which was originally derived for a DSL channel can be likewise applied to the FSO channel.

For further investigations, first we need to analytically verify that the SINR algorithm always returns the optimal WPT in strict senses. If not, we may need an iterative algorithm with memory which traces and saves all possibilities of $SINR_{av}$, as in the Viterbi algorithm. Second, while the OFDM design is relatively free from ISI due to the presence of a guard interval, WPT is not immune from ISI. Therefore, we need a channel equalizer. Besides, as OFDM needs FDE as a countermeasure against ICI, we

need to combat ICI in WPT, too. But there are no definite answers about the best ICI-equalization schemes for WPT, yet. Furthermore, it needs to be clearly explained if the WPT algorithm can still give us benefits even at the costs of equalization for ICI and ISI.

Chapter 8

Conclusions

In this chapter, the author would like to summarize, draw conclusions, and propose future research topics.

In this thesis, we approached the FSO/RF hybrid systems in the context of signal processing schemes through DSP technologies. Even though the FSO/RF hybrid systems have certain advantages for both military and commercial applications, proper signal processing schemes have yet to come. Therefore, rather than focusing on channel modeling efforts, we introduced existing channel models, and focused on developing signal processing schemes.

Since the military air-to-ground FSO link is highly dispersive, we introduced the TEQ which was traditionally investigated in landline environments such as DSL or cable internet. We evaluated the TEQ performance of various design methods in various metrics in the FSO channel. We also evaluated the BER of a TEQ-plus-Viterbi equalizer scheme, and the results showed that the proposed receiver could work relatively well at low-to-mid optical thickness. These results gave us insight into how to design the TEQ properly, and into the highs and lows of representative TEQ algorithms.

We also suggested a method to model the channel estimation errors, and evaluated the BER performance under channel estimation errors. When compared with the results from DFEs under channel estimation errors, the results showed that the TEQ is more sensitive to channel estimation errors than the DFE, although the TEQ surely has

advantages in the BER performance. As a countermeasure, based on the model of channel estimation errors, we calculated the TEQ adaptation intervals.

We also showed results from conceptual investigations on how to use a waveform shaping apparatus as an optical frequency domain equalizer. Besides, we extended a WPT-based spectrum division algorithm to FSO and presented the results. This algorithm, an alternative to the existing block-based transmission schemes such as OFDM, has certain highs and lows. Most of all, proper ways of equalization against ISI and ICI have yet to come for WPT algorithms.

On the RF link, we adopted an 802.20 channel model, and built a system based on the techniques such as MIMO-OFDM, MIMO-TEQ and space-frequency block codes. When applied to a MIMO-OFDM link, the MIMO-TEQ not only offers an advantage of enhancing spectral efficiency, but also has the property of changing the 3D correlation matrix in the frequency/spatial domain. Thus, depending on the capability of the MIMO-TEQ in terms of SCIR length and channel correlation, we could see enhancement in BER or not. We further examined this statement by testing with various linear space-frequency block codes. Significant efforts were also made in this thesis to review the formulas of the existing literature, and in presenting them in a unified end-to-end framework. We could find some test cases where the presence of TEQs helped enhance not only the spectral efficiency but also the BER performance.

As for the conclusions, the TEQ is most advantageous in highly dispersive channels such as FSO channels. In the wireless RF channels, where the delay spread is not that severe, it depends on many factors. For RF SISO channels, TEQ offers the possibility of enhanced spectral efficiency for OFDM links, but at the cost of SNR. For

RF MIMO links, the performance depends on how the shortened MIMO channel works together with the space frequency block codes used.

For future research, the author suggests several topics. First, there is research interest in optimization. For instance, even though the hybrid link truly offers benefits, once we have more constraints such as transmit power considered on top of the physical channel determined by the weather conditions, we will need ways to make smart decisions. In particular, since the aerial vehicles are limited in terms of power availability, we can extend this to a routing problem on a cooperative network. In this sense, the author proposes research on network layer algorithms where many stations are involved. One good method is cross-layer optimization. Second, whereas the author depended on Monte Carlo simulations mostly due to the system complexity, the investigations in this thesis can be further extended to analytical approaches. Third, there can be ways that we can change the channel's correlation properties as desired, and the author would like to propose this as a countermeasure to improve the channel correlation properties when the MIMO receive antennas are closely located.

Bibliography

1. Koen Vanbleu, "Advanced Equalization Techniques for DMT-Based Systems," Ph.D. dissertation, Katholieke Universiteit Leuven, Oct 2004.

2. John G. Proakis, "Digital Communications," 4th edition, McGraw-Hill, Boston, 2001.

3. M. Kavehrad and J. Salz, "Cross-polarization cancellation and equalization in digital transmission over dually polarized multipath fading channels," AT&T Technical Journal, Vol. 64, No.10, pp. 2211 - 2245, Dec 1985.

4. D. D. Falconer and F. R. Magee, "Adaptive channel memory truncation for maximum likelihood sequence estimation," Bell Sys. Tech. Journal, Vol. 9, pp. 1541 - 1562, Nov 1973.

5. P. J. W. Melsa, R. C. Younce and C. E. Rohrs, "Impulse response shortening for discrete multitone transceivers," IEEE Transactions on Communications, Vol. 44, Issue 12, pp. 1662 - 1672, Dec 1996.

6. N. Al-Dhahir and J. M. Cioffi, "Optimum finite-length equalization for multicarrier transceivers," IEEE Transactions on Communications, Vol. 44, No. 1, pp. 56 - 64, Jan 1996.

7. M. V. Bladel and M. Moenceclay, "Time-domain equalization for multicarrier communications," Proc. IEEE Global Telecom. Conf., pp. 167 - 170, Nov 1995.

8. N. Al-Dhahir and J. M. Cioffi, "A bandwidth-optimized reduced-complexity equalized multicarrier transceiver," IEEE Transactions on Communications, Vol. 45, No. 8, pp. 948 - 956, Aug 1997.

9. R. Schur, J. Speidel and R. Angerbauer, "Reduction of guard interval by impulse compression for DMT modulation on twisted pair cables," Proc. IEEE Global Telecom. Conf., Vol. 3, pp. 1632 - 1636, San Francisco, CA, USA, Nov 2000.

10. M. Milosevic, L. F. C. Pessoa and B. L. Evans, "Simultaneous multichannel time domain equalizer design based on the maximum composite shortening SNR," Conference Record of the Thirty-Sixth Asilomar Conference on Signals, Systems and Computers, Vol. 2, pp. 1895 - 1899, Pacific Grove, CA, USA, 3 - 6 Nov 2002.

11. Haiping Wu, "A Case Study on Multiple-Input Multiple-Ouput (MIMO) Communication Systems," Ph.D. dissertation, The Pennsylvania State University, Dec 2005.

12. H. Weichel, “Laser Beam Propagation in the Atmosphere,” SPIE Optical Engineering Press, Bellingham, WA, 1990.

13. E. A. Bucher, “Computer simulation of light pulse propagation for communication through thick clouds," Applied Optics, Vol. 12, pp. 2391 - 2400, Oct 1973.

14. T. Light, D. M. Suszcynsky, M. W. Kirkland and A. R. Jacobson, “Simulations of lightning optical waveforms as seen through clouds by satellites," Journal of Geophysical Research, pp. 17103 - 17114, Aug 2001.

15. Belal Y. Hamzeh, “Multi-rate wireless optical communications in cloud obscured channels,” Ph.D. dissertation, The Pennsylvania State University, Dec 2005.

16. A. P. Ciervo, “Propagation through optically thick media," Applied Optics, Vol. 34, pp. 7137 - 7148, Oct 1995.

17. J. S. Chow, J. C. Tu and J. M. Cioffi, “A discrete multitone transceiver system for HDSL applications,” IEEE Journal on Selected Areas in Communications, Vol. 9, No. 6, pp. 895 – 908, Aug 1991.

18. T. Keller and L. Hanzo, “Adaptive multicarrier modulation: A convenient framework for time-frequency processing in wireless communications,” Proceedings of IEEE, Vol. 88, No. 5, pp. 611 – 640, May 2000.

19. Z. Wang and G. B. Giannakis, “Wireless multicarrier communications,” IEEE Signal Processing Magazine, Vol. 17, No. 3, pp. 29 – 48, May 2000.

20. H. Rohling, T. May, K. Bruninghaus and R. Grunheid, “Broad-band OFDM radio transmissions for multimedia applications,” Proc. IEEE, Vol. 87, No. 10, pp. 1778 – 1789, Oct 1999.

21. David Falconer, Sirikiat Lek Ariyavisitakul, Anader Benyamin-Seeyar and Brian Eidson, “Frequency Domain Equalization for Single-Carrier Broadband Wireless Systems,” IEEE Communications Magazine, pp. 58 – 66, Apr 2002.

22. S. Arnon, D. Sadot and N. S. Kopeika, “Analysis of optical pulse distortion through clouds for satellite to earth adaptive optical communication,” Journal of Modern Optics, Vol. 41, No. 8, pp. 1591 - 1605, Aug 1994.

23. G. Mooradian and M. Geller, “Temporal and Angular Spreading of Blue – Green Pulses in Clouds,” Applied Optics, Vol. 21, No. 9, pp. 1572 – 1577, May 1982.

24. G. Mooradian, M. Geller, L. Stotts, D. Stephens and R. Krautwald, “Blue-green pulsed propagation through fog,” Appl. Opt., Vol. 18, No. 4, pp. 429 – 441, Feb 1979.

25. R. Elliot, "Multiple Scattering of Optical Pulses in Scale Model Clouds," Applied Optics, Vol. 22, No. 17, Sep 1983.

26. C. Fragouli, N. Al-Dhahir, S. N. Diggavi and W. Turin, "Prefiltered space-time M-BCJR equalizer for frequency-selective channels," IEEE Transactions on Communications, Vol. 50, Issue 5, pp. 742 – 753, May 2002.

27. 802.20 Ch Modeling SubGroup, (Sep 6 2005) "802.20 Channel Models Document for IEEE 802.20 MBWA System Simulations – 802.20-PD-08," [Online] Available: http://grouper.ieee.org/groups/802/20/P_Docs/IEEE_802.20-PD-08.doc.

28. Laurent Schumacher, Jean Philippe Kermoal, Frank Frederiksen, Klaus I. Pedersen, Albert Algans and Preben E. Mogensen, (Feb 8 2001), "IST-1999-11729 METRA D2 MIMO Channel Characterization," [Online] Available: http://www.ist-imetra.org/metra/deliverables/AAU-WP2-D2-V1.1.pdf.

29. Gordon L. Stuber, "Principles of Mobile Communication," 2nd edition, Springer, 2001

30. Naofal Al-Dhahir, "FIR Channel-Shortening Equalizers for MIMO ISI Channels," IEEE Transactions on Communications, Vol. 49, No. 2, pp. 213 – 218, Feb 2001.

31. Mohinder Jankiraman, "Space-Time Codes and MIMO Systems", Artech House Publishers, 2004.

32. Hamid Jafarkhani, "Space-Time Coding: Theory and Practice", Cambridge University Press, 2005.

33. Siavash M. Alamouti, "A Simple Transmit Diversity Technique for Wireless Communications," IEEE Journal On Select Areas In Communications, Vol. 16, No. 8, pp. 1451 – 1458, Oct 1998.

34. Donnacha Daly, "Efficient Multi-Carrier Communication on the Digital Subscriber Loop", Ph.D. dissertation, University College Dublin National University of Ireland, May 2003.

35. Xiaoming Zhu and Joseph M. Kahn, "Free-Space Optical Communication Through Atmospheric Turbulence Channels," IEEE Transactions on Communications, Vol. 50, No. 8, pp. 1293 – 1300, Aug 2002.

36. Xiaoming Zhu and Joseph M. Kahn, "Performance Bounds for Coded Free-Space Optical Communications," IEEE Transactions on Communications, Vol. 51, No. 8, pp. 1233 – 1239, Aug 2003.

37. Xiaoming Zhu and Joseph M. Kahn, "Markov Chain Model in Maximum-Likelihood Sequence Detection for Free-Space Optical Communication Through Atmospheric Turbulence Channels," IEEE Transactions on Communications, Vol. 51, No. 3, pp. 509 – 516, Mar 2003.

38. M. Kavehrad and B. Hamzeh, "Laser Communication System Using Wavelet-Based Multi-Rate Signaling," Proceedings of IEEE MILCOM, Monterey, CA, USA, Nov 2004.

39. B. Hamzeh and M. Kavehrad, "Free Space Optics Supporting Multi-user Communications for Wireless Mesh Networks," Proceedings of Optics East, Philadelphia, PA, USA, Oct 2004.

40. S. Lee and M. Kavehrad,"Airborne Laser Communications with Impulse Response Shortening and Viterbi Decoding," Proceedings of the IEEE MILCOM, Washington, D.C., USA, Oct 2006.

41. M. M. Wefers and K. A. Nelson, "Analysis of programmable ultra-short waveform generation using liquid-crystal spatial light modulators," Journal of the Optical Society of America B, Vol. 12, No. 7, pp.1343 - 1362, Jul 1995.

42. A. Efimov, C. Schaffer and D. H. Reitze, "Programmable shaping of ultrabroad-bandwidth pulses from a Ti:sapphire laser," Journal of the Optical Society of America B, Vol. 12, No. 10, pp.1968 - 1980, Oct 1995.

43. A. M. Weiner, "Femtosecond optical pulse shaping and processing," Progress in Quantum Electronics, v. 19, pp. 161 - 237, 1995.

44. M. M. Wefers and K. A. Nelson, "Space-time profiles of shaped ultrafast optical waveforms," IEEE Journal of Quantum Electronics, Vol. 32, No. 1, pp. 161 - 172, 1996.

45. K. Takasago, M. Takekawa, M. Suzuki, K. Komori and F. Kannari, "Evaluation of femtosecond pulse shaping with low-loss phase-only masks," IEEE Journal of Selected Topics in Quantum Electronics, Vol. 4, No. 2, pp. 346 - 352, 1998.

46. A. M. Weiner and A. M. Kan'an, "Femto-second pulse shaping for synthesis, processing and time-to-space conversion of ultra-fast optical waveforms," IEEE Journal of Selected Topics in Quantum Electronics, Vol. 4, No. 2, pp. 317 - 331, 1998.

47. S. Jivkova, B. Hamzeh and M. Kavehrad, "Pulse Shaping for Ultrashort Pulsed FSO Communications Systems," Proceedings of WMSCI'05, Orlando, FL, USA, Jul 2005.

48. Wikipedia, (Jan 1 2007) "Moore's law" [Online] Available: http://en.wikipedia.org/wiki/Moore's_law#_note-SSCSnewsletterSept06.

49. C. A. Eldering, M. L. Sylla and J. A. Eisenach, "Is there a Moore's law for bandwidth?," IEEE Communications Magazine, Vol. 37, Issue 10, pp. 117 - 121, Oct 1999.

50. Naofal Al-Dhahir and Ali H. Sayed, "The Finite-Length Multi-Input Multi-Output MMSE-DFE," IEEE Transactions on Signal Processing, Vol. 48, No. 10, pp. 2921 - 2936, Oct 2000.

51 S. M. Navidpour, B. Hamzeh and M. Kavehrad, "Multi-rate fractal free space optical communications using Fountain codes," Proceedings of Optics East, Boston, MA, USA, Oct 2005.

52. Y. Alqudah and M. Kavehrad, "On Optimum Order of Angle Diversity with Maximal Ratio Combining Receivers for Broadband Indoor Optical Wireless Communications," Annual Review of Communications, Vol. 57, ISBN: 1-931695-28-8, Nov 2004.

53. M. Kavehrad and S. Jivkova, "Indoor Broadband Optical Wireless Communications: Optical Subsystems Designs and Their Impact on the Channel Characteristics," IEEE Wireless Communications Magazine, Vol. 10, No. 2, pp. 30 - 35, Apr 2003.

54. K. Akhavan, M. Kavehrad and S. Jivkova, "High Speed Power Efficient Indoor Wireless Infrared Communication Using Code Combining, PART- I," IEEE Transactions on Communications, Vol. 50, No. 7, Jul 2002.

55. K. Akhavan, M. Kavehrad and S. Jivkova, "High Speed Power Efficient Indoor Wireless Infrared Communication Using Code Combining, PART- II," IEEE Transactions on Communications, Vol. 50, No. 9, Sep 2002.

56. S. Soliman, S. Glazko and P. Agashe, "GPS receiver sensitivity enhancement in wireless applications," IEEE MTT-S Symposium on Technologies for Wireless Applications, pp. 181 - 186, Feb 21 - 24 1999.

57. R. Akturan and W. J. Vogel, "Path diversity for LEO satellite-PCS in the urban environment," IEEE Transactions on Antennas and Propagation, Vol. 45, Issue 7, pp. 1107 - 1116, Jul 1997.

58. R. De Gaudenzi and F.Giannetti, "DS-CDMA satellite diversity reception for personal satellite communication: satellite-to-mobile link performance analysis," IEEE Transactions on Vehicular Technology, Vol. 47, Issue 2, pp. 658 – 672, May 1998.

59. T. Hatsuda, Y. Yamadaa J. Osada, T. Kobayasi, Y. Aoki and T. Kato, "Measured results of urban satellite-diversity (Sat. D) and space-diversity (SD) characteristics for mobile broadcast geostationary satellite system," IEEE Antennas and Propagation Society International Symposium, Vol. 3, pp. 117 - 120, Jul 8 - 13 2001.

60. Kazunari Shirai, Yoshitaka Ozaki and Hiroyasu Fukaya, (Aug 23 1994) "Diversity type global positioning system for motor vehicles," [Online] Available: http://patft.uspto.gov/netacgi/nph-Parser?Sect2=PTO1&Sect2=HITOFF&p=1&u=%2Fnetahtml%2FPTO%2Fsearch-bool.html&r=1&f=G&l=50&d=PALL&RefSrch=yes&Query=PN%2F5341301.

61. R. Klukas, G. Lachapelle, C. Ma and G.-I. Jee, "GPS signal fading model for urban centres," IEE Proceedings Microwaves, Antennas and Propagation, Vol. 150, Issue 4, pp. 245 - 252, Aug 2003.

62. Richard K. Martin, Jaiganesh Balakrishnan, William A. Sethares and C. Richard Johnson, Jr., "A Blind Adaptive TEQ for Multicarrier Systems," IEEE Signal Processing Letters, Vol. 9, No. 11, pp. 341 - 343, Nov 2002.

63. Joseph S. Accetta and David L. Shumaker, "The Infrared & Electro-Optical Systems Handbook Volume 2 Atmospheric Propagation of Radiation," Infrared Information Analysis Center, Ann Arbor, MI, USA and SPIE Optical Engineering Press, Bellingham, WA, USA, 1993.

64. G. W. Wornell, "Emerging applications of multirate signal processing and wavelets in digital communications," Proceedings of the IEEE, Vol. 84, Issue 4, pp. 586 - 603, Apr 1996.

65. A. R. Lindsey, "Wavelet packet modulation for orthogonally multiplexed communication," IEEE Transactions on Signal Processing, Vol. 45, Issue 5, pp. 1336 - 1339, May 1997.

66. L. Atzori, D. D. Giusto and M. Murroni, "Performance analysis of fractal modulation transmission over fast-fading wireless channels," IEEE Transactions on Broadcasting, Vol. 48, Issue 2, pp. 103 - 110, Jun 2002.

67. R. K. Martin, K. Vanbleu, M. Ding, G. Ysebaert, M. Milosevic, B. L. Evans, M. Moonen and C. R. Johnson, Jr., "Unification and evaluation of equalization structures and design algorithms for discrete multitone modulation systems," IEEE Transactions on Signal Processing, Vol. 53, Issue 10, Part 1, pp. 3880 – 3894, Oct 2005.

68. G. J. Foschini and M. J. Gans, "On limits of wireless communications in a fading environment when using multiple antennas," Wireless Personal Communications, Vol. 6, No. 3, pp. 311 - 335, Mar 1998.

69. N. Chiurtu, B. Rimoldi and E. Telatar, "On the capacity of multi-antenna Gaussian Channels," 2001 IEEE International Symposium on Information Theory, pp. 53, 24 - 29 Jun 2001.

70 Andrea Goldsmith, "Wireless Communications," Cambridge University Press, Aug 2005.

71 V. Tarokh, H. Jafarkhani and A. R. Calderbank, "Space-time block codes from orthogonal designs," IEEE Transactions on Information Theory, Vol. 45, Issue 5, pp. 1456 – 1467, Jul 1999.

72 H. Jafarkhani, "A quasi-orthogonal space-time block code," IEEE Wireless Communications and Networking Conference, Vol. 1, pp. 42 – 45, 23 – 28 Sep 2000.

73 Z. Liu, G. B. Giannakis and B. L. Hughes, "Double differential space-time block coding for time-selective fading channels," IEEE Wireless Communications and Networking Conference, Vol. 1, pp. 13 – 17, 23 – 28 Sep 2000.

74 O. Tirkkonen, A. Boariu and A. Hottinen, "Minimal non-orthogonality rate 1 space-time block code for 3+ Tx antennas," IEEE Sixth International Symposium on Spread Spectrum Techniques and Applications, Vol. 2, pp. 429 – 432, 6 – 8 Sep 2000.

75 A. Dabak, S. Hosur and R. Negi, "Space time block coded transmit antenna diversity scheme for WCDMA," IEEE Wireless Communications and Networking Conference, Vol. 3, pp. 1466 – 1469, 21 – 24 Sep 1999.

76. Yi Gong and K. B. Letaief, "Performance of space-time trellis coding over Nakagami fading channels," IEEE Vehicular Technology Conference, Vol. 2, pp. 1405 – 1409, 6 - 9 May 2001.

77. Y. Li and X.-G. Xia, "A Family of Distributed Space-Time Trellis Codes With Asynchronous Cooperative Diversity," IEEE Transactions on Communications, Vol. 55, Issue 4, pp. 790 – 800, Apr 2007.

78. Z. Safar and K. J. R. Liu, "Systematic space-time trellis code construction for correlated Rayleigh-fading channels," IEEE Transactions on Information Theory, Vol. 50, Issue 11, pp. 2855 – 2865, Nov 2004.

79. C. Kose and R. D. Wesel, "Universal space-time trellis codes," IEEE Transactions on Information Theory, Vol. 49, Issue 10, pp. 2717 – 2727, Oct 2003.

80. M. Uysal and C. N. Georghiades, "Effect of shadowing on the performance of space-time trellis-coded systems," IEEE Transactions on Wireless Communications, Vol. 3, Issue 4, pp. 1037 – 1042, Jul 2004.

81. Dong Wang and Xiang-Gen Xia, "Super-orthogonal differential space-time trellis coding and decoding," IEEE Journal on Selected Areas in Communications, Vol. 23, Issue 9, pp. 1788 – 1798, Sep 2005.

82. H. Jafarkhani and N. Seshadri, "Super-orthogonal space-time trellis codes," IEEE Transactions on Information Theory, Vol. 49, Issue 4, pp. 937 – 950, Apr 2003.

83. P. W. Wolniansky, G. J. Foschini, G. D. Golden and R. A. Valenzuela, "V-Blast: An architecture for realizing very high data rates over the rich-scattering channel," International Symposium on Signals, Systems, and Electronics, pp. 295 – 300, 29 Sep - 2 Oct 1998.

84. G. Lebrun, J. Gao and M. Faulkner, "MIMO transmission over a time-varying channel using SVD," IEEE Transactions on Wireless Communications, Vol. 4, Issue 2, pp. 757 – 764, Mar 2005.

85. Naofal Al-Dhahir, "Single-carrier frequency-domain equalization for space-time block-coded transmissions over frequency-selective fading channels," IEEE Communications Letters, Vol. 5, Issue 7, pp. 304 – 306, Jul 2001.

86. F. Pancaldi and G. M. Vitetta, "Frequency-domain equalization for space-time block-coded systems," IEEE Transactions on Wireless Communications, Vol. 4, Issue 6, pp. 2907 – 2916, Nov 2005.

87. D. P. Palomar and M. A. Lagunas, "Joint transmit-receive space-time equalization in spatially correlated MIMO channels: a beamforming approach," IEEE Journal on Selected Areas in Communications, Vol. 21, Issue 5, pp. 730 – 743, Jun 2003.

88. W. H. Gerstacker, F. Obernosterer, R. Schober, A. T. Lehmann, A. Lampe and P. Gunreben, "Equalization concepts for Alamouti's space-time block code," IEEE Transactions on Communications, Vol. 52, Issue 7, pp. 1178 – 1190, July 2004.

89. Xu Zhu and R.D. Murch, "Layered space-time equalization for wireless MIMO systems," IEEE Transactions on Wireless Communications, Vol. 2, Issue 6, pp. 1189 – 1203, Nov 2003.

90. G. Leus and M. Moonen, "Per-tone equalization for MIMO OFDM systems," IEEE Transactions on Signal Processing, Vol. 51, Issue 11, pp. 2965 – 2975, Nov 2003.

91. Taiwen Tang and R. W. Heath Jr. "Space-time interference cancellation in MIMO-OFDM systems," IEEE Transactions on Vehicular Technology, Vol. 54, Issue 5, pp. 1802 – 1816, Sep 2005.

92. Li Youming, "Maximum shortening SNR design for MIMO channels," IEEE International Symposium on Microwave, Antenna, Propagation and EMC

Technologies for Wireless Communications, Vol. 2, pp. 1488 – 1491, 8 - 12 Aug 2005.

93. M. Secondini, E. Forestieri and G. Prati, "Adaptive minimum MSE controlled PLC optical equalizer for chromatic dispersion compensation," Journal of Lightwave Technology, Vol. 21, Issue 10, pp. 2322 – 2331, Oct 2003.

94. W. Xi and T. Adali, "Integrated MAP Equalization and Coding for Optical-Fiber-Communication Systems," Journal of Lightwave Technology, Vol. 24, Issue 10, pp. 3663 – 3670, Oct 2006.

95. Anthony J. Weiss, "On the Performance of Electrical Equalization in Optical Fiber Transmission Systems," IEEE Photonics Technology Letters, Vol. 15, No. 9, pp. 1225 – 1227, Sep 2003.

96. T. Hirooka and M. Nakazawa, "Optical adaptive equalization of high-speed signals using time-domain optical Fourier transformation," Journal of Lightwave Technology, Vol. 24, Issue 7, pp. 2530 – 2540, Jul 2006.

97. G. L. Stuber, J. R. Barry, S. W. McLaughlin, Ye Li, M. A. Ingram and T.G. Pratt, "Broadband MIMO-OFDM wireless communications," Proceedings of the IEEE, Vol. 92, Issue 2, pp. 271 – 294, Feb 2004.

98 Y. G. Li, J. H.Winters and N. R. Sollenberger, "MIMO-OFDM for wireless communications: signal detection with enhanced channel estimation," IEEE Transactions on Communications, Vol. 50, Issue 9, pp. 1471 – 1477, Sep 2002.

99 C. Dubuc, D. Starks, T. Creasy and Yong Hou, "A MIMO-OFDM prototype for next-generation wireless WANs," IEEE Communications Magazine, Vol. 42, Issue 12, pp. 82 – 87, Dec 2004.

100 B. Lu, Guosen Yue and Xiaodong Wang, "Performance analysis and design optimization of LDPC-coded MIMO OFDM systems," IEEE Transactions on Signal Processing, Vol. 52, Issue 2, pp. 348 – 361, Feb 2004.

101. M. Fozunbal, S. W. McLaughlin and R. W.Schafer, "On space-time-frequency coding over MIMO-OFDM systems," IEEE Transactions on Wireless Communications, Vol. 4, Issue 1, pp. 320 – 331, Jan 2005.

VITA

Sangwoo Lee

Sangwoo Lee received his B.S. degree in electrical engineering from Yonsei Univ., Seoul, Korea in 1998. From Jan ’98 to Jul ’01, he worked with LG Electronics as an associate engineer. He has been being affiliated with the Center for Information and Communications Technology Research (CICTR) since May 2002. He received his M.S. degree in electrical engineering from the Pennsylvania State Univ., University Park, US in 2003, and has been pursuing his Ph.D. degree at the same university since then. His main research interest is in free-space optical communications, resource-efficient multicarrier modulation systems, MIMO signal processing schemes, equalization schemes, and 3G and beyond mobile communications. He has several IEEE and SPIE publications.

Publications

- Sangwoo Lee, "A Fixed Radio System using MIMO Cancellation and Equalization; P erformance Issues”, M.S. dissertation, The Pennsylvania State University, May 2003
- H. Wu, S. Lee and M. Kavehrad, “A Fixed Radio System using MIMO Cancellation a nd Equalization and its Performance Model,” Proceedings of IEEE PIMRC, Barcelon a, Spain, Sep 2004
- Sangwoo Lee, Belal Hamzeh and Mohsen Kavehrad, “Airborne Laser Communicatio ns and Performance Enhancement by Equalization,” Photonics West 2006, San Jose, CA, USA, Jan 2006
- Sangwoo Lee and Mohsen Kavehrad, “Airborne Laser Communications Using Wavel et Packet Modulation and its Performance Enhancement by Equalization,” Defense an d Security Symposium 2006, Orlando, FL, USA, Apr 2006
- Sangwoo Lee and Mohsen Kavehrad, “Airborne Laser Communications with Impulse Response Shortening and Viterbi Decoding,” MILCOM 2006, Washington D C, USA, Oct 2006
- Sangwoo Lee and Mohsen Kavehrad, “Free-Space Optical Communications with Cha nnel Shortening Filter and Viterbi Equalizer,” submitted to IEEE Transactions on Wir eless Communications